

TECHNISCHE UNIVERSITÄT DRESDEN
FAKULTÄT MASCHINENWESEN
Lehrstuhl für Laser- und Oberflächentechnik

**Atmospheric pressure plasma jet deposition of Si-based coupling
films as surface preparation for structural adhesive bonding in
the aircraft industry**

Comparison of joint durability after APPJ-CVD and solution derived silane treatments

Dipl.-Ing. Philipp Bringmann
(Geb. am 30.01.1981 in Schrobenhausen)

Dissertation
zur
Erlangung des akademischen Grades eines

**Doktoringenieurs
(Dr.-Ing.)**

Gutachter der Dissertation: 1. Prof. Dr.-Ing. habil. E. Beyer (TU Dresden)
2. Prof. Dr. G. Critchlow (Loughborough University)

Tag der Verteidigung: 02. Dezember 2015

Acknowledgements

First of all, I'd like to sincerely thank Prof. Dr.-Ing. habil. Dr. h.c. Eckhard Beyer and Dr. rer. nat. Irene Jansen of TU Dresden for supervising and guiding me during the completion of my doctoral thesis.

My deep gratitude also goes to Prof. Dr. Gary Critchlow of Loughborough University for the many fruitful discussions and especially for taking over the role as referee of this dissertation.

I am also very grateful to Dr. Franz Gammel for his guidance and support during my time at EADS Innovation Works. Many thanks to all my former colleagues at EADS Innovation Works for the good team work, excellent working atmosphere and, above all, your friendship. In particular, I'm very thankful to Dr. Jürgen Wehr for his continuous support and valuable remarks to the thesis; to Theo Hack for the very knowledgeable input and fruitful discussions regarding all corrosion aspects of this work; to Oliver Rohr for his help concerning plasma deposition and surface pre-treatment (and for sharing the office with me) and to Max Kolb for his help with XPS and SEM analyses. I'm also much indebted to my good friend Dr. Dominik Raps for his advice on electrochemistry.

The support with SEM, TEM and XPS analysis as well as the valuable discussions on interfaces and sol-gel films by and with Dr. Stefan Dieckhoff and Dr. Malte Burchardt of Fraunhofer IFAM and with Dr. Martin Beneke of Airbus Bremen are greatly appreciated.

For the AES and CD-XPS analyses I'm very thankful to Dr. Wolfgang Unger and Dr. Thomas Groß of BAM in Berlin. I'm also grateful to OFG Analytik GmbH, Münster, for the ToF-SIMS measurements and in particular to Dr. Roger Dietrich for the various discussions concerning this technique.

Moreover, this work could not have been completed without the understanding and support of my management at my current employer, Airbus; I'm especially grateful to Dr. Michael Schoenwetter.

Most importantly, this thesis is built on the support, love and understanding of my friends, my family and Julia.

Table of contents

Acknowledgements	III
Table of contents	V
List of abbreviations.....	VII
Abstract	IX
Zusammenfassung.....	XI
1 Introduction.....	1
2 Theoretical background.....	7
2.1 Polymer adhesion on aluminium surfaces.....	7
2.1.1 Aluminium surfaces	7
2.1.2 Epoxy-aluminium interphase	8
2.2 Surface treatments of aluminium	10
2.2.1 Surface pre-treatment.....	11
2.2.2 Silane and sol-gel coupling films.....	12
2.2.3 APPJ-CVD of Si-based coupling films.....	15
2.3 Durability of bonded aluminium joints	16
2.3.1 Hydrothermal ageing in hot-wet conditions.....	16
2.3.2 Bondline corrosion	18
2.4 Gap analysis	20
3 Experimental	23
3.1 Sample preparation	23
3.2 Mechanical and durability testing	28
3.3 Surface and interface analyses	30
3.4 Electrochemical analyses	34
4 Results and discussion.....	37
4.1 Plasma film characterisation and influence on adhesion.....	37
4.1.1 Film thickness, morphology and chemical composition.....	37
4.1.2 Chemical functionality of surface layer	45
4.1.3 Correlation of thin film properties with joint strength	47
4.2 Aluminium surface characterisation and influence on adhesion	50
4.2.1 Surface roughness and topography	50
4.2.2 Aluminium oxide characterisation	54
4.2.2.1 Oxide thickness.....	54
4.2.2.2 Chemical state of surface oxides.....	57

4.2.3	Analysis of the interface between aluminium oxide and plasma film.....	62
4.2.4	Correlation of surface pre-treatment and strength of plasma treated joints	67
4.3	Durability of bonded joints	72
4.3.1	Interface stability under external loads and aqueous attack	73
4.3.1.1	Interface stability under cyclic loads and immersion in water	73
4.3.1.2	Interface stability under permanent load in a hot-wet environment.....	78
4.3.2	Long-term stability in hostile environments	80
4.3.2.1	Bondline stability in hot-wet conditions	81
4.3.2.2	Bondline stability in corrosive atmosphere	85
4.3.2.3	Bondline corrosion mechanism for Si-based treatments	102
4.4	Summary of findings and plasma-silane-combination.....	120
5	Conclusion and outlook	127
A	Appendix	131
A.1	Thin film characterisation and influence on adhesion.....	131
A.2	Oxide characterisation and influence on adhesion	134
A.3	Joint durability	145
B	Bibliography	155

List of abbreviations

AFM	atomic force microscopy
APPJ	atmospheric pressure plasma jet
APS	3-aminopropyltriethoxysilane
ARALL	aramide-aluminium laminates
C	capacitance
CAA	chromic acid anodising
CD-XPS	chemical derivatisation X-ray photoelectron spectroscopy
CPE	constant phase element
CSA	chromic sulphuric acid
CSP	chromic sulphuric acid pickling
CVD	chemical vapour deposition
DSTO	Defence Science and Technology Organisation
EAL	effective attenuation length
EASA	European Aviation Safety Agency
EDX	energy-dispersive X-ray spectroscopy
EELS	electron energy loss spectroscopy
EIS	electrochemical impedance spectroscopy
FAA	Federal Aviation Administration
FPL	Forest Products Laboratory
FTIR	Fourier transform infrared spectroscopy
FWHM	full width at half maximum
G_I	fracture energy (mode I)
GLARE	glass laminate aluminium reinforced epoxy
GPS	3-glycidoxypropyltrimethoxysilane
HMDSN	hexamethyldisilazane
HMDSO	hexamethyldisiloxane
IMFP	inelastic mean free path
LSM	laser scanning microscope
MDL	mechanically deformed layer
OMCTS	octamethylcyclotetrasiloxane
PAA	phosphoric acid anodising
PMMA	poly(methyl methacrylate)
PSA	phosphoric sulphuric acid anodising

PTFE	polytetrafluoroethylene
R	load ratio (dynamic single lap shear testing)
R	resistance (electrochemical impedance spectroscopy)
RAIRS	reflection absorption infrared spectroscopy
RT	room temperature
SEM	scanning electron microscope
SLJ	single lap shear joint
SLM	standard litre per minute
SST	salt spray test
STEM	scanning transmission electron microscope
TDCB	tapered double cantilever beam
TEM	transmission electron microscope
TEOS	tetraethyl orthosilicate
TFAA	trifluoroacetic anhydride
ToF-SIMS	time-of-flight secondary ion mass spectrometry
TPOZ	tetrapropyl zirconate
ω	frequency
XPS	X-ray photoelectron spectroscopy
Y	pseudo capacitance

Abstract

Damages of metallic aircraft structures that occur during manufacturing, assembly and in service require local repair. Especially with current service-life extensions of ageing aircraft fleets, the importance of such repair methods is increasing. Typically, the repair of smaller damages on aluminium fuselage or wing skins is done by riveting a patch onto the flawed structure. However, the use of rivets reduces the strength of the structure and promotes fatigue. Joining the patch by adhesive bonding would not only offer more homogenous load distribution and weight savings, but even an increase of structural integrity. Metal adhesive bonding is commonly used in aeronautics, but requires elaborated surface treatments of the adherends, employing hazardous chemicals like chromates, due to the high durability demands. Furthermore, these treatments are usually tank processes that are not suitable for local repairs. Hence, there is a strong need for locally applicable surface preparation methods that allow safe and reliable adhesive bonding of primary aircraft structures.

The aim of this thesis is to assess the – still emerging – method of atmospheric pressure plasma deposition of silicon (Si) containing compounds concerning its suitability as surface preparation for adhesive bonding of aluminium aerostructures. Atmospheric plasma deposition is not yet used in the aircraft industry, and the knowledge on functionality of this technology concerning bonding of aluminium parts is limited. Moreover, the durability requirements of the aircraft industry greatly exceed the standards in other industries. Hence, special attention is paid to a thorough analysis of the key characteristics of the deposited coupling films and their effectiveness in terms of adhesion promotion as well as joint durability under particularly hostile conditions. In order to do so, the altering mechanisms of the treated joints and the behaviour of the coupling films during accelerated ageing will be investigated in detail for the first time in this thesis. Furthermore, the influence of the aluminium surface pre-treatment (i.e. topography and oxide properties of the substrate) on the overall joint performance after coupling film deposition is thoroughly examined. Based on these findings, the surface preparation is optimised, and a process is developed to achieve maximal joint performance.

As alternative local surface treatments prior to adhesive bonding, solution derived deposition of silane and sol-gel films have already been widely investigated and can be considered as reference, even though these techniques are rarely used in civil aeronautics. The knowledge on their effectiveness and capabilities in corrosive atmosphere is still very limited. Therefore, all analyses of degradation mechanisms are conducted for both plasma deposition and wet-chemical reference treatments to reveal the differences and communalities of the two Si-based coupling films. Physical and chemical analysis of the films, the oxides and the interfaces reveal differing, but interdependent failure mechanisms that are inhibited differently by the individual coupling films.

Using the optimum deposition parameters, plasma films of only several nanometres in thickness significantly enlarge the corrosion resistance of bonded joints, reaching almost the level of anodising treatments with several micrometres thick oxides and strongly outperforming solution derived silane treatments. However, plasma film performance is found to be largely dependent on the precursor selection. With plasma deposition of 3-glycidoxypropyltrimethoxysilane, which has not been reported before, highest joint stability is achieved. Moreover, it is discovered that the properties of plasma and solution derived silane based films are complementary. It is shown that an optimised combined plasma and wet-chemical treatment process provides even superior resistance to bondline corrosion than state-of-the-art anodising techniques.

Zusammenfassung

Beschädigungen metallischer Flugzeugstrukturen, die sowohl während der Produktion als auch im Betrieb verursacht werden können, bedürfen lokaler Reparaturverfahren. Insbesondere durch die Verlängerung der Lebenszeiten derzeitiger Flugzeugflotten gewinnen effektive Reparaturmaßnahmen an Bedeutung. In der Regel werden kleinere Schäden in der Außenhaut durch Nieten eines Patches auf die geschädigte Stelle behoben. Allerdings mindert die Nietung die Festigkeit und die Ermüdungsbeständigkeit der Primärstruktur. Dagegen eröffnet strukturelles Kleben des Patches gleichmäßige Lastverteilung, Gewichteinsparung und sogar höhere Festigkeiten. Strukturelles Kleben ist durchaus verbreitet in der zivilen Luftfahrtindustrie nicht aber in lokaler Anwendung. Die gängigen Oberflächenvorbehandlungsverfahren sind aufwendige Badprozesse, die nicht für die lokale Reparatur geeignet sind und darüber hinaus noch große Mengen umwelt- und gesundheitsschädlicher Chemikalien, wie Chromate, bedürfen. Deshalb werden dringend lokale Oberflächenbehandlungen benötigt, die sichere und zuverlässige strukturelle Klebungen ermöglichen.

Das Ziel dieser Arbeit ist eine detaillierte Bewertung der chemischen Gasphasenabscheidung mittels einer Plasmajetquelle unter Atmosphärendruck (APPJ-CVD) bezüglich ihrer Eignung als Oberflächenbehandlung für das strukturelle Kleben von Aluminiumflugzeugstrukturen. APPJ-CVD wird noch nicht in der Luftfahrtindustrie eingesetzt und das Wissen über die Funktionsweise der abgeschiedenen Haftvermittlerschichten auf Aluminium ist relativ gering. Aufgrund der extremen Anforderungen der Luftfahrt bezüglich Alterungsbeständigkeit von strukturellen Klebungen liegt das Augenmerk auf dem Verständnis der entscheidenden Schichteigenschaften, der Funktionsweise der Beschichtungen in Bezug auf die Haftung und der Alterungsstabilität in aggressiven Medien. Um dieses Verständnis zu erlangen, werden die Alterungsmechanismen an der Grenzfläche sowie die Veränderungen der Haftvermittlerschichten im Detail untersucht. Darüber hinaus wird der Einfluss der Aluminiumvorbehandlung beziehungsweise der daraus resultierenden Oberflächentopographie und Oxidzusammensetzung auf die Stabilität der Klebung eingehend analysiert. Basierend auf diesen Untersuchungen wird ein neuer, optimierter Behandlungsprozess entwickelt.

Als alternative lokale Behandlungsverfahren wurden nasschemisch abgeschiedene Silan- und Sol-Gel basierte Haftvermittlerschichten bereits ausgiebig untersucht. Obwohl diese kaum Verwendung in der zivilen Luftfahrtindustrie finden, können sie durchaus als Referenz angesehen werden. Allerdings ist der Wissensstand bezüglich ihrer Alterungsstabilität in korrosiver Atmosphäre immer noch sehr begrenzt. Deshalb werden alle Stabilitätsuntersuchungen sowohl für Plasma- als auch für nasschemisch abgeschiedene Haftvermittlerschichten durchgeführt, um Gemeinsamkeiten und Unterschiede dieser beiden siliziumbasierten Beschichtungen herauszustellen. Physikalische und chemische Analysen der Schichten, der Aluminiumoxide und der Grenzflächen zeigen drei voneinander abhängige Schadensmechanismen, die durch die verschiedenen Behandlungsverfahren unterschiedlich gemindert werden. Trotz einer Schichtdicke von nur wenigen Nanometern erhöhen die Plasmapolymerschichten die Korrosionsbeständigkeit der Klebfugen deutlich; nasschemische Silanabscheidung vermag dies jedoch nicht. Allerdings ist die Leistungsfähigkeit der Plasmaabscheidung stark von der Auswahl des Precursors abhängig. Durch Plasmaabscheidung von 3-Glycidylxypropyltrimethoxysilan, das normalerweise nicht für die Gasphasenabscheidung verwendet wird, wurde die höchste Stabilität der Klebungen erreicht. Zudem zeigt sich, dass die Eigenschaften der Plasma- und nasschemisch abgeschiedenen Schichten komplementär sind. Durch Verbindung beider Verfahren wird erstmals eine bessere Beständigkeit gegen Klebfugenkorrosion erzielt als mit einem qualifizierten Anodisierprozess.

1 Introduction

Surface preparation for adhesive bonding of aircraft structures

The history of adhesive bonding of primary aircraft structures goes back more than 70 years, which was even before the wide use of aluminium as major structural material. With the development of synthetic polymers in the late 1930s and early 1940s, adhesive bonding was introduced to join wooden wing and fuselage structures by pioneering companies like Fokker and de Havilland [1], [2]. Due to the first adhesives being brittle and tending to crack, breakthrough of the technology was not achieved until the advancements in chemical functionalization of the thermosetting phenolic adhesives, developed by de Bruyne in the mid 1940s [3], which significantly enhanced fracture toughness. Aluminium alloys replaced wood as construction material in those days, and adhesive bonding, which offered weight savings and especially increased fatigue life compared to traditional joining by mechanical fastening, became widely used in aircraft manufacturing.

In the late 1960s, with the evolution from high-temperature-curing and still relatively brittle phenolic adhesives to 120 °C hardening epoxy adhesives, which allowed higher fatigue resistance of the aluminium alloys, it became apparent that ageing of the bonded joint needed to be considered. While phenolic resins produced very stable bonds, the novel epoxy systems were quite sensitive to moisture, leading to adhesion failure at the polymer-metal interface. Therefore, low-viscous bonding primers, which are a mixture consisting of epoxy, epoxynovolak and phenolic resins in volatile solvents, were introduced. Nevertheless, in-service aircraft inspections in the 1970s revealed that the combination of primer, epoxy adhesives and pickling of aluminium in chromic-sulphuric acid (CSA), which was the predominant surface preparation at that time, did not provide sufficient durability. Already after a few short years of service, joint delamination with a corroded bondline was discovered occasionally [2]. Particularly bonded joints in the lower fuselage, the so-called bilge area, where the condensation derived electrolytic bilge solution accumulates, were to large extents affected [4], [5]. The analysis of the damages showed that the whole system of the bonded joint, i.e. alloy, surface treatment, primer and adhesive, affected the occurrence and degree of bondline degradation; if epoxy adhesives were used, especially the surface treatment was of crucial importance for the bondline stability. In general, the quality of the surface preparation is considered nowadays as the most important factor for successful adhesive bonding [6]. It was found that anodising in chromic acid (CAA), normally referred to as Bengough-Stuart process and which had been already developed in the 1920s for corrosion protection [7], is a well suitable surface preparation technique for the creation of durable joints. Alternatively, a phosphoric acid anodising (PAA) process developed by the Boeing company [8] provides similar protection against bondline corrosion but creates more sensitive surfaces that make part handling during the manufacturing process more difficult. Both anodising processes are preceded by a CSA pickling step. Generally speaking, anodising processes are robust but require extensive knowledge of the process and its boundaries as well as strict process control. It has been demonstrated that with these surface treatments durable bonds are achieved; even if the edge sealing is damaged, and the joint is exposed to corrosive media, the degradation is minimized to a level that does not run the risk of complete joint failure.

Still, a certain mistrust against adhesive bonding remains in the industry until today, which is mainly caused by the inability to assess the quality of a bonded joint by non-destructive means. Hence, a fail-safe fatigue strength approach is followed according to FAR 23.573 when designing primary structures of civil and most military aircrafts, where multiple load paths assure that the remaining structure provides the required strength (limit load capacity) even after loss of the bonded joint. The safe life approach without alternative load paths, where no crack formation may occur during the whole life span of the airframe, is limited to some military applications, like the wing structure of the F-18 [9], [10]. The risk of the safe life approach is, however, that the joint will not fail due to loads but due to degradation of the interface. In general, hardly any cohesion failure, i.e. failure due to overloading (bad design), of properly cured bonded

joints has been reported. More or less all known bond failures were caused by ageing of the joints, especially if improper surface preparation was used. To ensure durability in the hostile conditions that can occur over the service life of an aircraft, various quality tests were established in the aircraft industry [11]. However, because of the structural redundancy, certification regulations only required – until recent years – the demonstration of initial static and fatigue strength for airworthiness [12]; additional requirements, demanding that surface treatment and bonding are conducted in accordance with process specifications and that corresponding quality assurance is in place, are also not directly targeting on the ageing resistance. Demonstration of bond durability had not been required until an update of the Advisory Circular AC 20-107 (now version “B”) of the FAA [13], [14] and the amendment of EASA’s AMC 20-29 [15] in 2009 and 2010 were issued. Both documents require that all metal interfaces have chemically activated surfaces and consider adhesion failure as unacceptable failure mode in any test. Still, they are not specific on how durability should be demonstrated. Due to the absence of specific regulations, a variety of accelerated test methods, like the wedge test in hot-wet conditions (ASTM D3762) or the exposure of bonded coupons to aggressive environments such as salt fog, jet fuel or hydraulic oil, are used in the industry to demonstrate ageing resistance of the bonded joints.

When qualified adhesives are employed, surface treatment is the most critical factor regarding durability. In particular the ability of the joints to resist displacement of the polymer-metal interface due to moisture and their stability against oxide transformation caused by hydration or corrosion is crucial. As mentioned above, durable bonds are achieved with proper surface treatments. The vast majority of the reported bond failures were caused by improper surface preparation and not by a bad execution of suitable treatment processes. Suitable treatments are typically tank processes with several cleaning and etching steps, followed by anodising at elevated temperatures, which, however, are highly energy-consuming and produce a large amount of liquid waste, because the whole part and not only the to-be-bonded area is treated. Furthermore, most of these processes contain carcinogenic chromates and other environmentally not benign substances in high quantity. Therefore, pre-treatments without CSA pickling and alternative anodising processes replacing CAA have been developed in recent years [16]-[18] and are currently being implemented in the aircraft industry. As tank processes, they are still limited to traditional component manufacturing and are not suitable for local applications like bonded repair or local surface preparation of integral and already equipped structures allowing new manufacturing concepts.

Due to ageing of aircraft fleets and extension of initially planned service lives, there is a strong need for effective repair of damages caused by fatigue, environmental degradation and impact [19], [20]. Bonded repair, i.e. adhesive bonding of a metallic or composite patch onto a damaged aircraft structure, is an advantageous alternative to classical mechanical repair techniques. The uniform stress distribution over a larger stress-bearing area allows a more efficient design and entails higher fatigue resistance. Bonded repair of structures made of fibre metal laminates, like GLARE or ARALL, is especially advantageous as the fibres of the structure are not damaged during the repair process, which is the case with fastener repair. Hence, the strength of the repaired structure exceeds the one of the initial structure and is not reduced by hole-drilling. Holes concentrate stresses and significantly reduce the fatigue life of any metal skin structure; in many cases the potential bolted repair case even defines the overall sizing, i.e. the thickness of the skin. Thus, bonded repair could allow smarter design, leading to significant weight savings. Additional advantages are, among others, a cost saving potential, the isolation of dissimilar materials by the dielectric adhesive preventing galvanic corrosion as well as the prevention of crevice corrosion by the sealed joint [9], [10], [20], [21].

Locally applicable surface preparation is needed to achieve durable repairs. Adaptations of PAA for local applications exist and provide similar stability in hot-wet conditions [22], but are difficult to handle, cannot be applied to all areas, require several hours and produce toxic waste. Moreover, they do not provide the same robustness, homogeneity and reliability as the tank processes, leading to a lower bondline corrosion resistance [23]. Thus, they are neither desired nor widely employed for commercial aircraft repairs. What is more, this unsatisfying surface treatment situation entailed certain mistrust against bonded repair of

metallic aircrafts in general. Therefore, reliable and locally applicable alternatives to anodising are needed to support the wide use of bonded repair.

Si-based local surface preparation techniques

At the Australian DSTO that pioneered bonded repair already in the 1970s [20], [21], a special surface preparation process was developed by Baker and Chester at the beginning of the 1990s [24]. It consisted of grit-blasting of the aluminium surface followed by the application of an aqueous solution of a silane adhesion promoter and, today, is commonly known as the “Australian Silane Surface Treatment”. The adhesion promoting capabilities of functionalised silanes were discovered in the 1940s and then systematically analysed and optimised by Plueddemann from the 1950s onwards [25]. The most commonly used silane, which is also employed by Baker and Chester, is 3-glycidoxypropyltrimethoxysilane (GPS). GPS can react with the hardener component of the adhesive via opening of its epoxy ring. After hydrolysis of the methoxy groups in acidic aqueous solution, the formed silanol groups bond strongly to the oxide. With strong bonding to both sides, the GPS derived film highly improves the stability of the aluminium-epoxy interface. Various studies on the effectiveness of GPS solutions have identified all major influencing factors on the resulting joint stability, like surface pre-treatment, solution chemistry and its impact on hydrolysis as well as curing conditions [26], [27]. Hence, the application parameters are well understood and the stabilisation of the bonded joint against aqueous attack has been demonstrated under multiple accelerated test conditions. This method is even used for military aircrafts with proven results after 20 years of service; however, bonding was not conducted in areas that are prone to corrosion.

Mid of the 1990s, the process – that involves thermal curing – was further developed by Blohowiak and co-workers at the Boeing Company, adding another metal-organic precursor for avoiding a dedicated high-temperature curing step [28]. This sol-gel process, often referred to as Boegel repair process, is also proposed for repair of civil aircrafts [29] and was commercialised as AC-130. Both with AC-130 and GPS application, similar hot-wet durability as with anodising is achieved after adequate mechanical surface pre-treatment, like grit-blasting [30]. While the laborious masking of the surrounding against the liquid that is required with these treatments is acceptable, bonded repair is still not common in commercial aviation due to a persistent lack of confidence. Both silane based processes require strict adherence to the preparation procedures as mixing of components, application and curing strongly impact the joint strength, with each step being a potential source for mistakes and deviations from the process.

The silane and sol-gel techniques have been extensively tested in hot and moist conditions, but knowledge on their behaviour in corrosive environments is very limited compared to anodising. First unpublished exploratory studies of the author revealed that the silane/sol-gel treatments do by far not provide equivalent resistance to corrosive degradation as anodising. However, high joint stability in corrosive atmosphere, as well as the understanding of the associated degradation mechanisms are essential to build further confidence in local adhesive bonding.

During the last 15 years, atmospheric pressure plasma jet chemical vapour deposition (APPJ-CVD) of functional coatings emerged as a dry alternative to wet-chemical deposition [31]. In plasma jet sources non-equilibrium plasma is created remotely and then blown onto the substrate by the gas flow [32]. Precursors are normally injected at the nozzle where the plasma exits the source, i.e. at the transition zone from excitation volume to the afterglow jet where plasma reactions (like fragmentation) occur instantly. Then, the activated fragments polymerise upon contact with the substrate surface and form a plasma polymer film. Most commonly, Si-organic precursors are employed for deposition of $\text{Si}_x\text{O}_y\text{C}_z$ films. Other than with low pressure plasma CVD, substrates are not limited by reactor size with the APPJ techniques, which allows fast in-line treatments integrated in production. Atmospheric plasma deposition is not yet used in aircraft manufacturing or maintenance. Only some experimental research on removal of contamination and activation of metallic surfaces using APPJ devices prior to silane or sol-gel application has been conducted [33], [34], demonstrating the feasibility of a potential plasma treatment in repair bonding. In other industries, like electronics or automotive, first APPJ-CVD applications are already implemented in production [35], [36]. In accelerated ageing tests these plasma films have shown to reduce delamination

and degradation of the interface between aluminium alloys and sealants or adhesives [37]-[39]. Generally speaking, Si-based plasma derived films were found to form strong interfaces with metal oxide surfaces [40] and to inhibit electrochemical reactions at the interface leading to de-adhesion [41], [42].

Even though these promising results were obtained with materials and under conditions differing from the ones used in aircraft industry, they indicate that atmospheric plasma deposition of Si-based precursors could be an alternative to current surface treatments for structural bonding in aeronautics. Nevertheless, in order to assess the capabilities of the plasma deposition, the key characteristics of the deposited coupling films must be identified and analysed with a particular focus on their effectiveness regarding interface stability and overall joint performance.

Today, different atmospheric plasma jet sources that vary in discharge type, electron or ion temperature and process gas exist [43]. Previous findings show that the silica-like coupling films deposited by a controlled arc-discharge source (Plasmatreat GmbH) with pressurized air as plasma gas lead to superior joint strengths compared to carbon-rich films derived from a direct barrier discharge (DBD) source with helium as process gas [44]. Therefore, this thesis investigates deposition of Si-organic precursors with this commercialised Plasmatreat APPJ system, also known as PlasmaPlus[®] process, regarding its potential as surface treatment for structural adhesive bonding of aluminium alloys in aircraft industry.

Scope, objectives and structure of the dissertation

The principal scope of this work is to evaluate the potential of APPJ deposition of Si-organic compounds as surface preparation for structural bonding of high strength aluminium aircraft structures. The aim is to correlate the scientific analysis of the deposited films and their interfaces – in their initial state as well as after ageing – to the performance of joints in terms of mechanical strength and stability in hostile environments. Since not all of the various requirements to adhesive joints needed for qualification in aeronautics can be covered exhaustively, the focus of this thesis lies on the most critical aspects for surface treatments providing a solid foundation for further assessment of this technology. Physical and chemical properties of the substrate surface and of the coupling film are correlated to the identified degradation mechanisms and then to the macroscopic test results. By understanding the characteristics and the degradation mechanisms, the capabilities and limitations of the process can be explained, allowing for the selection of the best process and generating of further confidence in the significance of the test results. It will be also shown that the process can be optimised by improving specific properties. Moreover, the performance of APPJ deposition is compared to state of the art anodising techniques and silane/sol-gel treatments. Degradation mechanisms of joints treated with silane based reference techniques are also studied in detail as this helps to understand the prevailing failure mechanisms and as the existing scientific data on degradation under corrosive conditions is rather limited.

The dissertation begins with a literature overview on the relevant scientific basics and state of the art processes regarding bonding of aluminium with epoxy adhesives. This part contains the characteristics of aluminium surfaces and the corresponding oxide as well as the influence of intermetallics found on the aerospace-typical Al-Cu (2000 series) alloys. Furthermore, the Al-epoxy interphase, including adhesion theories and bond formation, is briefly discussed, before the functionality of Si-organic based treatments is explained. This surface treatment section covers the aluminium surface pre-treatment, i.e. mechanical or chemical removal of the native oxide layer, which is the first step of every surface preparation process, as well as deposition of coupling films based on Si-organic compounds; Si-based treatments being the solution derived GPS/sol-gel techniques and plasma deposition. The literature overview further comprises major aspects concerning ageing of bonded aluminium joints, including hydrothermal ageing of aluminium and epoxy polymers as well as the deterioration of the interface. Special focus lies on the degradation mechanism of Al-Cu alloy joints in corrosive media, the bondline corrosion. The literature overview closes with a gap analysis comparing the current level of knowledge with the required information to judge whether APPJ-CVD is truly a potential surface treatment for adhesive bonding and explaining the corresponding investigations that will be covered within the main part of this work.

Before the results are presented and discussed, the experimental processes and employed materials will be briefly described and all relevant process parameters will be displayed. Moreover, all employed test and characterisation methods will be specified in this section.

The core part of this dissertation assesses and discusses the key aspects of APPJ deposition for adhesive bonding of aluminium structures in detail. In particular, the focus lies on three main objectives that are currently underreported in available studies:

- 1) Investigation of the impact of precursor type on the properties of the plasma films and correlate these to the mechanical joint strength
- 2) Determination the influence of the surface pre-treatment on the mechanical strength and the durability of APPJ-CVD treated joints
- 3) Understanding and comparison of the ageing mechanisms of APPJ-CVD and silane/sol-gel treated joints in hot-wet and corrosive conditions.

This part provides an integral view on microscopic properties of the substrate surface and the coupling films, on the prevailing damage mechanisms and on the overall joint performance. The focus is directed towards the ageing behaviour of the joints in hot-wet and corrosive environment. The identified degradation mechanisms and functionalities of the coupling films are correlated explaining macroscopic joint performance and allowing an optimisation of the surface preparation process. Test results are compared to state-of-the-art surface treatments to grade the obtained stability with regard to industry requirements.

Ultimately, it will be shown that the qualities of the silane and plasma derived coupling films, which are to a large extent complementary, can be combined to a treatment process that even outperforms state-of-the-art anodising processes.

Finally, the overall conclusion will be drawn, putting the findings in the broader context of structural bonding in aeronautics and providing an outlook for further research and optimisation.

2 Theoretical background

2.1 Polymer adhesion on aluminium surfaces

2.1.1 Aluminium surfaces

With its low standard electrode potential ($E^\circ = -1.66$ V), aluminium is very reactive and not thermodynamically stable in contact with water. However, due to the high electronegativity and affinity to oxygen the surface is covered by a dense, a few nanometres thin, passivation oxide layer that is instantly formed in ambient air. The non-crystalline film consists of an anhydrous γ - Al_2O_3 “bulk” and a hydrous top layer reported to be of oxyhydroxide (AlOOH) and trihydroxide ($\text{Al}(\text{OH})_3$) nature [45]-[49]. Thermodynamic considerations reveal that for thin films the amorphous state is even more favourable than a crystalline structure [50]. Exposure of aluminium to moist air or water below 90 °C leads to formation of a pseudoboehmite layer covered with loosely bound bayerite crystals [49], [51], [52]. Pseudoboehmite is poorly crystallised gelatinous boehmite with water molecules intercalated between the octahedral layers. Aluminium belongs to the category of metals where the oxidation state of the outermost layer and the barrier film are similar, i.e. the highest oxidation state Al^{3+} [47], [49], [51], [53], [54]. As the molecular volume of the oxide film is about 50 % higher than the one of the aluminium, the oxide layer is under compression which allows a certain deformation without rupture. Having an inert insulating character, the oxide layer acts as a very effective corrosion barrier [47], [53], [55]. The amphoteric oxide film is stable in the pH range roughly between 4 and 9 with a minimum solubility at pH 5. Below and above this range aluminium corrodes yielding Al^{3+} respectively AlO_2^- [56] [57]. The surface oxides have acidic and basic Lewis properties with alkalinity and acidity depending on the surface conditioning method [58]. Even in neutral environments the native oxide film is susceptible to further hydration in humid atmosphere at elevated temperatures [51].

Despite its high corrosion resistance, pure aluminium is not employed in aircraft manufacturing due to its poor mechanical properties. Instead, high-strength and damage tolerant alloys, like the Cu-rich 2000-series (e.g. AA 2024), are used. With relatively high concentrations of Cu and Mg (Table 2.1) these alloys are very prone to corrosion, especially as Cu-rich intermetallics are formed during alloy solidification creating local galvanic elements that initialise local corrosion (pitting). It has been demonstrated that the prevailing Al_2CuMg intermetallic particles (S-phase) already dissolve upon exposure to electrolytes with very low chloride concentrations [59]. Though initially anodic to the matrix, the S-phase changes its character with ongoing Cu-enrichment leading to dissolution of the surrounding matrix. Other intermetallics like Al-Cu-Fe-Mn or the θ -phase (Al_2Cu) are cathodic and cause corrosive attack of the matrix from the beginning [60]. In total, Hughes et al. recently identified nine different phase compositions for AA2024-T3 [61]. For corrosion protection reasons these alloys are often used in clad state, i.e. a pure aluminium clad layer is rolled onto the base alloy.

Table 2.1: Elemental composition (wt.%) of AA 2024-T3 according to ASTM B209-10 [62]

Cu	Mg	Fe	Si	Mn	Zn	Ti	Cr	Al
3.8 - 4.9	1.2 - 1.8	0.5	0.5	0.3 - 0.9	0.25	0.15	0.1	remainder

During the hot rolling process the sheet aluminium is contaminated with carbonaceous release agents that need to be removed before further processing. Besides contamination, formation of crystalline γ - Al_2O_3 due to the high temperature of the rolling process occurs [49]. Moreover, a so-called mechanically deformed layer (MDL) of a few microns thickness obtaining inhomogeneous properties is formed during rolling at the surface of the metal sheets. Hence, all sheets need to undergo a surface pre-treatment process that

removes the MDL, the initial oxide and the contamination. Typically, removal is carried out by alkaline cleaning and chemical etching. During the etching process the intermetallics present at the surface are removed, which entails an increase of roughness due to creation of pits. Alternatively, mechanical abrasion can be employed for local applications. Abrasion techniques like grit-blasting can involve high temperatures at the surface that may impact the oxide formation. Thus, oxide composition and surface roughness depend strongly on the employed surface pre-treatment technique and can differ largely if chemical or mechanical surface finishing is applied [49]. Both chemical state and surface morphology can have a distinct influence on interfacial bonding to the polymer.

2.1.2 Epoxy-aluminium interphase

The polymer-metal interphase region is the most important area of an adhesive joint because its stability will define the locus of failure of the joint. If the bonding process, including proper surface preparation, is well performed, the joint will fail either in the adherend or cohesively inside the adhesive. The latter case would be considered as bad design in real structures but represents the best case in standard destructive tests. If materials and processes are not properly selected or if the process is not carried out correctly, adhesion failure may occur at the interface or the joint may fail cohesively near the interface. This chapter consciously considers the interphase (and not only the interface), i.e. the interface and the region close to it, as the whole sector can be affected by interfacial reactions. Interphase/interface stability is closely linked to the term adhesion. Due to the complexity of a polymer-metal interphase, where interlinked chemical, physical and structural aspects need to be considered, no universal theory of adhesion exists [63], but there are a number of adhesion theories explaining the experimentally detected adhesion. Before providing a brief overview on these theories, the actual term “adhesion” should be distinguished into *fundamental adhesion*, which concerns the atomic forces at the interface and *practical adhesion*, which refers to the measured joint strength in destructive testing [64]. Adhesion theories fall into the first category and though adhesion forces certainly impact the practically determined adhesion, other properties like the fracture toughness of the adhesive, or, more general, the energy dissipation by elastic or plastic deformation have also to be considered for practical adhesion. To technically quantify adhesion for engineering purposes independent of the employed test procedure or adherend, the concept of fracture mechanics was firstly discussed by Griffith as early as 1920, who basically suggested that flaws govern the strength of a material [65]. This led to the definition of the term *fracture energy*, which is the energy required for a flaw to propagate through the material [1], [66]. With brittle adhesives, catastrophic joint failure might occur when applying relatively low loads in spite of excellent interfacial adhesion [67]. Thus, technically relevant epoxide adhesives are usually toughened.

In principle, adhesion theories are based on mechanical, thermodynamic and molecular dynamic considerations. Various theoretical works on adhesion phenomena exist, partly using different terminology and grouping of effects. The author will therefore focus on the basic four theories of adhesive bonding named by the Federal Aviation Administration based on the publication of Kinloch [68], [69], which is also recommended for comprehensive studies:

- 1) the mechanical interlock theory
- 2) the diffusion model
- 3) the electrostatic attractive model
- 4) the adsorption theory

As a brief historical background, the mechanical and the adsorption theories go back to the pioneering work of McBain and Hopkins in the 1920s, who distinguished *specific adhesion*, based on interactions between surface and adhesive, and the *mechanical adhesion* of liquid adhesives penetrating the pores of the adherend and solidifying [70]. In 1948 Deryagin and Krotova established the electrostatic theory [71], and in the 1960s, Voyutskii brought forward the diffusion theory [72]; excellent overviews on adhesion theories are provided by Packham [73] and Allen [74] and are recommended for further reference.

The mechanical interlock theory is based on a certain anchoring of the adhesive filling pores and undercuts. Relevant surface roughness may range from nanometres up to several hundred micrometres [75]. Besides interlocking, the enhanced adhesion is derived by the enlarged interface area associated with more interactions. Microporous surfaces (as created by anodising processes) have demonstrated to be especially effective in providing strong polymer-metal adhesive bonds [76]-[78]. By filling the pores, the adhesive creates a metal-polymer microcomposite that alters the stress distribution, reducing the stress level at the interface and increasing the plastic energy losses as a higher quantity of polymer is deformed during fracture [73], [75], [79], [80].

The diffusion theory proposes that the molecules of both materials can diffuse across the interface, creating a diffuse interphase. The model was established for unvulcanised rubber but has been extended to polymer-polymer interfaces like primer to adhesive and even to polymer-metal interfaces [73]. The diffusion of metallic ions into the adhesive was demonstrated by Boerio more than 20 years ago, who also showed that the metallic substrate has a significant influence on the structure of the polymer interphase [81]. A comparison of a model epoxy/anhydride adhesive on AA2024 and copper surfaces showed that the anhydride removed cuprous ions from the Cu-oxide layer and forms a layer of Cu-carboxylates, whereas this effect does not occur on the Al-oxide. The Cu in AA2024 appears in the form of an aluminide underneath the surface and does not react with the anhydride. Diffusion of metallic ions into the adhesive may have a detrimental effect on the interphase. Application of an epoxy adhesive on an aluminium oxide can entail dissolution of the surface by the alkaline hardener component. The dissolved ions diffuse into the polymer forming a metal-amine complex. If the complex concentration exceeds solubility the complexes crystallize and reduce the mechanical stability of the interphase [82], [83].

The electrostatic theory postulates a transfer of electrons via the interface that is regarded as double layer possessing capacitor-like behaviour: during electron transfer positive and negative charges are created that attract each other by Coulomb forces [84]. Electrostatic forces are considered relevant for inter-particle adhesion [67], but several publications point out that common adhesive bonding can be explained without it [73], [85]-[87].

The adsorption theory correlates adhesion phenomena to adsorption of fluids onto solid surfaces distinguishing between *physisorption* and *chemisorption*, depending on the type of short-range intermolecular or inter-atomic forces similar to the ones that act in the structure of matter [88]. It is considered as the most relevant model explaining the interface behaviour of adhesive bonds [68]. Secondary, i.e. physical, forces range from mere London dispersion forces, which are independent of the chemical grouping, and dipole interactions to hydrogen bonding. As Al-O bonds form a natural dipole and as aluminium oxide surfaces are normally hydrated, both dipole and hydrogen bonding have a distinct impact on the adhesion of epoxide adhesives on aluminium substrates. Chemical bonding involves primary bonds like covalent, metallic or ionic interactions. Besides primary and secondary bonding, it has been demonstrated that Lewis acid-base interactions play a significant role in the context of adhesion. Especially the work performed by Fowkes in the 1960s, who found a correlation between the molar enthalpy of the acid-base reaction and the acid-base part of the work of adhesion [89]-[92], is considered as groundbreaking. Watts et al., who studied adsorption of a commercial epoxide adhesive on hydrated aluminium surfaces, demonstrated that adsorption is of the chemisorption type with strong indication of acid-base interactions (including hydrogen bonding) between the hydroxyl groups and the hardener component [93]. Whereas van der Waals and Lewis acid-base forces are significant for the work of adhesion between a liquid and a solid surface, i.e. for the wetting of the surface by the liquid, they are not sufficient to ensure the integrity of a polymer-metal interface under aqueous attack. Watts suggested a simplified model of interfacial bonding in which a certain bond energy per unit area and, thus, a similar initial overall bond strength can be achieved with a high number of weak bonds as well as with a few strong bonds. However, if water ingresses into the bondline, the few strong (e.g. covalent) bonds will largely remain, whereas the weak bonds will be displaced [94]. Hence, the formation of primary bonds is desired to achieve long-term stable adhesive joints. The postulate of covalent bond formation is in particular linked to silane coupling agents, which are supposed to bond to metallic oxides via a Si-O-Me bridge. Though modern surface

analytical techniques can provide strong indication for the formation of primary bonds at the interface, their existence is still in dispute. In any case, the calculated theoretical strength by far exceeds the practically achieved adhesion even if only weak secondary forces are considered [88]. Altogether, it should be kept in mind the adhesion theories cannot be completely separated from each other and remain models not the invariant truth [73].

Independent of the prevailing adhesion mechanism, it is obvious that any surface contamination of the adherend disturbs interfacial bonding. Furthermore, surface contaminants may diffuse into the polymer affecting the cross-linking of the interphase region; but even without the presence of contaminants the strength of the polymer close to the adherend surface can differ from the bulk polymer due to air entrapment or reduced cross-linking density as monomers attached to the surface cannot react as freely as within the bulk. This region is normally referred to as *weak boundary layer* (WBL) [95]. Brockmann and co-workers have detected an influence of the surface treatment on the cross-linking density of the employed polymer primer which was accompanied by a change in the locus of failure [2]. Hence, both polymer and adherend surface affect the properties of the interphase and, therefore, the stability of the joint.

As previously mentioned, not only the polymer side but also the interphase on the aluminium side can be subject to weakening. For example acidic and alkaline environments outside the stability range of pH 4-9 harm the oxide layer. Above all, hydration of the oxide is considered as most common degradation of adhesive bonded joints in service [68], [77]. Despite the influence of the polymer, practical experience with qualified epoxide adhesives shows that the stability of the aluminium surface, i.e. its resistance against hydration and corrosion, is decisive for the durability of the bonded joint.

2.2 Surface treatments of aluminium

Surface preparation is considered as the critical element for adhesive bonding of aircraft structures defining the strength of the interface and ensuring joint integrity. The FAA considers three surface characteristics as essential for proper surface treatment: free of contamination, chemically active and resistant to hydration [68].

These requirements have led to today's anodising techniques, where the aluminium surface is anodically oxidised in an acidic electrolyte forming a porous oxide film of up to several micrometres thickness.¹ Traditional anodising processes involve the use of carcinogenic hexavalent chromium and, therefore, alternative techniques have been developed in recent years with alternative electrolytes, post treatments or involving alternate current [16]-[18], [96], [97]. Some of these, like phosphoric sulphuric acid anodising (PSA), are even already implemented in manufacturing of aircraft structures today [98]. Nevertheless, as a typical tank process, anodising is hardly suitable for local applications. Locally applicable adaptations of the chromic acid anodising (CAA) process (e.g. Dalistick[®], Dalic company) are used in maintenance and repair but do not solve the problem of hazardous waste. Local versions of phosphoric acid anodising (PAA) exist as well [22], [99] but are inconvenient and not desired for bonded repair [100].

The application of GPS, respectively of related sol-gel treatments, is a promising and already employed alternative to anodising. Even though it is only rarely used in commercial aviation, it should be considered as the benchmark technique for local structural adhesive bonding. The main focus of this work is put on the evolving atmospheric pressure plasma deposition technology in comparison to the standard silane treatments. For this reason, the subsequent chapter will only regard the GPS/sol-gel and APPJ-CVD processes.²

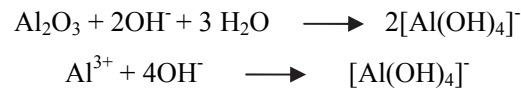
¹ Anodising is not discussed here in detail as there are various publications available [103], [245] and as this dissertation will focus on local treatments using silicon-organic compounds.

² Yet, several other surface treatments for aluminium based on silicon chemistry exist today – like the application of other silane coupling agents, e.g. APS or bis-silanes [240]-[242], silication by flame pyrolysis or by tribochemical reactions

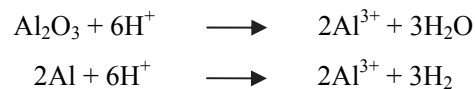
Application of a coupling film is usually only the last step of a multistep surface preparation process, succeeding cleaning, deoxidisation and activation of the aluminium surface. Here, these preceding steps are referred to as surface pre-treatment or conditioning, which is expected to have a significant influence on the performance of the overall preparation process and which will be discussed briefly in the next chapter before focussing on coupling films.

2.2.1 Surface pre-treatment

The previous chapter on aluminium surfaces already pointed out that the initial surface of sheet aluminium formed during rolling contains contaminations, a non-uniform oxide with inclusions and mechanical deformations. As contaminations impact the surface characteristics, like wettability and adhesion, and as inclusions and cracks reduce the fatigue life, the affected surface needs to be removed. Surface pre-treatment³ creates a clean and uniform surface with reliable properties. Due to the polar nature of the Al-O bonds and the hydrated top layer, the oxide can also be considered as chemically active. In ambient conditions this activity will always lead to certain physisorption of hydrocarbons, which, however, is tolerable for adhesive bonding. Deoxidation is most commonly carried out by a wet-chemical process chain consisting of cleaning in alkaline detergents at elevated temperature, followed by alkaline and acidic etching. Material removal is predominantly achieved by alkaline etching (like in caustic soda), where the oxide and the base aluminium dissolve exothermically forming hydrogen and aluminates:



As some alloying elements like copper or transition metals are insoluble in the base, they remain at the surface forming a film of loosely bound dark smut. This smut can be removed by immersion in acids creating a bright metallic appearance – the process of desmutting is also called brightening. Due to the instability of the aluminium oxide below pH 4 acids also have a certain etching effect dissolving the base material and the oxide:



Etching in acids is also referred to as pickling. The acid type strongly influences the degree of material removal as well as the structure or thickness of the formed oxide film. Therefore, the acidic treatment is often used to create a specific oxide texture. Pickling in chromic sulphuric acid (CSP) used to be widely employed to form a relatively thick, open porous oxide film that is beneficial for adhesive bonding. Contrarily, nitric acid does hardly etch aluminium. Yet, it also creates a relatively porous oxide whereas fluoride containing desmutters are reported to form less structured surfaces [77], [101]. In spite of the pronounced structure and the incorporation of chromates, even CSP does not provide sufficient resistance against hydration and corrosion [2]; thus, sole chemical conditioning is not satisfactory for adhesive bonding of aluminium with epoxides.

Besides chemical etching, material removal can also be achieved physically, either by a high local energy influx, like laser ablation [102], or by mechanical abrasion. Abrasion treatments like grinding or blasting are common standard pre-treatment processes for bonded repair in military aviation. Again, the purpose is twofold: removal of original surface protection (paint) and creation of an enlarged active surface that allows stress diffusion and interlocking through undercuts. Alumina grit-blasting is known to provide high

[244], [246], [247] or the combination of silane and laser treatment [243] – but are not used in aircraft manufacturing and, therefore, are not further considered here.

³ In this thesis, the term *pre-treatment* (also referred to as conditioning or deoxidising) is defined as the removal of the initial surface layer. It is distinguished from the term *surface preparation* (also surface treatment) which consists of all process steps prior to adhesive bonding – including application of a coupling film or anodising. This distinction is not generally common in literature but is introduced to enhance clarity.

initial joint strength, but does not provide sufficient durability for aerospace applications [103]-[105]. The formed interface with the polymer is not resistant against hydrodynamic displacement and hydration of the oxide.

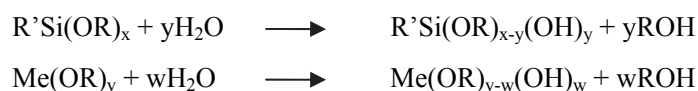
Comparing dry (mechanical) and wet (chemical) surface pre-treatments, significant differences exist with regard to roughness as well as oxide thickness and morphology. Abrasion techniques lead to high macro-roughness, but without distinct micro- or even nanostructures, whereas etching can cause macroscopically smooth surfaces with pronounced microstructure. Furthermore, it has been reported that the oxide composition after grit-blasting differs significantly from wet-chemically derived oxides [49]. Thus, a strong impact on adhesion and durability of the interface is not surprising. Moreover, this influence is reported to remain even if the adherends are coated with a silane based coupling film afterwards [30], [100], [106], [107], making surface conditioning one of the major parameters defining the performance of the surface preparation process and, ultimately, joint stability.

2.2.2 Silane and sol-gel coupling films

The coupling films discussed within this chapter are derived from deposition of aqueous solutions of hydrolysed silane coupling agents acting as precursors for film formation on the metal surface. When speaking of silanes in an adhesion context, the term does not refer to SiH_4 or its halide-containing derivatives but is commonly accepted for silicon-alkoxides (alkoxysilanes), in most cases organofunctional silicon-alkoxides. The alkoxy groups are hydrolysable, whereas the organofunctional group remains and is normally selected for a specific purpose, like the bonding to a certain adhesive. Due to this dual inorganic and organic nature silanes are well suited to link the polymer-oxide interface [25].

Numerous silane coupling agents and application processes exist today and the corresponding publications exceed one's reading capacity. As a starting point, the author recommends the special edition of the International Journal of Adhesion & Adhesives focusing solely on silane coupling agents [108]. The focus within this dissertation is directed towards the most commonly employed silane based processes promoting adhesion between aerospace aluminium alloys and epoxide adhesives: GPS deposition, also known as the *Australian Silane Surface Treatment* developed by Baker and Chester [24], and the sol-gel *AC-130*, also known as *Boegel-EPII* developed by Blohowiak and co-workers [28]. Before discussing both treatments in greater detail, a brief overview on the basic reactions of alkoxides in aqueous solutions, their polymerisation and film formation is presented.

In their initial state, the organofunctional silicon or other metal alkoxide precursors are not soluble in water. However, they react upon contact with water by hydrolysis of the alkoxy groups, which can be catalysed by either acids or bases:



Most silanes precursors are then soluble in the aqueous solution due to the formation of silanol groups and alcohol during hydrolysis. After that, the monomers can polymerise via condensation of two silanol groups or one silanol and one alkoxy group producing siloxane (Si-O-Si) bonds and releasing water or alcohol. Condensation begins before hydrolysis is complete – both reaction run in parallel and compete with each other. Various chemical species can be formed ranging from dimers, oligomers, up to particles and branched networks depending on the reaction time, temperature, pH and solvent nature, i.e. water and alcohol concentration. The creation of glassy materials by hydrolysis and condensation is referred to as *sol-gel process*. The name is derived from the initial state, a colloidal suspension of oligomers, the sol, transforming into a continuous inorganic network with entrapped liquid creating a gel transition state. With further reaction the gel is then transformed either into a porous foam or into a dense film mostly depending on pH and water concentration [109]. According to Le Chatelier's principle, high water concentration promotes hydrolysis, whereas high alcohol concentration reduces its degree. Moreover, condensation

generally increases with reaction time [110], [111]. As mentioned above, hydrolysis is catalysed by acidic and basic pH with a minimum at pH 7, whereas the condensation reaction is minimal between pH 4 and 5 [112]. For coupling films it is desirable to achieve full hydrolysis and minimal condensation at the application of the sol to obtain the maximum number of silanol groups as potential bonding partners to the aluminium oxide [110], [113]. Furthermore, the maximal number of silanol groups will lead to formation of a highly cross-linked dense film upon curing. Hence, low concentrated, acidic catalysed silane solutions are used for promoting hydrolysis by protonation of the alkoxy group. The corresponding nucleophilic attack mechanism is displayed in Fig. 2.1. In spite of an improved surface wetting high methanol or ethanol solutions are not preferable as they inhibit hydrolysis and can even cause a backward reaction called alcoholysis [25], [113]-[116]. After hydrolysis the application window is limited to high monomer concentrations which results in a relatively short pot life. In this case the sol is, thus, rather a solution of the hydrolysed precursor than a colloidal suspension.

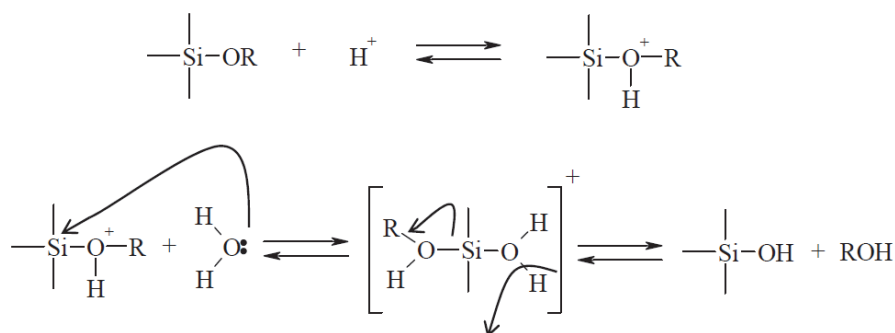


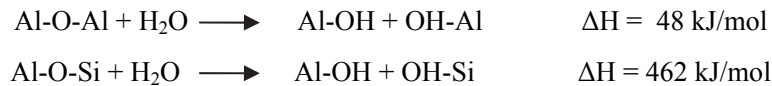
Fig. 2.1: Acid catalysed silane hydrolysis mechanism [57]

In contrast, transition metal precursors like zirconium-*n*-propoxide are more reactive than silanes and their reactivity needs to be decreased with complexing agents to avoid precipitation; acetic acid or acetates are most often employed for this purpose. The higher hydrocarbon chain length of the alkoxy groups (most often propoxy and butoxy) of transition metal precursors also reduces the reactivity compared to the methoxy and ethoxy groups with silanes. Still, a certain oligomer formation cannot be avoided [117]. Other than most silanes, transition metal precursors do not contain organofunctional groups, which means that all groups can participate in the inorganic network formation, increasing the crosslinking density.

If organofunctional silanes are used, dedicated organic characteristics can be added to the tailored inorganic network. Through formation of interlinked inorganic-organic hybrids (class II), multifunctional coatings can be created offering a variety of potential applications [118]. In general, the organic part increases the flexibility, especially if the silanes possess unreactive spacer groups, and avoids film rupture during curing and substrate deformation. If the organic groups polymerise, e.g. by addition of cross-linking agents, high barrier films with high corrosion or wear resistance are obtained [57], [119], [120]. With coupling films, polymerisation of the organic part is not desired because the functional groups, like the epoxy-ring of GPS, are needed for reaction with the adhesive.

Rattana et al., who studied the adsorption of a commercial epoxide film adhesive with GPS treated and only grit-blasted aluminium surfaces, demonstrated primary bond formation between the silane and the adhesive. More precisely, the curing agent of the adhesive reacts with the epoxy-ring of the GPS derived layer [121]. This is of particular importance as later studies with mere DGEBA solution revealed that monomer molecules are indeed chemisorbed on the surface but only via Lewis acid-base interactions; covalent bond formation does not occur [93], [122]. However, it needs to be considered that the adsorption studies did not involve a high-temperature curing step which may influence the bonding situation and could lead to ring opening and polymerisation reactions even without the presence of a curing agent. It is likely that thermal curing during typical adhesive bonding processes further enhances the bond formation between epoxide and coupling agent.

Considering now the bond formation to the oxide surface, it has been already stated above that the number of silanol groups, i.e. the degree of hydrolysis, increases the interface stability. Covalent bond formation via condensation reaction of the silanol groups with surface hydroxyls had been first postulated by Plueddemann and was later supported for the GPS-aluminium interface by different analytical methods like RAIRS and ToF-SIMS [115], [123]. The existence of primary bonds at the interface is especially important for obtaining sufficient durability in hot-wet conditions by inhibiting hydrodynamic displacement [94], [124]. Furthermore, suppression of oxide hydration is decisive for the integrity of the interphase. Thermodynamic considerations reveal a significantly higher enthalpy of the potentially formed Al-O-Si bonds compared to the Al-O-Al bonds in a boehmite modification. The corresponding calculations of the Gibbs free energy show that the energy needed to break the Al-O-Si bonds is approximately one order of magnitude higher than the one needed to hydrolyse the Al-O-Al [125]:



Experimental work confirms that GPS films delay hydration of the aluminium oxide [124], [126]. According to the reversible hydrolysis model established by Plueddemann, the covalent bonds formed at the interface may indeed be ruptured under stress and aqueous attack but can even reform afterwards [25]. Besides the strong bonding of the silanol groups, it was shown that the epoxy group reacts with the surface as well [127]. Covalent bonds between silanol and surface hydroxyls are formed first and then followed by Lewis acid-base interactions of the glycidyl group [128].

In addition to its bonding to the polymer and to the substrate, the intrinsic film properties also influence the durability of the bonded joint. After application the thin film transforms from a gel state into a dense film. It was shown that the curing conditions affect the crosslinking density of the film. The structure of a GPS derived film changes with thermal curing above 50 °C, increasing the siloxane bond formation [129]. Hence, thermal curing is found to have a positive effect on joint integrity in hot-wet conditions [26]. However, Bertelsen and Boerio demonstrated that thermal curing at 120 °C is not only beneficial for the siloxane network formation, but also causes opening of the epoxy ring, which is detrimental for the durability [26], [110].

Based on all the findings described above, the actual process parameters of the Australian Silane Surface Treatment appear to be a logical consequence, despite the fact that the empirical process had been developed before most of the analytical studies were performed. Baker and Chester proposed to apply an aqueous 1 % GPS solution on grit-blasted aluminium (50 µm alumina grit) after a hydrolysis time of 60 min and then to dry the coupling film for 60 min at 80 °C [24]. Solution pH is not mentioned, but it is very likely that it is acidic since natural solutions in DI water are reported to go down to pH 4.5 [130]. Kuhbander and Mazza later on refined the process, lifting the curing temperature to 93 °C and specifying the acidity at pH = 5 [26]. Their process parameters were subsequently confirmed by an extensive study by Abel et al. [27]. The acidic pH 5, the high water content and the absence of methanol enhance the hydrolysis without favouring oligomerisation. 60 min hydrolysis is in the middle of the reported range of time needed until hydrolysis is complete – 30 min [110] to 90 min [111] – and is still too short for distinct oligomerisation and or even opening of the epoxy ring. Thus, a true aqueous solution of silanetriols is applied – not a colloidal suspension – forming a thin gel layer which then transforms into a dense siloxane film with unreacted glycidyl groups during thermal curing.

As a dedicated thermal curing step is time-consuming and not desirable for local applications, the GPS treatment was modified by addition of zirconium n-propoxide (Tetrapropoxyzirconium, TPOZ) by the Boeing Company allowing RT curing [28]. Due to its very high reactivity TPOZ, which comes as n-propanol solution, is coordinated with acetic acid forming a less reactive complex. TPOZ not only has four reactive sites to participate in the inorganic network, it also catalyses the condensation reaction, thus, enhancing the crosslinking density and enlarging the barrier properties [109], [119]. The improved crosslinking allows an increase of precursor concentration: Liu et al. obtained highest fracture energies on

grit-blasted or sanded substrates with solutions of around 3 to 5 % precursor concentration [131]. The optimal drying/curing time was found to be 75 min, after which maximal fracture energies are achieved. Surprisingly, durability decreases with increasing drying time above 75 min, which was ascribed to a higher network density, which in turn reduces the interdiffusion of the adhesive that is apparently needed to enhance the stability against moisture attack [132]. As for the GPS treatment, a significant difference of joint performance can be detected depending on the surface pre-treatment. Blasting with 50 μm alumina grit is found to perform best of all local pre-treatments and could even be further improved by subsequent etching step adding a distinct nanostructure [30], [133]. It was demonstrated that the application of the commercialised AC-130 sol-gel system, which has a precursor concentration of approximately 3 % and a molar ratio of GPS to TPOZ of around four, leads to even slightly higher durability on grit-blasted aluminium adherends compared to the GPS treatment [30].

2.2.3 APPJ-CVD of Si-based coupling films

Plasma at atmospheric pressure can be generated by various discharge types applying a wide range of energies to different gases, producing excited species and ions. In principle, there are two types of plasmas: thermal plasmas, where ion and electron temperatures are approximately equal (equilibrium plasma), and cold or nonthermal plasmas, where electron temperature is significantly above gas temperature (non-equilibrium plasma). Atmospheric pressure plasmas considered in this work belong to the cold plasma category and, therefore, allow treatment without damaging the substrates. Three different electron and ion frequencies are typically discriminated for nonthermal plasmas: low frequency (< 1 MHz), radio frequency (< 1 GHz) and microwave plasmas. Typical discharge types include corona, dielectric barrier and low-energy controlled arcs, operating in the low frequency domain as well as RF and microwave induced discharges [43], [134]. Film deposition in atmospheric plasmas emerged in the late 1990s after the development of plasma jet sources [31], [135]. Non-thermal atmospheric pressure plasma deposition can be separated in two different approaches: the indirect, or jet deposition, and the direct deposition. In case of the latter, the substrate is located between the electrodes, i.e. active species are created directly close to the substrate surface. This technology is – however – not yet as mature as jet deposition and is not suitable for 3D geometries [32].

Contrarily, in case of the plasma jet deposition, the plasma and the active species are generated remotely and are then blown – usually through a nozzle – onto the substrate by the gas flow. Precursors are injected at the end of the nozzle at the transition of excitation volume and afterglow jet to avoid deposition inside the plasma source. After injection, precursors can either be fragmented or may react with the plasma gas or the ambient air. After contact with the substrate surface, the active species polymerise, forming a closed film. Plasma energy, carrier gas as well as concentration and reactivity of the precursor need to be adjusted to obtain polymerised films, rather than uncured films or already polymerised particles. Most common precursors are Si-organic compounds like hexamethyldisiloxane (HMDSO), tetraethyl orthosilicate (TEOS) or hexamethyldisilazane (HMDSN) creating films that are either inorganic and glass like or more organic and siloxane/silazane like in their nature, depending on process parameters and precursor selection. Creation of other oxide films like aluminium and titanium oxide or even non-oxide ceramics has been demonstrated in other works as well [136]-[138].

In contrast to the solution derived silane treatments, atmospheric pressure plasma deposition of coupling films derived from Si-organic compounds has not been considered as surface preparation technique for adhesive bonding of aluminium aerostructures until today. Instead, only activation and removal of contamination by atmospheric plasma was investigated (as intermediate step before silane or sol-gel application) for bonded aircraft repair [33], [34], without, however, achieving significant improvement in performance. Sole plasma activation of aluminium surfaces in atmospheric or low pressure has demonstrated to influence the interphase formation and to improve adhesion of epoxy systems [139], [140] but is insufficient to achieve long-term stability.

On the contrary, atmospheric plasma deposition of Si-organic precursors improves corrosion resistance of aluminium alloys [39], [141], [142] as well as adhesion and durability on metallic substrates like steel and titanium [143]-[145]. More importantly, it was recently shown that APPJ-CVD of Si-based coupling films increases the durability of aluminium joints bonded with silicone or epoxy adhesives in corrosive environments [37], [39], [146]. Although different materials were employed, these results are of particular interest as they are coherent with the results obtained within this present work and as the used jet devices are very much alike⁴. Consistent with own previous work, it was shown that inorganic oxide films are more suitable as adhesion promoting layers than films with a large hydrocarbon content [39], [44]. Even though the mentioned publications do not analyse the degradation or protection mechanisms in detail, it is very likely that the results shown in the following chapters can be transferred to joints of other aluminium alloys and polymers.

Comparable results were also obtained with low pressure plasma deposition, where silica-like coatings outperformed siloxane type films as coupling layers on aluminium, leading to excellent durability [107]. Generally speaking, structure and composition of atmospheric plasma derived silica-like films resemble to the ones obtained under low pressure [147], [148], which is promising as these films are known to adhere well to aluminium substrates [138], with evidence even pointing to covalent bond formation [149]-[151] and to significant inhibition of electrochemical degradation reactions [41], [42], [152].

2.3 Durability of bonded aluminium joints

In the past, the development of structural adhesives was mostly driven by mechanical properties, i.e. intrinsic strength as well as plastic deformation capabilities under static and fatigue loads, but not by durability aspects. However, in-service damages caused by static or dynamic overloading hardly ever occur as applied loads are small compared to fracture loads and as critical peel conditions are avoided by proper design. Contrarily, exposure to hostile environments is hardly avoidable in aircrafts as moisture can diffuse through sealants and as corrosive solutions accumulate at the bottom of the fuselage made of condensed water mixed with other substances like aggressive hydraulic oil [2]. Hence, exposure to the major aggressive media, water/moisture and corrosive solutions, have to be considered. Other hostile environments, like the exposure to jet fuel or hydraulic fluid, are not considered here as these environments rather affect the adhesive than the surface treatment [153]. In the following, the two major degradation conditions are discussed in detail: hydrothermal ageing in hot-wet conditions and bondline corrosion, which is a specific anodic degradation mechanism detected on aluminium structures in corrosive environments.

2.3.1 Hydrothermal ageing in hot-wet conditions

Principally, exposure to moisture at elevated temperatures may lead to three different types of degradation: the adhesive might be displaced from the adherend at the interface, the adhesive may lose its integrity or the substrate degrades due to reactions with water.

As discussed in chapter 2.1.2, adhesion at the epoxy-aluminium interface relies mostly on secondary intermolecular forces. Thermodynamic consideration performed by Kinloch et al. revealed that the epoxy-aluminium interface is only stable at dry conditions while thermodynamics drive the displacement of the adhesive upon contact with water. The corresponding work of adhesion changes from 230 mJ/m² to approximately -140 mJ/m² in presence of the more polar water molecules [79]. Moreover, electrostatic interactions (Coulomb forces) at the interface are directly reduced upon moisture ingress due to the higher dielectric coefficient of water. This explains the superior behaviour of joints with primary interfacial bonds

⁴ A similar air plasma jet source with slightly higher pulse peak power was well characterised by Bhatt et al. who determined gas temperature as $T_g \approx 600-800$ K, electron temperature as $T_e \approx 0.7$ eV and vibrational temperature as $T_v \approx 0.3$ eV [176].

compared to those with secondary bonds after exposure to moisture, despite similar initial strength [94]. Besides the nature of the interactions, the speed of the water ingress obviously impacts on the long-term stability. Generally speaking, water ingress is controlled by diffusion of water molecules through the adhesive. Even if the crosslinking density of the adhesive is low and exposure temperatures are high, several hours or days are needed for significant water diffusion through the bulk polymer. Yet, it was shown that ingress at the interface can be six [154] or even 14 times [155] faster than in the bulk. In principle, the damage of the aqueous attack is reversible after desorption of the water, but as the range of the secondary interaction is very small, the displacement can be permanent. If the interface is under mechanical stress, the displacement will advance rapidly, leading to immediate joint failure.

In contrast, the degradation of the adhesive itself is known to be almost fully reversible. The mechanical strength obtained after water desorption can reach a similar level as the initial strength [63], [156]. Typical effects of moisture ingress are swelling and plasticisation, i.e. a reduction of the glass transition temperature, which is especially pronounced at elevated temperatures [157]. The degree of plasticisation decreases with increasing network density of the epoxy adhesive [49]. Thus, temperature and pressure hardening 1-component film adhesives employed in aerospace are less prone to degradation than 2-component RT curing ones. Mubashar et al., who studied the moisture absorption of the qualified aerospace adhesive FM 73 during immersion in water at 50 °C, demonstrated that the diffusion into this film adhesive is of a delayed dual Fickian type with two absorption phases. Based on this bulk diffusion, water concentration in single lap joints was simulated, which showed that even after 182 d at 50 °C the water concentration at the centre of the joint is minimal. Hence, hydrothermal degradation of the bulk adhesive can be seen as rather unproblematic. However, as previously stated, crosslinking density and diffusion can vary between the bulk and the interphase region [158] and can be impacted by the employed surface treatment; differences in polymer network formation were observed between etched and grit-blasted or anodised adherends [2], [49]. Besides the barrier properties of the adhesive, the state of the hardener component – i.e. its concentration and integration into the polymer network – can affect the durability of the bonded joint. These highly alkaline components can be washed out upon water absorption and degrade the aluminium adherends. Yet, in this work, using the qualified FM 73 film adhesive, which demonstrates excellent stability in water, this leaching effect does not occur [2].

Hydrothermal degradation of the aluminium adherend due to hydration is regarded as the most critical issue concerning durability of bonded joints and, hence, the enhancement of resistance to hydration is considered an essential feature of any surface preparation process [68]. Hydration of pure aluminium surfaces immersed at different temperatures up to 100 °C was well investigated by Alwitt in the 1970s, who measured the weight gain associated with the growth of a hydrated film. Hydration was found to start after a certain induction period, with both length of this period and hydration speed being strongly temperature-dependent. Strong hydroxide growth associated with pseudoboehmite formation was detected with temperatures of 50 °C and above [51]. However, Underhill and Rider did not observe this induction period when investigating hydration of AA 7075 clad and AA 2024 bare alloys in water at 40 and 50 °C by means of FTIR. The formation of hydroxyl groups starts instantly upon immersion even at 40 °C. Still, when studying weight gain, the obtained results were consistent with Alwitt's data, which shows that hydration occurs immediately, but the extensive pseudoboehmite formation, which leads to a strong increase in weight and thickness of the film, follows with a certain delay; the second step is by far more pronounced at 50 °C. Hydroxide films formed at 40 °C are, at least at the beginning, less porous than the gel-like pseudoboehmite with its high amounts of incorporated water molecules. Nevertheless, after 60 min, a certain porous microstructure is also formed at 40 °C, though being by far less distinct than at 50 °C [159].

A good overview on pseudoboehmite formation can be found in Bockenheimer's publication based on the work performed by Alwitt [51], Wefers and Misra [45], [46], [160], as well as Nylund and Olefjord [48] [161]: the Al-oxide reacts with water to AlOOH , forming a boehmite like network structure held together by H-bridges, which incorporates water molecules also bound by hydrogen bonds. The formation of this gel-like layer is kinetically controlled. As the thickness of the initial oxide layer is decreasing, the electrical field at the metal-oxide-interface is increased, which leads to diffusion of the Al^{3+} ions into the gel-like

layer, where hydration occurs inside the film upon contact with water. Thus, aluminium is indirectly dissolved and film growth takes place at the oxide-hydroxide interface or within the gel layer, increasing the overall film thickness. Film growth limits itself by inhibiting the diffusion of water molecules through the gel with increasing film thickness. At the gel-film-water interface, $\text{Al}(\text{OH})_3$ in amorphous or crystalline form (bayerite) is formed by solution and precipitation of the hydroxide [49]. Venables, who studied the porosity and microstructure of porous pickling oxide films immersed in water at 80 °C, detected three stages of hydration after a short incubation time, where, at least visibly, not much change can be observed: at first, the initial porosity decreases as pores are filled with growing hydroxide, then the surface roughens distinctly, followed by the formation of the characteristic “cornflake” structure of pseudoboehmite. These results are confirmed by the aforementioned investigations by Underhill and Rider at 40/50 °C [159], which is of particular importance as one may argue that water immersion at 80 °C does not correspond to any real life conditions, whereas 40 °C can be easily reached in service.

Nevertheless, it has to be considered that immersion of the substrate does not equal the conditions in a bonded joint where the adherend surface is covered by the adhesive and, thus, hydration is limited – at least pre-failure. For bonded joints, it was demonstrated that polymer crosslinking density affects the degree of hydration of the aluminium substrate, which is significantly higher in a less cross-linked interphase [49]. Furthermore, it was shown that immersion in water has a more detrimental effect on aluminium-epoxy joints than 100 % rh at the same temperature [162]. Still, Venables detected distinct hydration of PAA treated adherends which was found to be the failure cause during wedge testing of adhesive joints at 65 °C, 95 % rh. [77]. Similar degradation was even observed at water temperatures below 30 °C, but it was also shown that the hydration only occurs in absence of a low-viscous polymer primer. The adhesive itself does not fully penetrate the anodising oxide and, thus, moisture penetrates the unfilled pores. If a primer is employed, hydration is only a post-failure effect even during dynamic testing in water [79], [163]. In contrast, similar testing of GPS treated aluminium joints indicated that hydration does occur before failure [164]. Therefore, analysis of the failure cause must be carried out very carefully, as the underlying mechanisms behind may well depend on surface preparation and test conditions.

As stated before, $\text{Al}(\text{OH})_3$ precipitates at the topmost surface of the hydroxide film and gel layer formation is limiting itself due to inhibition of water diffusion. However, if the pH of the solution is below or above the stability range, the solubility of the hydroxide increases and the film dissolves leading then to continuous direct Al^{3+} dissolution and hydroxide formation. In case permanent direct oxide and aluminium dissolution is reached, the process is referred to as *corrosion* [49].

2.3.2 Bondline corrosion

Besides the damages induced by moisture, an even more severe degradation type can occur upon exposure to corrosive environments like the condensation derived bilge solution that accumulates inside the airframe. Distinct corrosion induced bondline damages were found during aircraft service inspections in the early 1970s, a few years after introduction of the epoxy adhesives. Several studies of this bondline corrosion clearly revealed surface preparation and cladding as crucial factors [2], [165]-[169]. Consequently, design principles, employed adhesives and surface preparation processes were changed leading to the use of today’s primers, adhesives and anodising techniques [2], [4], [5]. Moreover, stringent durability testing was introduced. It was demonstrated that the failure found in service can be reproduced in an accelerated manner by placing joint coupons with uncovered rough edges into a salt spray chamber. The rough edges promote initial corrosion and are starting points for degradation of the bondline. This so-called bondline corrosion test is performed for qualification and quality control typically up to 300 d [170].

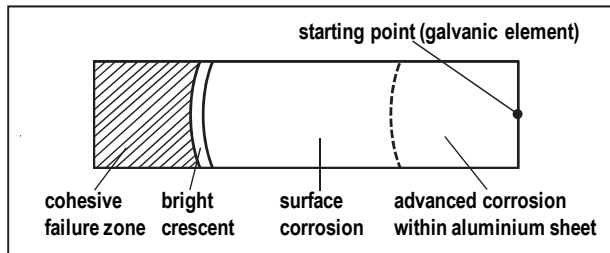


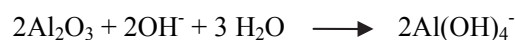
Fig. 2.2: Scheme of macroscopic bondline corrosion according to Brockmann et al. [2]

Ground-breaking investigations on the corresponding degradation mechanism were conducted by Brockmann and colleagues, who studied bondline corrosion of anodised substrates with different epoxy primers and adhesives [2]. The detected mechanism was further refined by Kelm [171]. Macroscopic consideration of the damaged bondline of the opened joint shows corroded semicircles around corrosion starting points, with corrosion intensity decreasing with distance from the initiating point. Adjacent to the cohesively failed adhesive a zone of macroscopically unharmed surface is observed, referred to as “bright crescent”, where adhesion failure occurs (Fig. 2.2). Microscopic examination of this region reveals a transformation of the oxide due to moisture, but no distinct corrosion. Inspection of anodising oxides at the delamination front even shows that oxide transformation occurs already below the adhesive that still fails cohesively; transformation of the oxide was found to start from the polymer side. Next to the bright crescent, an area of surface corrosion was detected. In the area of bright crescent and surface corrosion a drop of pH of the electrolyte to pH 3-4 was observed. Surface corrosion is followed by heavy corrosion that reaches into the base material and whose degree is increasing towards the sample edge.

Generally speaking, the degree of bondline corrosion is dependent on both adhesive and especially surface treatment, with anodising outperforming sole pickling in chromic sulphuric acid (CSP). Higher oxide quantity is beneficial for bondline corrosion resistance. Moreover, the corrosion intensity is largely influenced by the presence of the pure aluminium clad layer and even the alloy itself [169]. While bondline corrosion is found on aerospace AA 2024 and AA 7075 alloys, particularly in clad state, it cannot be initiated on 1xxx or 5xxx alloys.

Multiple reactions are detected at the inorganic/organic interphase region, like reversible ad- and desorption and irreversible degradation reactions, all of which are of crucial importance to the bondline stability. Based on detailed analysis of this region, Brockmann et al. identified two major degradation mechanisms: the alkaline and the acid failure mechanism, which are differentiated by the pH of the primary degradation.

The alkaline mechanism originates from dissolution of low molecular weight alkaline hardener components caused by water ingress into the epoxy polymer. These components then diffuse to the interface. Due to the increase of pH above the stability limit of 8, the oxide is dissolved by the following reaction:



Hence, the extent of this degradation should mainly be dependent on the amount of soluble hardener components and the stability of the oxide. However, no correlation between the quantity and alkalinity of these components could be established and similar degradation was detected with joints bonded with phenolic adhesives that guarantee acidic conditions in the boundary layer. This led to the conclusion that damage is mostly caused by the thermodynamic instability of the oxide layer in presence of H_2O , which has been discussed in the previous chapter.

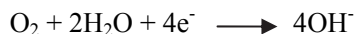
In any case, the acidic failure mechanism is considered as the far more important degradation process and is normally referred to as “bondline corrosion”. With this mechanism, acidic conditions are detected around the crack tip, more precisely in the bright crescent and the area of surface corrosion. The associated drop to pH 3-4 is caused by an anodic dissolution of aluminium that progresses from the open edge:



It is followed by diffusion of acid hydrogens into the bondline dissolving the oxide (primary failure):

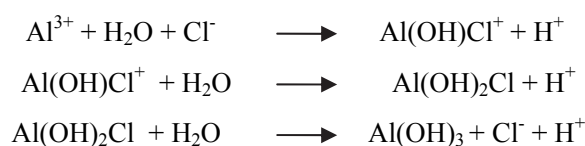


The corresponding cathodic reaction is the reduction of oxygen that occurs near the sample edge creating an alkaline zone (advanced corrosion zone):



Consequently, an acidic influence zone inside the crevice around the delamination front and an alkaline influence zone near the sample edge are formed. Bondline corrosion is highly dependent on the occurrence of initial bimetallic corrosion. Therefore, bondline corrosion is normally only observed on clad material due to the formation of a galvanic element between the more noble Cu containing alloy (cathode) and the pure aluminium cladding [2]. Moreover, the condition of the open edge of the bondline is of significant importance to the degree of bondline corrosion. Bondline corrosion is usually initiated from small mechanical damages of the edges, for example caused by hole-drilling.

The oxide dissolution reaction was later reviewed by Kelm, who demonstrated that low pH, i.e. the H^+ ions, and the presence of chlorides are not sufficient to dissolve anodising oxides, which requires the presence of Al^{3+} ions. A degradation mechanism involving oxide hydrolysis by aluminium-chloro or aluminium-hydroxo-chloro complexes was proposed⁵:



Summarising the bondline corrosion model, it is assumed that the pure Al of the clad layer is anodically dissolved at the open edge due to galvanic corrosion. The formed Al^{3+} creates Al-chloro complexes in the electrolyte, which then dissolve the oxide film already below the area of cohesion failure. The increased concentration of H^+ in the crevice is followed by migration of Cl^- into the bondline forming a highly concentrated Al-chloro complex solution. Consequently, an active Al/ AlCl_3 electrode is created. In addition, the hot-wet environment may also cause a certain hydration in the opened crevice.

The last decades have proven that bondline corrosion can be almost fully suppressed if adequate surface treatments (which are now industry standard) are used and if adhesive bonding in corrosion sensitive sectors is avoided. Therefore, no scientific investigation considering bondline corrosion and hardly any test studies on exposure of bonded aerospace aluminium joints to corrosive atmospheres have been published. Alternative surface preparation methods are mainly assessed only in dry and wet/humid conditions. Nevertheless, bondline corrosion stability still needs to be considered as absolutely crucial when proposing alternative processes for adhesive bonding of primary aircraft structures.

2.4 Gap analysis

Since there are currently no reliable, locally applicable, or non-hazardous surface treatments used for adhesive bonding of metallic aircraft structures in commercial aviation, this dissertation considers the promising Si-based surface preparation methods. The previous chapters provided a brief overview of the scientific background related to these techniques, as well as to bonding and durability of aluminium joints in general. Against this background, the aim of this chapter is threefold: a) to identify the scientific and technical gap that needs to be filled in order to evaluate whether these surface treatments are eligible for adhesive bonding of primary aircraft structures, b) to outline what will be done in this dissertation to fill this gap, and c) to sketch how this question will be answered.

Generally speaking, the scientific understanding and the technical knowledge on APPJ-CVD films for adhesive bonding is relatively limited compared to anodising or silane treatments and is not sufficient to

⁵ The oxide dissolution model based on chloro complexes was, however, not fully verified as its author could not detect the presence of such complexes [171].

allow a proper judgement of the capabilities of this technique; available studies do not go beyond film characterisation and a few basic mechanical and durability tests, without however thoroughly correlating film properties to test results or considering prevailing altering mechanisms. The exceedingly high requirements for bonded aircraft structures are also not considered. In contrast, this thesis exposes plasma treated samples to challenging mechanical and durability tests. The aim of this dissertation is to provide a solid foundation for the assessment of this technology by focussing on the most critical aspects for surface treatments, being peel strength and durability in hot-wet and corrosive conditions (salt fog). This in turn means that the exhaustive coverage of each and every of the various requirements needed for qualification of surface treatments for adhesive bonding lies beyond the scope of this work.

Film characterisation in previous research has been limited to bulk film properties and generally does neither analyse the surface chemistry of the film nor the interface to the substrate material, which is essential to understand the mode of action of atmospheric plasma derived coupling films. Besides bulk film characterisation, this thesis therefore also includes detailed chemical and topographic analyses of the topmost film surface, as well as a thorough investigation of the interface between plasma polymer and Al-oxide surface. Corresponding analysing techniques comprise SEM, XPS sputter depth profiling, AFM, STEM, high-resolution XPS and ToF-SIMS. Different types and quantities of precursors are employed; the corresponding film properties are ascertained and systematically correlated to the joint performance during peel testing. The detected connection of film surface chemistry and peel resistance leads to a selection of the most promising systems. A comparison of obtained peel resistances to those of state-of-the-art surface preparation techniques allows a grading of the results with regard to specific industry requirements. More importantly, this correlation identifies the key drivers for the performance of Si-based coupling films. Such comprehensive correlation has not yet been achieved in any of the studies available.

Another research gap revealed by literature analysis is the effect of the surface pre-treatment of the aluminium substrates: While surface properties of the base material after different conditioning techniques have been investigated in principle, the combination of plasma deposition with surface pre-treatment has not yet been studied – other than for silane treatments, where this subject has been frequently addressed. Hence, the characterisation of the substrate surface condition and its correlation to the overall stability and durability of the APPJ-CVD treated joints are key aspects of this dissertation. The analyses contain a comparison of etching derived oxides with oxides formed by grit-blasting, characterising associated roughness and topography, as well as oxide composition, thickness and level of hydration. Employed techniques are LSM, SEM, XPS depth profiling, TEM, high resolution XPS and CD-XPS. The determined properties are correlated to peel test result, identifying the most important characteristics concerning mechanical stability of the joint. Based on the correlation detected between surface pre-treatment and peel resistance, a preferred pre-treatment is selected.

Besides the correlation of physical and chemical properties (of substrate surfaces and APPJ-CVD coupling films) with macroscopic joint strengths, these properties are additionally correlated to resistance of the treated joints against multiple environments, which induce degradation, for the first time in this thesis. This degradation is mainly simulated by standard accelerated ageing tests (bondline corrosion, humidity and wedge tests), which have proven to very well represent in-service damages that occur with state-of-the-art surface treatments. Moreover, these durability tests are very selective concerning the quality of the surface preparation but are rather uncommon in scientific studies. Different scenarios, combining different mechanical and environmental loads, need to be considered in order to gain a comprehensive view on the joint durability. As there is currently no standard test for combining dynamic loading and exposure to moisture, an additional test is developed, which simulates degradation after a typical number of load cycles experienced by an aircraft structure over its life span.

To fully understand the correlation between film/surface properties and test results, it is crucial to analyse the failure and degradation mechanisms first. For this end, loci of failure as well as alterations of the interface region are studied. Moreover, detailed investigations of the degradation mechanism during exposure of bonded aluminium joints have not yet been published for APPJ-CVD systems. Even for the

well-studied silane and sol-gel systems, knowledge on their behaviour in corrosive atmosphere is marginal – all existing studies focus on thick aluminium oxide derived from anodising or pickling. Therefore, a large part of this dissertation investigates the prevailing alteration mechanisms of the interphase region in hostile environments representing accelerated real-life conditions, like humidity, water or salt fog. Based on these investigations, in particular based on the comparison of coated and uncoated substrates, the effectiveness and functionality of the different Si-based treatments are explained with regard to all of the identified mechanisms. These analyses are predominantly carried out by SEM, TEM and STEM. To ascertain the postulated modes of operation of the coupling films, electrochemical techniques, like EIS and potentiodynamic scans, are employed. Conditions of these tests are adapted to the conditions occurring in the crack tip region during bondline corrosion and have not been employed in research before.

Altogether, this dissertation establishes an integral understanding of the physical/chemical properties of the substrate surface and of the coupling film, of the identified degradation mechanisms and, in consequence, of the macroscopic joint performance. Based on the findings, an optimal treatment process is developed, combining plasma and solution derived deposition. Overall performance is put in perspective to state-of-the-art techniques, allowing a firm judgement on the capabilities and limitations of surface treatments involving APPJ-CVD for structural bonding applications.

3 Experimental

3.1 Sample preparation

Aluminium substrates

All AA 2024 substrates are in T3/T351 heat treatment state. AA 2024 is either used bare or with clad layer. To ensure reproducibility, all specimens for a specific test are cut from the same bare or clad sheet. For all bonded samples, the rolling direction is similar to the test direction. The dimensions of the to-be-bonded panels and the samples for electrochemical investigations cut from the AA 2024 sheets are presented in Table 3.1. Adhesion and durability test samples are cut to the required coupon sizes after bonding as described at a later stage.

Table 3.1: Dimensions of employed AA 2024 panels prior to adhesive bonding or physical/chemical characterisation

test method	adherend	dimensions [mm x mm x mm]	cladding
floating roller peel	base sheet	250 x 200 x 1.6	bare/clad
	peel sheet	300 x 200 x 0.6	bare/clad
wedge test	both sides	150 x 150 x 3.2	clad
cyclic lap-shear	both sides	200 x 200 x 1.6	clad
hot/wet exposure	base sheet	250 x 200 x 1.6	bare/clad
	peel sheet	250 x 200 x 0.8	bare/clad
bondline corrosion	base sheet	250 x 200 x 1.6	bare/clad
	peel sheet	250 x 200 x 0.8	bare/clad
electrochemical characterisation, LSM		150 x 80 x 1.2	bare/clad

Surface pre-treatment

Here, the term surface pre-treatment, or conditioning, refers here to the surface preparation steps employed to remove contamination, the initial oxide film and the mechanically deformed layer, as well as to create differing surface properties. Three different pre-treatment techniques are used, which all include similar cleaning and alkaline etching steps and vary only in the final treatment step, which determines their name. Apart from initial solvent cleaning, all cleaning and etching steps are tank processes. Typically, it is not necessary to etch and desmut surfaces before grit-blasting, as grit-blasting fully removes the oxide formed during etching, i.e. the oxide properties are independent of the initial state. However, the metal sheets are strongly contaminated during the rolling process. Consequently, the initial etching procedure is applied to ensure that all contamination of the aluminium panels is removed on both sides of the panels before grit-blasting. In particular during dip-coating, the contamination of the coating solution must be avoided.

Smut-Go NC pickling (Smut-go NC):

Turco-Liquid Smut-Go NC is a chromate-free acidic solution to desmut and deoxidise aluminium alloys that contains ferric sulphate, nitric acid, sodium hydrogendifluoride and sulphuric acid [172]. Smut-Go NC is normally used prior to anodising and not as final pre-treatment step. Process details are displayed in Table 3.2.

Table 3.2: Smut-Go NC pre-treatment process

#	process step	product name	supplier	temperature [C]	immersion time [min]
1	solvent cleaning	isopropyl alcohol	ABCR	RT	---
2	alkaline cleaning	Metaclean T2001	Chemie-Vertrieb Hannover	65	15
3	rinsing	DI water		RT	5
4	alkaline etching	P3-Almeco 51	Henkel Surface Technologies	35	3
5	rinsing	DI water		RT	5
6	acidic pickling	Turco Liquid Smut-Go NC	Henkel Surface Technologies	40	5
7	rinsing	DI water (tank)		RT	5
8	rinsing	DI water (spray)		RT	2

Nitric acid (HNO₃) pickling:

Nitric acid diluted with DI water to 150 g/l is used as alternative process step for deoxidation and desmutting of AA 2024 panels. Similar to Smut-go NC, HNO₃ etching is typically not used as final pre-treatment step. Process details are displayed in Table 3.3.

Table 3.3: HNO₃ pre-treatment process

#	process step	product name	supplier	temperature [C]	immersion time [min]
1	solvent cleaning	isopropyl alcohol	ABCR	RT	---
2	alkaline cleaning	Metaclean T2001	Chemie-Vertrieb Hannover	65	15
3	rinsing	DI water		RT	5
4	alkaline etching	P3-Almeco 51	Henkel Surface Technologies	35	3
5	rinsing	DI water		RT	5
6	acidic pickling	nitric acid (HNO ₃), 150 g/l	diverse, technical grade	RT	15
7	rinsing	DI water		RT	5
8	rinsing	DI water (spray)		RT	2

Grit-blasting:

Grit-blasting is conducted manually with fresh alumina grit in a cabinet under the conditions shown in Table 3.4. Prior to grit-blasting, the samples are cleaned and etched similarly to the HNO₃ pickled substrates. The only deviation is an immersion time of only 5 min in HNO₃, which is fully sufficient to remove the smut. Longer immersion to create a distinct oxide morphology is not needed, because the pickling oxide is fully removed during grit-blasting. To obtain a uniform matt appearance, blasting is performed perpendicular and along to the rolling direction in square-wave-like movements, where the blast area of each pass overlaps with the preceding one. In total, the surface is blasted four times: twice perpendicular and twice along the rolling direction. Directions alternate beginning with perpendicular to and finishing in rolling direction. Loose grit is removed with dried, oil-free compressed air.

Table 3.4: Grit-blasting process parameters

process parameters	
grit	white fused aluminium oxide
nominal grit diameter	50 μm
fluid	dried oil-free compressed air
pressure	5 bar
distance	10 cm
angle	90°

Phosphoric sulphuric acid anodising (PSA)

Reference samples for adhesion and durability testing are anodised in phosphoric sulphuric acid according to the process parameters displayed in Table 3.5. Anodising is preceded by the Smut-Go NC pickling process described above without the final spray rinsing step.

Table 3.5: PSA process parameters

process parameters	
[H ₃ PO ₄]	120 g/l
[H ₂ SO ₄]	80 g/l
[Al] dissolved	2-5 g/l
bath temperature	28 C
immersion time (total)	23 min
voltage (plateau)	18 V
time at plateau voltage	20 min
ramp	6 V/min
ramp time	3 min
DI rinsing (spray)	1 min
DI rinsing (tank)	15 min
DI rinsing (spray)	2 min

A typical aluminium oxide structure formed by PSA is shown in Fig. 3.1.

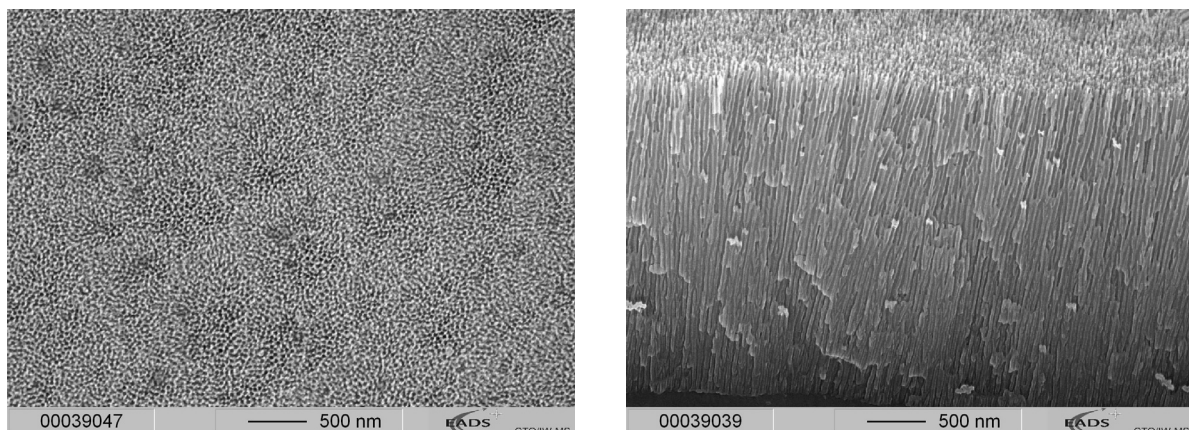


Fig. 3.1: SEM images of PSA derived oxide layer on AA 2024 clad: top view (left) and fracture (right)

Precursors

The employed precursors for solution and plasma deposition are listed in Table 3.6. All precursors are used as received.

Table 3.6: List of employed precursors

precursor	abbrev.	M [g/mol]	supplier
3-glycidoxypropyltrimethoxysilane	GPS	236.2	ABCR
tetraethyl orthosilicate	TEOS	208.2	ABCR
hexamethyldisiloxane	HMDSO	162.4	ABCR
octamethylcyclotetrasiloxane	OMCTS	296.6	ABCR
AC-130 (4-component kit)	AC-130		Advanced Chemistry & Technology

Coupling film deposition

Process parameters of the employed silane based treatments, GPS and AC-130, as well as of the atmospheric plasma deposition are specified in the following paragraphs.

GPS application:

GPS is removed from refrigerated storage sufficiently before usage allowing adjustment to room temperature. 1 % (v/v) aqueous solutions are created by adding the GPS to DI water. The pH of the solution is adjusted to pH = 5 with acetic acid. GPS is hydrolysed for 1 h under constant stirring at room temperature prior to application. The GPS solution is decanted into a tank for dip coating. GPS treatment parameters are based on the published optimal process conditions [26], [173], but contrary to the referenced publications, the aluminium panels are immersed for only two minutes in the silane solution to allow comparability with the AC-130 application, where the exposure to the precursor solution also lasts two minutes. The panels are then withdrawn at 30 cm/min. The silane coated panels remain on edge and excess silane solution at the lower edge is removed carefully with a clean, dry tissue. The panels are allowed to dry for 10 min before they are put vertically in a fan-assisted oven for 60 min, curing at 93 °C. After curing the panels are allowed to cool to ambient temperature. Due to its aqueous nature the wet film contracts during drying creating large deviations in film thickness, from several tens of nanometres to less than 10 nm.

AC-130 application:

AC-130 is prepared according the instructions provided on the 4-component kit and applied according the official application guide of the manufacturer [174]. At first, GPS and water, as well as zirconium (IV) n-propoxide solution (70 wt.% in 1-propanol) and acetic acid are mixed and allowed to react before both mixtures are joined. Minimum incubation time is 30 min. Despite its pot life of 10 h, the sol is applied within 2 h after incubation. AC-130 is applied by spray-drenching at room temperature, i.e. the sol is sprayed in excess onto the surface of the upright panels. The surface is kept continuously wet for at least 2 min and the excess solution is allowed to run off. The panels are then allowed to drain for 15 min and sol accumulating at the lower edge is removed carefully with a clean, dry tissue. The panels remain in vertical position without contact to fully dry and cure for additional 75 min at ambient conditions.

Atmospheric pressure plasma jet chemical vapour deposition (APPJ-CVD):

A commercialised atmospheric pressure plasma source manufactured by Plasmatrete GmbH (Steinhagen) is employed for deposition of all plasma derived coupling films. A non-equilibrium plasma jet is created by the Openair[®] process, where the plasma is generated by an arc discharge that is controlled by a gyrating gas stream inside the nozzle. Dry, oil-free compressed air is used as plasma gas. The air flow rate cannot be directly controlled and displayed, but is reported to be around 20 to 30 l/min [39], [175]. The plasma source is potential-free to the substrate to avoid sparkover. Plasma analysis of a similar source measured gas temperatures of $T_g \approx 600\text{-}800$ K, electron temperatures of $T_e \approx 0.7$ eV and vibrational temperatures of $T_v \approx 0.3$ eV [176]. Plasma deposition is conducted by injection of vaporised precursor at the end of the nozzle. This process is also referred to as PlasmaPlus[®] technology. More details on the plasma source can be found in Fig. 3.2 and in the corresponding patent [135].

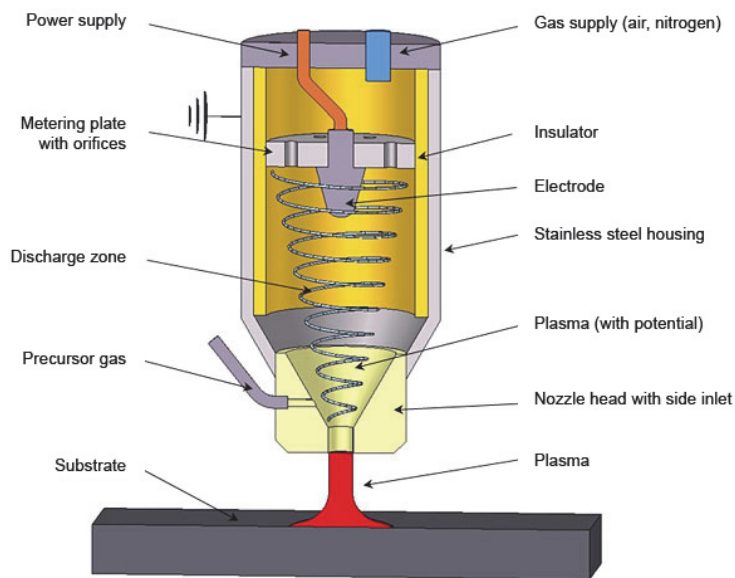


Fig. 3.2: PlasmaPlus® deposition nozzle according to [177]; (property of Plasmamatreat GmbH)

linear actuators, with CNC programming allowing a reproducible movement over the sample surface. The plasma treatment is carried out under a suction hood to capture the generated ozone. All process parameters are displayed in Table 3.7.

The liquid precursors are transformed into gas-state by means of a tempered bubbler with helium as carrier gas. Feed flow rates are controlled by a mass flow controller with a range of 0.5 to 5 SLM. The precursor feed flow does not have a significant impact on electron or gas temperature [176]. Maximal employed HMDSO feed flow rate is 1 SLM, whereas the other precursors are deposited up to 5 SLM feed flow. The precursor is activated and fragmented inside the jet (afterglow) and forms a film upon contact with the substrate surface. The plasma jet is moved over the surface in a square-wave-like manner with a step width of 3 mm creating an overlap of approximately 50 % between each deposition line to ensure homogenous film thickness. Movement is carried out with a computer controlled xyz-device with

Table 3.7: APPJ-CVD process parameters

process parameters	
plasma generator	Plasmamatreat FG3001
electrical power input	appr. 700 W
excitation frequency	19 kHz
plasma gas	compressed air (dry, oil-free)
air inlet pressure	3 bar
nozzle type	PT6458-4
appr. plasma jet diameter	6 mm
nozzle speed (parallel to surface)	100 mm/s
distance nozzle-surface	12 mm
bubbler temperature	30 °C / 80 °C (GPS)
bubbler/carrier gas	He
carrier gas feed flow rate	0.5 - 5 SLM

Adhesive bonding

Two different epoxy adhesives are employed for bonding of the aluminium panels: DP 490 and FM 73. Corresponding bonding processes are described in the following two paragraphs.

DP 490:

The Scotch-Weld EPX Epoxy Adhesive DP 490 (3M), a thixotropic two component adhesive, is used in initial peel testing of plasma treated joints. However, it does not fulfil aeronautics standards and is not qualified. Nevertheless, it is known to behave quite similar to temperature- and pressure-curing epoxy film adhesives used in aircraft industry. Base and accelerator component (mix ratio 2:1 vol.) are separated inside

the cartridge and are mixed using a manual applicator gun with a mixer nozzle from where the adhesive is deposited in excess onto the larger adherend (peel sheet). It is then homogeneously distributed with a scraper before the smaller adherend (base sheet) is placed on top. Fresh cartridges are used for every bonding series. Adhesive bonding is conducted within no more than 2 h after the final surface preparation step. Both adherends are placed in a PTFE covered metal jig that fixes the bondline thickness at 0.2 mm and allows excessive polymer to be pressed out at the edges. A contact pressure of 1.4 bar is applied with a hydraulic press during 24 h curing at ambient temperature (23 ± 2 °C). Afterwards the bonded panels are removed from the jig and placed in a fan-assisted oven for 1 h continued curing at 80 °C to achieve full strength. Further processing for mechanical testing is carried out after at least 2 h of cool down to ensure that ambient temperature is reached. Coupons are cut with a disc saw according to the specifications of the peel test.

FM 73:

FM[®] 73 (Cytec Engineered Materials) is a rubber-toughened epoxy film adhesive qualified for aerospace applications and designed to provide sufficient structural integrity from -55 °C to 82 °C. The adhesive is removed 24 h before processing from storage at -18 °C (in sealed plastic bags) to allow adaptation to room temperature. All joints for mechanical and durability testing are made with the FM 73 M.06 film (yellow), which is supported by a polyester mat and has a nominal bondline thickness of 0.25 mm. “Open” joints for EIS measurements are made with the FM 73 M.03 film (green), which is also supported by a polyester mat, but with a nominal thickness of 0.13 mm to obtain a lower dielectric barrier. Glass transition temperature is approximately 100 °C [178]. The quality of the adhesive films is periodically assured by differential scanning calorimetry and thermogravimetric analysis. Adhesive bonding is conducted in an autoclave within no more than 2 h after the final surface preparation step. Contact pressure is obtained by vacuum bagging plus application of 2.5 bar external pressure. Once full pressure is applied the panels are heated with 2 °C/min to 125 °C and remain at this temperature for 75 min. Cooling rate is maximal 2 °C/min under pressure. For EIS specimens a PTFE foil is placed between the adhesive film and one adherend. Sample cutting is carried out according the test specifications described in the following chapter.

3.2 Mechanical and durability testing

Peel test

The employed roller peel test set-up is in accordance with DIN EN 2243-2, except for using AA 2024 peel sheets⁶ with a thickness of 0.6 mm instead of 0.5 mm as defined by the standard. The original scope of this test procedure is to determine the resistance of the adhesive against peel loads. However this test is also considered as very distinctive for surface treatments. To further assess the effectiveness of surface preparation techniques, the test is modified by injection of water into the bondline, the so-called wet-peel test by floating-roller method according to ISO 14676. Peel testing is carried out at ambient temperature (23 ± 2 °C) along the rolling direction of the test coupons in a computer controlled Z010 (Zwick Roell) tensile testing machine with a floating-roller fixture attached to the load cell. Peel specimens are cut from the bonded panels with a circular saw and have a nominal width of 25 mm. The exact width is measured with a precision vernier calliper at both ends and the middle of the coupon and the average value is entered into the software mask. The loose end of the peel sheet is gripped in the jaw of the testing machine. The samples are peeled at a constant separation speed of 100 mm/min. After peeling of at least 75 mm, the crosshead is stopped and several drops of water containing 1 % detergent are injected into the crack opening. Separation is continued until approximately 10 mm before the edge of the joint. At least the first 20 mm (dry) and the first 10 mm after water injection (wet) are disregarded and only the two areas of stable loads are considered for the average peel strength calculation conducted by the testing software.

⁶ The thinner adherend panels are referred to as “peel sheets” as this side of the coupons is peeled off.

Dynamic lap shear test in water

Dynamic lap shear testing in water is not a standardised test for bonded joints. The succeeding paragraphs will detail sample preparation and test procedure.

Sample preparation:

Six 150 x 25 mm samples are cut from the centre of the 200 x 200 mm bonded panels with a circular saw. The long edges follow the rolling direction of the adherends. Each adherend side is cut in two by milling a 2 mm wide groove – perpendicular to the long side – through the metal, but not the adhesive. The inner edge of each groove is in exactly 4 mm distance to the transversal centre plane of the specimen but diametrical to the centre creating an overlap of 8 mm. Hence the resulting single lap area is 200 mm². Sample length and overlap are reduced compared to standard single lap sample geometries for static testing (DIN EN 2243-1). The length is decreased to reduce the bending moment and to allow three samples to be tested at one time. The overlap is decreased to reduce the applied loads in order to avoid fatigue fracture within the aluminium adherend. Holes of 5 mm diameter are drilled through both sides of the specimen in 10 mm distance to the sample ends to allow mounting into the test device.

Test conditions:

A computer-controlled Schenck PSA 10 kN servo-hydraulic machine is used for all tests. A string of three specimens is placed in a row. The samples are connected via stainless steel plates and bolts; fixation to the machine is done with stainless steel bolts as well. The mounting allows an alignment of the sample direction in line with the load direction. Dynamic loading is conducted under permanent tension with a maximal load $F_{\max} = 1.2$ kN and a load ratio of $R = 0.1$. Tests are performed at 25 Hz up to maximal 10^7 load cycles. Testing is conducted at ambient conditions (only one reference system) or during immersion of the specimens in DI water at 50 ± 0.2 °C. Water is constantly circulated through a PMMA cylinder entering at the bottom and draining at the top. Water temperature is monitored close to the samples and controlled by a refrigerated heating circulation system (Julabo F32). Fatigue life is calculated as average of all test samples. The complete set-up is presented in Fig. 3.3. If the maximum number of load cycles is reached without failure, samples are dried and the remaining shear strength is tested statically in a tensile test machine (Zwick Roell Z1010) at ambient conditions.

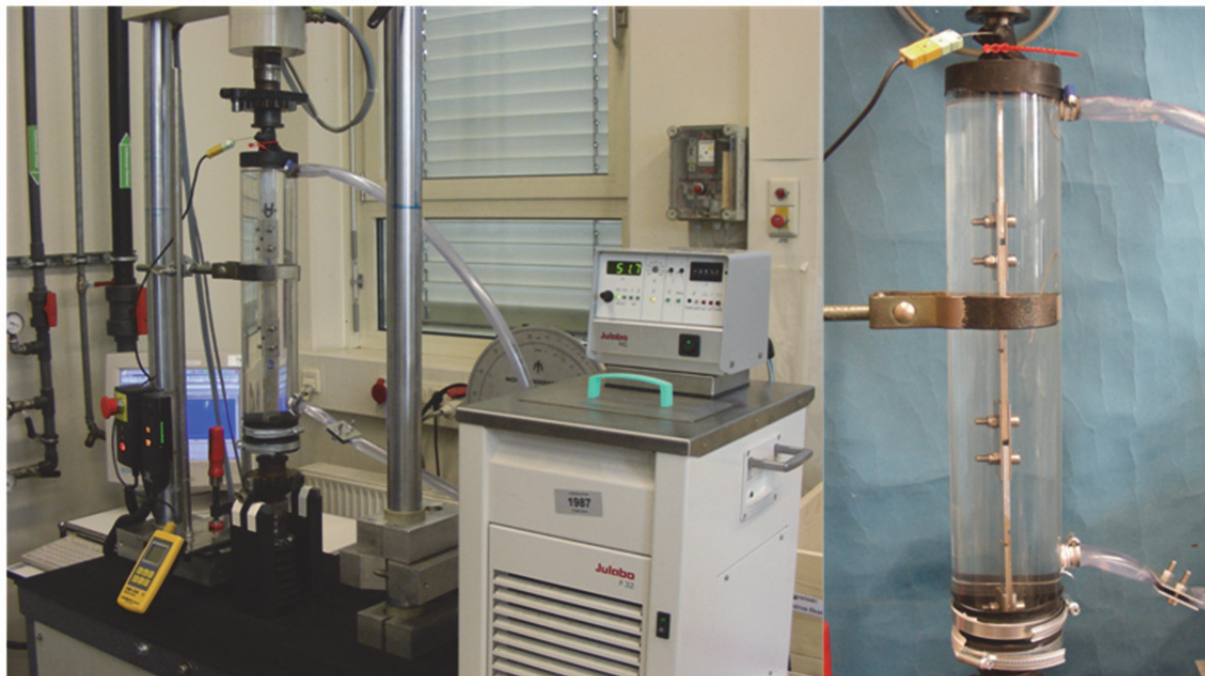


Fig. 3.3: Experimental set-up of dynamic single lap shear testing; sample area with 3 specimens in water (right)

Wedge test

Wedge testing is carried out in principle accordance to standard DIN 65448 with the exception of the use of a 50 power optical microscope to locate the crack tip, whereas the standard requires only 40 power. Cr-Ni wedges are forced into the bondline with the help of a tensile testing machine at a constant speed of 2 mm/s. Specimens are stored under ambient conditions for 24 h before the initial crack length is determined. Hot-wet exposure is carried out in a climate chamber at 50 °C and 96 % rh. Corrosion tests are conducted in a salt spray chamber (35 °C, 5 % NaCl). Specimens are removed from the chamber and crack length/extension is measured within 15 min.

Bondline corrosion and condensation water tests

Bondline corrosion tests are performed in accordance with the Airbus standard AITM 5-0009. Bonded samples are exposed to 5 % NaCl neutral salt fog in a chamber according to ASTM B117 at 35 °C without application of mechanical loads. The samples are removed after exposure, rinsed in tap water and then peeled open. The extent of bondline corrosion is expressed by the quotient of corroded/delaminated area and total bond area:

$$\text{extent of bondline corrosion} = \frac{\text{corroded bond area}}{\text{initial bond area}} \times 100 [\%]$$

The rate of bondline corrosion is displayed as a linear trendline derived from the measured extent of bondline corrosion per exposure time. Other than described in the standard the samples are removed from the salt fog chamber already after 15, 30 and 45 d and not after 45, 90, 180 and 300 d, which are the typical intervals for anodised samples in combination with chromate loaded primers.

Six 200 x 25 mm samples are cut with a band saw from one bonded panel along the rolling direction. As the properties of the sawn faces are highly impacting the bondline corrosion extent the blade needs to be specified: a new blade with 14 teeth per inch is employed and operated at 8 to 10 m/s. The blade is not lubricated and no other material has been cut with it.

Similar sample geometries and the same cutting process are used for producing the samples for the condensation water test. Samples are exposed up to 45 d in a condensation climate chamber with 100 % rh at 35 °C. The extent of degradation was determined consistently to the bondline corrosion.

For both tests, samples are put upright into a rack with an angle of approximately 6° relative to the vertical. Six specimens per exposure period are tested – with only two specimens cut from the same bonded panel.

3.3 Surface and interface analyses

X-ray photoelectron spectroscopy (XPS)

If not indicated differently below, a Quantum 2000 Scanning ESCA Microprobe (Physical Electronics) system equipped with a monochromatic Al K α source operated at 15 kV and 24 W is used to obtain the XPS spectra. Chamber pressure is reduced to 6 x 10⁻⁹ mbar before measuring. Probes with a diameter of 100 or 200 μ m are examined with an electron take-off angle of 45°⁷ and a resulting sampling depth of approximately 50 Å. The analysis times are kept short for minimizing radiation damage to the sample. Employed sensitivity factors are: carbon, 0.278; oxygen, 0.780; nitrogen, 0.477 representing the average values of the manufacturer. Elemental composition survey scans are carried out at low energy resolution (0–1350 eV) with a pass energy of 117.4 eV – high resolution scans with a pass energy of 11.75 eV. Charge neutralisation is conducted using a low energy ion beam and a low energy electron beam. Elemental composition measurements are repeated twice. Displayed values represent the average of both measurements.

⁷ Take-off angle for the characterisation of the HNO₃ derived oxide is 90°.

Sputter depth profiling is performed by Ar bombardment with an acceleration voltage of 2 kV on an area of $2 \times 2 \text{ mm}^2$ with resulting sputter rates between 7 and 12 nm/min calibrated on SiO_2 (Si wafer). Oxide or film thickness is approximated by consideration of the oxygen gradient, i.e. by determining the sputter time needed to reach half maximum concentration.

XPS spectra for the calculation of the aluminium oxide thickness and for the calculation of hydroxide content of the grit-blasted and Smut-Go NC etched samples in chapter 4.2.2.2 are carried out at the “Bundesanstalt für Materialforschung und -prüfung” (BAM) using an AXIS Ultra DLD (Kratos Analytical) with a monochromatic Al $K\alpha$ source. Analysed area corresponds approximately to a rectangle of $700 \times 300 \mu\text{m}$ [179]. Angle of emission is 90° .

Chemical derivatisation X-ray photoelectron spectroscopy (CD-XPS)

Derivatisation and XPS analysis are carried out by the BAM according to the author’s specification. Derivatisation of the hydroxyl groups at the aluminium surfaces is performed in a polypropylene tube filled with trifluoroacetic anhydride, TFAA, (99 %, Aldrich) under ambient atmosphere at normal pressure for 24 h according to the procedure published by Ono et al. [179], [180]. It is assumed that the following derivatisation reaction occurs:



CD-XPS spectra of the TFAA-derivatised substrates are obtained with an ESCALAB 200X (VG Instruments) spectrometer with non-monochromatic Al $K\alpha$ excitation, which allows a large area of about 5 mm diameter to be analysed. Angle of emission is 75° .

Calculation of the hydroxyl concentration is derived from the fluoride and aluminium concentrations identified in an XPS survey spectra. An example of the XPS spectra after derivatisation is displayed in appendix Fig. A.15. The inorganic fluoride (F^-) is subtracted from the overall fluoride signal as both F^- and CF_3 signals can be separated easily. The remaining fluoride concentration needs to be divided by the Al_{ox} (oxidically bound Al) concentration and the factor 3 due to the equation shown above to obtain the hydroxyl concentration. The Al_{ox} concentration is calculated from the overall Al concentration of the survey spectrum multiplied by the ratio of oxidic aluminium determined by XPS analysis of the non-derivatised samples.

Scanning electron microscopy (SEM)

A Jeol JSM-6320F field emission scanning electron microscope is employed for high resolution optical surface and interface analysis. The lateral resolution is approximately 1.5 nm. Samples are fractured in liquid nitrogen (cryofracture) to allow a side view on the fractured oxide layers and coupling films. Pt is sputtered onto the samples to reduce charging. Energy-dispersive X-ray spectroscopy (EDX) for determination chemical composition is carried out with a Bruker AXS, ESPRIT 8.0 allowing a detection of elements with an atomic number of $z = 5$ or higher.

Some SEM investigations are performed by the Fraunhofer-Institut für Fertigungstechnik und Angewandte Materialforschung (IFAM) according to the author’s specification, using a LEO 1530-Gemini (Zeiss) field emission scanning electron microscope with a lateral resolution of approximately 1.0 nm. Corresponding micrographs are labelled “IFAM”.

Transmission electron microscopy (TEM)

TEM and high resolution TEM investigations as well as scanning transmission electron microscopy (STEM) are performed using a Philips Tecnai 30 FEG analytical electron microscope equipped with EDX, HAADF and EELS facilities. Prior to microscopy electron-transparent sections are cut with a Leica Ultracut UCT ultramicrotome. Sections with nominal thickness of 100-200 nm are derived from final sectioning normal to the polymer-metal interphase of the specimens with a diamond knife encapsulated in polymerised resin. Sample preparation and analysis are conducted by IFAM according to the author’s specification; all TEM and STEM images displayed in this work are produced by IFAM.

Laser scanning microscopy (LSM)

LSM is conducted with a LEXT OLS4000 (Olympus) device with a 100x magnification lens to determine roughness and topography (surface factor). The measurements are carried out on 5 different areas (128 x 96 μm) on two different samples to level out local inhomogeneities. Maximal optical resolution is 0.12 μm lateral and 10 nm in z-axis, which equals the index step of the z-motor.

Atomic force microscopy (AFM)

The topography of the TEOS derived plasma-polymer film was investigated using a Digital Instruments Nanoscope III AFM fitted with a silicon tip covered with PtIr_5 in tapping mode to avoid scratching of the sample surface.

Auger electron spectroscopy (AES)

The AES mapping of the AA 2024 bare substrate after Smut-Go NC conditioning was performed by the BAM according to the author's specification, using a PHI-700 Scanning Electron Nanoprobe (Physical Electronics) with an excitation energy of the electrons of 20 keV at 10 nA and an Ar-ion bombardment energy of 3keV at 2 μA . Diameter of the individual analysing spots is approximately 20 nm.

Time of flight secondary ion mass spectrometry (ToF-SIMS)

Analysis of the chemical bonding state and the composition at the interphase are performed with a TOF-SIMS IV (ION-TOF) by OFG Analytik GmbH (Muenster, Germany) according to the author's specification. Survey analysis is carried out in static SIMS mode, depth profiling in dynamic mode with higher energy ion bombardment. Positive and negative spectra are analysed. Mass resolution ($\Delta m/m$) is < 5000 . Depth profiling is obtained by gentle Cs^+ sputtering at 0.5 keV. Detailed process parameters are shown in Table 3.8.

Table 3.8: ToF-SIMS parameters for the 3 analysed plasma films

		precursor	GPS (5 SLM)	GPS (5 SLM)	TEOS (0.5 SLM)	
		ToF-SIMS parameters		substrate	AA 2024 bare	AA 2024 bare
		pre-treatment	grit-blasted (Al ₂ O ₃ , 50 μm)	polished 30 s conditioned (HNO ₃)	polished 30 s conditioned (HNO ₃)	
overview - static SIMS	positive and negative	primary ions	Ar ⁺	Ar ⁺	Ar ⁺	
		energy [keV]	10	10	10	
		area [μm ²]	100.0 x 100.0	100.0 x 100.0	100.0 x 100.0	
		ion dose [cm ⁻²]	2.50 x 10 ⁸	2.50 x 10 ⁸	2.50 x 10 ⁸	
		current [pA]	0.50	0.50	0.50	
		time [s]	80	80	80	
sputter depth profiling - dynamic SIMS	positive	analysis parameters	primary ions	Bi ⁺	Bi ⁺	Bi ⁺
			energy [keV]	25	25	25
			area [μm ²]	99.6 x 99.6	99.6 x 99.6	115.2 x 115.2
			ion dose [cm ⁻²]	6.49 x 10 ¹³	3.31 x 10 ¹³	6.15 x 10 ¹³
			current [pA]	1.20	1.30	1.30
	negative	sputter parameters	primary ions	Cs ⁺	Cs ⁺	Cs ⁺
			energy [keV]	0.50	0.50	0.50
			area [μm ²]	300.0 x 300.0	400.0 x 400.0	400.0 x 400.0
			ion dose [cm ⁻²]	4.77 x 10 ¹⁷	6.95 x 10 ¹⁶	1.73 x 10 ¹⁷
			current [nA]	80.00	44.00	44.00
	positive	analysis parameters	primary ions	Bi ⁺	Bi ⁺	Bi ⁺
			energy [keV]	25	25	25
			area [μm ²]	99.6 x 99.6	99.6 x 99.6	96.7 x 96.7
			ion dose [cm ⁻²]	6.49 x 10 ¹³	1.29 x 10 ¹⁴	2.31 x 10 ¹⁴
			current [pA]	1.20	1.30	1.30
negative	sputter parameters	primary ions	Cs ⁺	Cs ⁺	Cs ⁺	
		energy [keV]	0.50	0.50	0.50	
		area [μm ²]	300.0 x 300.0	400.0 x 400.0	400.0 x 400.0	
		ion dose [cm ⁻²]	4.77 x 10 ¹⁷	2.70 x 10 ¹⁷	4.58 x 10 ¹⁷	
		current [nA]	80.00	44.00	44.00	

3.4 Electrochemical analyses

The principle experimental set-up for potentiodynamic polarisation and impedance spectroscopy is similar for all measurements. A PMMA cylinder with a diameter of 30 mm is bonded onto the coated or uncoated sample with a polysiloxane adhesive, which is cured for 24 h at ambient conditions. The cylinder is then filled with electrolyte. The substrate acts as the working electrode and the 2.5 mm² platinum counter electrode as well as the reference electrode are immersed into the electrolyte. A schematic illustration of the set-up is displayed in Fig. 3.4.

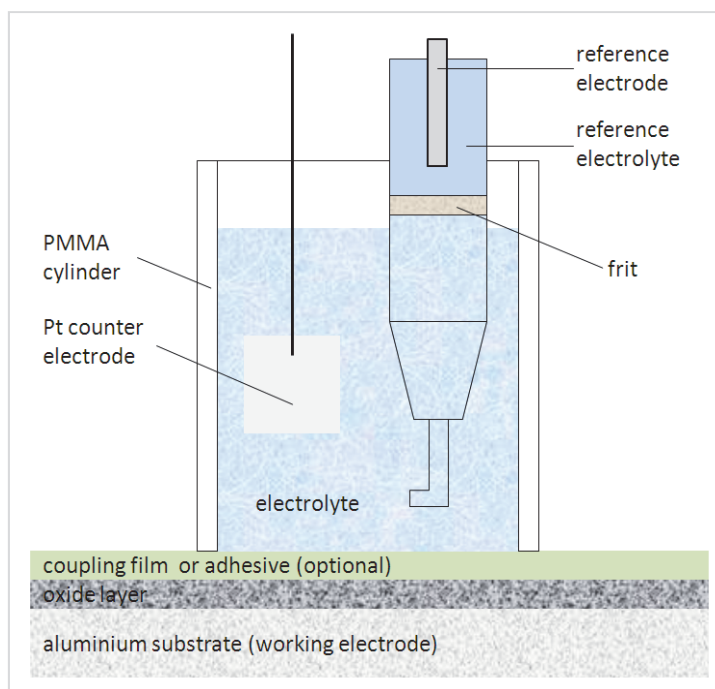


Fig. 3.4: Schematic experimental set-up for electrochemical analyses

Potentiodynamic polarisation

HNO₃ etched AA 2024 bare substrates are used for potentiodynamic polarisation experiments. Polarisation is performed directly after exposure to the 0.05 m NaCl (aq) electrolyte solution with a Gamry Reference 600 potentiostat and a saturated calomel reference electrode (SCE). The potential is varied ranging from -0.8 V to 0 V with a scan rate of 0.5 mV/s.

Electrochemical impedance spectroscopy (EIS)

EIS measurements for the evaluation of the diffusion barrier properties of the epoxide adhesive (chapter 4.3.2.3) are conducted on AA 2024 bare substrates etched with Smut-Go NC or anodised in phosphoric-sulphuric acid and then coated with the FM 73 M.03 film adhesive. 0.05 m NaCl (aq) is used as electrolyte. An EG&G Instruments Model 283 potentiostat equipped with a frequency response detector Model 1025 is employed to obtain the impedance spectra. 50 mV sinusoidal perturbations are applied over a frequency range from 0.01 Hz to 100 kHz with 10 intermediate frequency steps per decade. Measurements are started after a stable open circuit potential (OCP) is reached, i.e. the OCP drift is < 0.1 mV/s. Impedance plots are fitted with the Gamry Echem Analyst software. Electrolyte exposure is maintained for 200 d.

EIS measurements for the evaluation of the stability of the oxide and the coupling films in acidic conditions are performed on AA 2024 clad substrates conditioned in HNO₃. As the oxide layer is very sensitive to chlorides, a 0.05 m potassium sulphate electrolyte is used for measuring. The ageing of the samples is carried out in a halide-free pH 4 buffer solution. After the desired exposure time, the puffer solution is removed from the PMMA cylinder which is then rinsed five times in DI water before the electrolyte is

filled in. The sample surface is not allowed to dry in-between these steps. A Gamry Reference 600 potentiostat with a mercury/mercurous sulphate (Hg/HgSO_4) reference electrode is employed to obtain the impedance spectra. 5 mV sinusoidal perturbations are applied over a frequency range from 0.01 Hz to 100 kHz with 10 intermediate frequency steps per decade. Measurements are started after a stable OCP is reached with a drift < 0.1 mV/s. Impedance plots are fitted with the Gamry Echem Analyst software. After the measurement, the electrolyte is removed, the cylinder is rinsed five times, and the buffer is refilled in order to continue the ageing process.

4 Results and discussion

As pointed out in the introduction, surface treatment is the key aspect of the durability of a bonded joint. The overall surface preparation consists of the pre-treatment of the metal adherends followed by deposition of the coupling film. For maximising joint performance, both coupling films and surface pre-treatment need to be optimised. In order to understand the impact of these two process steps, they are firstly considered independently. Film properties after APPJ-CVD are considered autonomously from the state of aluminium oxide surface and the surfaces formed after the different conditioning methods are characterised before application of the coupling films. Subsequently, overall joint integrity with regard to adhesion and durability is determined and correlated to surface and film properties. Special attention is paid to the resistance of the treated joints against bondline corrosion and the corresponding degradation mechanism of the aluminium adherends after plasma and silane deposition.

4.1 Plasma film characterisation and influence on adhesion

APPJ-CVD derived films are characterised in terms of chemical composition, film thickness and topography. Furthermore, the chemical state of the film surface is characterised to explain the diverging adhesion of the polymer on the individual coupling films.

4.1.1 Film thickness, morphology and chemical composition

Four different Si-organic precursors are employed for the plasma deposition of films. Beside the most commonly employed HMDSO and TEOS, OMCTS and GPS are used. Precursors are injected by means of a helium flow directed through a bubbler. The experimental set-up allows a variation of the feed flow between 0.5 and 5 SLM. Film thickness of the deposited plasma polymers depends highly on the vapour pressure of the precursor [44]. As vapour pressure differs largely between the employed precursors (Table 4.4), a variation of feed flow allows deposition of plasma films with similar thickness derived from different precursors. By comparing different feed flows for one precursor, the impact of the film thickness can be determined.

Table 4.1: Elemental composition [at.%] by XPS survey of AA 2024 bare coated with plasma films

	C	O1s	Al	Si	Cu	N
HMDSO 0.5 SLM	16.5	56.7	-	26.8	-	-
OMCTS 5 SLM	14.0	59.2	2.2	24.6	-	-
TEOS 5 SLM	13.1	60.8	1.1	25.0	-	-
TEOS 0.5 SLM	18.2	55.4	2.9	23.2	0.3	-
GPS 5 SLM	22.3	53.5	4.1	19.2	0.6	0.3

After several preliminary tests, five different parameters are selected to study plasma film properties. Due to its high vapour pressure and consequently, a high deposition rate, HMDSO deposition creates films of relatively high thicknesses already at low precursor feed flow rates. Thus, HMDSO coatings are deposited at only 0.5 SLM. Contrarily, deposition of GPS leads to extremely thin films due to its very low vapour pressure. Even with 5 SLM helium flow, the bubbler needs to be heated to 80 °C in order to achieve a measurable film thickness⁸. For TEOS and OMCTS the maximum feed flow of 5 SLM is used to obtain

⁸ For HMDSO, OMCTS and TEOS the bubbler temperature is 30 °C.

film thicknesses that are roughly the same order of magnitude as with HMDSO. Additionally, 0.5 SLM TEOS deposition is used to obtain a film of comparable thickness to the GPS film. XPS sputter depth profiles corresponding to the five selected parameters are displayed in Fig. 4.1.

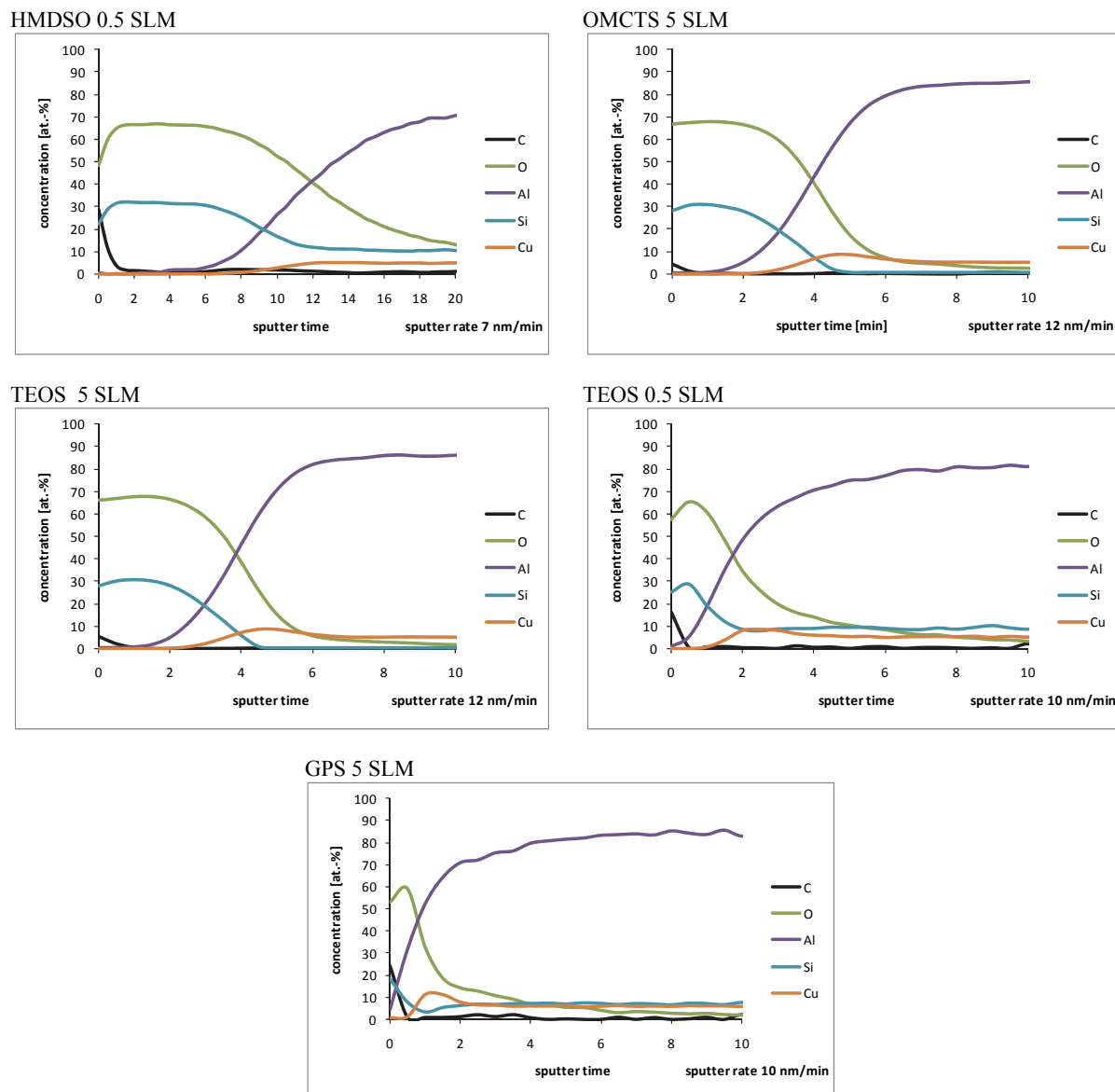


Fig. 4.1: XPS sputter depth profiles of plasma films on AA 2024 bare (Smut-Go NC)

Film thickness, like chemical composition, is estimated by XPS sputter depth profiling first and then verified by SEM images of fractured coatings. It is calculated by multiplying sputter time through the coating and sputter rate. The interface between oxide and plasma film is defined as half of the maximum of the silicon concentration. Hence, sputter time corresponds to the interval from the beginning up until the time when this concentration is reached. Fig. 4.1 shows the depth profiles for the five selected parameters. As visible in the sputter profiles, all surfaces are covered with a certain amount of carbon, which is, at least to a certain extent, adventitious carbon contamination that is adsorbed from ambient air due to an associated reduction of surface free energy – surface carbon concentrations determined XPS surface surveys are displayed in Table 4.1. Therefore, the maximum Si concentration is not reached directly at the surface, but once the carbon concentration is minimal. Calculated XPS film thicknesses are shown in Table 4.2 and Table 4.3.

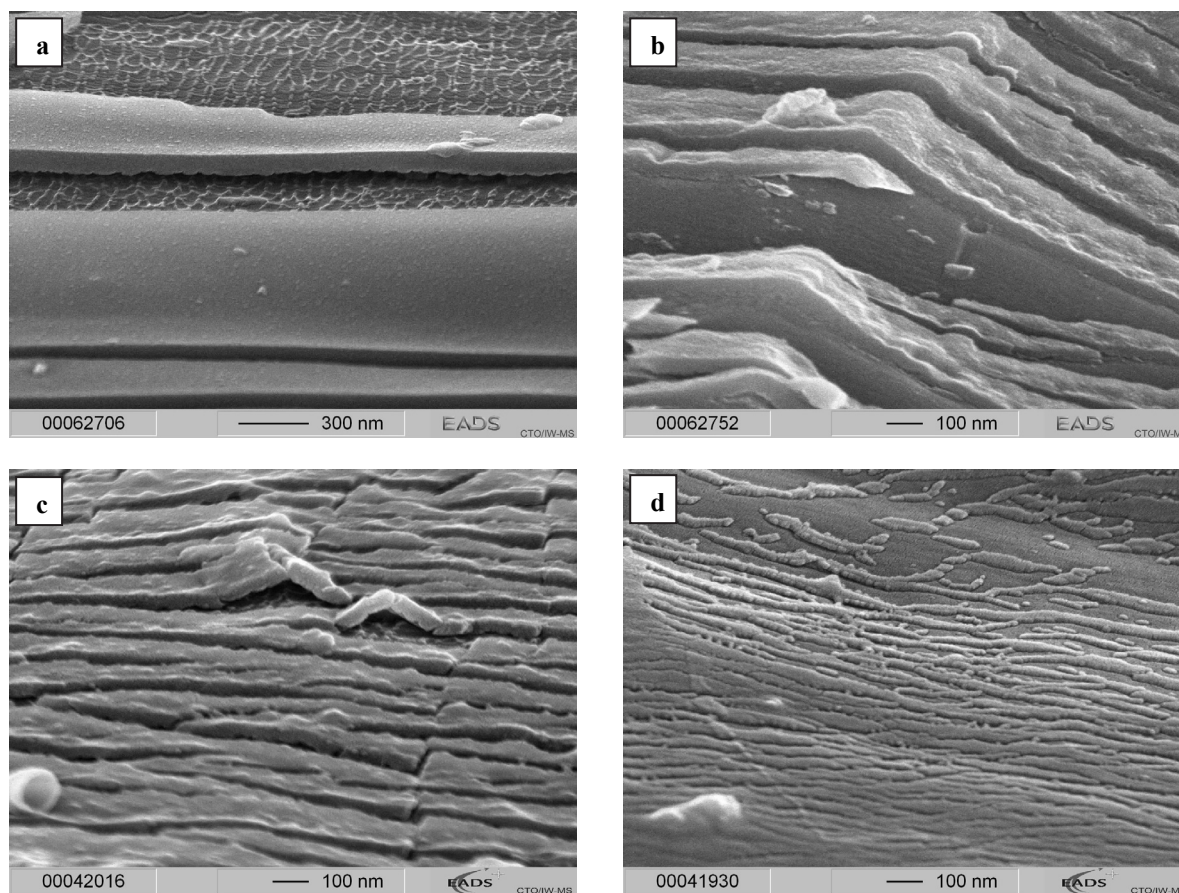


Fig. 4.2: SEM fracture images of 0.5 SLM HMDSO (a), 5 SLM OMCTS (b), 5 SLM TEOS (c) and 0.5 SLM TEOS (d) derived plasma films on AA 2024 bare (Smut-Go NC)

When comparing the results obtained with XPS and SEM, the magnitude of the average film thicknesses measured in the SEM images is approximately 1.4 times higher than the one determined by depth profiling where sputter rates are calibrated on pure SiO_2 on Si wafer. Apparently, the oxidic films generated by plasma deposition are less resistant against ion etching as the thermally generated silica on the reference wafer, which is known to be very dense and resistant to etching. This indicates that the deposited films are more porous and less cross-linked (due to OH-groups) than thermally generated silica films. Representative SEM images of fractured plasma films are displayed in Fig. 4.2. Limited by resolution, only the thicknesses of the 0.5 SLM HMDSO, the 5 SLM TEOS and the 5 SLM OMCTS derived films can be measured reasonably via SEM images. Unfortunately, 0.5 SLM TEOS and especially the 5 SLM GPS films cannot be clearly separated from the oxide and the micrographs of the cryofractured samples do not show upright breaking edges that allow estimation.

Table 4.2: Comparison of film thickness measured by XPS depth profiling and SEM images

	measured film thickness [nm]		SEM/XPS
	XPS	SEM	
HMDSO 0.5 SLM	64	90 ± 20	1.4
TEOS 5 SLM	39	55 ± 10	1.4
OMCTS 5 SLM	40	55 ± 10	1.4

Table 4.2 opposes the XPS and SEM film thicknesses. SEM values displayed in this table correspond to the midrange, i.e. the average of the minimum and maximum values found at the examined areas, i.e. they are not the exact mean. As thickness varies significantly, the midrange should only be considered as indication

and not as exact value. In any case, it is not the intent to precisely determine the true thickness value, but rather to give the right order of magnitude to be able to appraise obtained results.

Based on these results it is assumed that the real thickness of the 0.5 SLM TEOS and the 5 SLM GPS film is approximately 1.4 times higher than estimation by XPS depth profiling. Measured and estimated film thicknesses of these films are shown in Table 4.3.

Table 4.3: Estimation of true thin film thickness based on XPS depth profiling results

	film thickness [nm]	
	XPS	estimated “real”
TEOS 0.5 SLM	10	14
GPS 5 SLM	4	6

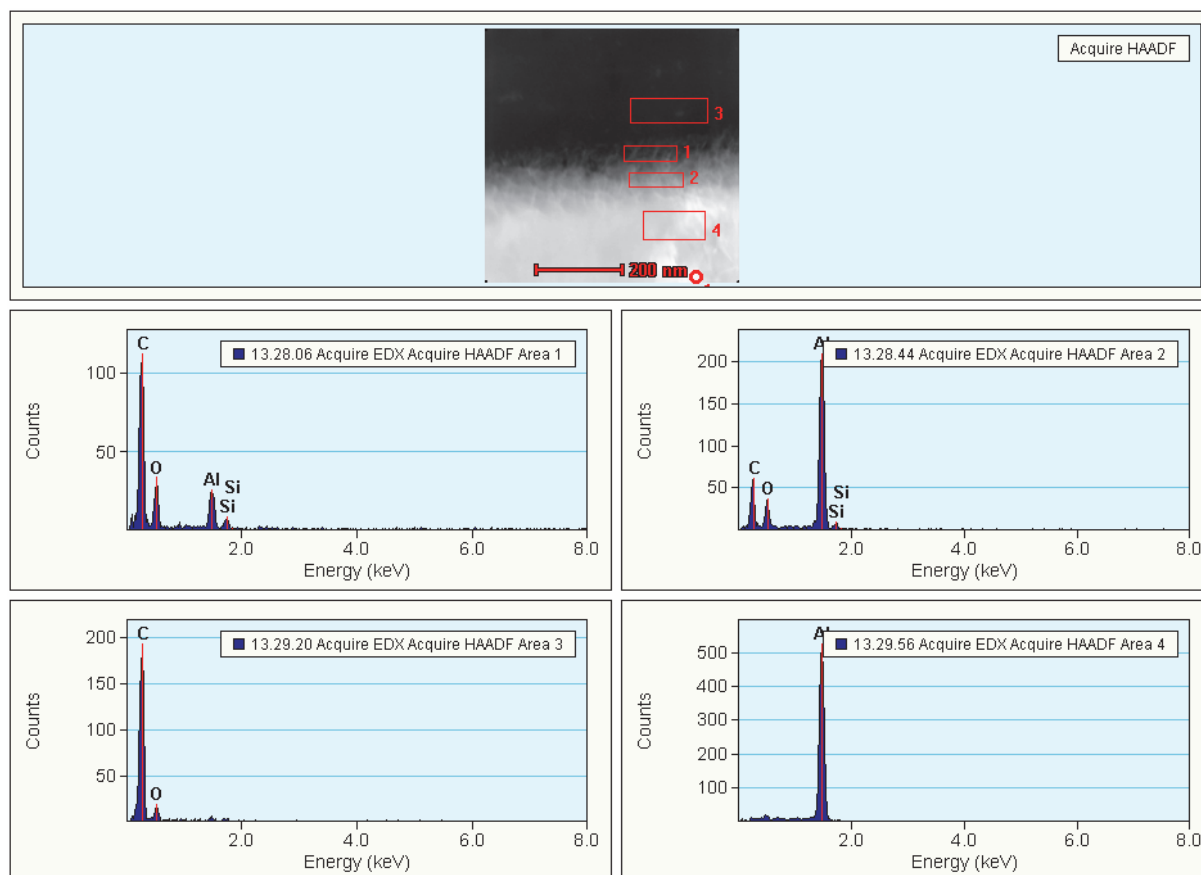


Fig. 4.3: STEM image of a GPS derived plasma film (5 SLM, 80 °C) on AA 2024 bare (HNO₃ pickling) with EDX interphase analysis (produced by IFAM)

Due to the inaccuracies associated with the multiplication factor and the short sputter time, these thickness estimations should, as before, be considered only as meaningful indications afflicted with uncertainties. Nevertheless, the SEM image in Fig. 4.2 d) confirms that the true layer thickness is above the one measured with XPS depth profiling. After deposition of 0.5 SLM TEOS the topography of the specimen surface changes distinctly. The fracture image show a homogenous coverage of the surface by thin globular films made of oxide and coating which cannot be distinguished but which is certainly thicker than the initial oxide film. The plasma coatings seem to be merged with the oxide, growing onto the globular oxide structure. The typical “oxide-net” microstructure which appears after deoxidation of AA 2024 bare with Smut-Go NC (see 4.2.1) has disappeared. Sole plasma activation does not cause such an effect as no visible

change in SEM analysis is detected. Still, certain oxide thickening of 1-3 nm by atmospheric plasma activation has been reported [141], [181] and might occur. In any case, all samples are activated before plasma deposition but do not undergo any visible change of the oxide structure.

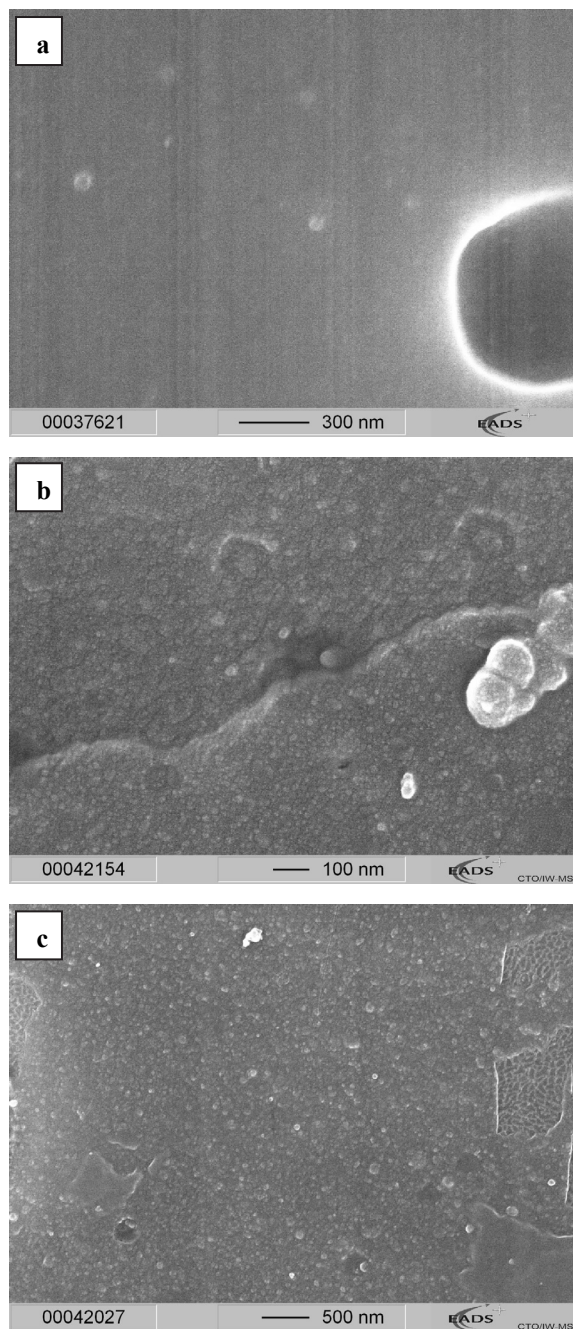


Fig. 4.4: Top-view SEM images of HMDSO (a), OMCTS (b) and TEOS (c) derived plasma films

more, the pronounced aluminium oxide signals support the assumption that the substrate surface is not fully concealed by the plasma polymer.

Altogether, the five different coating parameters lead to two different categories of coupling films: on the one hand, the continuous closed (thick) films of several tens of nanometres thickness obtained with

With layer thickness < 15 nm, it can be assumed that the aluminium oxide is covered but probably not fully concealed by the plasma layer and may still impact the surface properties. Nevertheless, it is likely that the plasma films dominate these properties. Chapter 4.2 discusses that the deoxidation pre-treatment Smut-Go NC employed in this case creates relatively smooth oxides, which allows a thorough study of the plasma films. Other etching processes, like pickling in HNO_3 , form open porous oxides. Even with these oxides the plasma polymer can penetrate the pores and cover the aluminium oxide layer. Fig. 4.3 displays a STEM image with EDX analysis of a microtomed cross cut of a HNO_3 pickled AA 2024 bare adherend coated with a 5 SLM GPS plasma film bonded to an epoxy adhesive. The Si signal in the EDX analysis is specific to the plasma film. In the upper part of the aluminium oxide (area 1) and even in the lower part of the oxide (area 2) a Si signal is observed, proving the presence of the plasma polymer. As distinct C signals are detected in area 1 and 2, it is assumed that the thin plasma film indeed penetrates and covers the oxide, but it does not conceal the porous microstructure that allows a penetration of the polymer. Again, the plasma polymer cannot be distinguished from the oxide, both forming one interspersed layer. Hence, a determination of the thickness of the GPS derived plasma film is not possible.

Besides microscopically rough surfaces, macro-rough surfaces obtained by classical mechanical abrasion techniques are very common pre-treatments for adhesive bonding. The Si/Si-oxide signals detected in ToF-SIMS surface analyses (Fig. 4.6 and Fig. 4.17) of a grit-blasted substrate coated with a 5 SLM GPS plasma film demonstrates that even macroscopically rough adherends are covered by plasma deposition. However, the analyses also show that the coverage is not uniform, but that certain “drops” of plasma polymer are distributed randomly over the evenly coated surface. Further-

0.5 SLM HMDSO, 5 SLM OMCTS and 5 SLM TEOS and, on the other hand, the 0.5 SLM TEOS and 5 SLM GPS derived thin films around or below 15 nm. The latter might be not fully concealing and the Al-oxide still influences the surface interactions; yet, these coatings dominate the surface conditions.

Considering the structure and topography of the thick plasma films, SEM images in Fig. 4.2 and especially the top-view images in Fig. 4.4 reveal distinct differences. HMDSO derived coatings have a very smooth surface where roughness lies below the resolution of the employed SEM devices⁹, which is consistent with published results obtained with a similar APPJ device [39], [175], [176]. Only very few scattered spheroidal areas appear but cannot be properly resolved. Contrarily, TEOS and OMCTS deposition creates a certain micro-roughness due to globular “drop-like” structures on the surface, presumably leading to higher surface area. This structure is assumed to be derived from spheroidal particles that merge into a closed film. Particles are likely to be formed as islands on the substrate surface starting from a nucleus. They may also originate from polymerisation starting in the gas phase. Similar morphology has already been reported for silica films deposited in low pressure [147], [148]. It is likely that the higher monomer concentration in the gas phase achieved with HMDSO leads to a higher number of nuclei on the surface that coalesce at an earlier stage forming a more uniform film. A more pronounced influence of the oxide on film formation of thinner films is also presumed.

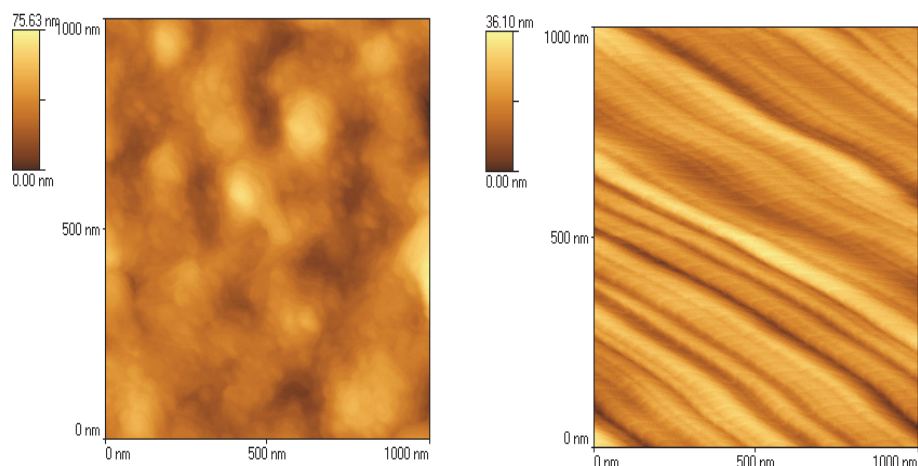


Fig. 4.5: AFM image of a 5 SLM TEOS plasma film surface (left) compared to the polished uncoated substrate (right)

However, as shown by Bhatt and co-workers, who studied HMDSO deposition with a similar device, a further increase of precursor concentration may cause powder formation in the gas phase and lead to a strong increase of micro-roughness [176]. Own experiments with 5 SLM HMDSO confirmed this finding as white powder is formed under this condition, whereas a feed flow of 3 SLM still creates compact films.

Comparing OMCTS and TEOS derived films, the spheres formed with TEOS¹⁰ are by trend larger in diameter (around and above 100 nm), whereas the surface of OMCTS plasma films consists largely of particles in the 10 to 20 nm range. Despite the globular appearance, the fracture images show that all films are continuous and relatively homogenous. They fully mask the original oxide and follow the substrate contour. As seen in the SEM top-view of the OMCTS film, the plasma film follows the larger features of the surface – here the edge of an etching pit – and, thus, does not significantly change the macro-roughness of the substrate. The globular film structure is exemplarily examined by AFM for the 5 SLM TEOS plasma coating on mirror polished aluminium (Fig. 4.5). AFM confirms the spheroidal structure consisting of larger drops of > 100 nm diameter. Moreover, smaller spheres of 10 to 50 nm are detected that cover the larger ones. The vertical variance of the film thickness is of the same order of magnitude as the small drops.

⁹ The large sphere visible in Fig. 4.4 (a) is contamination.

¹⁰ Due to sample preparation the plasma film breaks off and the oxide net is visible in some areas of Fig. 4.4 c).

The polishing grooves of around 20 to 30 nm depth are completely covered by the coating, which is consistent with the previously determined coating thickness of approximately 55 nm.

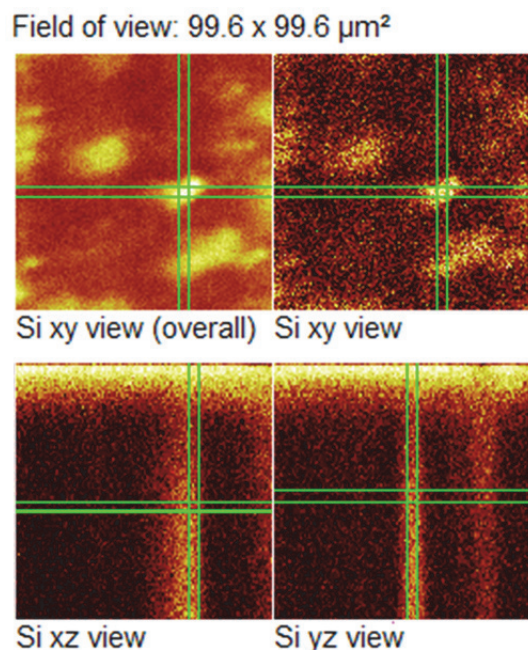


Fig. 4.6: Negative ToF-SIMS Si mapping before (top-left) and after 200 s ion etching (top-right); time resolved view of Si intensity (below); (produced by OFG Analytik GmbH)

The topography of the thin GPS and 0.5 SLM TEOS films cannot be assessed with the given electron microscopic or tactile methods. To at least investigate the evenness of GPS plasma films, time resolved ToF-SIMS mapping (negative mode) of Si concentration before and after ion etching is used. Though ToF-SIMS is not a quantitative technique, the Si intensity in the mapping images can be seen as qualitative indicator with regard to local film thickness. A respective mapping of a plasma GPS film on AA 2024 is shown in Fig. 4.6 (the higher the Si signal, the brighter the colour). The upper two pictures represent the Si signal before ion sputtering (left), where Si is present over the complete analysed area, and after 200 s of ion etching (right), where only Si-containing islands remain at the places where the initial Si concentration was highest. The two images below show a time resolved cross-cut along the xz and yz plains. The height axis z correlates with sputter time, i.e. the upper edge corresponds to $t = 0$ s and the lower edge to $t = 200$ s. Before and after ion etching, some “Si-drops” are visible that indicating the areas of high film thickness. This clearly illustrates that the film thickness is not uniform showing presumably spheroidal particles embedded in the thin

film. Nevertheless, the whole surface is to a certain extend covered with Si, i.e. with plasma polymer. Moreover, the depth profiling reveals a concentration gradient towards the oxide confirming the postulated formation of an interspersed layer with the aluminium oxide. In the first approximately 20 s of ion etching, the plasma polymer concentration appears to be relatively high, followed by roughly another 20 s lasting transition period. After that Si is only locally visible in the high-concentration areas mentioned above. Hence, plasma polymer concentration is high in upper half of this mixed layer and decreases significantly in the lower half. This distribution was already indicated by the EDX analysis of the ultramicrotomed cross-section presented before.

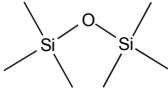
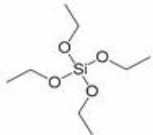
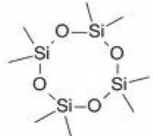
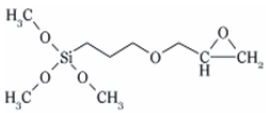
In summary, the smooth, homogenous and compact structure of HMDSO plasma films is likely to be beneficial for the barrier properties but might be detrimental with regard to adhesion to the polymer. Contrarily, the distinct micro-roughness of 5 SLM TEOS and OMCTS film surfaces are assumed to have a positive effect through enlarging the contact area to the adhesive. 0.5 SLM TEOS and 5 SLM GPS films are not uniform but fully cover the surface without completely masking the oxide structure. Thus, the microstructure derived from surface conditioning still has a major impact on the surface area.

Besides film thickness and topography, chemical composition of the plasma films is an important characteristic. Bulk film composition is determined via XPS depth profiling. Atomic concentrations are taken after sputtering until the C concentration remains stable in order to avoid corruption by the hydrocarbon surface contamination. 5 SLM precursor feed specimens are used for chemical composition measurements. To obtain a determinable film composition, the depth profiling of the GPS derived film was conducted after multiple coating cycles (Fig. A.1) as the chemical composition of the film cannot be distinguished from surface contamination after only one deposition cycle (Fig. 4.1).

Contrary to film thickness and topography, the precursor type does not seem to significantly influence the composition of the plasma coating. The bulk of all films consist of almost stoichiometric Si-dioxide with

very low carbon content, i.e. the largely different Si:O:C ratios of the employed precursors are not at all reflected in the resulting films after plasma polymerisation (Table 4.4). Due to the high gas temperature and the presence of oxygen, the precursors are defragmented and completely oxidised in the air plasma forming silica films [176]. High-resolution XPS analysis of the Si 2p signal (Fig. A.2) shows only fully oxidised species which confirms the inorganic character of the plasma polymers. With an O:Si ratio of approximately 2.2 the oxygen concentration in all films is even slightly over-stoichiometrical. Similar oxygen concentrations have been detected for low pressure derived silica-like plasma polymers [148], [151], but with higher carbon concentrations. It has been demonstrated by XPS and RAIRS that an excess in oxygen concentration is associated to non-bridging oxygen, i.e. to silanol groups. Angle dependent XPS analysis revealed that the silanol concentration is highest at the film surface [149], [151]. However, most low pressure plasma derived films, where significant silanol concentrations were detected, obtain a higher excess of oxygen [149], [151], [182]. As silanol concentration decreases with energy, whereas Si-O-Si crosslinking increases [182], it can be assumed that the deposition with the APPJ device employed here leads to relatively limited Si-OH concentrations, but to highly dense films. Even though the analysis of the sputter rate revealed that the deposited plasma films are less dense than thermally grown silica films, they are presumably effective barriers with a strong interface to the aluminium oxide. To the author's knowledge, none of the silica like coatings derived from atmospheric pressure plasma described in literature obtains such a low carbon content. The distinct presence of carbon on the surface as seen in Fig. 4.1 and Table 4.1 may indicate that some less fragmented precursor might be present at the top surface (see chapter 0), but is mostly caused to adventitious carbon contamination.

Table 4.4: Precursor structure, vapour pressure, Si:O:C ratio of precursor [183]-[186] and composition of plasma films (bulk)

name	chem. structure	precursor		atomic concentration plasma film [at.%]		
		vapour pressure at 20 °C	Si:O:C	Si	O	C
HMDSO		2.0 kPa	2:1:6	31	68	1
TEOS		1.1 hPa	1:4:8	31	68	1
OMCTS		1.0 hPa	4:4:8	31	68	1
GPS		1.1 Pa	1:5:9	31	68	1

4.1.2 Chemical functionality of surface layer

When examining low pressure derived plasma silica coupling films, Dillingham concluded in 2008 that “chemical composition of the surface of the plasma polymerized films is critical to adhesive joint durability” [151]. Thus, it is not sufficient to only characterise the bulk film properties, but the state of the topmost surface layer must be analysed, too.

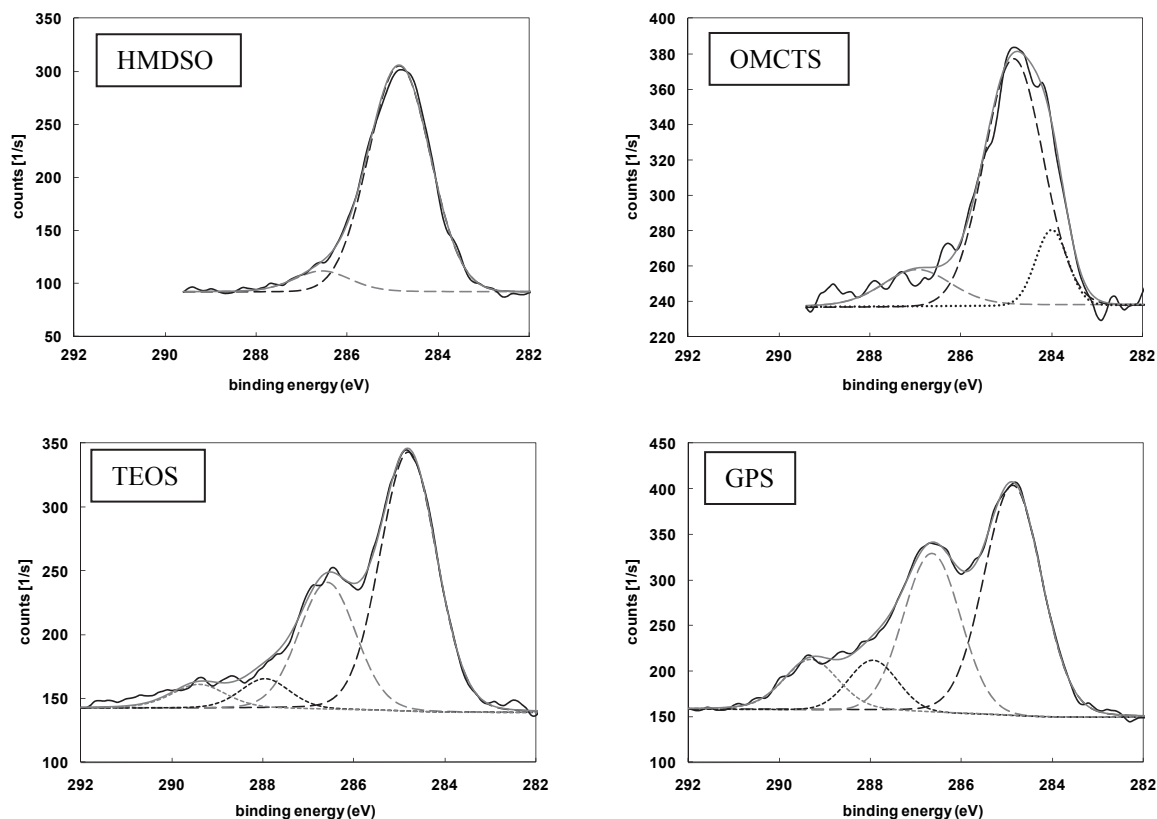


Fig. 4.7: 45° High resolution XPS spectra of the C 1s peak of deposited plasma polymers

XPS surveys and sputter depth profiles of the plasma polymer films displayed in the previous chapter reveal some differences in the carbon concentration at the topmost surface. This is considered as a first indicator that some of this carbon may not be associated to mere contamination but consists of less or even not fragmented precursor. To prove this assumption, high resolution XPS spectra of the C 1s binding energy region are made for the different plasma films. All surfaces exposed to ambient air typically show hydrocarbon contamination with a corresponding peak around 284.5 to 285.0 eV¹¹. The energy shift of this peak corresponding to other bonds is, however, more important than the absolute binding energy itself. Normally, C 1s spectra of mere ambient contamination on aluminium hardly contain signals of oxidised carbon species [113]. The C 1s spectrum of the solely etched reference sample only indicates a minor carbonate appearance with a signal around 289.3 eV (Fig. 4.8). If all plasma polymers are similar independent of the precursor as suggested by the bulk analysis, their C 1s spectra, respectively the one of the associated contamination, ought to be similar.

However, the 45° high resolution C 1s spectra (Fig. 4.7) reveal distinct differences between the carbon functionality of each plasma polymer surface. Indeed, HMDSO derived films show only a slight broadening of the hydrocarbon peak (284.8 eV) towards higher binding energies with a small signal that

¹¹ The C1s peak is traditionally used to calibrate the XPS spectra.

corresponds to C-O single bonds (ca. 286.5 eV). As the HMDSO molecule contains only C-H and C-Si bonds, the C-O bond has to be formed during plasma polymerisation or it originates from contamination. In terms of functional groups, the C-O signal can be originated by either ether-groups (C-O-C), C-O-Si bonds or hydroxyl groups on the surface. Due to the predominant hydrocarbon signal, the presence of unprocessed HMDSO on the surface cannot be fully verified. C 1s analysis of OMCTS based coatings provides an analogue picture with a slightly more pronounced C-O signal but also with higher scattering. Yet, the signal contains an important feature on the side of lower binding energies. A distinct shoulder at 284.0 eV with approximately 0.7 eV shift from the main hydrocarbon signal is observed. This shift corresponds exactly to the mean shift reported for Si-C groups [187]. The presence of Si-C groups at the surface is likely to be an indicator for some not reacted precursor as the consideration of the bulk film composition shows that Si-C bonds are hardly formed during plasma polymerisation. As OMCTS monomers have the highest number of Si-C bonds, it is not surprising that this shoulder is only pronounced with the respective plasma films. Closer inspection of the C 1s signal of the HMDSO film indicates also a little Si-C shoulder, but which is by far not as distinct and does not allow a meaningful fit. The TEOS molecule does not have any C-Si bonds, and GPS has only one. Therefore, no C-Si signal is detected. Generally speaking, the Si-C bonds are only visible in the C 1s signals, but not in the Si 2p ones, where the fully oxidised Si⁴⁺ signal is predominant (Fig. A.2). Compared to the silicon in the bulk, this little amount of C-Si bonds at the surface is insignificant. As carbon concentration is only significant at the topmost surface the analysis of the C 1s is the most meaningful. As for HMDSO, the C-O bonds of the OMCTS derived film are likely to be created during the plasma polymerisation process. The relative intensity increase, which is very small, could be explained by the higher O:C ratio in the precursor molecule.

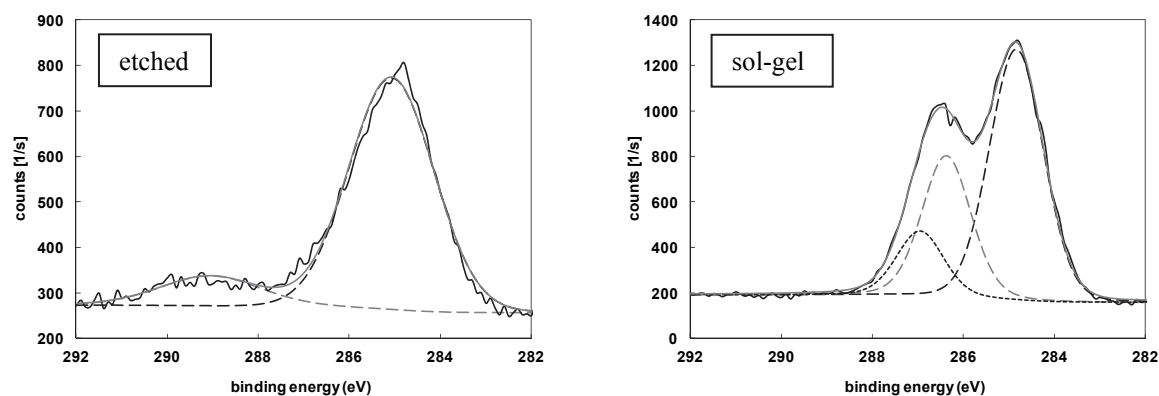


Fig. 4.8: 45° High resolution XPS spectra of the C 1s peak of AA 2024 bare (Smut-Go NC) and a GPS based sol-gel film

Contrary to the methyl-siloxane precursors HMDSO and OMCTS, the use of the silane – or more precisely Si-alkoxide – precursors TEOS and GPS leads to an intensive widening of the C 1s signal with a distinct shift towards C-O bonds. The relative intensity of the C-O peak is higher for GPS than for TEOS which corresponds to the higher number of C-O bonds inside the precursor molecule. The detected shift around 2.0 eV is characteristic for the epoxy ring. This is another indicator for the top surface layer of the plasma polymer consisting of organic parts, which originate from the precursor molecule and which are not completely fragmented inside the plasma torch. Moreover, the surface layer of both plasma films contains even further oxidised species, i.e. other functional groups that cause a larger peak shift, like C=O or O-C-O (≈ 287.9 eV) and O-C=O (≈ 289.2 eV), are created during plasma polymerisation. The signal of the latter – especially in the case of the TEOS film – could be partly derived from carbonates that are present in minor concentration at the substrate surface as seen in the spectrum of the etched reference (Fig. 4.8). Comparing the C 1s signal of the GPS based plasma polymer to the one of a sol-gel coating (Fig. 4.8) consisting mainly of hydrolysed and condensed GPS, both spectra appear to be relatively similar. The relative peak intensities of C-C to C-O bonds match between sol-gel and plasma film, which also supports the assumption of not fragmented organic parts residing on the plasma polymer surface. In C 1s spectra of solution derived GPS films [188] the C-O peak is normally higher than the hydrocarbon peak, which

suggests that, here, the GPS precursor at surface after plasma deposition still contains some hydrolysable methoxy groups. Nevertheless, the higher oxidised species of the plasma film mark a significant difference. The spectrum of sol-gel or GPS coatings do not show any further oxidised states of the carbon. In general, the existence of polar oxygen containing functional groups is beneficial for the adhesion of epoxy polymers as they are potential bonding partners for the adhesive monomer or the hardener component. As pointed out previously, high resolution XPS analyses of the Si 2p signal (Fig. A.2) reveals that the silicon is fully oxidised. Considering the O:Si ratio, it is likely that some silanol groups exist at the surface which may also have a positive effect on adhesion [149], [151]. Some researchers also suggest the peak location of the fully oxidised Si 2p signal provides information concerning the structure of the silica network. In particular, this “structure induced chemical shift” is presumed to relate to the bridging angle of the tetrahedral units like $\text{Si}[\text{O}_x(\text{OH})_y]$ ($x + y = 4$), which SiO_2 contains naturally [189], [190]. The smaller binding energy of GPS films compared to HMDSO, TEOS and OMCTS ones could be associated to a smaller bond angle between the Si-O-Si bridge in-between the tetrahedra. However, as this assumption does not affect the chemical state of the film and as it is unlikely to impact the performance of the plasma film as coupling layer, it is not further considered.

4.1.3 Correlation of thin film properties with joint strength

As a first step, the adhesion performance of bonded joints after deposition of various coupling layers is investigated independently of the surface pre-treatment, i.e. only one reliable and reproducible (but not optimised) surface conditioning technique is employed on the same base material prior to deposition of the coupling layers.

As demonstrated in the previous chapters, the precursor choice has no significant influence on the chemical composition of the bulk film, but it leads to distinct changes in carbon functionality at the top surface. The aim of this chapter is now to correlate these film properties with the results obtained from mechanical testing of bonded joints.

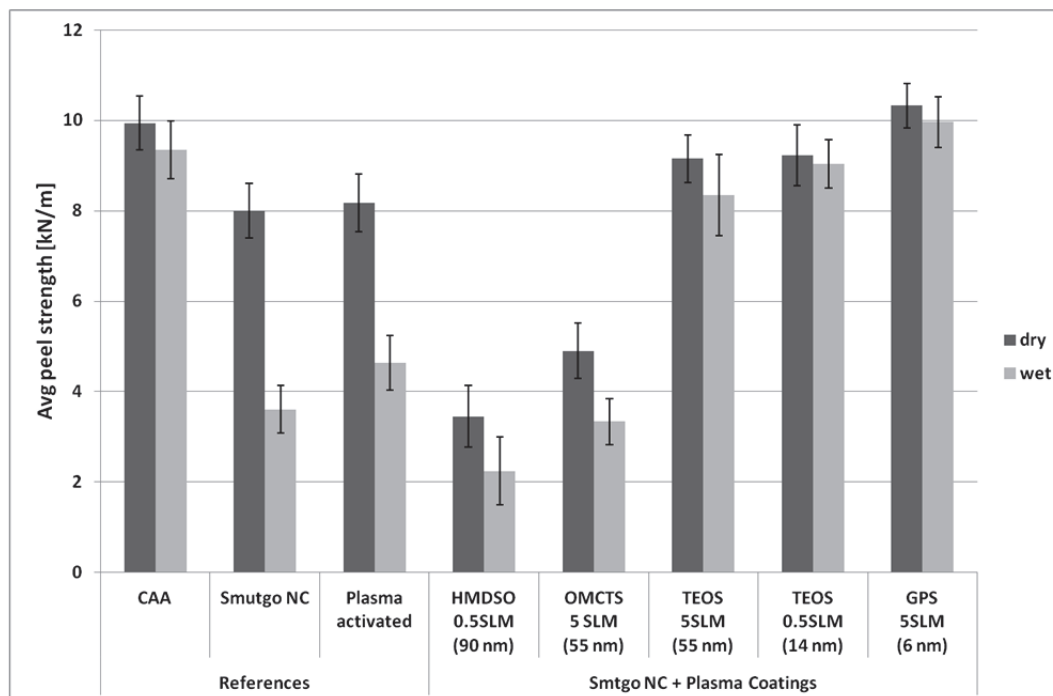


Fig. 4.9: Average peel strength of AA 2024 bare/DP 490 roller peel joints after different surface treatments

Peel testing is a powerful method to distinguish the quality of surface treatments. The peel strength is a combination of resistance to fracture as well as to elastic and plastic deformation. Hence, the obtained

values are not a direct measure of the interfacial adhesion, but are an indicator for the integrity of the bonded joint under deformation and external load. Therefore, the obtained peel strengths may only be compared if test set-up and materials are the same. If these parameters are fixed, the test allows good comparison between surface preparations, but only as long as cohesion failure is not reached. Cohesion failure should be achieved with every good surface treatment, but this requires optimisation of surface conditioning. Fig. 4.9 shows the average peel strengths of AA 2024 bare joints bonded with the two-component, paste-like DP 490 epoxy adhesive. The corresponding values table are shown in Table A.1. The adherends are coated with the different plasma films described above after alkaline etching and acidic desmutting with Smut-Go NC. As references CAA, sole Smut-Go-NC etching and Smut-Go NC etching in combination with plasma activation (without film deposition) are used. Plasma activation is carried out before each film deposition in order to remove adsorbed organic contamination and to create functional oxide groups that allow a better linkage to the plasma polymer film.

Sole activation is not sufficient to significantly increase the adhesion of the polymer to the aluminium surface as the peel strength is similar to one obtained after etching. In particular the drastic deterioration of the peel strength after injection of water into the bondline cannot be averted. This reduction can directly be seen in a change of locus of failure: whereas the failure is partly cohesive in the polymer under dry conditions, the failure mode changes to pure adhesion failure in the presence of water. Fracture images of the transition area between dry and wet peel testing can be found in the appendix Fig. A.3.

Unlike sole activation, plasma deposition distinctly influences the joint stability. Depending on the precursor selection, peel strength is either significantly decreased (HMDSO, OMCTS) or increased (TEOS, GPS). HMDSO and OMCTS act as release films, where – even during dry testing – fracture mode becomes solely interfacial. SEM analysis of the peel sheet after testing (Fig. 4.10) reveals the weak interface being between plasma polymer and adhesive. Contrarily, TEOS and GPS improve fracture behaviour leading to mostly or even full cohesion failure under dry and wet conditions, achieving peel strengths comparable to state-of-the-art treatments. Especially after GPS deposition, specimens show even superior joint integrity compared to CAA and silane/sol-gel treated ones, both in terms of peel strengths and fracture behaviour.¹² It appears as if peel strength results of TEOS treatment improve slightly with reduced precursor feed flow rate, i.e. with decreased film thickness, but this difference in peel strength is marginal considering the measurement deviation. However, the fracture behaviour after 0.5 SLM TEOS deposition is significantly superior being almost completely cohesive.

SEM imaging helps to analyse this thickness dependency. The SEM image of a peel sheet coated with 5 SLM TEOS after testing shows certain areas where the plasma film is detached from the Al-oxide surface (Fig. A.4). The brittle silica like film breaks and partly delaminates from the ductile Al-substrate. Hence, the failure can be described as mixed mode consisting of mostly cohesion failure with areas of adhesive failure, which are then divided into interfacial failure between adhesive and plasma polymer and interfacial failure between plasma polymer and Al-oxide. It is assumed that the reduced film thickness decreases residual stress in the plasma film and interfacial stress between film and substrate. As it is assumed that coatings derived from 0.5 SLM TEOS and 5 SLM GPS do not form completely closed films, these plasma films are able to follow the deformation of the ductile base material. Thus, film delamination from Al-oxide is reduced and overall peel strength is increased. Moreover, it is likely that the distinct oxide microstructure, which is not fully masked by the thinner TEOS plasma film, is advantageous for the stability of the interface due to the larger surface area. Apparently, the low film thickness of the thinner films is enough to dominate the surface properties and higher deposition is not necessary. Lommatzsch and Ihde, who investigated plasma deposition of coupling films with a similar APPJ device, achieved best adhesion results with a film thickness of 7 nm [39].

Comparing the peel results with the film characterisation of the previous chapter, it becomes clear that bulk film properties are not decisive with regard to joint performance – at least for silica like films. While

¹² A table of measured peel strengths of all different treatments including wet-chemical GPS and AC-130 deposition is shown in Table A.1.

chemical composition of the bulk of all films is similar, i.e. independent of the employed precursor, adhesion varies strongly. Unsurprisingly, the inorganic films all adhere well to the aluminium oxide layer, which is in-line with published results obtained with low and atmospheric pressure plasma derived coupling films [39], [44], [147], [151]. Peel test results of TEOS coatings indeed indicate a slight deterioration in peel strength with increasing film thickness due to rigid and brittle character of the plasma films. Nevertheless, only small areas of delamination appear; this detachment occurs solely if a strong bonding between plasma polymer and epoxy adhesive is achieved. As even the thicker films remain on the oxide surface, conclusions should certainly not be drawn from considering film thickness alone; in particular as film thickness is similar for OMCTS and TEOS derived coatings.

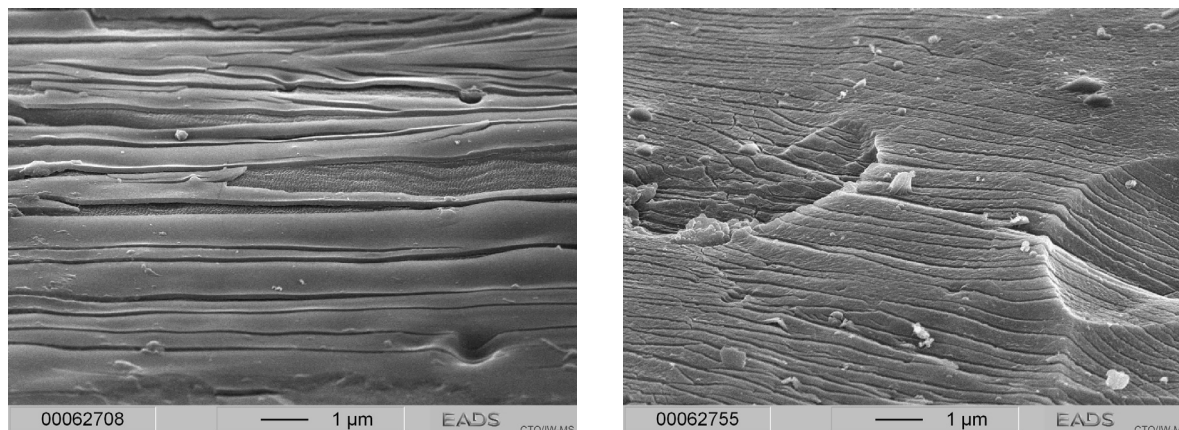


Fig. 4.10: SEM images of AA 2024 bare (Smut-Go NC) peel sheets with 0.5 SLM HMDSO (left) 5 SLM OMCTS (right) plasma polymer films after testing; cracks are derived from sample preparation (cryofacture)

On the contrary, surface chemistry of the plasma films is found to be of key importance for adhesion of an epoxy polymer to the APPJ-CVD films. This interface is significantly more affected by the precursor type. Peel tests clearly reveal opposing properties after deposition of silanes and deposition of siloxanes. Whereas GPS and TEOS increase the peel strength, HMDSO and OMCTS decrease it drastically. A correlation to the high resolution XPS analysis (chapter 0) reveals a direct dependency of the peel strength on the carbon functionality. The existence of polar C-O bonds, or even more polar carbonyl and carboxyl groups, allows a stronger linkage of the adhesive via Lewis acid-base, or potentially even covalent bonding. The superior results achieved with GPS compared to TEOS also follow the peak intensity of oxidised carbon species. It is assumed that not fully fragmented monomers are present at the film surface and, hence, the epoxy ring of the GPS is likely to react with the hardener of the polymer. As GPS is a well-known coupling agent for oxide-epoxy interfaces, the positive effect is apparent. Generally, the presence of residues of the hydrolysable silanes seems to be beneficial for adhesion. The ethoxy and methoxy groups of the precursor are replaced by hydroxyls after reaction with the surface water, which then can react further with the silica film below. In case of HMDSO and OMCTS, unreacted, non-polar methylsiloxane precursors form a release film that reduces the adhesion to the polar epoxy adhesive.

Altogether, floating roller peel test results reveal a strong dependency on precursor type correlating to the bonding state of the carbon atoms at the film surface. The interface between plasma polymer and polymer appears to be critical, whereas all films adhere well on the Al-oxide due to their similar chemical nature. Existence of polar groups enhances the bonding to the polar epoxy adhesive. The topography of the deposited films has a certain influence on the resulting peel strength of the joint, with even films being inferior, but it is unlikely that the observed differences can solely be associated to this characteristic. As performance of the silanes is significantly superior to the performance of methylsiloxanes, the results support the assumption that unreacted precursor monomers are present at the film surface. The peel strengths obtained with TEOS and GPS plasma treated adherends confirm the high potential of the plasma polymers as coupling films for adhesive bonding of aluminium alloys. In particular with films below 20 nm thickness, anodising level is achieved or even exceeded. Compared to wet-chemical silane treatments, these

plasma films even outperform GPS and especially AC-130 in wet peel strength (Table A.1) and in fracture behaviour. However, it will be shown in Chapter 0 that joint performance is strongly dependent on the applied surface pre-treatment and the employed adhesive. Despite a similar coupling behaviour of DP 490 and FM 73 known from practical experience, the GPS solution treatment leads to higher peel strengths than plasma deposition if the more rigid FM 73 film adhesive is used. Furthermore, peel resistance of not aged specimens represents only one part of joint performance. Chapter 4.3 will focus on durability of bonded joints.

As a consequence of the results of this chapter, only TEOS and GPS plasma deposition is considered for further adhesion and durability investigations. First precursor evaluation has been conducted with DP 490 due to easier processing. With the focus on most suitable precursors GPS and TEOS, the certified film adhesive FM 73, which is a standard adhesive in aeronautics to assess the quality of a surface treatment, will be used in all further testing.

4.2 Aluminium surface characterisation and influence on adhesion

Various work has been performed on silane based adhesion promoters and coupling agents to improve bonding of epoxide adhesives to high strength aluminium.¹³ Most of it detected a strong dependency of the overall joint performance on the surface pre-treatment prior to application of the coupling agent [30], [34], [100], [126], [133], [188], [191]-[193]. A similar effect was also shown for low pressure plasma derived silica coupling films [107]. Thus, in order to understand the capabilities of a surface preparation process involving APPJ deposition, as well as to further optimise it, the state of the aluminium surface after preceding surface pre-treatment has to be characterised and its influence on the interface and the resulting joint strength must to be understood. Therefore, the following section seeks to explore geometrical aspects, like topography and roughness, thickness and chemical composition of the oxide surface, as well as interfacial bonding.

4.2.1 Surface roughness and topography

Even though the structure of any surface, rough or smooth, is a rather obvious characteristic, its characterisation is by far not trivial. Especially if surfaces of a different nature are compared, the evaluation and quantification of physical characteristics is difficult. Apparent rough surfaces can be smooth on a smaller scale and smooth surfaces turn out to have a distinct structure on a nanometre scale. Moreover, surface roughness is known to have a significant impact on the strength of bonded joints with interlocking, causing deflection of stress from the interface and initiating plastic dissipation within a larger volume of material [80].

The determination of average roughness (R_a) and maximum height of profile (R_t) is a common way to easily quantify the structure of surfaces. However, both values do not provide any information on the shape of the structure, i.e. two surfaces with similar roughness may look completely different. Nevertheless, these standardized measurands are useful to classify surfaces and allow – to certain extent – a comparison of results with the work of others, at least in the case of similar surface pre-treatments. For example, Liu et al. even found a direct correlation between R_a of an aluminium surface and the critical fracture energy of a sol-gel coupling layer for adhesive bonding [133]. Besides R_a and R_t , the topography of the aluminium surfaces after different surface pre-treatments is characterised using laser scanning microscopy (LSM). With a lateral resolution of 120 nm and a vertical resolution of 10 nm, LSM can be used to determine the topography and the roughness of the employed surfaces in a meaningful way. Though it does not provide information on the nanostructure like AFM, it can measure surfaces with vertical differences of several

¹³ The author refrains from naming specific references, as the number is too high to accommodate within this thesis. Publications most relevant to this work are referred to at other points of this thesis.

micrometres on lateral areas that are large enough to be representative. The roughness and structure characterised by LSM is here also referred to macro(scopic) roughness or structure to distinguish from finer structures that are visible with electron microscopy. SEM is employed to further characterise the pre-treated substrates. In order to classify the surface pre-treatments used, two additional categories are introduced: micro-roughness (or microstructure) and nanostructure (also referred to as oxide texture). Typical microstructures are for example the some tens of nanometre wide pores in anodising films – SEM images of oxides formed with the reference treatment PSA are displayed in Fig. A.5. Typical nanostructures are pickling oxides with pores or fibrils of approximately 10 nm. Obviously, boundaries of these categories are blurred and SEM can anyhow not be used to quantify structure or surface area. However, all three categories help to visualise the differences of the investigated surfaces and to explain qualitatively the different obtained peel strengths (chapter 0).

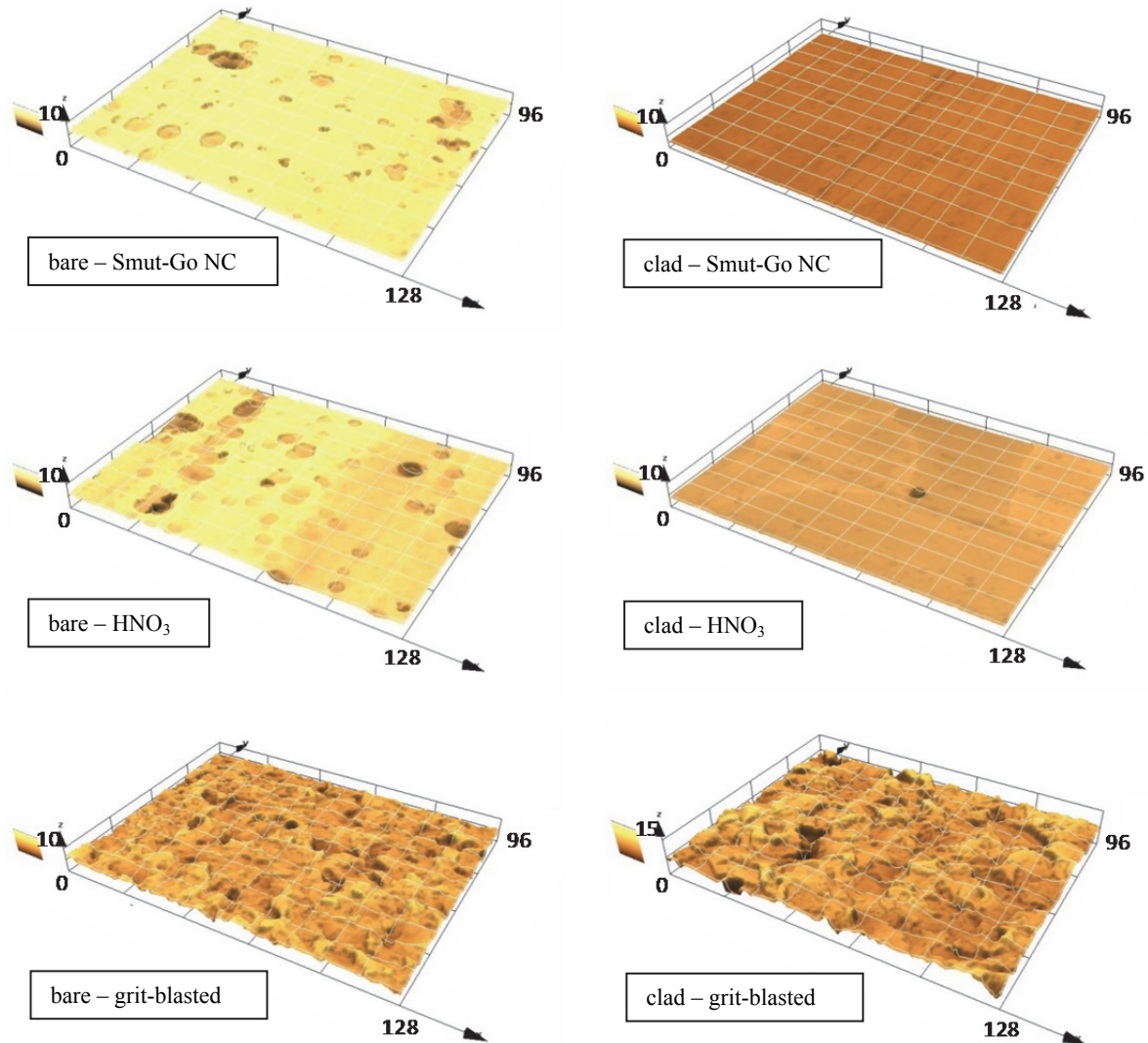


Fig. 4.11: LSM 3D profiles of AA 2024 bare and clad surfaces after different surface pre-treatments [μm]

Table 4.5 displays the measured roughness values for the used AA 2024 bare and clad substrates derived from the LSM profiles shown in Fig. 4.11. Both etching procedures, finishing with Smut-Go NC or HNO_3 , lead to similar macro-roughness. Due to the absence of intermetallics in the pure aluminium clad layer, the chemical etching processes lead to different roughness depending if bare or clad material is used. With clad substrates uniform smooth surfaces with average roughness, values of $R_a < 0.1 \mu\text{m}$ are obtained. With bare AA 2024 the roughness increases significantly because of pits formed during removal of the intermetallic

phases in the etching process. Contrary to the chemical treatments, blasting with fine 50 μm alumina grit forms rough surfaces. The topography of the corundum-blasted surfaces is consistent with images found in literature [49], [194], showing a ragged surface covered with sharp edges and undercuts. The distinct peaks and valleys originate from the sharp edges of the alumina grains. Average and maximum roughness are depending on the blasting parameters, like particle size, pressure and distance, as well as material properties. Roughness increases when using clad materials due to the deeper impact of the grains in the softer pure aluminium. With an average grain size of 50 μm , the employed blasting process can be considered as relatively soft abrasion. Obtained roughness values are in-line with published results derived under quite similar conditions [133].

Table 4.5: Surface characteristics of AA 2024 bare and clad after different surface pre-treatments

AA 2024 bare	R_a	R_t	surface factor
Smut-Go NC	$0.23 \mu\text{m} \pm 0.06 \mu\text{m}$	$5.15 \mu\text{m} \pm 0.23 \mu\text{m}$	$105.4 \% \pm 1.4 \%$
HNO_3	$0.25 \mu\text{m} \pm 0.05 \mu\text{m}$	$5.32 \mu\text{m} \pm 0.15 \mu\text{m}$	$106.4 \% \pm 0.2 \%$
grit-blasted (50 μm)	$1.56 \mu\text{m} \pm 0.28 \mu\text{m}$	$23.7 \mu\text{m} \pm 1.8 \mu\text{m}$	$128.1 \% \pm 1.1 \%$
AA 2024 clad	R_a	R_t	surface factor
Smut-Go NC	$0.077 \mu\text{m} \pm 0.005 \mu\text{m}$	$1.41 \mu\text{m} \pm 0.24 \mu\text{m}$	$101.5 \% \pm 0.4 \%$
HNO_3	$0.073 \mu\text{m} \pm 0.003 \mu\text{m}$	$1.23 \mu\text{m} \pm 0.14 \mu\text{m}$	$101.0 \% \pm 0.2 \%$
grit-blasted (50 μm)	$1.82 \mu\text{m} \pm 0.14 \mu\text{m}$	$31.2 \mu\text{m} \pm 9.8 \mu\text{m}$	$134.7 \% \pm 1.0 \%$

Besides differences in surface roughness, the LSM profiles reveal discrepancies in the homogeneity of the surfaces. While grit-blasting leads to a relatively homogenous distribution of peaks or valleys on bare and clad, etching forms only smooth uniform surfaces on clad specimens; on bare, pits are randomly distributed over the surface. These pits can reach depths of several microns, but the remaining surface is approximately as even as the etched clad surfaces. To further compare the performance of joints with etched and blasted surfaces, a so-called surface factor is introduced (Table 4.5). This factor gives an idea of the actual surface area that is wetted by the adhesive, i.e. the surface factor is the ratio of the overall surface area of the measured field divided by the area of the measurement field (ideal area of zero roughness). As especially the surface of the bare etched samples is not uniform, the measurements of the surface factor is carried out on 5 different areas (128 x 96 μm) on two different samples to level out inhomogeneities. The surface factor is dependent on the resolution and, therefore, not a fixed constant and can only be used to compare substrates under identical measuring conditions – a direct correlation to analogical characterisation of similar materials (e.g. found in [193], [194]) is therefore not possible. The values given here are measured at a 100x magnification with the above mentioned resolution. The measured surface area is about 20-30 % higher for the mechanical treatment compared to etching. Moreover, the undercuts of the grit-blasted are known to be beneficial to joint strength, allowing mechanical interlocking [194].

Even though the LSM measurements can distinguish roughness up to several nanometres, the informative value on the true surface structure in the sub micrometre range is limited. Therefore, the micro- and nanostructure of the surfaces are further (qualitatively) analysed with high-resolution SEM. Despite their distinct macro-roughness, the blasted surfaces can be considered as smooth on this scale (Fig. A.6), i.e. the air-formed oxide is uniform without a distinct texture, which is consistent with images found in literature [49]. In contrast, etching processes are known to impact oxide formation. Alkaline etching causes relatively uniform planar material removal, whereas acidic pickling can create specific oxide structures. Comparing the two employed acids, the formed oxides display significant differences (Fig. 4.12): Smut-Go NC creates a pronounced net-like microstructure on bare AA 2024 with a mesh width of several tens of nanometres (a) and a very smooth uniform oxide on clad surfaces without any microstructure or open pores (b). Contrarily, HNO_3 does not create such a microstructure on bare material, but leads to pore-formation within the oxide layer. The porous oxide texture is even more open and distinct on clad substrates (d, f) than on bare ones

(c, e). The absence of a distinct oxide structure of the samples desmuted in Smut-Go NC, which largely consists of HNO_3 , is caused by the strong etching effect of the fluorides in the etchant [77], [101].

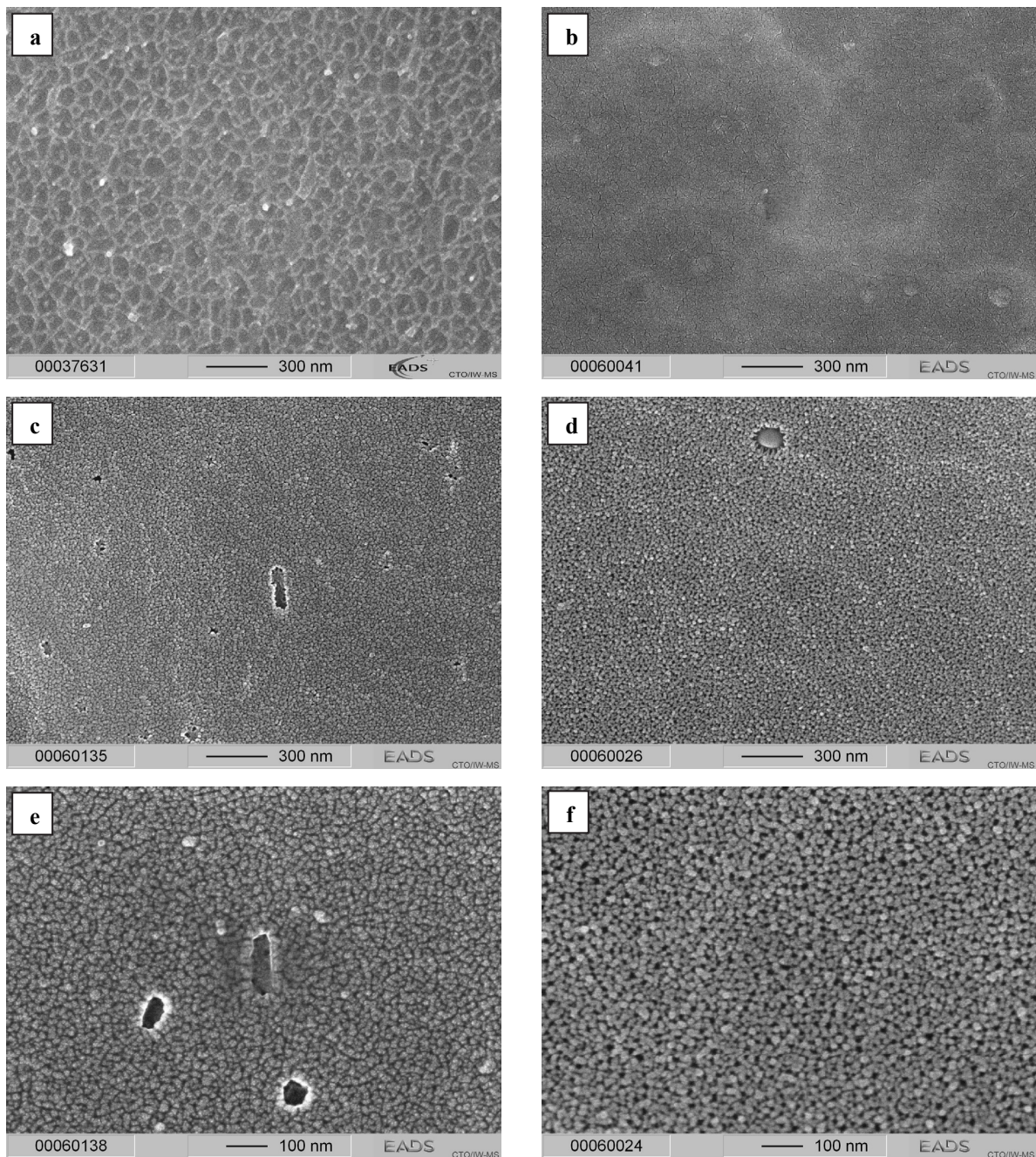


Fig. 4.12: Top-view SEM images of oxides formed on AA 2024 bare (left) and clad (right) after etching with Smut-Go NC (a, b) and HNO_3 (c-f)

Before deposition of a plasma film, each sample surface is activated by the plasma torch. This air plasma treatment can be considered as precision cleaning and activation of the surface, both removing hydrocarbons and creating functional groups by breaking oxide bonds. A change in topography after plasma activation is not detected. A certain oxide growth up to 3 nm is reported for a similar plasma device [141], but which cannot be detected using SEM and is unlikely to have a significant influence on the adhesion. However, if the distance between specimen and nozzle is too small, sparkovers between nozzle and substrate can occur creating crater-like impacts of melted aluminium (Fig. A.7). The deposition parameters employed here avoid such breakdown.

4.2.2 Aluminium oxide characterisation

Besides structure and surface area, the chemical state of the aluminium oxide is also relevant for the adhesion of a coupling layer to the substrate. Surface chemistry, i.e. the functionality of the oxide, may affect the interactions with the deposited film; it is known that hydroxyl groups are present on aluminium oxide surface influencing the formation of chemical bonds [195]-[197]. Hydroxyl groups are more likely to form covalent Al-O-Si bonds with the silane precursors via hydrolysis than Al_2O_3 . Moreover, the nature of the oxide may as well impact its long-term stability in humid or corrosive environments and, thus, affect the durability of the bonded joint. Especially the thickness of the oxide is known to influence corrosion resistance in general and the resistance to bondline corrosion in particular. Investigations by Brockmann and co-workers [2] showed that higher oxide thickness of anodising films is highly advantageous compared to thinner pickling oxides if this type of interface corrosion occurs.

In the aircraft industry, anodising is mostly used to create thick oxides of more than $1\ \mu\text{m}$ for applications in harsh environments. The surface pre-treatments employed here, chemical etching and grit-blasting, do not create such oxides, because the oxide is formed “naturally” either in the etching/rinsing solution or in ambient air. This formation under “wet” (in water) or “dry” (in ambient air) conditions may lead to a different nature of the oxide. Both etching and grit-blasting first remove the initial oxide layer. In case of grit-blasting a new “dry” oxide layer is then formed instantly under ambient conditions after removal. During the impact of the corundum grains, energy in form of heat is released, which might affect the nature and thickness of the oxide. Nevertheless, water molecules are always present at the surface of Al-oxide exposed to ambient atmosphere (adsorbed surface water) which causes hydration [47], [52], [55]. Contrary to the air-formed oxides, both oxide formation and removal during etching in an aqueous solution happens in parallel; hydroxide formation is more likely in this environment. Furthermore, hydration continues during the final rinsing phase in deionised water at RT [51].

To understand adhesion of coupling films and durability of bonded joints, it is therefore mandatory to investigate and compare the chemistry and thickness of the oxides formed after the different surface pre-treatment methods employed.

4.2.2.1 Oxide thickness

Depending on thickness, several analysis techniques are used to determine oxide thickness on bare and clad AA 2024 alloys formed after the different employed surface pre-treatments.

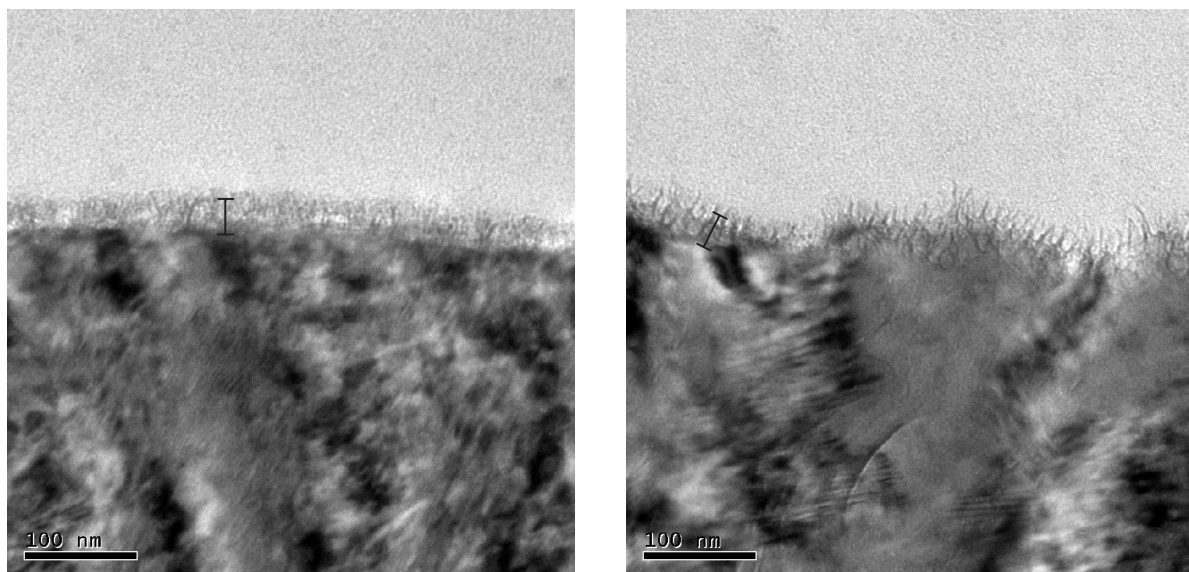


Fig. 4.13: TEM images of HNO_3 derived oxide layers on AA 2024 bare (left) and clad (right); bars = 30 nm

As HNO_3 pickling creates the thickest oxide films of the used methods, oxide thickness can be measured directly in TEM images of an ultramicrotomed section (Fig. 4.13) or in SEM fracture images (Fig. A.8). Both optical methods reveal a relatively similar thickness of 30-40 nm on both bare and clad substrates; 30 nm bars are shown in Fig. 4.13. The images also confirm that the oxide formed on pure aluminium is more open/porous. TEM analysis also indicates that oxide thickness varies more across the examined section on clad than on bare material. XPS depth profiling confirms the optical thickness estimation. Fig. 4.14 exemplarily displays a sputter profile through a HNO_3 derived oxide on AA 2024 bare. Using the half-maximum method, the end of the oxide layer is reached around 3.9 to 4.1 min which corresponds to an approximated film thickness of 32 nm.¹⁴

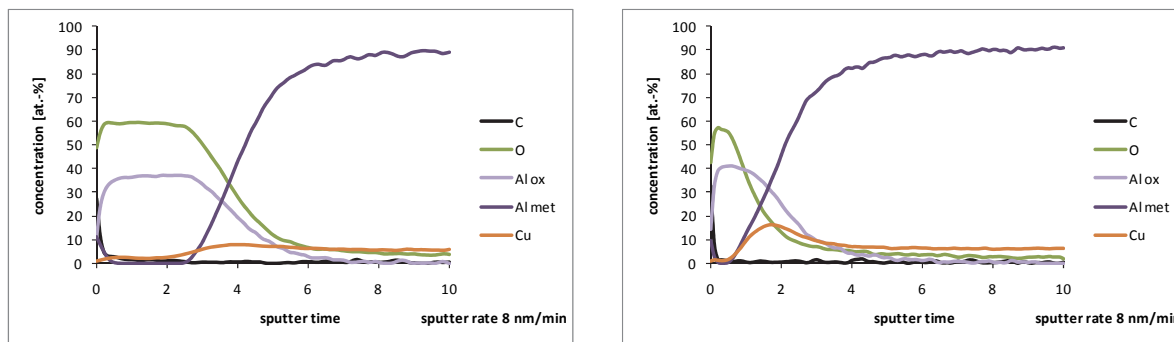


Fig. 4.14: XPS sputter depth profiles through oxide layers on AA 2024 bare formed after HNO_3 (left) and Smut-Go NC (right) pickling

Contrary to HNO_3 derived oxides, oxide thickness of Smut-Go NC pickled and grit-blasted surfaces cannot be determined with the employed TEM and SEM instruments. TEM images of the corresponding ultramicrotomed sections (Fig. A.9) reveal that the resolution is not high enough to distinguish precisely between bulk and oxide, because this transition is not as distinct as for HNO_3 and because the overall thickness appears to be below 10 nm. As previously mentioned, the fluorides (sodium hydrogen difluoride) in the HNO_3 based etchant prevent oxide built-up [77], [101]. Air-formed oxides are known to be only a few nanometres thick [52], [53]. In these cases, the use of depth profiling is also limited. Considering the sputter profile of a Smut-Go NC conditioned AA 2024 bare surface shown in Fig. 4.14, the estimated oxide thickness would be approximately 15 to 20 nm. However, depth profiling becomes more imprecise with thinner films. In particular, rough surfaces lead to high deviation from the real thickness. Thus, depth profiling through grit-blasted surfaces does not even create exploitable results due to the low oxide thickness < 10 nm compared to the high roughness of the surface with more than 20 μm maximum peak to valley distance. The corresponding sputter profiles show that oxygen is still present after several minutes of ion etching (not shown) leading to severe overestimation of the oxide thickness. Hence, it can be safely assumed that in the case of the Smut-Go NC pickled specimen the depth profile also overestimates the oxide thickness significantly, i.e. that the measure is not accurate enough. Nevertheless, the depth profile reveals a certain Cu enrichment close to the surface of Smut-Go NC treated substrates, more precisely, at the metal-oxide interface. Similar copper concentration increase is reported with FPL¹⁵ etched AA 2024 and is believed to be detrimental for durability of bonded joints [76].

This assumption is confirmed by high resolution XPS, where a metallic Al 2p peak is visible (Fig. A.10). Due to the limited penetration depth of the X-rays, this indicates that oxide thickness is below 10 nm. Nevertheless, all results show that Smut-Go NC, contrary to HNO_3 , has a pronounced etching effect, which reduces the overall oxide thickness.

In order to reasonably estimate oxide thickness of the Smut-Go NC pickled and grit-blasted samples, the Al 2p core level in high-resolution XPS measurements is considered. The Lambert-Beer law is employed to

¹⁴ The sputter rate calibrated on SiO_2 (Si wafer) may deviate from true sputter rate on hydrated Al-oxide.

¹⁵ Forest Products Laboratories process: etching in an aqueous sodium dichromate-sulphuric acid solution.

calculate the oxide thickness from the ratio of the Al 2p oxide to metal peak intensities. As 95 % of the detected electrons are within a depth of three times the inelastic mean free path (IMFP) of the analysed material [198], this method can only be used for thin oxide films where a metal peak is still visible, i.e. oxide thickness is not higher than three times the IMFP of aluminium oxide; with an IMFP of approximately 3 nm¹⁶ [199] under the employed XPS conditions, the analysing depth is around 10 nm. The following equation, firstly proposed by Strohmeier [55], calculates film thickness from Al 2p oxide to metal peak ratio (I_o/I_m):

$$d_{xps}(nm) = \lambda_o \sin\theta \ln\left(\frac{N_m \lambda_m I_o}{N_o \lambda_o I_m} + 1\right)$$

where θ is the take-off angle of the emitted photoelectrons ($\theta = 90^\circ$) and N_m/N_o is the volume density ratio of aluminium to aluminium oxide. Literature values used in this calculation vary from 1.28 to 1.6 [52], [55], [128], [200] for γ -Al₂O₃. In this study a ratio of $N_m/N_o = 1.5$ is used. Even though the pickling and air-formed oxides do not fully consist of this oxide type, this ratio is commonly employed and should not differ as much from reality as to deviate the calculated thickness significantly [52], [55]. λ_o and λ_m are the IMFPs of the oxide and the metallic aluminium. Tanuma et al. first published IMFP values over a broad energy range [199] – the Al 2p photoelectron energy associated to Al K α radiation corresponds to $\lambda_o = 2.8$ nm and $\lambda_m = 2.6$ nm – and then refined them three years later to $\lambda_o = 2.81$ nm and $\lambda_m = 2.57$ nm for the employed radiation [201], [202]. This method was critically questioned, because plasmon losses, i.e. energy losses of the electrons going through the metal and the oxide, from the primary core-level peaks are not considered. However, Alexander et al. confirmed this approach, verifying obtained results by TEM measurements, which do not rely on assumptions on film composition [200].¹⁷ In this work, Strohmeier's density ratio and the revised IMFP values by Tanuma and co-workers are used. It needs to be stated that other researchers have used other density ratios and IMFPs or effective attenuation lengths (EALs) that lead to slightly different results [128]. Nevertheless, published results are comparable with the obtained oxide film thicknesses d_{xps} presented in Table 4.6 – the corresponding Al 2p signals including fit of the metallic and oxide peak can be found in Fig. A.10. In any case, it goes beyond the scope of this dissertation to precisely define the film thickness up to 0.1 nm; the aim is to estimate the order of magnitude of oxide thickness and to compare the formed oxides after the different pre-treatments.

Table 4.6: Calculated oxide thickness d_{xps} of AA 2024 bare/clad after Smut-Go NC pickling and grit-blasting

		[Al _{met}]	[Al _{ox}]	θ	d_{xps} [nm]
Smut-Go NC	bare	0.090	0.910	90°	7.6 ± 0.8
	clad	0.129	0.871	90°	6.5 ± 0.7
grit-blasted	bare	0.049	0.951	90°	9.3 ± 1.0
	clad	0.061	0.939	90°	8.7 ± 0.9

Oxide film thickness estimation for both grit-blasting and Smut-Go NC pickling are below 10 nm. Surprisingly, the oxide formation in ambient air after grit-blasting appears to create slightly thicker oxides than Smut-Go NC pickling. As mentioned previously, the fluorides in the etchant have a distinct etching effect preventing oxide growth. Still, hydration can occur during rinsing and storage in ambient conditions. The results of the grit-blasted samples are higher than the values expected for air-formed films (2-5 nm) [47], [52], [128] and indicate that significant hydration already occurred under the prevailing conditions. Under truly dry conditions, oxide thickness should not exceed 2 nm [48]. The pronounced roughness of the grit-blasted surfaces might also lead to a certain overestimation of oxide thickness as the true take-off angle is not always 90°. Nevertheless, both oxide thicknesses are in the same range and should not lead to distinct

¹⁶ For Al K α radiation (1486.6 eV), the kinetic energy of Al 2p photoelectrons is approximately 1413 eV [55].

¹⁷ Alexander et al. used effective attenuation lengths (EALs) instead of IMFPs. EALs are specific to the employed XPS instrument. In general, using the different IMFP values above or the EAL values determined by Alexander will only lead to a deviation of several Angstrom. This level of preciseness certainly cannot be reached with the technical surfaces in this work.

differences in stability of the bonded joint. HNO_3 derived oxides, however, might lead to an increased durability due to their higher thickness. While bare and clad substrates have a certain influence on the structure of the oxides formed during the chemical etching processes, oxide thickness does not differ significantly. Altogether, all surface pre-treatment methods employed create oxides that are at least two orders of magnitude thinner than the ones formed by the standard anodising procedures.

4.2.2.2 Chemical state of surface oxides

Previous investigations revealed a significant influence of the different surface pre-treatments methods on oxide thickness and texture. Hence, a potential similar impact on the chemical state of the oxides needs to be analysed. Chemical composition and functionality, as well as contamination of the surface layer, are considered especially as different and even contradictory results can be found in literature. Bockenheimer's analysis of corundum blasted Al surfaces suggests a formation of an oxide with under-stoichiometric oxygen concentration in ambient air. This is surprising, since it has been shown that the adsorbed water present on surfaces in ambient atmosphere breaks oxide bonds, and a hydrated top layer is formed [47], [52], [196]. Hydroxide formation is even detected during desiccator storage of magnetron-sputtered aluminium [52]. Anyhow, such an aluminium-rich oxide would differ significantly from the hydroxide-rich oxides expected after immersion in aqueous solutions, where formation of a pseudoboehmite layer covered with bayerite crystals has been reported [51]. Chemical nature of the oxide, respective hydroxide is recognized to be of significant importance for the surface properties [195], [196], i.e. for interface and long-term stability of bonded joints. Jussila et al. detected a direct correlation between the degree of bonding of an amino silane and the concentration of hydroxyl groups present at steel surfaces [203]. Hence, potential differences of the oxide films derived from the employed surface pre-treatments need to be identified. Furthermore, contamination or residues of the etching or grit-blasting processes might deteriorate the stability of the interface.

Table 4.7: Elemental composition of oxide surfaces calculated from XPS survey spectra [at.%]

		C 1s	O 1s	Al 2p	Cu 2p3		
grit-blasted	bare	12.7	54.3	25.8	0.5		
	clad	12.3	54.7	26	---		
Smut-Go NC	bare	18.5	50.5	27.2	1.0		
	clad	18.0	52.5	25.8	---		
HNO_3	bare	18.3	53.6	25.2	1.2		
	clad	16.9	55.9	25.9	---		

		F 1s	S 2p	Mg 1s	N 1s	Si 2p	Na 1s
grit-blasted	bare	0.4	---	1.3	0.1	---	5.0
	clad	0.3	0.1	0.2	0.2	---	4.3
Smut-Go NC	bare	2.2	0.7	---	---	---	---
	clad	2.6	1.1	---	---	---	---
HNO_3	bare	0.4	---	---	0.5	0.6	0.1
	clad	0.5	---	---	0.4	0.5	---

Before focussing on the functionality of the topmost surface layer, the chemical composition of the different oxide surfaces is determined via XPS analysis. The average of two survey measurements is presented in Table 4.7. Corresponding survey spectra are displayed in Fig. A.11. In summary, the elemental analyses reveal quite similar concentrations of the prevailing elements (aluminium and oxygen) but also display significant differences in the concentration of minor elements.

Not surprisingly, O and Al are the most prevalent elements on all oxide surfaces. The over-stoichiometric O/Al ratio of approximately two indicates significant hydroxide content; a detailed analysis regarding the

hydroxyl concentration will be shown in a following paragraph. As already visible in the sputter profiles displayed in the previous chapter, the surfaces are covered with adventitious carbon contamination, which is slightly more pronounced for the etched sample surfaces than for the grit-blasted ones. C1s analyses show that this contamination consists mostly of hydrocarbons without functional groups (Fig. A.13). A certain C-O3 contamination, probably carbonates, is detected on Smut-Go NC and in particular on grit-blasted surfaces, whereas the carbon contamination of the HNO₃ etched samples do not show this type of oxidation state, but reveals a distinct presence of C-O and C-O2 functionalities. The lateral distribution of the contamination is exemplarily investigated for etched samples on a Smut-Go NC treated AA 2024 bare sample. Auger mapping (Fig. A.12) shows a homogenous coverage of carbon on the complete surface, i.e. the contamination is not localized. Similar results are published for grit-blasted samples [49]. As Smut-Go NC solution contains fluorides, fluorine is detected throughout the surface after the etching process. The fluorine concentrations above 2 at.% might lead to an increased susceptibility to corrosion of the Smut-Go NC treated substrates. The net-like microstructure of the Smut-Go NC oxide formed on the bare alloy is not reflected in the element mappings, i.e. the pickling effect is merely topographical and not accompanied by differences in chemical composition.

Expectedly, Cu is only present at all bare alloy surfaces and not on the clad samples with their pure aluminium surface layer. This presence of copper makes bare samples generally more susceptible to corrosion – the clad alloys are used due to their enhanced corrosion resistance. However, bondline corrosion of a bonded joint follows a different mechanism, which is more pronounced for clad samples (chapter 2.3.2). Relatively high Na concentrations of 4-5 at.% are detected on grit-blasted surfaces, which is consistent with published analysis of Al surfaces after corundum blasting [49]. It is assumed that the sodium is transferred from the alumina surface onto the specimen. Looking at the nature of the corresponding carbon contamination, which reveals a relatively high amount of carbonates (Fig. A.13), it is likely that the alumina grit is contaminated with sodium carbonate which is transferred during the contact between grit and Al-surface. Being less noble than Al, the presence of Na on the specimen surface does not need to be detrimental with regard to oxide stability in moisture.

As already mentioned above, the O to Al ratios of the different XPS survey spectra indicate a high level of hydration. In order to estimate the OH concentration and to conclude on the nature of the oxide surface, two different methods based on XPS measurements are employed. At first, the oxide O_{ox}/Al_{ox} ratios of the survey are used to calculate the concentration of Al-OH and Al-O bonds. Then the OH content will be determined via a constraint curve fitting of the O 1s peak proposed by Alexander et al. [52].

For the calculation, the metallic aluminium needs to be subtracted from the measured Al concentration. The Al_{met} and Al_{ox} percentages of the Smut-Go NC and grit-blasted oxides that were already used for the oxide thickness calculation (chapter 4.2.2.1) are employed. With thicknesses of approximately 30-40 nm, the Al 2p signal is fully oxidic for HNO₃ derived oxides, i.e. Al_{ox} = 100 at.%. Furthermore, oxygen bound to carbon needs to be eliminated from the calculation. Therefore, the binding state of carbon is considered. The percentages of C-O, C-O2, and C-O3 species are taken from the C 1s high-resolution spectra (Fig. A.13), and the corresponding oxygen concentration is subtracted from the overall oxygen concentration. A potential bonding of oxygen to the minor occurrent elements is neglected, because the deviation is marginal and because the precise bonding state of these elements is unknown. In terms of copper on bare alloys, the XPS spectra show Cu 2p_{3/2} peaks around 933 eV which can be correlated to both Cu(0) and Cu(I); Cu(II) does not occur as satellite peaks are not detected between 940 eV and 950 eV. The results of the calculation of the estimated oxide/hydroxide composition for the different surface conditioning methods are displayed in Table 4.8.

Table 4.8: Elemental Al-oxide composition [at.%] and calculated oxide/hydroxide percentages

		[Al]	Al _{ox} /Al	[Al _{ox}]	[O]	[C _{total}]	[C C-O3]	[C C-O2]	[C C-O]	[O _{ox}]
grit-blasted	bare	25.8	0.95	24.5	54.3	12.7	2.0	0.0	0.0	48.3
	clad	26.0	0.94	24.4	54.7	12.3	2.0	0.0	0.0	48.7
Smut-Go NC	bare	27.2	0.91	24.8	50.5	18.5	1.8	0.0	0.0	45.2
	clad	25.8	0.87	22.5	52.5	18.0	1.3	0.0	0.0	48.5
HNO ₃	bare	25.2	1.00	25.2	53.6	18.3	0.0	2.3	4.8	44.3
	clad	25.9	1.00	25.9	55.9	16.9	0.0	2.5	2.7	48.3

		Calculated Al-O and Al-OH concentrations		
		O _{ox} /Al _{ox}	[Al-O-Al]	[Al-OH]
grit-blasted	bare	1.97	52.3%	47.7%
	clad	2.00	50.3%	49.7%
Smut-Go NC	bare	1.83	64.3%	35.7%
	clad	2.16	39.0%	61.0%
HNO ₃	bare	1.76	70.5%	29.5%
	clad	1.87	60.8%	39.2%

All samples display significantly higher O_{ox}/Al_{ox} ratios than the 1.5 of anhydrous Al₂O₃, confirming that hydration occurs both in water and in ambient conditions. Surprisingly, oxides formed after grit-blasting in “dry” conditions appear to contain more hydroxide groups than most of the etching-derived oxides. Apparently, the existing moisture in the air is sufficient to hydrate the initially formed oxide. Both grit-blasted substrates obtain a high ratio of approximately 2, which leads to a theoretical Al-OH concentration of 50 % (and 50 % Al-O). AlOOH is known as pseudoboehmite, a gel-like, hardly crystallized type of boehmite, which was firstly investigated by Papée [204] and which is known to be formed after immersion of Al in boiling water [51]. However, the reported O_{ox}/Al_{ox} ratios of pseudoboehmite are higher than 2 (2.2-2.5) due to excess water embedded between the oxyhydroxide layers [52], [204]. The obtained ratio is consistent with published results for air-formed films stored under ambient conditions [52].

For thin oxides, the XPS analysis provides an average of the chemical composition throughout the complete film. Thus, it is assumed that even the air-formed oxide film is an oxyhydroxide with an increasing degree of hydration towards the surface. It is most likely that the topmost surface consists of a several nanometre thick, fully hydrated Al(OH)₃ layer. Unexpectedly, the Smut-Go NC pickled bare and clad substrates display distinct differences in O_{ox}/Al_{ox} ratios – bare 1.83 vs. clad 2.16. Compared to grit-blasting, the bare surfaces appear less hydrated and the clad ones display higher hydroxide concentration. This difference cannot fully be explained. Due to uncertainties of the calculation method, e.g. derived from the carbon contamination, the obtained results must be considered carefully and should not be taken as absolute. Yet, the highest OH-concentration is estimated for the oxide film created by the Smut-Go NC process on clad samples, which is the thinnest of all tested oxides. An influence of film thickness on the average OH-concentration is very likely. Due to the presence of water molecules at the surface – either through rinsing or ambient moisture – that leads to full hydroxylation of the topmost part of the oxide, the relative hydroxide share is increased [51]. Vice versa, the thicker HNO₃ derived oxides show lower hydroxide concentrations as the bulk oxide is more predominant in the analysis. Again the OH ratio is higher for clad surfaces than on bare ones, but with a less distinct difference being as seen with Smut-Go NC etching. This difference can hardly be explained by chemical assumptions regarding a different nature of bare and clad oxides. Even though bare and clad samples are known to form differently shaped oxides, their chemical nature should be similar. The O_{ox}/Al_{ox} ratio of around 1.8 of the oxide surface after HNO₃ etching is approximately 0.2 higher than the ratio obtained with sputter depth profiling (1.60 ± 0.05) shown

in Fig. 4.14. This supports the assumption that the “bulk” of the oxide film is less hydrated and that it is covered with a highly hydrated top layer.

In summary, the obtained ratios indicate that both of the thin oxyhydroxides, derived from grit-blasting and Smut-Go NC etching, only have a very small “bulk”¹⁸ that consists of less hydrated oxide, whereas this oxide core is pronounced in the thicker HNO₃ oxide films. It has to be stated that the calculation method can only give an order of magnitude due to uncertainties derived from the technical grade base materials and eventual local variances. Moreover, the quantification of the Al 2p and C 1s peak fitting has a distinct impact on the calculation results. Nevertheless, the results show that independent of “wet” or “dry” oxide formation, a significant amount of hydroxyl bonding partners for the coupling layer is formed with all surface pre-treatments.

An alternative quantification method to determine the Al-O and Al-OH concentration using a highly constraint XPS curve fitting of the O 1s peak was proposed by Alexander and co-workers [52]. Using pseudoboehmite references, the binding energy distances of the oxide and hydroxide O 1s component peaks from the Al-oxide (Al 2p) peak of air-formed oxides was determined. Previously it was found that O 1s and oxide Al 2p signals shift in a similar manner independent of the shift of the C 1s peak [205], which is normally used as reference. For oxide species, the binding energy separation to the Al 2p was found to be 456.6 ± 0.1 eV, for hydroxide 458.0 ± 0.1 eV. The shape, i.e. the Gaussian to Lorentzian ratio, and the width (FWHM) is constrained to be equal for both components; asymmetry is not permitted. The constraints with regard to peak shape and separation are necessary to obtain reliable results fitting two components into the symmetrical O 1s peak. Results of the XPS analysis are shown in Table 4.9. The corresponding high-resolution spectra and fitting curves of the O 1s signal are presented in appendix Fig. A.14. Even though technical-grade alloys are used, the peak positions of O1 (Al-O) and O2 (Al-OH) components derived from the curve fitting are in line with the binding energy differences proposed by Alexander and colleagues. The O_{ox}/Al_{ox} ratios are then calculated back from oxide and hydroxide concentrations.

Table 4.9: XPS peak position and curve fitting of Al 2p_{ox} and O 1s O/OH components¹⁹

		Al 2p oxide			O1: Al-O-Al			O2: Al-OH			Separation [eV]	
		Pos [eV]	FWHM [eV]	G/L	Pos [eV]	FWHM [eV]	G/L	Pos [eV]	FWHM [eV]	G/L	Δ Al2p _{ox} -O1	Δ Al2p _{ox} -O2
grit-blasted	bare	74.25	1.63	0.70	530.83	1.60	0.70	532.09	1.60	0.70	456.58	457.84
	clad	74.18	1.56	0.70	530.96	1.80	0.70	532.19	1.80	0.70	456.78	458.01
Smut-Go NC	bare	74.56	1.78	0.70	531.19	1.60	0.70	532.47	1.60	0.70	456.63	457.91
	clad	74.48	1.91	0.70	531.27	1.80	0.70	532.58	1.80	0.70	456.79	458.10
HNO ₃	bare	74.17	2.38	1.00	530.75	2.31	0.93	532.14	2.31	0.93	456.58	457.97
	clad	74.07	2.31	0.96	530.76	2.41	0.93	532.16	2.41	0.93	456.69	458.09

Table 4.10: XPS quantitative curve fitting O 1s O/OH components and derived O_{ox}/Al_{ox} ratio

		Fitting O 1s		
		[Al-O]	[Al-OH]	O _{ox} /Al _{ox}
grit-blasted	bare	56.3%	42.6%	1.92
	clad	54.5%	45.5%	1.94
Smut-Go NC	bare	59.1%	40.9%	1.89
	clad	44.0%	56.0%	2.08
HNO ₃	bare	63.5%	36.5%	1.83
	clad	68.9%	31.1%	1.78

¹⁸ It is assumed that the “bulk” of the thin oxide films is smaller than the hydrated surface hydroxide.

¹⁹ Grit-blasted and Smut-Go NC etched samples were analysed by the BAM.

In principle, the constraint O 1s curve fitting results (Table 4.10) confirm the calculated Al-O and Al-OH concentrations shown before. The deviation between calculated and fitted values of all component concentrations is below 10 % (absolute), in most cases below 5 %. The fitting-derived O_{ox}/Al_{ox} ratios deviate less than 0.1 from the calculated ones. Again, the oxyhydroxide formed on clad material after Smut-Go NC etching has the highest OH concentration, but the difference to the other films is not as pronounced. Contrary to the results of the calculation, the OH ratio of the HNO_3 derived oxide is slightly higher on bare than on clad. Hence, it is assumed that the chemical composition is the same on bare and clad. Similar to the calculation, the O_{ox}/Al_{ox} ratio of HNO_3 oxides is around 1.8 and confirms the existence of less hydrated core (sputter profile reveals 1.60 ± 0.05) and a highly hydrated top layer. This “bulk” oxide is by far less pronounced for the other investigated oxide films. As for the calculation method, this method is afflicted with some uncertainty, e.g. the precise positioning of the Al 2p peak. Moreover, the oxygen bound to the carbon contamination which may contribute to the OH signal is not considered [196]. However, other researchers have shown that such a correction is maximal 5 % [197]. In any case, it is not the aim of this work to determine the exact absolute Al-OH concentration, but to identify differences in the chemical nature of the oxides of the substrates after the employed surface pre-treatments.

To conclude, the investigations confirm that all aluminium oxide films are oxyhydroxides with a significant amount of surface hydroxyl groups that are potential bonding partners for the coupling films. The higher thickness and the lower hydroxyl content of the HNO_3 derived layers is presumably beneficial in terms of environmental resistance. Furthermore, the obtained results suggest that the chemical nature of the grit-blasted surfaces exposed to ambient air is similar as the etching oxide films. Consequently, the chemical state of the oxide does not cause differences in joint stability observed with the different pre-treatments.

Table 4.11: Percentage of accessible surface OH-groups (Al-OH/Al-O-X) detected by CD-XPS

		[Al-OH _{surface}]
grit-blasted	bare	11 %
	clad	11 %
Smut-Go NC	bare	19 %
	clad	12 %

In order to verify the similarity in chemical nature of the “dry” and the “wet” oxide, grit-blasted and Smut-Go NC treated surfaces are compared by using XPS analysis after chemical derivatisation (CD-XPS)²⁰. CD-XPS is a well-known method for the characterisation of polymer surfaces [206]. Ono et al. used an atmospheric-pressure derivatisation with trifluoroacetic anhydride (TFAA) to determine hydroxyl residues on lithium niobate films [180]. A similar approach is employed here for investigating the concentration of accessible Al-OH groups at the surface, i.e. the accessible OH groups are substituted by the trifluoroacetyl groups and then the amount of organically-bound fluorine on the surface is determined by XPS [179].²¹ No comparable investigations of aluminium oxide films are known from literature. Contrary to the O 1s curve fitting described above, this method does not reveal the total percentage of hydroxyl groups but the percentage of the ones that are accessible for reaction (Table 4.11). A corresponding XPS high resolution spectrum of the derivatised C 1s peak is displayed in Fig. A.15. As expected, the ratio of these OH-groups is significantly lower than the previously estimated total amount. Nevertheless, all samples show that more than 10 % of all oxidised species, i.e. more than 20 % of all hydroxyl groups, are accessible OH-groups. Hence, a sufficient number of bonding partners is available on all employed surfaces to interact with the coupling layers. While the results between bare and clad base material do not differ for grit-blasted samples, Smut-Go NC leads to different results on bare and clad specimens. In contrast to the O 1s curve

²⁰ HNO_3 derived oxides are not investigated as it is assumed that their upper surface layer is similar to the Smut-Go NC derived ones and as relative quantification compared to the complete oxide is not possible due to the limited penetration depths of the X-Rays.

²¹ Derivatisation and XPS analysis are performed by the BAM – more details on procedure and OH⁻ calculation are shown in chapter 3.3.

fitting the OH-concentration is higher on the bare surfaces. This effect can be explained by means of surface topography: unlike grit-blasting and Smut-Go NC etching of clad surfaces, Smut-Go NC pickling of bare surfaces creates a distinct microstructure (chapter 4.2.1) increasing the surface-to-volume ratio, which means that more hydroxyl groups that exist in the upper oxide are actually accessible.

Summarising this chapter, it can be stated that hydroxyl-rich oxyhydroxide films are formed after all employed surface pre-treatment techniques, which offer multiple potential interaction sites for the coupling films. A significant difference in chemical nature between air-formed and water-derived oxides cannot be detected. Thus, adhesion performance differences can be correlated to surface topography only. Fluorides are detected after pickling with Smut-Go NC, which may be detrimental for long-term stability.

4.2.3 Analysis of the interface between aluminium oxide and plasma film

Having detected accessible, reactive aluminium hydroxyl groups at the surface, the chemical interactions between these groups and the plasma derived coupling films must be considered. As mentioned in chapter 2.2.2, various works have been published on the formation of covalent bonds between hydrolysed silanes and oxidic surfaces. Similar predictions were made for plasma CVD films on metals (chapter 2.2.3). In recent years, ToF-SIMS has become a standard technique to assess the binding state at polymer-metal interfaces. Especially for silane coupling agents it has been presented as the method of choice to prove the existence of covalent bonds between coupling film and aluminium oxides [115], [128], [207].

The fragment that is mainly considered in the positive spectrum has a nominal mass of 71 amu. Cave and Kinloch were the first to assign this mass to an AlOSi^+ fragment when examining self-assembly silane coupling films by SIMS [208]. Furthermore, they indicated that fragments of a nominal mass of 103 u and 119 u could be additional signs for the existence of Al-O-Si bonds as they could be assigned to AlO_3Si^- and AlO_4Si^- . This assumption is derived from analogous FeO_3Si^- and FeO_4Si^- fragments found previously by Cayless and Perry, who investigated steel surfaces after silane application [209]. However, due to limited resolution of the employed device, an unambiguous proof of their assumption could not be provided, since a differentiation from other fragments with a similar nominal mass was not possible. Identification of the analysed ions is always difficult, because Si and Al differ by only one atomic mass unit, i.e. silicon can hardly be distinguished from a hydrogen atom bound to aluminium.

Abel et al. were arguably first to find an indisputable evidence for the formation of covalent bonds between GPS and aluminium surfaces. Using high-mass resolution ToF-SIMS the AlOSi^+ fragment with an exact calculated mass of 70.9534 u could be assigned to the measured signal peak around 70.95 u; the precise experimental value is 70.9515, but a determination to the fourth decimal place seems questionable due to the limited maximal resolution of the employed device. Nevertheless, it was proven by comparative analyses of pure aluminium that the major part of this signal is derived from the AlOSi^+ ion and not from the potential alternative Al_2OH^+ . Other fragments with nominal mass of 71 found in the positive spectrum, like Si_2CH_3^+ or $\text{SiOC}_2\text{H}_5^+$, could be distinguished unambiguously due to their larger mass difference. Thus, the fragment with a mass of 70.95 u can be seen as indicator for covalent bonds between silicon, oxygen and aluminium. As interfaces are naturally buried under the film, a gentle sputtering process is used to uncover this region. The required ion dose for this process clearly exceeds the one of the primary ions, but it is considered as appropriate technique to investigate silane-metal interfaces. By using this depth profiling technique, it was shown that the 70.95 u signal is mostly linked to the AlOSi^+ fragment, but the contribution of the Al_2OH^+ fragment to the signal increases after most of the film is removed and the aluminium oxide is reached [115]. Therefore, a similar technique is applied in this work.

Sample surfaces are analysed directly (static SIMS) with a low primary ion density to ensure analysis of a non-etched area and during gentle sputter depth profiling (dynamic SIMS). Even during gentle ion etching, hydrocarbon fragments will be destroyed, but which is not problematic as the focus in the positive spectrum is put on the detection of the AlOSi^+ fragment. However, more recent studies indicate that the existence of these ions do not automatically implicate that the corresponding covalent bonds existed before the analysis

[210], [211]. The fragment could as well be an artefact created during the bombardment with primary ions, respectively during sputtering. Wapner and Grundmeier detected the 99.9 u FeSiO^+ fragments in the positive ToF-SIMS spectrum indicating covalent bonding of a HMDSO derived plasma layer on iron. Yet, similar ions also appeared analysing a modified reference specimen coated with a thin film of polysiloxane oil. Certainly, covalent bonds are not formed between the silicone oil and the iron surface. The relative intensity of the 99.9 u ion even exceeded the one measured for the plasma coated sample during sputter profiling of this reference [210]. Analogous results were reported for aluminium, where the AlOSi^+ fragment was detected while examining specimens covered with polysiloxane oil [211].

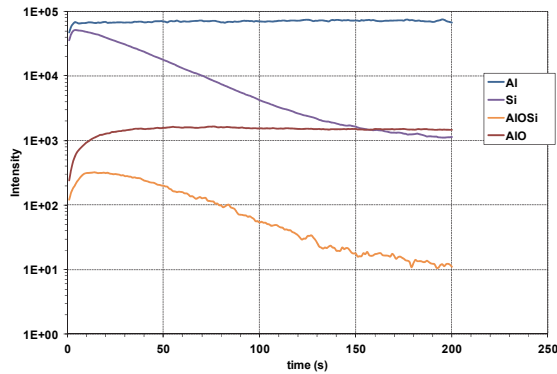
Even though these findings do not refute the covalent bonding theory, the sole existence of the 70.95 u ion as proof for covalent bonding is questionable. Thus, in addition to considering this fragment, other ions are regarded in the negative spectrum. As stated above, fragments with nominal mass 103 u and 119 u have been identified as indicators. Typical fragments of silicates in the negative spectrum are, among others, SiO_2^- and SiO_3H^- , whereas AlO^- , AlO_2^- and Al_2O_3^- are typical for aluminium oxides. Therefore, it is likely that SiO_2AlO^- , $\text{SiO}_2\text{AlO}_2^-$ and $(\text{SiO}_2)_2\text{AlO}_2^-$ or $\text{SiO}_3\text{H}(\text{Al}_2\text{O}_3)^-$ ions with respective masses of 102.94 u, 118.94 u and 178.91 u are detected. To the author's knowledge, these fragments have not been reported to appear in blank tests. Still, other Al-oxide/hydroxide derived ions with a similar mass can occur. $(\text{Al}_2\text{O}_3)\text{OH}^-$ (118.95 u) and $(\text{Al}_2\text{O}_3)\text{AlO}_2(\text{H}_2\text{O})^-$ (178.93 u) cannot be distinguished with confidence from the above mentioned fragments with equal nominal mass – however, no Al-oxide fragment is expected at 103 u. Still, depth profiling will show that these fragments only appear at the interphase region and decrease from there along the silicate SiO_2^- and SiO_3H^- signals, which means that they contain Si and do not only consist of Al, O and H.

Three different APPJ-CVD treated specimens are analysed using static SIMS and sputter depths profiling in positive and negative mode to investigate covalent bond formation between plasma polymer films and grit-blasted or HNO_3 conditioned surfaces: GPS (5 SLM) plasma films on grit-blasted and HNO_3 etched AA 2024 bare, as well as TEOS (0.5 SLM) derived films on HNO_3 etched AA 2024 bare. The etched substrates are polished first to obtain a distinct interface, i.e. to shorten the transition interphase region in the sputter profile. After polishing, these samples are degreased and conditioned in HNO_3 , followed by rinsing in deionised water. The precise parameters of each ToF-SIMS are displayed in Table 3.8; all overview spectra and a summary table of the relevant fragments are shown in the appendix, in Fig. A.16-18 and Table A.2.

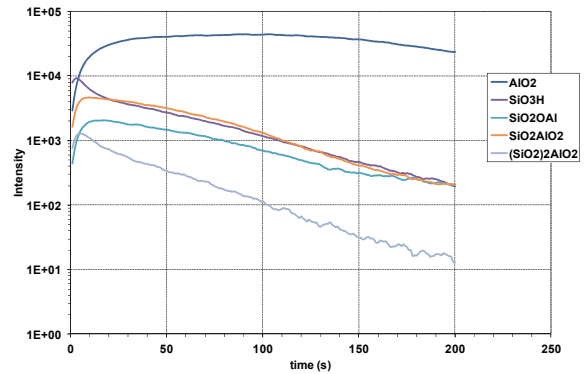
Not surprisingly, the static SIMS spectra (Fig. A.16) of the GPS derived plasma polymer film on the grit-blasted substrate contains distinct Si/silicate, Al/Al-oxide and Cu signals, as well as traces of Mg and Na. Si^+ is indeed the prevalent ion in positive mode, but the strong Al^+ and the significant Cu^+ and AlO^+ signals suggest that the film is very thin and not fully closed; this is coherent with the XPS depth profile of chapter 4.1.1. The presence of sodium, which is a contamination originating from alumina grit-blasting, also supports this finding. Additional contaminations found are aliphatic and aromatic hydrocarbons, like phthalates, as well as polydimethylsiloxane, which is known to be an impurity in the precursor. Part of the hydrocarbon signals might be related to less fragmented precursor, like the signal at 57 u ($\text{C}_3\text{H}_5\text{O}^+$), which has been associated to the epoxy-ring bound to CH_2^+ in previous ToF-SIMS investigations of solution derived GPS coupling films [116]. The sought-after AlOSi^+ ion appears in the spectrum but at a low intensity. Due to the low ion dose, signals from the contaminations are quite pronounced overlaying the signals of the film and the interface. In the negative spectrum silicate fragments as SiO_2^- , SiO_3H^- and SiO_5H^- are predominant. The considered alumosilicate fragments could however not be detected without doubt; only the fragment at 179 u, potentially $(\text{SiO}_2)_2\text{AlO}_2^-$ or $\text{SiO}_3\text{H}(\text{Al}_2\text{O}_3)^-$, appears in the overview spectrum, but cannot be identified unambiguously.

The results obtained with the HNO_3 etched specimen coated with GPS plasma films do not differ significantly from the ones discussed before. Strong Al^+ and Cu^+ signals appear in the positive overview spectrum with an Al intensity exceeding even the Si signal. Hence, the plasma polymer appears to be even slightly thinner than the layer deposited on grit-blasted aluminium.

Contrary to GPS, TEOS deposition creates a closed film. Positive and negative overview spectra reveal that Si/silicate fragments of the coupling film are predominant, whereas Al is not visible. However, Cu and Cu-oxides appear, which cannot be fully explained, but is assumed to be surface contamination originating from the polishing process. The film is closed, so there is no open interface, i.e. no interface related species can be seen. Again, phthalates and other organic contamination are found. Altogether the static SIMS measurements only provide little evidence for the formation of covalent bonds as only few interface alumosilicate fragments could be detected. However, the interface might be buried under the coupling film and contamination.



GPS (5 SLM), grit-blasted – positive mode



GPS (5 SLM), grit-blasted – negative mode

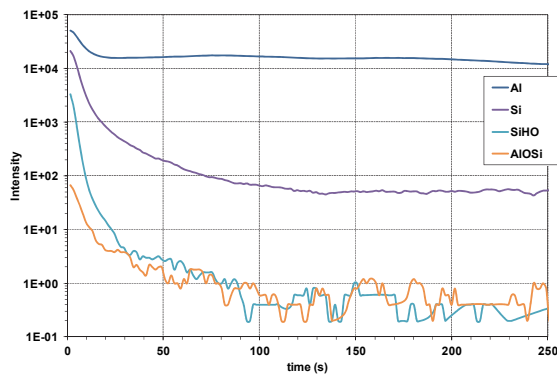
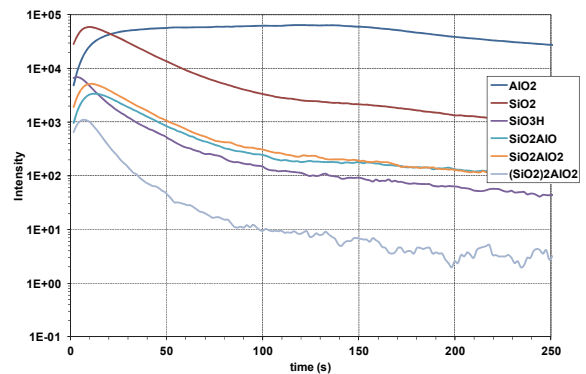
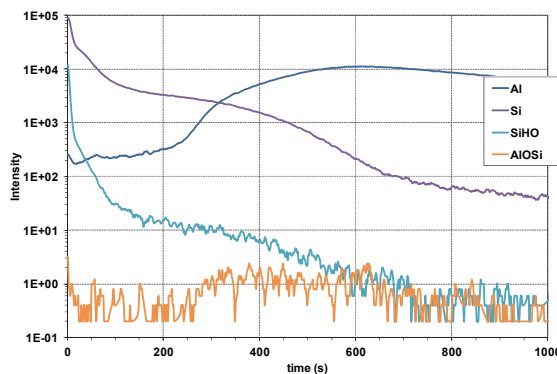
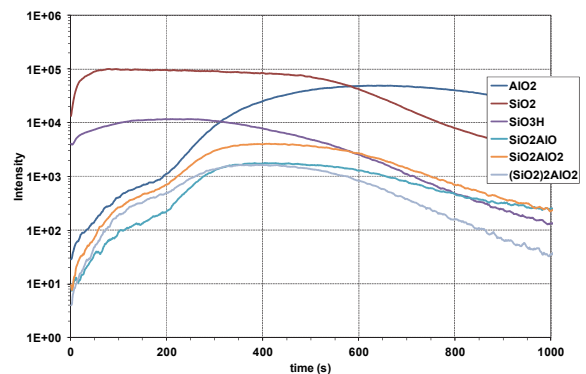
GPS (5 SLM), HNO₃ – positive modeGPS (5 SLM), HNO₃ – negative modeTEOS (0.5 SLM), HNO₃ – positive modeTEOS (0.5 SLM), HNO₃ – negative mode

Fig. 4.15: ToF-SIMS sputter depth profiles of APPJ-CVD films on AA 2024 bare (parameters in chapter 3.3; raw data produced at OFG Analytik GmbH)

Higher ion doses are employed during depth profiling for removing organic content and penetrating deeper into the sample. Admittedly, an increase of ion dose also increases the potential of artefact formation due to ion bombardment. Fig. 4.15 shows the sputter profiles of all analysed systems. In both depth profiles (positive and negative mode) of the GPS plasma-coated and grit-blasted surface, the oxide is clearly present from the beginning with high Al^+ respectively high AlO_2^- signals. The interface is directly visible from the start, revealing a distinct presence of SiOAl^+ ions in positive mode and of $\text{SiO}_2\text{AlO}_2^-$, SiO_2AlO^- and $(\text{SiO}_2)_2\text{AlO}_2^-$ in negative mode. At first, the intensity of the AlOSi^+ increases shortly along the AlO^+ curve before decreasing along the Si^+ signal. Analogous observations are made in the negative profile, where the intensity of the interface-fragments augments similarly to the AlO_2^- ions before falling proportional to the SiO_3H^- intensity. Thus, all of the considered aluminosilicate fragments are true interfacial species and are not just aluminium oxide fragments.

Consequently, a clear indication for the formation of covalent bonds is given. Fig. 4.16 displays the reconstructed spectrum corresponding to the interphase region after 2 to 16 s of sputtering showing the aluminosilicate fragments. Al-oxide and silicate ions are both predominant in this region. When interpreting the depth profile, it must be taken into consideration that the interphase region is very wide, because the substrate surface is very uneven, i.e. rough, and is covered with an inhomogeneous coupling film (as pointed out in chapter 4.1.1). A lateral mapping (negative mode) of the analysed area is conducted at the beginning of the ion etching to retrieve more information on the local prevalence of the interface ion $\text{SiO}_2\text{AlO}_2^-$ compared to aluminium and silicon. This mapping (Fig. 4.17) displays a distinct inhomogeneity in the Si distribution that exceeds the inhomogeneity of the overall ion distribution. The overall detected quantity of Al and Si is approximately the same, but the Si presence is very much focused on the few “Si-drops” with high film thickness, whereas the Al signal is more even but still showing significant differences due to roughness. The areas where high Si-intensity coincides with strong Al or AlO_2 signals are “hills” in the rough surface profile. There, the etching effect is higher and, thus, more secondary ions are created. $(\text{SiO}_2)_2\text{AlO}_2$ fragments are detected almost across the whole probe surface following mainly the Al and AlO_2^- signals. Intensity is low at the “Si-drops”. This finding supports the assumption that the investigated fragments occur only at the interface and that high film thickness covers the interface.

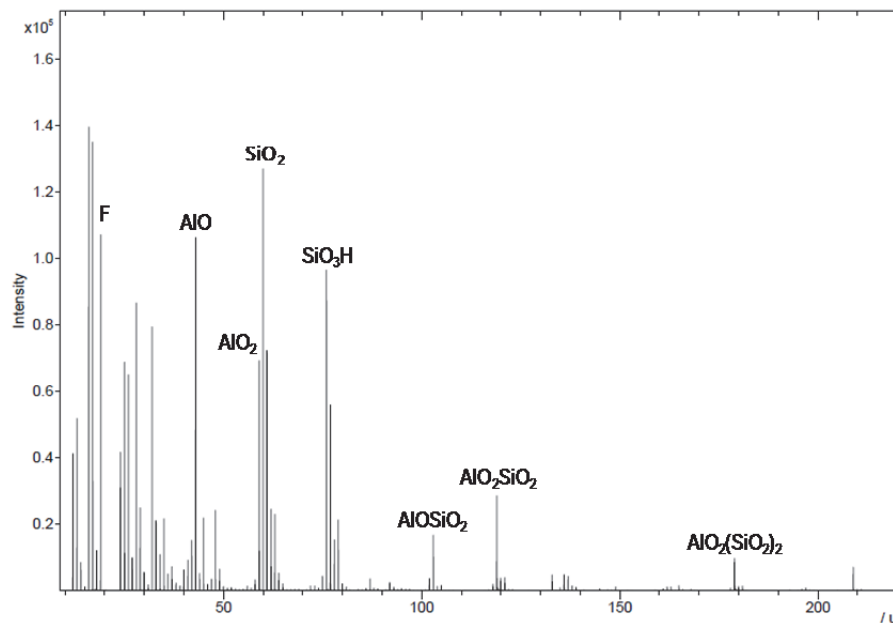


Fig. 4.16: Negative ToF-SIMS spectrum of interphase region of GPS plasma film on grit-blasted AA 2024 bare (reconstructed from sputter depth profile; produced by OFG Analytik GmbH)

Field of view: 99.6 x 99.6 μm^2

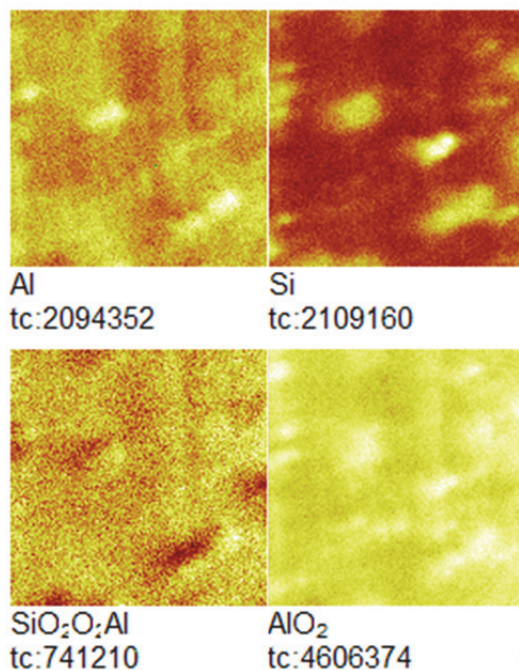


Fig. 4.17: Negative ToF-SIMS lateral maps at the start of sputter depth profiling of GPS Plasma coated grit-blasted AA 2024 bare (tc = total count; produced by OFG Analytik GmbH)

Considering now the polished HNO_3 conditioned GPS coated sample, a shorter interphase region is observed. Despite the gentle etching conditions the silicate signals decrease rapidly with sputter times whereas Al-oxide signals augment: after 20 to 30 s the intensity of film related fragments is reduced to half-maximum or below and the substrate related signals have reached maximum. Thus, the film is interspersed with the oxide formed during acidic conditioning and the interphase region is instantly reached upon sputtering. The profiles confirm previous findings: all ions associated with covalent bonds – AlOSi^+ in positive mode, as well as SiO_2AlO^- , $\text{SiO}_2\text{AlO}_2^-$ and $(\text{SiO}_2)_2\text{AlO}_2^-$ in negative mode – are detected. The intensities of these fragments again first follow the trend of aluminium oxide and then the silicate concentration.

Analysing the depth profiles of the polished specimen coated with the TEOS derived plasma film, it is evident that the interphase region is not reached as directly as with the GPS film. Only after approximately 200 s, indicated by a strong increase in Al^+ , AlO_2^- and alumosilicate fragment intensities, the interphase begins. Surprisingly, the AlOSi^+ ion could not be detected in positive mode throughout that region. Generally speaking, with an unexpected, strong drop of silicon and silicate intensities directly at the beginning, the

intensities of the positive ions are not very meaningful in this instance. In negative mode, intensities of silicate fragments remain high the first 400 s, while decreasing to approximately 50 % after 600 s. After that, the decrease progresses more rapidly. The alumosilicate ions peak between 350 and 500 s before falling along with the silicate signals, confirming their interfacial nature. Even though the substrate was polished prior to conditioning, the interphase is somewhat blurred due to uneven film thickness. Moreover, the course of silicate and Al-oxide intensities support the previous finding that the coupling film penetrates the open oxide forming an interspersed layer.

Altogether, strong indication for covalent bonding of APPJ-CVD derived silica-like films to the aluminium oxide of both, grit-blasted and HNO_3 conditioned, substrates is presented even if the question whether covalent bonding occurs cannot be indisputably affirmed; this would require additional confirmation by alternative methods, like Reflection Adsorption Infrared Spectroscopy (RAIRS), on specially prepared specimens for fine analysis and exceeds the scope of this work. Nevertheless, if one follows the postulate of covalent bond formation after application of hydrolysed silanes, it is very likely that such bond formation also occurs in the highly energetic plasma, which has been already been verified for low pressure plasma derived silica films [149]-[151]. The presumably covalent bonding and the penetration of aluminium oxide by the plasma derived coupling film augur stable interface formation which will be demonstrated later on in mechanical and durability testing of bonded joints.

4.2.4 Correlation of surface pre-treatment and strength of plasma treated joints

The introductory section of chapter 2.2 pointed out the strong influence of surface pre-treatment and the resulting surface condition on the performance of bonded joints. In the previous chapters, the surfaces created after the different surface pre-treatment techniques on AA 2024 bare and clad substrates were intensively studied, revealing significant differences in roughness and oxide topography, as well as similarities in chemical state of the formed oxides. Moreover, the interface between these oxides and the different APPJ-CVD derived coupling films was investigated, showing a certain penetration of the oxide structure by the plasma polymer and suggesting covalent bond formation. Chapter 4.1.3 provided a first assessment of plasma derived coupling films. A pronounced dependency of the joint performance on the properties of the film surface was detected, and the high potential of GPS and TEOS deposition was indicated. However, the employed DP 490 paste adhesive does not fulfil the demanding requirements of the aircraft industry and, hence, is only used for first screening tests. In the following, joints are bonded with the qualified high-strength temperature- and pressure-curing film adhesive FM 73, which is the standard adhesive for evaluation of the surface preparation of aluminium alloys with regard to adhesion and durability. Thus, the aim of this chapter is to systematically correlate the above mentioned surface and film characteristics with adhesion performance, i.e. with the mechanical strength of the bonded joint. Furthermore, this performance is appraised by comparison to state-of-the-art silane and sol-gel treatments.

As this method is found to be the most demanding test for metal surface treatments, floating roller peel tests are conducted again. Each test is performed in dry and wet condition, i.e. peel strength is measured before and after injections of water (1 % v/v surfactant) into the bondline. Wet testing is an additional stability differentiator, because the water instantly eliminates weak secondary bonds. Grit-blasting and alkaline etching in combination with Smut-Go NC or HNO₃ pickling are used as surface conditioning techniques for bare and clad AA 2024 samples before deposition of the plasma or solution derived coupling films. As previously described, grit-blasting creates macro-rough surfaces without pronounced microstructure or oxide texture. Etching produces smooth surfaces on clad and some irregular roughness on bare substrates due to pits created by removal of intermetallics. During desmutting in HNO₃ an open texture is formed (more pronounced on clad surfaces) with voids of approximately 10 nm, whereas Smut-Go NC does not create such texture. Smut-Go NC, however, does create a net-like oxide microstructure with a roughly 100 nm wide mesh on bare surfaces. The resulting six different surfaces are coated with either 5 SLM GPS or 0.5 SLM TEOS derived plasma films, respectively either 1 % aqueous GPS solution or AC-130. Corresponding peel test results are displayed in Fig. 4.18 (dry) and Fig. 4.19 (wet).

Basically, no differences between dry and wet testing are observed for stable joints (cohesion failure). Wet testing only makes a difference where at least partial adhesion failure occurs, i.e. where the interface is directly exposed. In these cases, the peel strength decreases roughly in line with the initial ratio of adhesion failure. Achieved peel strengths clearly depend on the employed surface pre-treatments and on the type of coupling film. Nevertheless, consistent trends with regard to surface pre-treatments, which are valid for all adhesion promoting films, can be deduced.

Before analysing the test performance of the differently treated joints, the error bars should be considered: peel strengths of the test coupons of several tested systems, especially those of the weaker ones, vary significantly along the bondline. Moreover, they also vary from specimen to specimen. This usually corresponds to an abrupt change in failure mode. Stable systems do not display such a variation of failure mode (cohesion failure). Still, certain deviations between the different coupons are measured, which are caused by the use of different batches of bonded joints and in particular by differences in the actual thickness of the adhesive.

Blasting with 50 µm alumina grit provides excellent joint strength in combination with all coupling films that reach anodising level and exceed the required 10 kN/m, which is the limit in manufacturing quality

control²². For reference, peel strengths of 13.8 ± 0.9 kN/m are measured with PSA on either bare or clad substrates in dry and wet testing, which corresponds to 100 % cohesion failure in the adhesive. Similar full cohesion failure is reached after grit-blasting with all employed treatments – in spite of their lower peel strength values, TEOS APPJ-CVD on clad and AC-130 on bare also fail 100 % cohesively. Apparently, the intrinsic strength of the adhesive in these test series is lower but still reaches the expected value provided by the adhesive manufacturer (12.8 kN/m [212]). Hence, the maximal possible joint strength is achieved with all coupling films on grit-blasted substrates. No significant difference is observed between clad and bare material, which is coherent with the similar roughness and oxide properties.

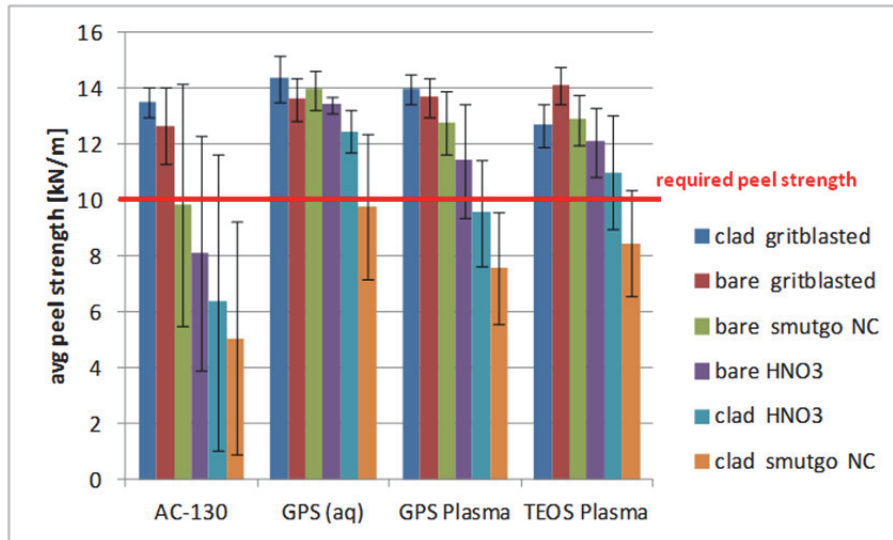


Fig. 4.18: Dry peel strength of adhesive joints of AA 2024 bare or clad – FM 73 adhesive

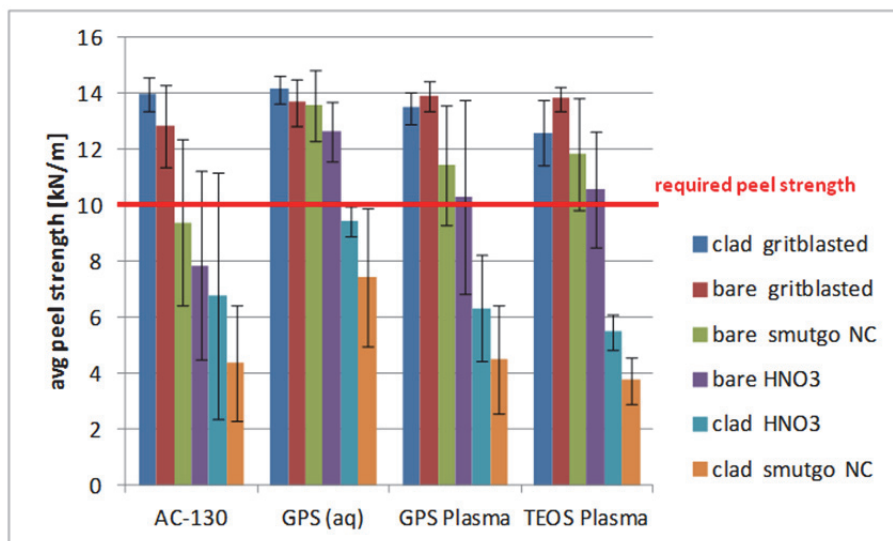


Fig. 4.19: Wet peel strength of adhesive joints of AA 2024 bare or clad – FM 73 adhesive

On the contrary, both acids result in a distinct difference between bare and clad substrates with bare outperforming clad. As surface chemistry is relatively similar, the difference can be assigned to the differences in topography. In dry testing, Smut-Go NC pre-treated AA 2024 bare joints display the highest peel strength of all etched samples; they almost match grit-blasting results for all employed coupling films

²² The thickness of the peel sheets used here is 0.6 mm and not 0.5 mm according to the standard. The higher sheet thickness increases the measured peel strengths by approximately 10 to 15 % (empirical experience) if cohesion failure is obtained. The difference is lower with interfacial failure.

except for AC-130. After water injection, grit-blasting level can only be achieved with the GPS solution – for all other samples peel strength deteriorates slightly. The roller peel results of bare samples also reveal a trend that peel strength obtained with HNO₃ are somewhat lower than with Smut-Go NC. As macro-roughness is equal for both processes, it is assumed that the net-like microstructure causes this difference. On clad, this structure is not formed, and Smut-Go NC etching leads to the lowest joint strength independent of the coupling film. It is very likely that the reason lies in the nano-texture, which is less pronounced than for HNO₃.

In summary, the expected significant impact of the surface pre-treatment on joint performance after silane or sol-gel application is confirmed and it is also detected for APPJ-CVD treatment. As surface chemistry is found to be relatively similar for all aluminium oxides, a qualitative correlation between peel resistance and surface roughness is established with macro-roughness being more important than microstructure and nano-texture:

grit-blasting clad/bare	>	Smut-Go NC bare	>	HNO₃ bare	>	HNO₃ clad	>	Smut-Go NC clad
macro-rough		µm-deep pits		µm-deep pits		smooth		smooth
no microstructure		net-like microstructure		no microstructure		no microstructure		no microstructure
no oxide texture		some oxide texture		open oxide texture		very open oxide texture		little oxide texture

Enhanced mechanical interlocking of rough surfaces is the most prevalent effect; compared to smooth samples, stress level at the interface is reduced. The pronounced dependency on macro-roughness is consistent with observations made by other researchers [49], [133], [194], [213]. Anodising uses a similar – but even more distinct – effect, forming a micro-composite between the thick porous oxide and the penetrating polymer that creates a stress transition zone with an intermediate modulus between the two different materials [1], [79]. The higher roughness also increases the volume of polymer that deforms plastically, i.e. it enlarges the plastic energy loss during fracture, leading to higher measured joint strength [80]. The open oxide texture formed in HNO₃ may increase the surface area but cannot sufficiently reduce the stresses at the interface due to the low macro-roughness.

Table 4.12: XPS elemental analysis results [at.%] and fracture behaviour of AA 2024 clad (HNO₃) adhesive joints after dry peel testing

	side	C	N	O	Na	Al	Si	Zr	% coh. failure	interfacial fracture type
GPS (aq)	m	74.13	2.46	18.45	1.84	0.65	0.68	-	40 ± 5	cohesion-near-interface
	a	76.91	1.84	19.54	0.7	-	0.4	-		
AC-130	m	74.65	2.51	17.14	2.18	0.51	1.97	0.24	20 ± 5	cohesion-near-interface and fracture of film
	a	67.71	-	24.36	3.35	-	3.83	0.75		
GPS Plasma	m	58.69	0.69	29.35	3.62	5.61	2.04	-	30 ± 5	cohesion-near interface and fracture of oxide/film
	a	60.58	0.7	30.44	2.94	3.72	1.62	-		
TEOS Plasma	m	50.94	1.01	32.22	5.28	4.19	4.54	-	35 ± 5	interfacial film/adhesive partly fracture of oxide/film partly cohesion-near-interface
	a	74.14	1.03	22.66	0.44	0.43	1.31	-		

Beside the surface pre-treatments, the coupling films themselves influence peel strength. In general, differences are only apparent with the etched specimens. Sole etching is not a desired conditioning for an industrial application but allows to further distinguish and to enhance understanding of the capabilities of the adhesion promoting layers. Of all tested processes, the aqueous GPS solution performs best, whereas the sol-gel coating, despite similar chemistry, is the weakest system. The differences in measured peel

strength between the GPS and the TEOS derived plasma films are insignificant; joint strength obtained with TEOS appear to be slightly higher in dry but lower in wet condition. XPS analysis of the fracture planes is performed on both sides (metal and adhesive) to precisely determine the failure type and to correlate fracture behaviour to the obtained peel strengths. HNO₃ pickling on clad material is chosen as representative surface conditioning technique for this analysis, because it creates highly reproducibly surfaces and the associated joint failure is mainly apparent interfacial. The elemental compositions of these areas of adhesion failure are displayed in Table 4.12 for dry and in Table 4.13 for wet testing. Both tables also contain an analysis of the fracture behaviour of the inspected specimens. The percentage of apparent cohesion failure is measured visually using a mm²-grid. High sodium concentrations are detected on all samples surfaces. It is assumed that this contamination originates from the water that is injected in the bondline.

Table 4.13: XPS elemental analysis results [at.%] and fracture behaviour of AA 2024 clad (HNO₃) adhesive joints after wet peel testing

	side	C	N	O	Na	Al	Si	Zr	% coh. failure	interfacial fracture type
GPS (aq)	m	63.75	1.1	24.7	5.39	2.46	0.47	-	25 ± 5	cohesion-near-interface with interfacial metal/adhesive parts (fracture of film)
	a	72.17	1.49	20.77	3.26	-	0.58	-		
AC-130	m	59.12	2.35	26.03	2.98	2.21	1.48	0.19	15 ± 5	cohesion-near-interface and fracture of film
	a	64.08	1.98	21.95	2.47	-	4.11	0.86		
GPS Plasma	m	42.55	0.77	37.47	1.53	13.38	2.66	-	10 ± 5	mostly interfacial film/adhesive partly fracture of oxide/film partly cohesion-near-interface
	a	68.02	1.31	23.83	2.44	2.43	0.89	-		
TEOS Plasma	m	50.69	0.89	33.09	3.17	7.89	3.15	-	10 ± 5	interfacial film/adhesive and fracture of oxide/film partly cohesion-near-interface
	a	60.46	1.12	28.67	2.74	3.66	2.35	-		

After dry testing, high carbon and nitrogen concentrations are detected on metal (m) and adhesive (a) side for samples treated with the aqueous GPS solution. Elemental composition is almost mirrored along the fracture plane, which is a strong sign for cohesion failure of the adhesive located very close by the interface. Only a small Al signal appears on the metallic side, which means that hardly any interfacial failure occurs. In the areas of interfacial failure, it is likely that the fracture path goes through the coupling layer as Si signals are found on both sides. This fracture behaviour confirms a strong linkage of the coupling film to both adhesive and oxide. This leads to the highest peel strength of tested films and to a higher ratio of cohesion failure. Moreover, the intact interfacial bonding confirms that for the practical adhesion determined by the peel test, mechanical aspects are more relevant than adhesion at the interface. Injection of water reduces peel strength and the degree of cohesion failure. Moreover, C and N concentrations decrease on the metallic side, whereas the Al signal becomes more distinct, pointing to an increased ratio of truly interfacial failure. Once again, fracture proceeds through the coupling film as Si is detected on both sides, while carbon concentration is the highest for all examined aluminium adherends. This means that the ratio of near-interface-cohesion failure is highest for samples treated with GPS solution, which is coherent with the highest measured peel strength.

AC-130 coated samples do not show any significant change of peel strength upon injection of water suggesting that the fracture behaviour remains relatively stable. Like GPS, AC-130 treated samples display high carbon concentrations on both sides. However, Si and Zr signals on both sides, especially as concentrations are higher on the adhesive side, are a distinct sign that failure also occurred within the film. Liu et al. found a similar fracture path through the sol-gel layer during asymmetric double cantilever beam testing [131]. With a film thickness of around 200 nm, the intrinsic stability of the coupling layer becomes

more important. Moreover, the AC-130 treatment process does not include a thermal curing step before application of the adhesive, which might entail a lower degree of crosslinking and, hence, a lower intrinsic strength compared to GPS treatment. However, this effect is unlikely to occur, because the adhesive is cured at 125 °C. In any case, it must be kept in mind that peel testing is associated with strong and complex deformations, which are not favourable for thick or brittle films. Furthermore the extremely large error bars indicate that the fracture mode is permanently changing and, thus, resulting in sizeable differences not only between the samples but also within one single sample. SEM analysis shows significant local differences in film thickness (Fig. A.19); this is probably one reason for this instable behaviour. This mixed fracture mode of near-interface-cohesion and cohesive within the film does not change significantly upon contact with water, but a slight increase of interfacial failure is indicated by an augmented Al concentration. Nevertheless, bonding to both polymer and oxide is strong.

When considering plasma coated specimens, lower carbon concentrations are traceable on the metallic side. On the one hand, this is due to low carbon content of the films. On the other hand, the part of cohesion failure close to the interface is lower, because other fracture types occur. When examining the GPS plasma coated sample, strong aluminium and silicon signals appear on both sides. Thus, it is possible that the fracture path passes through the interspersed oxide-plasma polymer layer and peel resistance is limited by the strength of the oxide-film composite. Taking into account the inhomogeneous structure of the GPS derived films with drop-like parts of high film thickness, it is, however, more likely that these parts are ruptured during interfacial failure and are then detected on the adhesive side. After water injection, the fracture moves further towards the interface between plasma polymer and adhesive; Al and Si concentrations increase on the metallic side, whereas the Si signal decreases on the adhesive side.

Surprisingly, the behaviour of TEOS derived plasma film is diametrical. Under dry conditions a certain amount of interfacial failure between plasma polymer and adhesive can be deduced from the Al and especially the high Si signal on the metal-side with little Al on the adhesive side. The appearance of Si on the adhesive side suggests some additional fracture of the coating. Upon contact with water, the fracture path appears to move further into the oxide, causing high Al concentrations on both sides and an enhanced Si signal on the adhesive side. Apparently water injection does not only weaken the interface but can also instantly weaken the oxide layer. The observed interfacial and oxide failure explains the low average peel strength measured. Both effects are intensified by the presence of water at the interface that reduces peel strength values even further. However, it should be considered that roller peel testing is a very harsh test and that peel loads are normally avoided design-wise. Nevertheless, adhesion between aluminium oxide and silica plasma film appears very strong, as it is never the locus of failure. Comparing plasma and solution derived films, the wet-chemical films appear to bond more strongly to the epoxy polymer, which is, due to their largely organic nature, not unexpected.

In brief, the expected distinct dependency of joint performance on the surface pre-treatment processes could be demonstrated for the silane as well as for the APPJ coated adherends. This dependency is mostly caused by the differing topographies that are essential for the state of stress at the interface. The excellent bonding between aluminium oxide and plasma polymer is confirmed, whereas the interface to the epoxide appears to be slightly weaker when compared to the solution based treatments. Nevertheless, 100 % cohesion failure and a peel strength similar to state of the art anodising techniques is achieved with GPS and TEOS derived plasma films in combination with alumina grit-blasting in dry and wet testing. Thus, the main adhesion requirement for bonded aerostructures is fulfilled. Work on different abrasion techniques for the silane and sol-gel treatments show that alternative mechanical abrasion techniques to grit-blasting, which is not the preferred pre-treatment for in-service repair, achieve similar results [33], [34]. It is likely that those techniques combined with APPJ-CVD would lead to satisfactory results; determining this, however, lies beyond the scope of this thesis.

Despite the injection of water in the bondline, peel testing can only differentiate between initial interphase stabilities, involving high stresses. Ageing of joints by continuous exposure to moisture or other

environments with or without application of loads has not been considered yet. This highly important aspect of joint performance must be investigated in detail and will be discussed in the following chapter.

4.3 Durability of bonded joints

Safe use of adhesive bonding in aeronautics requires stability of bonded joints in many different hostile environments, like temperatures reaching up to 80 °C and -55 °C, or immersion in aggressive low-pH hydraulic oil or aircraft fuel [11]. Moreover, the joints have to withstand hot and humid conditions as well as corrosive fluids, like Bilge solution, which is an electrolytic condensation product that congregates at the bottom of the fuselage. As not all these requirements can be tested within this thesis, the focus is directed towards the resistance against moisture at elevated temperatures and the resistance against corrosive atmospheres. Aircraft fuel and hydraulic oil mainly degrade the polymer and not the metal adherend [153]; as a resistant qualified adhesive is used in this thesis, immersion in such organic liquids does not need to be considered.

Hot-wet exposure is widely used in literature as major test to determine durability of joints. The immersion in a corrosive atmosphere is not very common in academia, but it represents the most critical requirement for adhesive bonding in aircraft industry. In the past, corrosion induced failures have even endangered the whole technology and led to the development of the anodising processes used today. With aircraft service-lives of up to 30 years and service inspection intervals of major structures of more than 5 years, the selected test criteria need to be harsh in order to simulate service-life in an accelerated manner. Furthermore, it is important to additionally combine stress and degrading environment at different levels – the combinations applied here range from close to service load conditions combined with exposure to water, up to exclusive exposure to very aggressive salt fog. Performing accelerated ageing tests indeed bares the risk of the mechanisms not being the same as in real service.²³ Therefore, this concern must be kept in mind when carefully choosing test conditions that should always be compared to standard tests with proven validity.

Exposure of bonded test coupons to water and humidity corresponds well to in-service conditions, where both humidity and elevated temperature occur. Moreover, ageing in moist atmospheres has been extensively studied: Abel et al. have for example shown that there is a threshold for humidity impact of approximately 55 % rh for aluminium-epoxy joints [164]. Below 55 % rh, degradation does not occur, whereas above this limit, joint deterioration proceeds – a process that is typically associated with a change of locus of failure from cohesion to apparent interfacial. For this reason, the humidity level in accelerated testing has to lie above this threshold. Humidity levels of 95 % rh or above and immersion in water are the most common test conditions. For simulation of a corrosive attack, an accelerated ageing in salt fog, the so called salt spray test (SST), is widely used and has been successfully correlated to in-service failure of bonded Al-joints in aeronautics [4].

The following chapters focus not only on the durability of APPJ-CVD treated joints in humid and corrosive atmosphere, but will also highlight the behaviour of joints coated with reference silane/sol-gel films. In most publications, only wedge tests at high humidity have been carried out, where silane based coupling films are known to perform well. Investigations on durability during exposure to corrosive atmospheres are however not very common and all corresponding mechanism studies were solely conducted with anodised or CSA pickled substrates. Therefore, both plasma derived and wet-chemical references are examined in equal measures.

²³ “When did boiling an egg ever produce a chicken?” [1]

4.3.1 Interface stability under external loads and aqueous attack

Certain influence of moisture on the integrity of adhesive joints has already been observed during wet roller peel testing. Still, its impact is limited to joints that display at least partly interfacial failure already before water injection. If interface stability reaches a certain level, water cannot access the interface and cause delamination; thus, a distinction of joint stability upon contact with water is not possible anymore. Moreover, this test does not provide information on the long-term damage mechanisms, like hydration of the oxide, plasticisation of the adhesive or disruption of bonds at the interface [79], [214]. Despite the postulate of covalent Al-O-Si bonding, these bonds are susceptible to hydrolysis due to their strong ionic character [215]. Weaker bonds, like acid-base or van-der-Waals interactions are even more sensitive to aqueous attack. As the overall aim of this dissertation is to assess surface preparations of aluminium adherends, it is important for the employed tests to target the stability of the interphase region and not the adhesive. Peel testing is a useful indicator, but it only determines the maximum joint strength under peel loads, whereas, in reality, bonded joints are exposed to significantly lower loads but over a longer period of time. Hence, different load levels and immersion times are combined in the following two chapters. Only one surface pre-treatment, grit-blasting, is considered, because etching will not lead to sufficient joint strength.

4.3.1.1 Interface stability under cyclic loads and immersion in water

Fatigue testing under cyclic loads is a common method to simulate stresses occurring over a complete service life. Most of the tests are performed in dry conditions, i.e. at low relative humidity. Even at low humidity, cyclic loading is known to have a significant larger damaging effect on adhesive bonds than static loading [164], [216]. Improved fracture behaviour due to silane treatments has also been demonstrated by using fatigue testing in dry conditions [164], [217]. However, dry testing does not correspond to the hostile conditions that occur during a complete lifecycle. The high fatigue resistance of the polymer and the associated common practice of dry fatigue testing under high loads are even considered as problematic by the FAA. On the one hand, design requirements ensure that cohesion failure does not occur in service, on the other hand, standard fatigue testing targets exactly at this failure type [68], [218]. Hence, joint alteration in humidity must be considered, especially as the interphase region of the metal joint is susceptible to aqueous attack [79]. It has been repeatedly demonstrated that the fatigue performance of adhesive joints decreases significantly in the presence of water [69], [79], [216], [217], [219].

Unfortunately, a standardised dynamic test in a moist environment does not exist, so the first objective of this chapter is to identify suitable and meaningful test conditions. Tapered double cantilever beam (TDCB) testing is frequently applied to ascertain the mode I fracture energy of the adhesive and to assess the surface preparation of the adhesively bonded joints. Yet, this method includes initial cracking followed by observation of crack growth, which is not corresponding to service conditions, since it neglects the step of crack formation.

Single lap shear joints (SLJ) are an alternative and have also been tested in high humidity or water [217], [219], [220]. The absence of the initial crack and the shear loads allow better alignment of the test with service life conditions. With these coupons, aqueous attack is less strong compared to the mode I (crack opening) tests, as water ingress can only occur along the edges. This means that test conditions must be chosen carefully in order to avoid that the adhesive itself fatigues before moisture induced degradation of the interface occurs. There are different ageing environments reported in literature, where immersion in water is the most common method [79], [163], [164], [217], [220]. High humidity has also shown to have a significant detrimental effect [164], [219]. Whether high humidity or water immersion is more severe, is not fully clarified: Kinloch et al. have demonstrated higher deterioration of aluminium/epoxy joints upon full immersion, as compared to 100 % rh, when testing monotonically loaded TDCB specimens [162], whereas Abel et al. found slightly lower fracture energies for silane treated joints at 100 % rh than for

immersed ones [164]. Ageing in water is normally carried out in the room temperature region up to 30 °C [79], [163], [164], [217] or at 50 °C [220], [221]. 50 °C allows faster penetration of the interface. It is not assumed that the debonding mechanism change significantly between RT and 50 °C, so this temperature is often used in standard tests and can be permitted for accelerated testing (even if not displacement but hydration is the failure cause). An extensive investigation of aluminium oxide formation in water by Alwitt has shown that the hydration mechanism is similar in a temperature range from 20 to 90 °C; it is only the rate that increases with temperature [51].

The test configuration employed here consists of SLJs immersed in 50 °C deionised water during cyclic testing in order to simulate service life loads in combination with aqueous attack.²⁴ Underhill and DuQuesnay showed that there is a fatigue limit even for only grit-blasted aluminium-epoxy joints at maximal fatigue stress of approximately 10 MPa in dry test conditions. This means that no damage occurs in the joint below that maximal stress level. In wet conditions, no such lower limit was detected. However, due to the geometry of the samples employed, they could not apply maximal fatigue stresses below 8 MPa, because failure occurred first within the adherend in these cases [217]. A similar geometry-dependent lower threshold of maximal fatigue loads was found by Shenoy [222]. Consequently, to avoid failure of the aluminium base material, when applying only low maximal fatigue loads, the thickness of the adherend needs to be increased. A relatively low load level is necessary, because the discrepancy of dry and wet testing decreases with increasing loads and the proportion of unwanted cohesion failure increases [217]. A similar trend was observed by Rushforth and co-workers, who detected that high bending moments above 14 MPa influence the fracture path, moving towards more cohesion failure. Contrarily, clear distinction between dry and wet, as well as between silane coated and untreated specimens, was achieved with low maximum loads, like 4 MPa (without failure in the base material) [219]. Moreover, high loads (30 to 80 % of the static strength) indeed reduce fatigue life and, thus, test time, but they do not represent real life conditions where up to 10 million cycles with smaller loads occur.

These findings clearly show that it is mandatory to apply only moderate loads (below the dry fatigue limit) to truly evaluate the impact of moisture on the interface and, consequently, the quality of the surface preparation. Moreover, a high number of load cycles is required to allow interface damage to proceed and to realistically simulate service life. Therefore, testing is conducted at a constant maximum fatigue load of 1.2 kN, which corresponds to an initial shear stress of 6 MPa (< 20 % of static strength) with a joint overlap of 200 mm², until 10⁷ fatigue cycles are reached. The relatively small overlap of 8 mm at a sample width of 25 mm is chosen to avoid higher loads causing failure in the 1.6 mm thick base material. Despite their common use as test coupons to evaluate performance of adhesive joints and their simple joint geometry, SLJs obtain a rather complex multi-axial stress state during testing [223]. Nevertheless, the configuration and loads employed here produce relatively low stress levels in the adhesive itself but are demanding for the interface. Underhill and DuQuesnay did not detect any dependency of fatigue life on the test frequency. For this reason, a relatively high frequency of 25 Hz is used in this work.

Contrary to the frequency, the load ratio R , i.e. the ratio of minimal to maximal applied load, was found to have a distinct impact on fatigue life and locus of failure. For the used FM 73 adhesive, Khoramishad and co-workers demonstrated that the fatigue life is approximately 50 times higher if $R = 0.5$ compared to $R = 0.1$, where the proportion of near-interfacial failure is significant higher [224]. It seems like test results for high load ratios are influenced more by the characteristics of the adhesive and less by the stability of the interface. Consequently, $R = 0.1$ is employed for all dynamic single lap shear tests.

Similar to the work carried out by Briskham and Smith, three specimens are mounted in a row, forming a string, and tested simultaneously [220].²⁵ After 10⁷ load cycles are reached, the specimens are dried allowing complete moisture desorption and then tested quasi-statically at a constant displacement rate of 0.1 mm/s, which allows further differentiation of the employed surface preparation processes.

²⁴ Crack growth upon mode I loading and environmental influence will be considered in static testing in the following chapter.

²⁵ For more information on test set-up and joint geometry please refer to chapter 3.2.

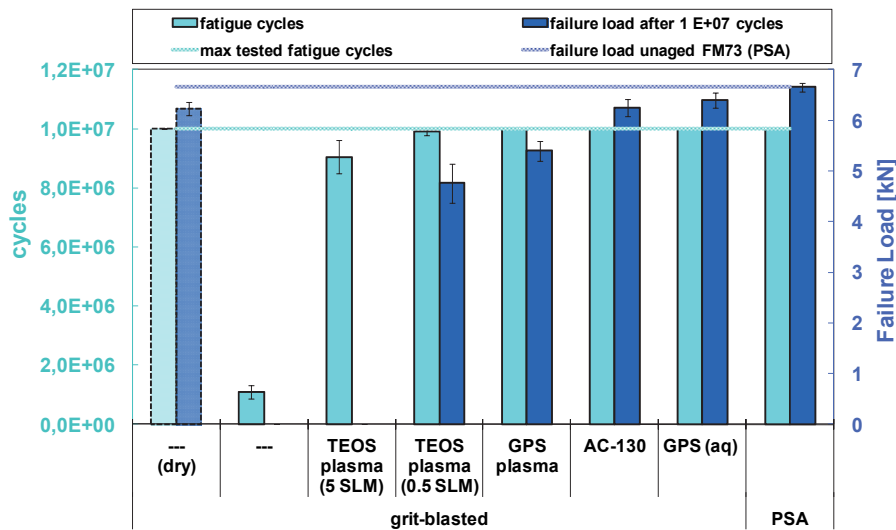


Fig. 4.20: Accomplished load cycles of dynamic lap shear testing (F_{\max} 1.2 kN, $R = 0.1$) of AA 2024 clad specimens in deionised water (50 °C) and quasi-static failure load after tested (dried samples).

All tested specimens are made of AA 2024 clad. Due to the good results achieved in the wet peel-test, only alumina (50 μm) blasting is chosen as surface pre-treatment before coupling film deposition. Once again, GPS and TEOS based plasma films are compared with the solution derived references GPS and AC-130. This time, samples coated with 5 SLM TEOS plasma films are tested additionally to investigate any potential influence of film thickness and its associated increased barrier properties. PSA is used as absolute reference. Dry testing (without immersion in water) is only performed for the solely grit-blasted samples, which are known to be the weakest of all considered joints, to confirm that test conditions are below the dry fatigue limit.

The results obtained on fatigue life cycles and quasi-static failure load are displayed in Fig. 4.20. Indeed, the required load cycles are reached in dry condition and the residual strength after testing is similar to a not fatigued sample, almost reaching the level achieved with anodised adherends. Yet, upon immersion in water at 50 °C no such fatigue limit is detected for grit-blasted samples and the measured fatigue life is approximately one order of magnitude below the required load cycles. This deterioration is expected and consistent with other published results [79], [164].

In general, the results obtained with coated adherends reveal a significant impact of the coupling films: All films largely improve fatigue life of the joints when compared to untreated ones. The specimens treated with the reference systems GPS and AC-130, as well as GPS plasma deposition, achieve the required 10^7 load cycles. Of the TEOS (0.5 SLM) plasma treated samples only two out of three reach the preset limit, while one fails shortly before (9.72×10^6), in contrast, all samples coated with the approximately 55 nm thick TEOS based plasma polymer fail to reach the limit. Thus, the employed test configuration allows a clear distinction between surface preparations even after short exposure times (< 5 d) due to dynamic loading. Unstressed samples do not reveal any damage after similar immersion intervals, which is coherent with the low diffusion rate of FM 73 determined by Mubashar and co-workers [221]. Diffusion through the adhesive alone cannot explain the large water ingress and the associated delamination that occurs during testing (Fig. 4.21). This means that the chosen combination of dynamic loads and water immersion specifically harms the interphase region.

To further assess the performance of the coupling films, samples are pulled to failure after the test. Since the aim is to display the area of delamination, i.e. the part of the interface that is irreversibly damaged, samples are allowed to dry for several days before forced water desorption at 50 °C, in order to avoid reversible wet-testing effects. FM 73 is known to completely recover upon drying [221].

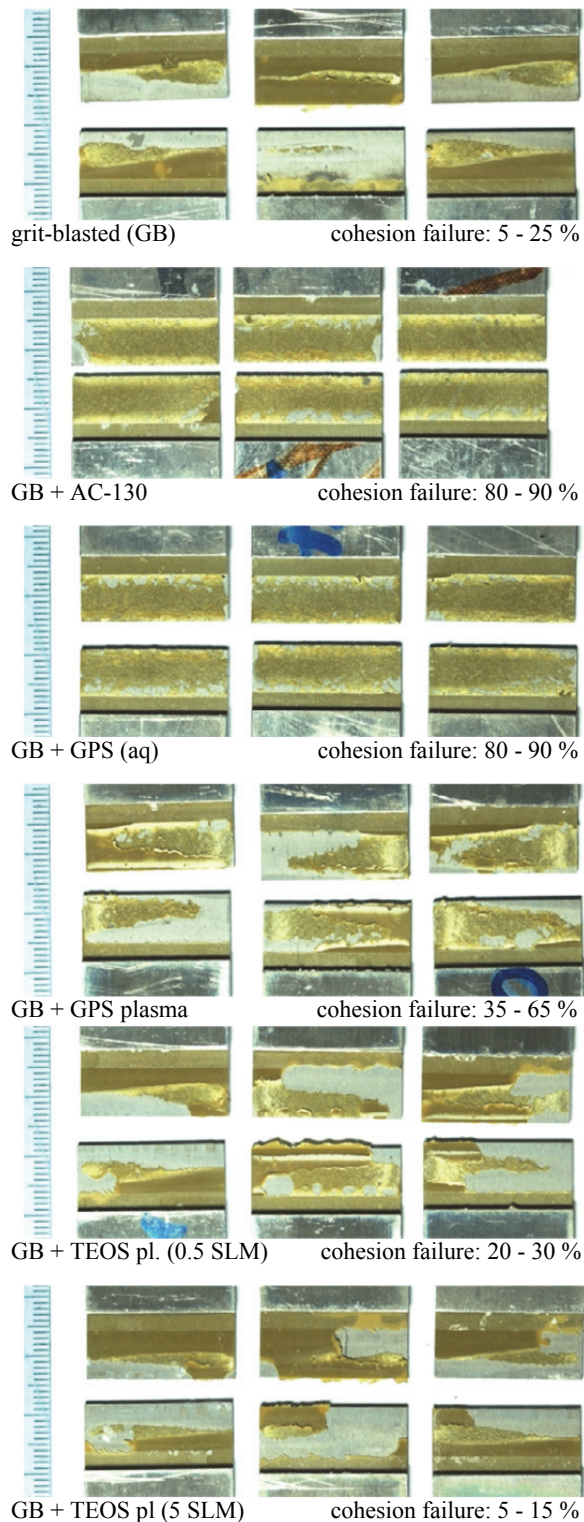


Fig. 4.21: Fracture surfaces of AA 2024 clad joints after dynamic (DI water, 50 °C) and quasi-static (dry) tensile testing

In terms of the quasi-static failure loads, AC-130 and GPS treatments lead to quite similar joint strengths almost on anodising level, whereas failure loads for all the GPS plasma treated samples and the two remaining 0.5 SLM TEOS plasma treated samples are clearly lower. The residual shear strengths of the joints with GPS based plasma films are slightly higher than the ones obtained with TEOS based films, which supports the results of chapter 4.1.3, where stronger bonding of the GPS plasma film to the adhesive is detected. PSA does not show any deterioration upon testing, and after drying the same shear strength as in unconditioned state is achieved. The measured shear strength of 33.3 MPa is significantly lower than the values provided by the manufacturer (46.1 MPa [212]), but is in the range reported in other publications [221], [224]. Moreover, different single lap shear sample geometries are used in each case, strongly influencing the values measured.

Despite relatively high failure loads, distinct delamination occurs for all except the anodised specimens. Fracture images of the coated joints are displayed in Fig. 4.21,²⁶ showing that delamination advances for all samples from the open edges towards the centre. It is clearly visible that the size of the central, unharmed, area depends strongly on the coupling film. The silane and sol-gel treated joints show only approximately 10 to 20 % of apparent interfacial failure, whereas those with plasma films are highly delaminated. The inferiority of APPJ-CVD treated samples is even more pronounced when compared to the residual strength test. Specimens coated with the thicker TEOS derived plasma polymer, which failed during fatigue testing, are almost fully delaminated. The ratio of apparent interfacial failure is quite similar – if not higher – to the solely grit-blasted specimens (but after significantly more load cycles). Judging from the proportion of the delaminated interface, this area apparently still contributes to the joint strength, because the remaining area of cohesion failure should not be sufficient to withstand the applied load right before failure. The thinner TEOS plasma polymer coatings lead to a moderate increase in cohesion failure, but still display interfacial failure up to 80 %. Once again, the GPS

²⁶ Fracture images after dynamic or quasi-static lap shear testing (depends on whether failure occurs before 10^7 load cycles or not).

plasma film outperforms the TEOS derived one. Still, on average, more than 50 % of the fracture area is apparent interfacial.

In order to ascertain the precise locus of failure of the coated samples, the areas of apparent interfacial failure are analysed by XPS. Elemental composition of the fracture planes on metal and adhesive sides are shown in Table 4.14. Corresponding spectra are displayed in appendix Fig. A.20.

Table 4.14: XPS elemental analysis results [at.%] and fracture analysis of AA 2024 clad (grit-blasted) adhesive joints treated with different coupling films after dynamic lap shear testing immersed in DI water at 50 °C

	side	C	N	O	Na	Al	Si	Zr	interfacial fracture type
GPS (aq)	m	76.83	0.59	19.35	-	-	3.23	-	mostly cohesion-near-interface partly fracture of film
	a	80.78	0.64	14.7	0.36	trace	3.14	-	
AC-130	m	57.22	1.05	30	1.6	8.5	1.44	0.18	fracture of film close to oxide partly cohesion-near-interface
	a	82.89	0.94	14.63	0.14	-	1.41	trace	
GPS Plasma	m	51.45	1.36	35.66	0.14	8.17	2.95	-	varying fracture path: partly fracture of interspersed oxide/film partly cohesion-near-interface
	a	66.84	1.67	25.18	0.35	1.75	4.21	-	
TEOS Plasma (0.5 SLM)	m	51.45	0.28	31.36	3.45	5.33	8.14	-	mixed fracture: film fracture & interfacial film-adhesive some cohesion-near-interface
	a	75.36	1.34	18.48	1.06	0.2	3.55	-	
TEOS Plasma (5 SLM)	m	30.36	0.7	45.62	3.84	0.49	18.99	-	interfacial film-adhesive partly film fracture
	a	77.22	1.04	17.18	-	-	4.56	-	

Silane treated samples show the highest carbon content on the metal side indicating cohesion failure near the interface. Distinct silicon signals are found on both sides, suggesting that failure occurs also inside the coupling film. Thus, the fracture path is likely to pass from the adhesive to the film and vice versa. The lack of Al on the metal side shows that only the upper region of the film is fractured, while the interface to aluminium oxide is not affected. The XPS overview spectra confirm this finding: Both spectra are similar except for a higher oxygen peak detected on the metal side, which is due to higher oxygen concentration in the cross-linked coupling film.

Fracture surfaces of the sol-gel treated specimen differ slightly. Strong aluminium and oxygen peaks appear on the spectrum of the metal side, which indicates that failure occurs largely close to the oxide. Nevertheless, the carbon and nitrogen signals on this side suggest that part of fracture happens within the adhesive, although certainly to a lower extent than for the GPS treated specimens. Again, Si is found on both sides pointing to film rupture. Liu et al. observed similar fracture behaviour with crack growth through the sol-gel layer when using asymmetric double cantilever beam test in high humidity. It was also shown that the hardener of the adhesive can diffuse into the sol-gel coating, which explains the relative high nitrogen signal on the aluminium side [131]. Surprisingly, the intensities of the Si and the Zr peaks are very low on both sides. It is assumed that the film is ruptured and only residues of the film remain attached to the adhesive and the Al-oxide. Major parts appear to be removed either by the water during dynamic testing or upon quasi-static joint opening.

Film fracture occurs also for the GPS plasma treatment as Si signals are strong on both fracture sides. Due to the interspersed character of film and oxide, the fracture path permeates both. Distinct aluminium and oxygen signals are visible on the adhesive side, indicating this oxide rupture. On the other side, the relatively high carbon and nitrogen concentrations suggest cohesion failure. Thus, the resulting fracture type is rather complex, permeating adhesive, coupling film and aluminium oxide.

Film and adhesive fracture also occurs on the sample covered with the thin 0.5 SLM TEOS film. Aluminium is hardly detected on the adhesive side, which proves that the fracture passes along the silica film above the Al-oxide. As the nitrogen concentration on the metal side and the oxygen concentration on

the adhesive side are relatively low, the proportion of cohesion-near-interface failure is certainly lower when compared to the GPS plasma treatment. This factor, in addition to the significantly more intensive Si signal on the metal side, also reveals a certain amount of adhesion failure between coupling film and adhesive.

This trend is more distinct with the 5 SLM TEOS treatment. Low carbon and nitrogen as well as high oxygen and silicon concentrations on the aluminium side clearly indicate adhesion failure between plasma film and polymer. It is therefore assumed that higher film thickness, on the one hand, enhances the integrity of the plasma film and, on the other hand, reduces the nano-texture leading to more interfacial failure. Some film fracture is likely to occur as well, which is coherent with the SEM investigations presented in chapter 4.1.3, where fractured fragments of the film were found to be detached from the metal surface. Nevertheless, most part of the film remains attached to the aluminium oxide.

These XPS results confirm that the interface between plasma polymer and adhesive must be considered as weaker compared to the interface to the aluminium oxide. Again, the epoxy adhesive adheres better to the GPS derived plasma film than to the TEOS based coatings.

In conclusion, the constant maximum load fatigue test applied here allows a fast and precise differentiation between effective surface preparations under realistic load conditions with a specific attack of the interface. The dynamic stress acts like a “pump” accelerating the ageing of the interphase region. The full recovery of unstressed FM 73 SLJs after drying [221] does not occur with the employed test method, which confirms that a combination of stress and exposure to aqueous environments has to be considered. The obtained results also confirm the need to deposit a coupling film. APPJ-CVD highly enhances the fatigue life of grit-blasted joints in water. With GPS plasma deposition, the required 10^7 load cycles are achieved. However, fatigue performance with the applied plasma coupling films is inferior to the solution derived films due to weaker bonding to the epoxy adhesive. Upon immersion in water, no fatigue limit is detected. Still, it is reasonable to stop the test at the required load cycles to avoid failure of the base material and to differentiate by determination of the residual joint strength in dry conditions. Despite the realistic load conditions, the immersion in water at 50 °C is very harsh and does not fully comply with real service conditions. Both dynamic loading and immersion in water strongly harm the polymer-metal interphase, but they are not representative for long-term degradation of the oxide. Thus, further investigation with increased exposure periods needs to be performed and is subject of the subsequent chapters.

4.3.1.2 Interface stability under permanent load in a hot-wet environment

Wedge (or cleavage) testing is a standard (ASTM 3762, DIN 65448) method to assess the durability of adhesive joints by measuring the crack propagation along the bondline in a hot and humid environment after insertion of a wedge that creates very high tensile stresses perpendicular to the bondline (mode I). The initial crack stops where the tensile stresses are right below tensile ultimate of the adhesive. Thus, the interface is under extreme stress and any weakening or damage of the interface will result in interfacial failure [14]. After insertion of the wedge into the bondline, the crack length is measured after 24 h in ambient dry conditions (initial crack). Then, crack growth is ascertained over exposure time in the hot-wet environment (50 °C, 96 % rh). More test details are provided in chapter 3.2. Wedge testing has proven to be a good indicator for long-term durability of adhesive bonded joints of anodised adherends. Moreover, Underhill et al., who compared wedge test results with dynamic single lap shear testing in dry conditions, found that wedge testing is an accurate predictor of fatigue life of silane treated joints [225].

The actual load at the crack tip is strongly depending on the crack length. At the beginning, this method could be considered as a very intensive wet adhesion test with high loads and short exposure times, allowing a fast evaluation on the stability of the stressed interphase region upon aqueous attack. With prolonged exposure to humidity increased ageing effects are likely to occur. However, at that time stress levels of the different samples diverge due to different crack lengths.

Silane and sol-gel treatments are known to improve the cleavage resistance of grit-blasted aluminium alloys significantly; even anodising level is reached in some tests [105], [106], [188], [193]. To the author's knowledge, no data on wedge test performance of APPJ-CVD treated adherends is available.

Fig. 4.22 presents the crack lengths for 5 SLM GPS and 0.5 SLM TEOS plasma coated specimens in comparison with the silane and sol-gel treat as well as untreated (solely grit-blasted) substrates. All coupling films are deposited on alumina blasted AA 2024 clad, while PSA acts as reference system.

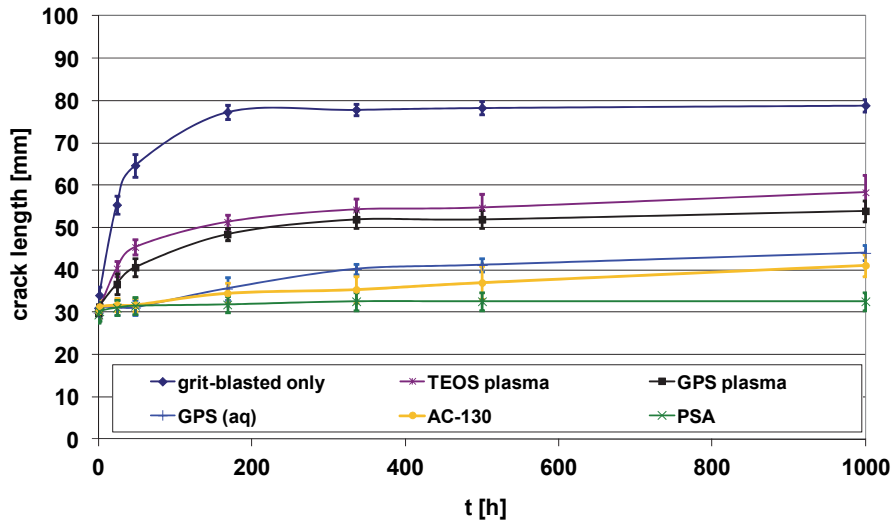


Fig. 4.22: Crack lengths of AA 2024 clad joints (FM73) in wedge test at 50 °C and 96 % rh

The average initial crack length through the adhesive (cohesion failure) in dry conditions is around 29 to 30 mm for all joints except for the solely grit-blasted joints (31 mm). Upon exposure to high humidity, cohesive crack growth within the adhesive of approximately 1 mm length is observed already after 75 min for all specimens, except for the solely blasted samples (≈ 3 mm), where the failure is interfacial. This difference between the untreated and coated specimens increases further with time. Distinct discrepancies between the coated joints become evident already after 24 h. While the joints treated with the solution derived coupling films continue to fail cohesively, the locus of failure changes for the plasma coated samples to interfacial. Similar change in locus of failure is observed for the silane and sol-gel coated samples after one week (168 h). At that point in time, crack propagation of solely grit-blasted joints has already reached a limit, where the stress level no longer critical and further crack growth rates are very low. APPJ-CVD still significantly improves cleavage resistance in comparison to no treatment but cannot match the reference treatments. Beyond 168 h of exposure, crack growth rates diminish, and propagation continues at a low speed. The silane and sol-gel coated systems display significant crack growth up to 336 h before growth rates decrease. Total crack length remains largely below those obtained with plasma deposition. Similar to previous tests, GPS derived plasma films perform better than TEOS derived plasma layers. The performance of AC-130 and GPS is again quite similar with a tendency towards lower crack lengths with AC-130, but differences are still within the deviation. PSA is the only surface preparation where the fracture path remains in the adhesive and which reaches a true threshold where no further crack propagation can be observed. All other samples fail at the interface and the crack continues to propagate with time – although at very low rates. Fracture images of the specimen after > 1000 h exposure are shown in Fig. A.21. When considering the associated fracture energies, the differences become even more distinct.

The fracture energy G_I [J/m^2] can be calculated using the following equation [226], [227]:

$$G_I = \frac{Y^2 E h^3 [3(a + 0.6h)^2 + h^2]}{16[(a + 0.6h)^3 + ah^2]^2}$$

where a is the crack length, E the Young's modulus of AA 2024 (73 GPa), h the thickness of the adherend (3.2 mm) and Y the crack opening displacement, i.e. the thickness of the wedge (3.2 mm). Fracture toughness values for the employed systems corresponding to the crack length displayed above are shown in Table 4.15.

Table 4.15: Fracture toughness of AA 2024 clad wedge test specimen (FM 73)

	Fracture Energy G_I [kJ/m ²]									
	Initial (24 h dry)	75 min		24 h		168 h		1000 h		
grit-blasted (GB)	3.85	+0.92 -0.71	2.73	+0.74 -0.55	0.424	+0.070 -0.058	0.116	+0.010 -0.0094	0.108	+0.0079 -0.0072
GB + GPS (aq)	4.42	+1.0 -0.80	3.83	+0.95 -0.73	3.83	+0.95 -0.73	2.30	+0.81 -0.56	1.03	+0.18 -0.15
GB + AC-130	4.26	+0.86 -0.69	3.71	+0.84 -0.65	3.52	+0.75 -0.59	2.58	+0.80 -0.58	1.34	+0.37 -0.27
GB + GPS plasma	4.46	+1.1 -0.82	3.71	+0.73 -0.58	2.06	+0.61 -0.45	0.710	+0.092 -0.079	0.469	+0.096 -0.076
GB + TEOS plasma	4.56	+1.3 -0.94	3.97	+1.2 -0.86	1.43	+0.26 -0.21	0.569	+0.078 -0.067	0.347	+0.11 -0.079
PSA	4.67	+1.4 -1.0	4.26	+1.5 -1.0	3.83	+0.98 -0.75	3.50	+0.90 -0.68	3.21	+0.93 -0.69

In summary, it can be stated that wedge test results confirm the data obtained from fatigue test in water. Despite a clear improvement in durability compared to solely grit-blasted specimens, the interface stability of plasma coated systems is significantly lower than that of solution treated samples; none of the local processes matches the performance of PSA. Crack propagation happens mostly in the first one to two weeks of exposure before crack growth rates decrease drastically. Hence, the test is well suited to evaluate the stability of stressed interfaces upon aqueous attack. However, it does not represent typical loads occurring in service; wedge test results not always correlate with actual service experience [10]. Moreover, this test does not provide sufficient information on potential degradation of either oxide or film during service life. Therefore, longer ageing intervals and exposure to more aggressive, corrosive environments will be examined in subsequent chapters.

4.3.2 Long-term stability in hostile environments

The analysis of long-term stability of the employed Si-based treatments is mostly performed without application of loads in order to avoid potential interference of load-induced degradation of the interface with the one caused by the environmental conditions. Two different ageing conditions are chosen, namely the exposure to neutral salt fog (5 % NaCl) at 35 °C and the exposure to 100 % rh in a condensation water test at the same temperature. The salt spray test (SST) of specially prepared test coupons (chapter 3.2) is one of the most critical durability tests for adhesive bonded joints and has proven to simulate the corrosion damages that occur in-service in an accelerated manner [2]. The associated anodic degradation mechanism is referred to as “bondline corrosion” and has been thoroughly investigated for anodised aluminium substrates [2], [171]. The test itself is normally referred to as “bondline corrosion test”. It is worth mentioning that the state of the sample edges plays a significant role in this test. The specimens are cut using a band saw that creates rough edges with small defects that act as starting point for corrosion or delamination.

In order to distinguish the influence of chlorides from the damages that originate from mere moisture, the second test is chosen to create similar conditions apart from the presence of NaCl. As oxide properties are known to have a distinct influence on long-term stability, different surface pre-treatments are used again.

Moreover, both clad and bare aluminium sheets need to be employed, as their respective ageing behaviours can differ significantly. Cladding is known to have a significant impact on the intensity of bondline corrosion [2], [171] due to the galvanic cell formed at the coupon edge between the base alloy and the pure Al sacrificial anode. In mere humidity both substrates are supposed to behave similarly.

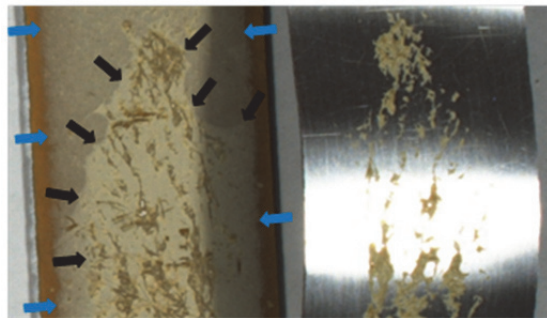


Fig. 4.23: Fracture surfaces of AA 2024 bare (Smut-Go NC) after 30 d at 35 °C, 100 % rh
black arrows: delamination front
blue arrows: oxide degradation front

In the following chapters, the behaviour of GPS and TEOS APPJ-CVD treated joints are compared with GPS and AC-130 coated, as well as with untreated samples. After this evaluation, conclusions on the potentially different degradation mechanisms will be drawn. In this instance, 5 SLM TEOS feed flow is used instead of 0.5 SLM in order to determine eventual film thickness effects and to be able to observe film changes with SEM. Typically, bondline corrosion testing of anodised samples coated with a highly chromate loaded bonding primer lasts up to 300 d. The systems employed here already display significant differences after less than 45 d, which is, consequently, chosen as maximum test interval. After exposure to both humid

and corrosive conditions, the joints are opened manually and the degraded area is analysed. As the failure mode is often not 100 % cohesive, especially after manual opening (high-angle peel of wet samples), the fracture surface needs to be carefully inspected to allow a distinction of the truly damaged interface from the unharmed interface that fails interfacially during the opening of the joint. Fig. 4.23 displays a part of the fracture plane of AA 2024 bare coupon pickled in Smut-Go NC after exposure to 100 % rh. Apparently almost the whole specimen displays adhesion failure. Nevertheless, not the complete interfacial area is affected by the ageing conditions. Examining the adhesive side, the delaminated areas (black arrows) can clearly be distinguished from the not degraded parts. Moreover, another colour transition is observed on the adhesive side, which is derived from transformation of the aluminium oxide (blue arrows). Depending on substrate, surface preparation and test conditions, the ratio of delaminated area to the one with oxide damages varies significantly and reaches up to 1 (no displacement occurs without oxide damage). In any case, delamination and oxide change are both considered as degradation of the interface and the percentage of the total damaged area is recorded after different exposure times.

4.3.2.1 Bondline stability in hot-wet conditions

The previously presented results of peel, wedge and cyclic lap shear tests have demonstrated the detrimental impact of moisture on the joint stability. In all of these tests, the presence of water or humidity aims at a weakening of the interface while loads are applied. For this reason and due to rather short exposure intervals (except for the wedge test), these tests are not fully adequate to assess the long-term stability of the interface against degradation. Yet, it is essential to consider potential changes of the oxide driven by thermodynamics in hot-wet environments when evaluating the durability of a joint, as these alterations may also lead to delamination and joint failure. Therefore, test samples with particularly rough edges are exposed to 100 % rh at 35 °C for up to 45 d without applying any loads in a condensation water chamber. After the test period, the percentage of the delaminated area is determined and the fracture surface is analysed. Fig. 4.24 compares the ratio of delamination after different surface treatments for AA 2024 bare and clad. Fig. A.22-24 display representative images of samples exposed to 100 % rh.

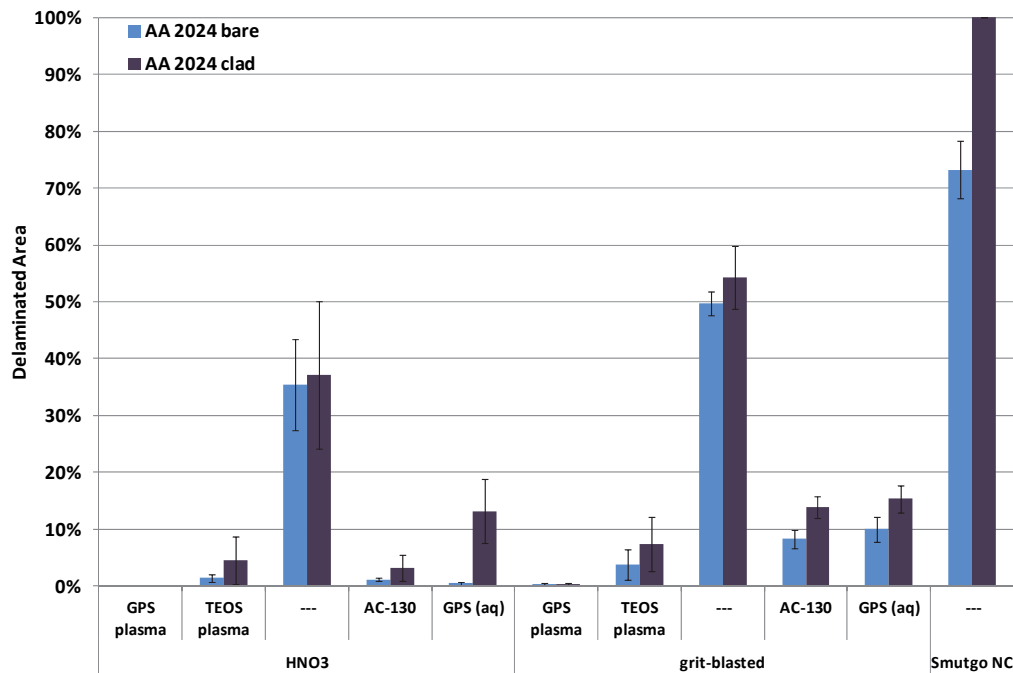


Fig. 4.24: Delaminated area of AA 2024-FM 73 joints after 45 d exposure to 100 % rh, 35 °C

When assessing the results of all three surface pre-treatments employed (grit-blasting, HNO₃ and Smut-Go NC pickling), distinct delamination is apparent for each of them. The mere presence of humidity at elevated temperature is sufficient to displace the secondary polymer-oxide bonds. Bulk diffusion through the FM 73 adhesive is relatively slow [221] and cannot explain the high level of delamination of the joints observed within several days, which means that moisture ingress happens along the interface. A comparison of the conditioning techniques reveals a trend of HNO₃ pickled surfaces forming more stable interfaces with the epoxy than grit-blasted and especially Smut-Go NC pickled surfaces. The thicker oxide with an open nano-



Fig. 4.25: Bondline corrosion detected on a Smut-Go NC pickled AA 2024 clad specimen after only 15 d exposure to mere hot-wet conditions (35 °C, 100 % rh)

structure appears to be advantageous compared to the macro-rough grit-blasted surfaces. For both methods, hardly any difference between bare and clad material can be observed, which is not surprising, because the formed oxides are quite similar. In case of Smut-Go-NC finished surfaces, the differences in oxide texture between bare and clad (as shown in chapter 4.2.1) are reflected in the results: delamination on the micro-rough bare oxides is significantly lower than on the smooth clad surfaces. The higher performance of the grit-blasted joints, whose oxides are smooth and of similar thickness, can be explained by the enlarged size of the interface area.

Moreover, Smut-Go NC pre-treated joints show a general tendency of being more prone to ageing and bondline corrosion (chapter 4.3.2.2). Fig. 4.25 shows clear macroscopic corrosion signs of a Smut-Go NC conditioned AA 2024 clad joint after only 15 d of exposure to humidity. Distinct corrosion after exposure to mere humidity is not expected, but its existence confirms not only the sensitivity of this desmutting technique but also reveals that the exposure to humidity can cause corrosion without the presence of salts in the DI water. It is assumed that dissolution of salts on the metal surface and a limitation of oxygen diffusion in the formed crevice, create a corrosive environment at the delamination front.²⁷ In sputter depth

²⁷ Limited oxygen diffusion through the electrolyte in a crevice reduces the pH (crevice corrosion).

profiling of Smut-Go NC etched bare substrates, a certain copper enrichment is observed right below the oxide (Fig. 4.14), which is likely to enhance corrosion as well. Moreover, XPS analysis of the elemental composition of the Smut-Go NC conditioned surface (Table 4.7) reveals a significant amount of fluorine which is thought to be a major cause of corrosion susceptibility. As the stability of the FM 73 adhesive is high, contribution from hardener components of the adhesive is not expected [2]. For the above mentioned reasons, Smut-Go NC pickling is not considered further as surface pre-treatment in combination with the coupling films. In any case, the strong impact of the surface condition on the bondline stability should be noted; pre-treatments must be carefully selected when evaluating or comparing the performance of coupling films or adhesion promoters.

A similar tendency of HNO₃ etching leading to slightly higher joint stability than grit-blasting is noticed when evaluating the stability of plasma and wet-chemical treated joints, in particular if silane/sol-gel coupling films are employed. This trend diverges from the results of the wet peel test, where blasting entails higher peel strengths than etching. This confirms that the peel test rather assesses the mechanical stability of the joint, i.e. its ability to dissipate energy, than to determine the stability of the polymer-metal interface. The absence of loads makes the positive effect of the mechanical interlocking and the associated stress reduction obsolete. Hence, the positive effect of the open nanostructure and the higher oxide thickness becomes more distinctive.

Another trend observed with the coated substrates is that delamination is lower on the bare alloy than on clad. Considering the deviation, this trend is however not always unambiguously detectable. It is certainly not expected, since the structure and composition of the oxide is relatively similar and the effect of humidity should be the same. As described in chapter 2.3.2, the dissolution of the sacrificial clad layer in corrosive atmosphere has a strong impact on the acidity in the crack and, thus, the degree of bondline corrosion. It is assumed that this effect occurs to some extent in mere humidity, but certainly not as distinct as in NaCl solution. However, the displayed results support only a tendency and not a distinct difference.

As shown in all the aforementioned chapters on durability, all used coupling films significantly improve the stability of the interface. Nevertheless, the trend observed here runs diametrical to the previous ones: plasma films suppress delamination to a higher extent than silane/sol-gel films. This difference is not visible on bare alloys pickled with HNO₃ as this combination of base material and surface pre-treatment is the most stable of all employed systems, but it becomes prominent on grit-blasted clad alloys (least stable combination). APPJ-CVD of GPS fully prevents any hydrodynamic displacement independent of bare/clad or surface pre-treatment. The superior performance of GPS compared to TEOS is consistent with the results obtained in the tests, which combine loads and aqueous attack, and can be correlated again to the previous XPS analysis that indicates more oxygen-functional groups at the film surface. However, adhesion between film and the epoxy polymer cannot be the only decisive criterion for joint integrity under these conditions, as the solution derived treatments have shown to form more stable interfaces with the adhesive than the plasma deposited films.

To explain the observed behaviour, further investigation of the fracture planes is needed. SEM analysis of the adherend oxide close to the delamination front reveals distinct differences between the plasma coated, the sol-gel coated and the untreated specimens (Fig. 4.26). In Fig. 4.26 a) the oxide of the solely HNO₃ etched clad adherend is shown. The delamination occurs straight at the polymer-oxide interface. No residues of the adhesive are visible. The image on the left displays the oxide at the crack tip. Shape and thickness are quite similar to the initial oxide formed with this etchant. Compared to the oxide of a non-aged sample (Fig. 4.12 f)), this oxide film appears to have already slightly²⁸ grown, while reducing its open texture. Directly behind the crack tip (middle of Fig. 4.26 a)), a certain oxide/hydroxide growth with some local variances is evident. This growth due to humidity and temperature first reduces the open pores of the oxide film before it enhances the overall thickness. The top view image of this region (right of Fig. 4.26 a)) reveals that these hydrated areas are unevenly distributed and that certain “lines” of hydration are formed.

²⁸ Beginning of oxide growth is difficult to distinguish from initial state due to resolution limit of the device.

Nevertheless, the degree of hydration appears to be rather low and to follow the crack tip. Therefore, it is assumed that the hydrodynamic displacement of the polymer causes crack propagation; hydration of the oxide and the base material is a post-failure event.

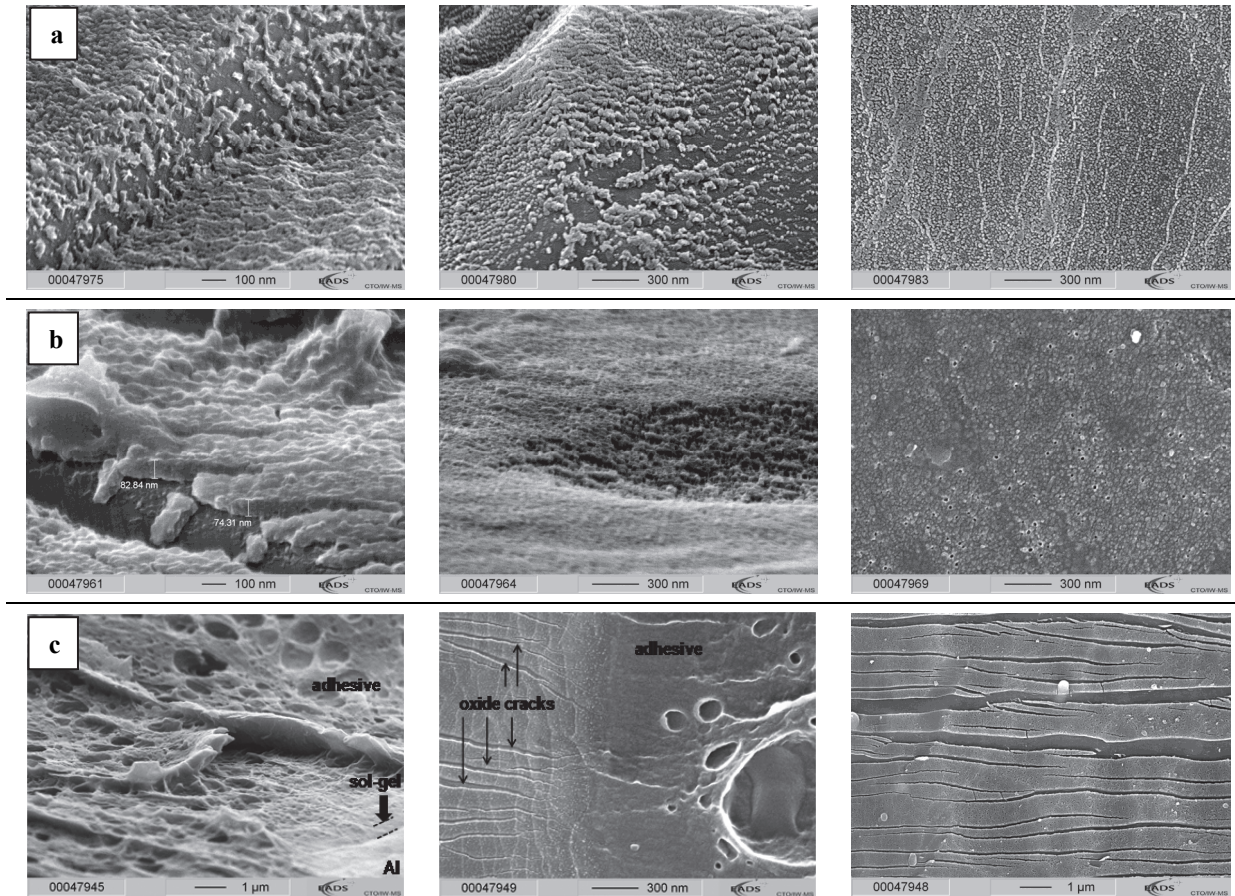


Fig. 4.26: SEM images (after cryofracture) of delamination front (left: at crack tip; middle: directly behind crack tip; right: inside crack) on AA 2024 clad specimens (HNO_3 pickling):
 a) uncoated b) TEOS plasma film (5 SLM) c) AC-130 after exposure to 35 °C, 100 % rh

Analogously, the crack tip region of a clad adherend coated with a 5 SLM derived TEOS plasma film is shown in Fig. 4.26 b). As for the solely etched samples, the adhesive delaminates from the oxide surface (in this case from the silica-like plasma film), while the plasma film remains attached to the aluminium oxide. Contrary to the uncoated aluminium oxide, the interspersed layer does not visibly change due to hydration. Layer thickness remains at the expected approximately 80 nm, i.e. no oxide/hydroxide growth by hydration is observed. Hence, the positive effect of the plasma films can be associated to the suppression of oxide hydration and to a reduction of hydrodynamic displacement; GPS derived plasma films reduce displacement more than TEOS based films, which is consistent with the previous chapters.

Despite a similar apparent interfacial failure, the failure mechanism for the AC-130 coated adherends diverges completely. The sol-gel coupling film does not remain on the oxide layer, but delaminates or fails very closely to the oxide. The left image in Fig. 4.26 c) reveals a direct fracture through the sol-gel film at the crack tip. Different than before, the sol-gel treatment leads to sharp transition from the intact joint – cohesion failure, i.e. adhesive remains on metal adherend – to the degraded area, where the sol-gel film is displaced from a hydrated oxide (middle of Fig. 4.26 c)). The distinct hydration can be seen from a lack of open oxide structure and from the visible cracking of the oxide during sample preparation which is an indicator for dense oxide/hydroxide films with thicknesses > 50 nm, i.e. significantly above the natural HNO_3 oxide. Cracking increases with distance from the delamination front (right of Fig. 4.26 c)) indicating

advanced hydration. Small craters are formed on the oxide film with continuing hydration, which is a first sign that hydroxide dissolution begins. Thus, it is very likely that hydration causes the delamination of the silane/sol-gel coupling film and not vice versa. Johnsen et al. detected that GPS derived coupling films are less stable in acidic than in neutral and alkaline pH media [228]. As a drop of pH at the tip of the crevice is assumed even in the relatively unaggressive humidity test, an enhanced desorption of the solution derived films is likely. The apparent higher extent of hydration at the delamination front of the sol-gel coated substrates (compared to uncoated ones) is very likely to be caused by suppression of hydrodynamic displacement and the accompanied increased exposure period of the oxide to the aggressive environment at the crack tip. Contrary to plasma coatings, the silane/sol-gel films cannot suppress the hydration of the aluminium surface below. EDX analysis support the SEM findings (see Table 4.16): different than with the plasma treated sample no Si signal is found on the delaminated surface initially coated with AC-130. Moreover, the oxygen signal is more pronounced and the Al signal is reduced for the sol-gel treated surface, which suggests significantly higher oxide/hydroxide thickness.

Table 4.16: EDX analysis of delaminated area of AA 2024 clad adherend after exposure to 35 °C, 100 % rh

	elemental composition [at.%]		
	HNO ₃ only	TEOS Plasma (5SLM)	AC-130
Al	72.3	75.0	62.3
O	9.5	11.0	26.0
C	18.2	12.9	11.7
Si	---	1.1	---

In conclusion, the exposure to this extreme humidity reveals two major failure causes: hydrodynamic displacement and hydration. Displacement appears to be less distinct than with the external loads of previous tests. In absence of a coupling film the hydrodynamic displacement proceeds without much influence of hydration. If plasma films are applied, hydration is fully suppressed and displacement is largely decreased. Contrarily, solution derived silane based treatments do not prevent oxide hydration, but strongly inhibit hydrodynamic displacement. The results confirm that the “weak” interface for plasma coated systems is between plasma polymer and adhesive, whereas it is between oxide and silane-layer for the aqueous silane deposition. Even if no loads are applied, coupling films are essential to reduce delamination. However, in absence of external loads the ability to protect the aluminium oxide from hydration becomes more important. Hence, the percentage of delaminated/degraded area is higher for solution derived films than for plasma coatings. As plasma deposition prevents hydration, the influence of the surface pre-treatment is insignificant if plasma deposition follows, whereas an impact is observed for silane/sol-gel treated specimens. With the resistance against hydration being more critical, the thicker, nano-structured oxide formed after HNO₃ pickling is superior to the grit-blasting oxide if solution derived films are deposited.

4.3.2.2 Bondline stability in corrosive atmosphere

The resistance against corrosion penetration along the bondline is probably the most challenging requirement for surface preparation techniques for adhesive bonding in aeronautics. Therefore, the behaviour of the plasma coated and silane/sol-gel treated joints in bondline corrosion testing represent one the main objectives of this work. Firstly, the degree of bondline corrosion is determined, before the degradation of the uncoated, the silane/sol-gel coated and the plasma coated substrates is analysed in detail in order to explain the different macroscopic behaviour and to draw conclusions on the prevailing mechanisms. Secondly, the next chapter will focus on these degradation mechanisms including additional investigations to substantiate the findings of this chapter.

In the 1970s, in-service inspections of aircrafts revealed only after a few years frequent occurrence of corrosive delamination of bonded epoxy joints, in particular on solely pickled aluminium surfaces, already after several years [4]. Consequently, the majority of studies on bondline corrosion have been performed

already in the 1970s [166], [167] and 1980s [2], [168], [169]. They have demonstrated clearly that bondline corrosion is dependent on the employed surface preparation and have led to the selection of today's most common anodising processes CAA and PAA. These studies also led to the development of an accelerated test, the so-called bondline corrosion test, where bonded coupons are exposed to salt fog (5 % NaCl in DI water) in an almost upright position. Samples must be cut with a band saw to create rough edges that act as starting point for local corrosion elements. Under these conditions, similar degradation as in-service is achieved.

For qualification and quality control in the aircraft industry, this test is typically performed with joints where highly chromate-loaded primers are applied after the surface preparation. The use of Cr(VI) compounds leaching out of the polymer allows inhibition of initial corrosion and a shift of corrosion potential [229]. Moreover, it was shown that the major benefit of the primer is derived from the thorough penetration of the porous pickling or anodising oxide [2]. While typical tests with primers last 300 d, even longer exposure times can be achieved without joint failure. It has also been proven that the primer impacts the boundary layer and the corrosion mechanism. Vice versa, the surface preparation also influences the crosslinking density of the primer at the interphase. Thus, any primer needs to be optimised for the used surface treatment. If a primer is not applied, this surface wetting aspect is not as important. For the employed one-component adhesive, a forced wetting of the surface caused by the pressure in the autoclave occurs, which makes differences in wetting behaviour marginal [230]. Preliminary tests have produced highly diverse results with different primers, so have other published results [30], [231]. Therefore, the author refrains from using a polymer primer in this test and the FM 73 adhesive is directly applied after surface preparation. Still, it must be kept in mind that bondline corrosion requirements of the aircraft industry (less than 30 % degraded bondline after 300 d) cannot be matched without a primer – not even with anodised adherends. For this reason, PSA, which complies with the requirement in combination with an adequate primer, is used as reference. The target is to achieve a similar level of bondline corrosion resistance with the local treatments.

As a final introductory remark before the actual results are discussed, it must be pointed out that “bondline corrosion” is used as umbrella term to describe any degradation or delamination of the bondline of test coupons exposed to salt fog, independently of the failure mechanism. As described in chapter 2.3.2, Brockmann et al. distinguish between an alkaline and an acidic corrosion mechanism, whereas only the acidic mechanism is referred to as bondline corrosion [2]. Here, the term bondline corrosion does neither distinguish between these mechanisms nor between displacement or hydration yet. The subsequent chapter will address the question of mechanism in greater detail.

Fig. 4.27 displays the degree of bondline corrosion (i.e. the percentage of degraded or delaminated part of the bondline) after 15 d, 30 d and 45 d of exposure to neutral salt fog at 35 °C. Corresponding pictures of representative samples are displayed in appendix Fig. A.26-29. Once again, tested systems consist of grit-blasted or HNO₃ pickled AA 2024 bare or clad adherends without further treatment, or coated with silane based or plasma derived coupling films. Bondline corrosion can occur very locally with some limited areas of the sample being highly corroded while others remain unaffected. In addition, distinct variations between the coupons of the same bonded plates are frequently observed. Thus, the average values of multiple samples and the resulting deviations need to be considered.

A first comparison between bare and clad substrates confirms the common experience “clad is bad” [169]; this time the difference is far more distinct than in the condensation water test in previous chapter 3.3.2.1. For all surface preparations employed, the extent of bondline corrosion is drastically higher for joints of clad material compared to the corresponding bare samples. Clad specimens that are solely etched or grit-blasted, as well as those coated with aqueous GPS or AC-130 are fully degraded after already 15 d, which means that the adherends separate without application of external force. Despite the fact that bondline corrosion is usually only considered as problematic on clad material, the obtained results reveal that significant degradation can also occur on bare substrates. After 45 d, degradation of the solely etched and

alumina blasted bare adherends almost reaches 100 %, which is approximately twice as high as the damage found due to humidity at the same temperature.

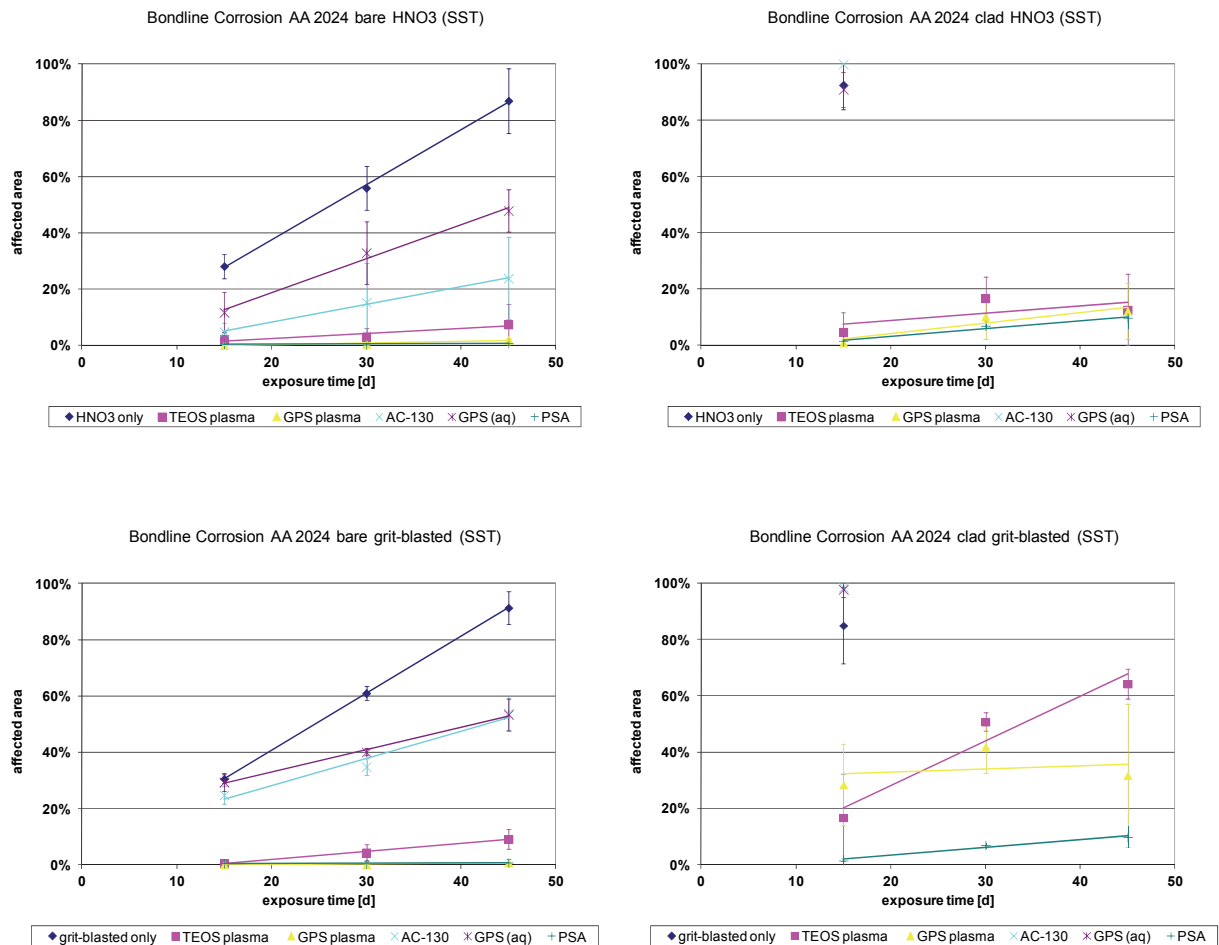


Fig. 4.27: Bondline corrosion test results of AA 2024 bare and clad joints (FM 73)

Previous studies have shown a dependency of bondline stability on the thickness of the oxide layer [2]. Compared to the anodising oxides investigated in these studies, the processes employed here create oxides that are 2-3 orders of magnitude thinner, which explains that severe bondline corrosion appears even on bare substrates. The PSA reference results that do not show any bondline corrosion on bare adherends confirm this assumption. In any case, the bondline samples display a similar type of damage on bare as on clad samples, just to a lower extent.

When comparing both pre-treatment techniques, no distinct differences are observed for both uncoated samples. Grit-blasting and HNO_3 pickling create joints that are very susceptible to degradation. On clad material, nearly the complete bondline is corroded after 15 d, whereas a similar extent of damage is reached after 45 d on bare. However, surface condition does have an impact on the degree of bondline corrosion if a coupling film is deposited. In this case, HNO_3 pickling appears to be superior – especially in combination with the plasma polymer films on clad surfaces. It seems like a certain level of bondline resistance and corrosion must be reached to disclose this difference. Similar to exposure in mere humidity, the advantages of the thicker, nano-structured pickling oxide outweighs the enlarged surface area of the macroscopically rough surface.

The most important outcome of the bondline stability investigation is that the employed plasma films reduce the level of degradation drastically and that this reduction is significantly higher compared to the wet-chemical silane based treatments. In spite of their excellent adhesion promotion capabilities, silanes

fail to reduce bondline corrosion on clad substrates. Nevertheless, silane application diminishes degradation on bare material, where the corrosive force is less strong; by trend AC-130 provides slightly more improvement than GPS. It is likely that this effect is caused by the enhanced stability of the interface in humidity as discussed in previous chapters. This result explicitly shows that additional corrosion-induced aspects of delamination must be considered and that silane and sol-gel coupling films react very sensitive to this type of bondline degradation. This sensitivity disqualifies their general use in the aircraft industry and limits potential applications to areas where exposure to corrosive media is limited and where inspection is uncomplicated, e.g. on the outer skin.

In contrast, GPS derived plasma films almost fully suppress degradation on bare adherends. Coherent with all preceding results, GPS plasma deposition produces by trend more stable joints than TEOS deposition. Nevertheless, the difference is relatively low, so that a potential benefit derived from the improved barrier properties compensating the weaker interface bonding cannot be fully excluded. Comparing these results with those obtained after exposure to 100 % humidity, distinct discrepancies only occur with clad joints. Thus, on bare substrates, plasma coatings reduce the degradation impact of the corrosive salt fog almost to the one of mere humidity, independently of the used surface pre-treatment. Moreover, GPS plasma deposition achieves similar performance as PSA on bare. Due to the higher corrosion driving force on clad surfaces, anodising level is not reached in any case with these substrates. However, in combination with HNO_3 etching, bondline corrosion resistance is not significantly below the PSA standard. As already mentioned, a clear difference between the employed surface conditioning techniques exists, where grit-blasting cannot match the acidic pickling. It appears that the thicker, open oxide structure that is penetrated by the coupling film is required in order to achieve degradation protection comparable to anodising. It should be emphasised that the thickness of these interspersed plasma-oxide layers are far below 100 nm, whereas anodising layers are normally around two to three microns thick. As additional reference, previous bondline corrosion test results of CSA pickled AA 2024 clad substrates should be considered, where oxide film thickness lies in the same range. Even though a chromate-loaded primer was applied after CSP, the degradation ratio of the bondline was found to be between 50 % and 100 % after 45 d [4], i.e. the performance level of plasma coated samples is by far not reached with CSP.

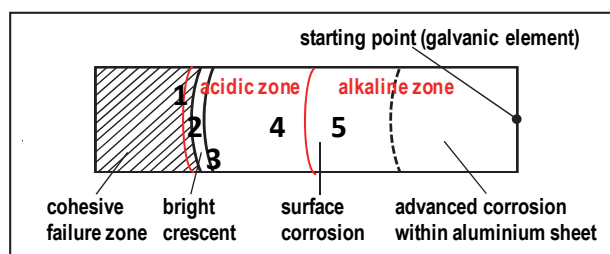


Fig. 4.28: Location of the 5 here investigated zones within the scheme of macroscopic bondline corrosion according to Brockmann et al. [2]

To investigate the cause for the different behaviours observed and to draw first conclusions on the damage mechanisms, XPS, SEM, EDX and TEM analyses of the crack tip region are performed on selected samples of uncoated, silane coating and plasma film category. Within this region, 5 different zones are distinguished. Fig. 4.28 shows the approximate location of the 5 zones within the schematic display of the macroscopic bondline corrosion identified by Brockmann et al. [2]. The region of advanced corrosion of the aluminium base

material with a corrosion depth of $> 60 \mu\text{m}$ found after very long exposure intervals is not considered within this study, as it does not provide any information regarding the degradation mechanism. In terms of degradation, this zone differs only from zone 5 with regard to corrosion intensity. This severity is hardly reached in this study, as exposure times are rather low in comparison with bondline corrosion investigations carried out with anodised, chromate-loaded systems.

Bondline failure analysis of uncoated AA 2024 substrates

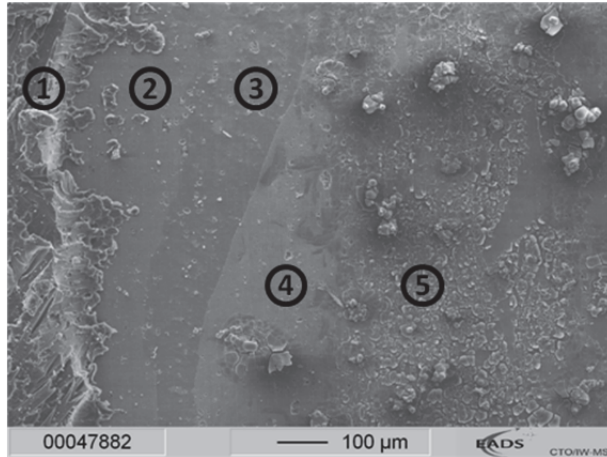


Fig. 4.29: SEM overview of degraded area behind the crack tip of a HNO_3 pickled AA 2024 bare adherend after bondline corrosion test

A SEM top view analysis of approximately the first millimetre of the degraded and delaminated area reveals several zones with different damage patterns (Fig. 4.29). Due to a slower progression of the bondline on bare surfaces leading to the formation of larger and more distinct zones, a bare AA 2024 substrate (HNO_3 etching) is chosen exemplarily for analysis. Contrary to grit-blasting, HNO_3 pickling creates an oxide that is visible in SEM imaging. Moreover, the high roughness of the blasted surfaces impedes the analysis. Still, analogous behaviour is detected on grit-blasted joints as well. 5 zones are identified in total. The first one is located below the cohesively failed adhesive at the buried metal-polymer interface. The adjacent sections 2 (grey) and 3 (dark grey) together form the bright crescent, i.e. are not discriminable

macroscopically. Zone 4 (light grey) corresponds to the area of beginning surface corrosion. Zone 5 (distinct corrosion products visible) follows further away from the delamination front (still in an area of surface corrosion) and is visible to the naked eye.

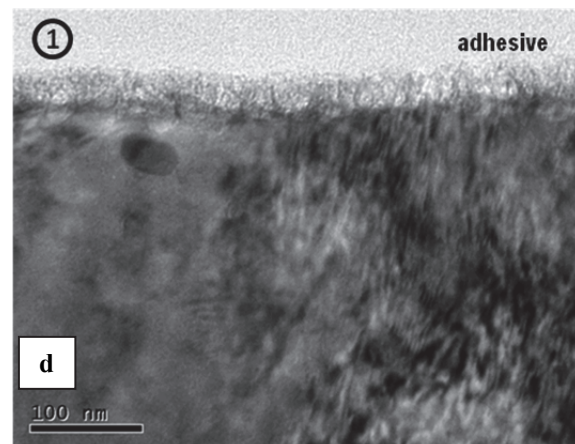
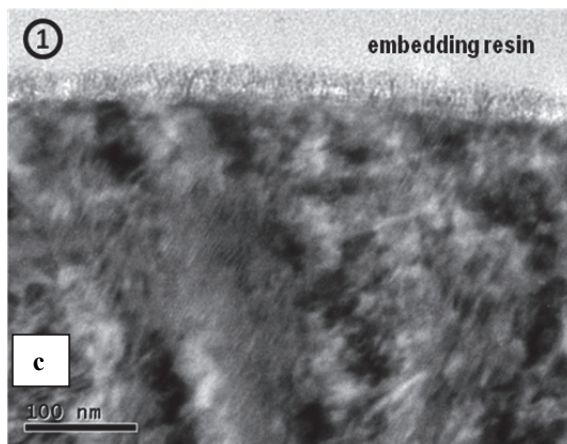
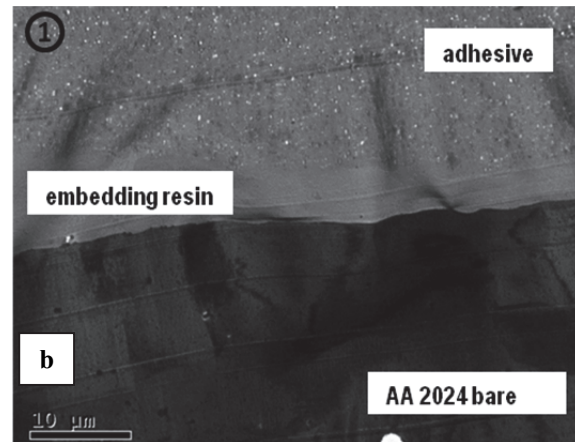
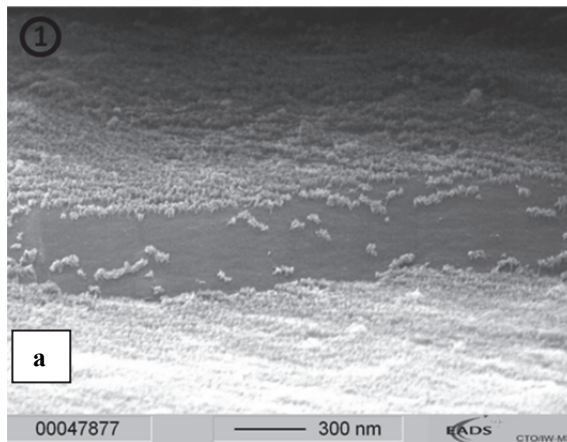


Fig. 4.30: SEM/TEM analysis of AA 2024 bare (HNO_3) oxide film in zone 1, below the cohesively failed FM 73

The interface of zone 1 is made visible by a side view on the cryofractured sample (along the delamination direction). Corresponding high resolution analyses using SEM and TEM are displayed in Fig. 4.30, where SEM image a) is a side view of the oxide below the delaminated adhesive directly in front of the bright crescent. Due to sample preparation, a displacement of the adhesive from the aluminium surface is very common. Therefore, no conclusions can be drawn whether the delamination has already advanced below the adhesive that still fails cohesively or not. Any displacement that already occurred during the exposure to salt fog is, however, very unlikely, because the oxide looks completely unharmed in spite of the aggressive atmosphere. TEM analysis reveals a delaminated area of approximately $100\ \mu\text{m}$ below the adhesive. Image b) shows this delamination. The crack between oxide and adhesive is filled with embedding resin used for ultramicrotomy. A comparison of the oxide layer of this region (c) with the one at an intact oxide-adhesive interface (d) again reveals no discrepancy. The oxide film is still in its initial state. As before, a (partial) displacement due to sample preparation cannot be excluded. Hence, it is assumed that the interface is already weakened by the presence of moisture, which leads to a displacement during sample preparation; an open delamination, i.e. a formation of a crack has however not yet taken place. This also suggests that displacement occurs prior to any further degradation happens. An acidic oxide dissolution below the cohesively failed polymer, as found by Brockmann et al., is not observed [2].

Different than zone 1, the not buried area of interfacial failure shows signs of degradation with increasing extent from zone 2 to zone 5. High resolution SEM analysis of the oxide film is presented in Fig. 4.31. Figures a), c) and e) are side views on the oxide layer close to the edge of the cryofracture taken to assess the oxide thickness of zones 2, 3 and 4, whereas changes in topography are determined from higher angles in images b), d) and f).

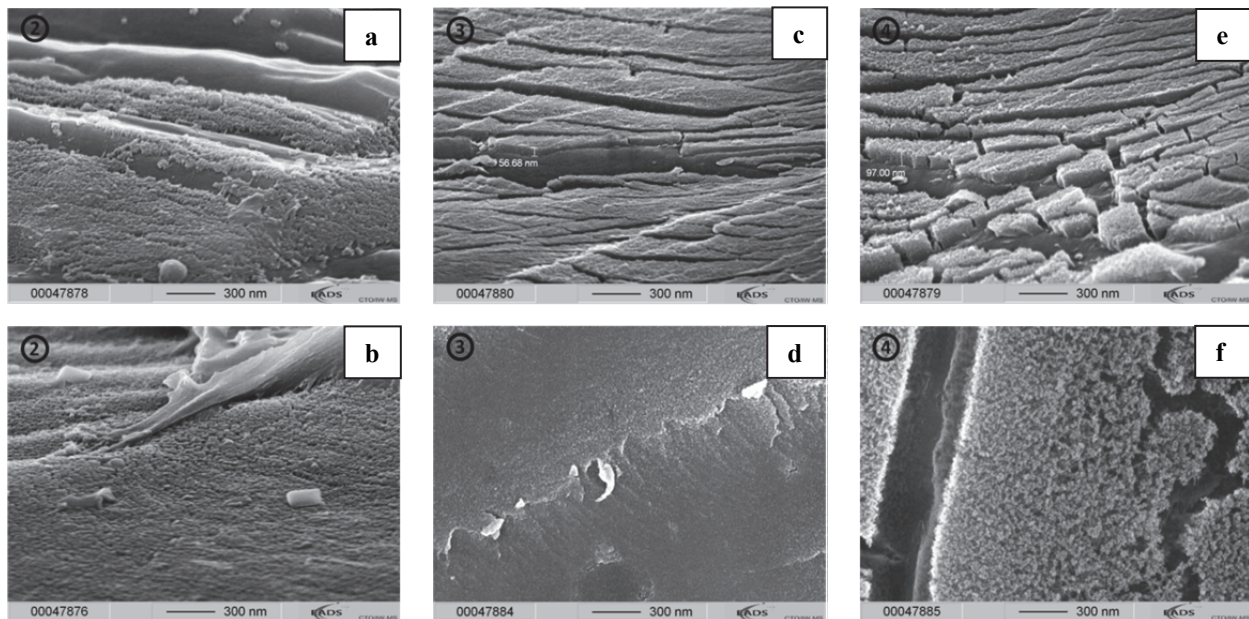


Fig. 4.31: SEM analysis of AA 2024 bare (HNO_3) oxide film in zones 2-4

Zone 2, i.e. the sector of the bright crescent adjacent to the adhesive, shows only small first signs of degradation. As visible in Fig. 4.31 a) and b), oxide thickness has slightly increased and open pores of the initial oxide start to narrow due to oxide/hydroxide growth. Similar to exposure in humid atmosphere, only hydration with some local variances of oxide thickness and porosity (a) takes place. As before, the detection of this first oxide growth is very difficult due to resolution limitations. However, the fact that the hydration extent is low supports the assumption that it only occurs after hydrodynamic displacement, and is not its cause. The transition from cohesion to adhesion failure seen in image b) does not reveal any delamination in front of zone 2 below the adhesive, which also suggests that the displacement found during TEM investigations originates from sample preparation. Besides the beginning hydration, the small NaCl

crystals found in zone 2 (b) provide proof that this sector has already been exposed to the hostile atmosphere, i.e. that a crevice is formed during testing. Nevertheless, no signs of dissolution of the oxide layer are apparent in this region, despite this corrosive test environment. Thus, it is concluded that the hydrodynamic displacement at the crack tip is followed rather by hydration due to the hot-wet environment, than by any degradation directly caused by the Al-chloride environment. An acidic dissolution of the oxide is not detected.

Hydration further continues in zone 3, entailing a significant increase of oxide thickness and a distinct loss of porosity. In particular, the aluminium oxide of this sector can be characterized by its very smooth surface, which causes the darker appearance in the overview SEM image (Fig. 4.29). The initial oxide texture is hardly visible anymore. Fig. 4.31 c) and d) display a compact oxide film of approximately 60 nm thickness with a very even surface²⁹ that tends to break close to the cryofracture edge (c). Like in zone 2, hydration appears to be the only degradation type happening. Although no anodic oxide dissolution is observed in this zone, the found degradation is in a way coherent with the analysis of anodised and CSA pickled adherends performed by Brockmann et al., who observed that the oxide within the bright crescent is “changed similar to the reactions which can be observed after ageing in moisture” [2]. In terms of degradation mechanism, zone 2 and 3 are the same. The surface of the bright crescent, which appears unharmed in visual inspection, is in fact strongly hydrated by the acidic and humid atmosphere close to the crack tip.

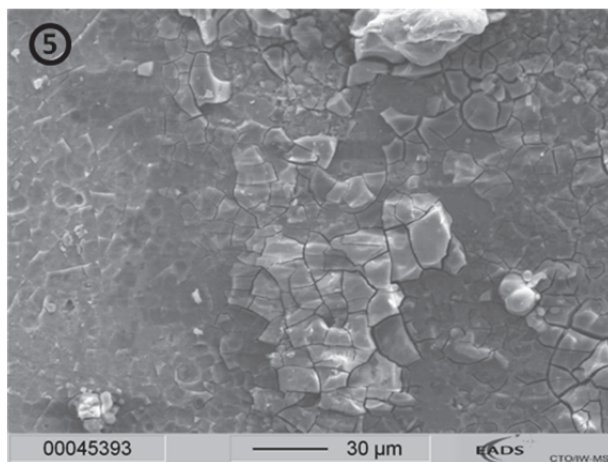


Fig. 4.32: SEM image of highly degraded AA 2024 bare (HNO_3) adherend surface (zone 5) due to bondline corrosion

While hydration advances with increasing distance from the delamination front, the oxide surface becomes porous again (zone 4) and, therefore, appears brighter in the SEM overview. The oxide film displayed in Fig. 4.31 e) and f) has grown by hydration to a thickness of around 100 nm. In comparison to zone 3, the surface reveals a fine, porous, dendritic structure, which resembles oxides that are immersed in inorganic acids at elevated temperatures. Underhill and Rider also found analogous porous film formation due to dissolution and precipitation of hydroxides in their study of hydration of similar alloys during immersion in neutral water at 40 °C and 50 °C [159].

In summary, the oxide changes observed in zones 2-4 follow the hydration steps identified by Venables, who discovered that hydration, mainly of the base material, first causes a reduction of porosity and a general film growth, before the growing oxyhydroxide film becomes rough again [77]. pH variations affect the dissolution and precipitation of the formed hydroxide. It is assumed that the pH drop in the crack tip significantly enhances hydroxide formation and dissolution, as does the presence of chlorides. This explains why the degree of hydration is significantly above that found for exposure to 100 % rh, where a formation of the fine dendritic structure is not observed. Film growth by hydration and hydroxide dissolution/precipitation due to a combination of hot-wet conditions and low pH both occur in parallel. Similar to the mechanism postulated by Brockmann et al. [2], oxide film dissolution in the acidic environment is observed. However, it is not the initial oxide is dissolved in this case, but the hydroxide formed before by hydration of the oxide and especially of the base material; as described in chapter 2.3.1, the aluminium dissolution occurs indirectly through the hydrated oxide film. Here, the damage mechanism

²⁹ The sample surface in image Fig. 4.31 d) is so smooth that the edge of an etching pit must be used to focus the electron beam in the SEM analysis.

is referred to as acidity-enhanced hydration as no direct dissolution of the aluminium in the electrolyte, i.e. no corrosion, occurs.

In contrast, zone 5 is characterised by flake-shaped corrosion products of several micrometres in diameter and thickness. On AA 2024 bare, size and number of the flakes are unevenly distributed with a local increase around the intermetallics. On clad surfaces, distribution is more homogenous while corrosion is more severe. As expected, elemental analysis reveals that the flakes consist of aluminium oxide/hydroxide (not shown), which is created by oxidation/hydration of anodically dissolved aluminium; anodic dissolution is caused by galvanic/bimetallic corrosion between Cu-rich intermetallics and aluminium matrix. The surface of zone 5 does no longer reveal any signs of the original oxide film or the hydration-typical hydroxide film. Both base material and oxide layer are dissolved directly by the electrolyte first; aluminium hydroxide is formed in solution and precipitates afterwards, leading to flake formation with smooth flake surfaces. Due to its hydroxide nature, this region is also called the alkaline zone. The aluminium dissolution may be the cause for bondline corrosion; however, it does not occur directly at the crack tip, but follows hydrothermal displacement, hydration and dissolution of the hydroxide. Nevertheless, the comparison of the magnitude of delamination in salt fog and mere humidity, as well as the different impact of the cladding in these conditions, clearly suggest that corrosion strongly intensifies displacement, hydration and hydroxide dissolution.³⁰

Bondline failure analysis of silane and sol-gel coated AA 2024 substrates

Neither results of a bondline corrosion test (or of a connatural test) of silane or sol-gel treated aluminium alloys joints, nor studies of the associated degradation mechanisms are currently published. As previously discussed, the reduction of bondline corrosion of an aluminium joint by GPS or AC-130 treatment is limited to bare substrates. On clad, degradation propagates so fast that any positive effect of the coupling film is nullified. For this reason, the corrosion mechanism is investigated primarily on bare substrates. In the following paragraphs, the failure mechanism of a AC-130 coated AA 2024 bare joint pickled in Smut-Go NC is investigated by SEM. In terms of bondline corrosion, joints desmuted in Smut-Go NC are indeed the most sensitive of all tested, but their specific oxide microstructure is very helpful to follow the oxide transformation happening at the crack tip. AC-130 is chosen for its higher and more uniform film thickness of around 200 nm. Failure mechanisms are found to be equal for GPS treated adherends and for other surface conditioning techniques employed on bare and clad. SEM Images of a similar analysis of a GPS coated, grit-blasted AA 2024 clad joint are displayed in appendix Fig. A.30.

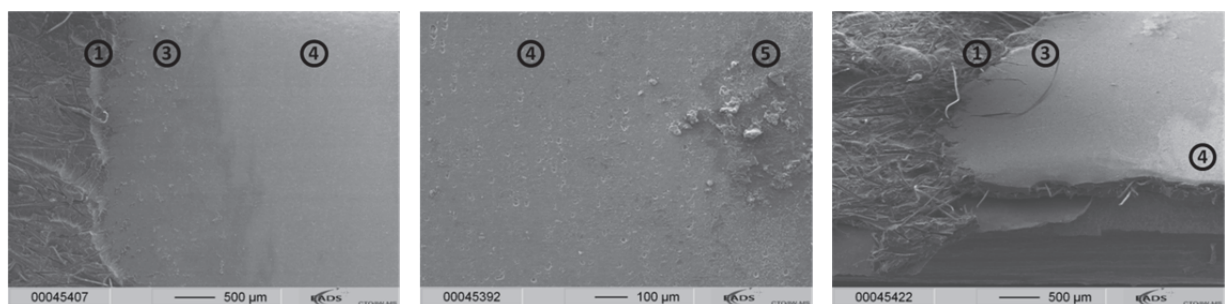


Fig. 4.33: SEM overview of corroded area of AA 2024 bare (Smut-Go NC) FM 73 joints; left & middle: metal side; right: adhesive side

In Fig. 4.33, the damaged area is separated in the same zones as discussed for the uncoated substrates. The SEM overview is relatively similar to the one of the untreated sample, except for the absence of zone 2, i.e. the bright crescent is not separated into two sections. The whole region adjacent to the delamination front

³⁰ Compared to other published bondline corrosion investigations that focus on anodised clad samples, the study of the mechanism on a solely etched bare substrate turned out to be more suitable to identify the prevailing degradation mechanisms, because, on the one hand, degradation advances rather slow on bare alloys and, on the other hand, the thin oxide does not lead to a very stable polymer-oxide composite layer that complicates the analysis.

appears in dark grey, which indicates a smooth surface. Furthermore, zones 3 and in particular 4 are significantly wider as compared to sole HNO_3 etching, where visible corrosion (zone 5) starts after a few hundred microns. Heavy corrosion starts only > 2 mm behind the crack tip with this system. Delamination advances the fastest on Smut-Go NC etched substrates and, therefore, the distance between the crack tip and the slower progressing galvanic corrosion is the widest. The image on the right displays the adhesive side, where the zones can be distinguished as well. The magnitude of these zones is strongly dependent on the pre-treatment, the coupling film and the base material. As displayed in Fig. A.30, the zones are distinctly narrower for the GPS coated grit-blasted clad substrate. In any case, further analysis with higher resolution is required to understand the occurring transformation and to detect similarities – or differences – with untreated joints.

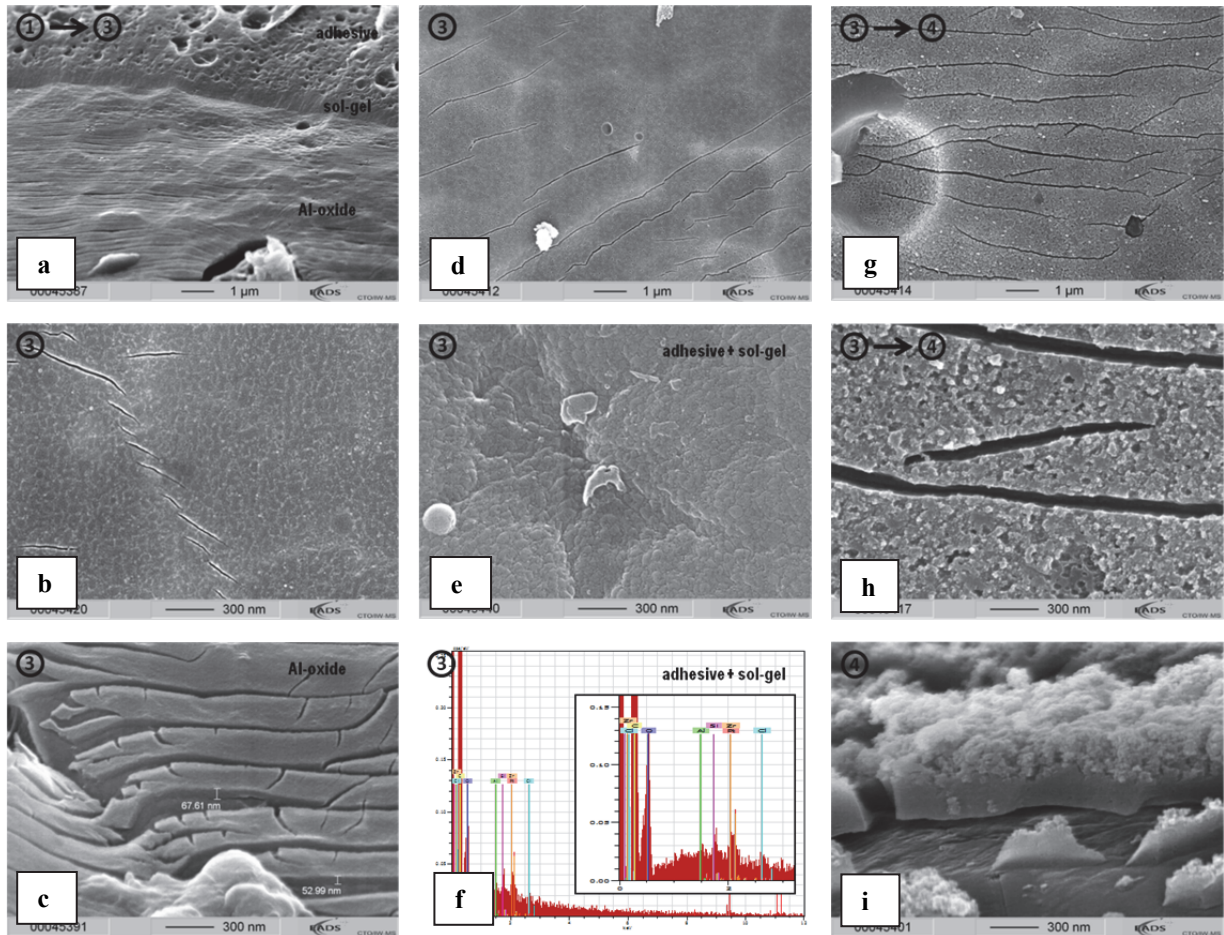


Fig. 4.34: SEM/EDX analysis of bondline corrosion on AC-130 coated AA 2024 bare (Smut-Go NC) joints

Besides the absence of a distinguishable zone 2, the more detailed analysis in Fig. 4.34 a) also reveals the absence of any delamination below the adhesive in zone 1. As observed after exposure to humidity, the SEM image shows a direct transition from cohesion failure to a delamination of the sol-gel film with a sharp crack through the sol-gel film. Moreover, a certain crack formation in the oxide layer indicates that oxide thickness has already increased around the crack tip. Thus, the interface is stable and no delamination occurs without degradation of the oxide layer. This again proves the outstanding adhesion promotion capabilities of the solution derived silane treatments, which were previously detected during fatigue testing in water. As a consequence, no zone 2 is observed, as the mere presence of moisture does not lead to

interfacial displacement, but a transition of the oxide is required to cause delamination.³¹ Considering the oxide of the delaminated area, the degradation is only apparent through the cracks in the oxide layer, which is again similar to the failure mechanism found due to humidity. After exposure to humidity, the HNO_3 derived oxide shows signs of modification directly at the delamination front, where hydration entails a closure of the porous structure. The question whether the oxide transformation starts from the adhesive/sol-gel side or from the substrate side could not be answered in the previous test; in order to find an answer, the use of Smut-Go NC conditioned bare samples turns out to be advantageous. Close consideration of the surface of the Smut-Go NC derived oxide directly behind the delamination front (Fig. 4.34 b)), indeed reveals some oxide cracking, but it also shows that the typical surface structure is fully intact, which suggests that oxide growth originates from the substrate side and not from the interface. This is consistent with the hydration mechanisms explained in chapter 2.3.1. It seems as if this aspect of the oxide degradation mechanism of silane or sol-gel coated aluminium surfaces deviates from that of anodising layers, where a transformation from the polymer side was observed [2].

As no transformation of the upper oxide surface is observed in this region, it is assumed that the interface between oxide and sol-gel/silane film is weakened; however, no real crack is formed, which means that the electrolyte does not yet enter. TEM analysis is employed to further investigate the oxide transformation.

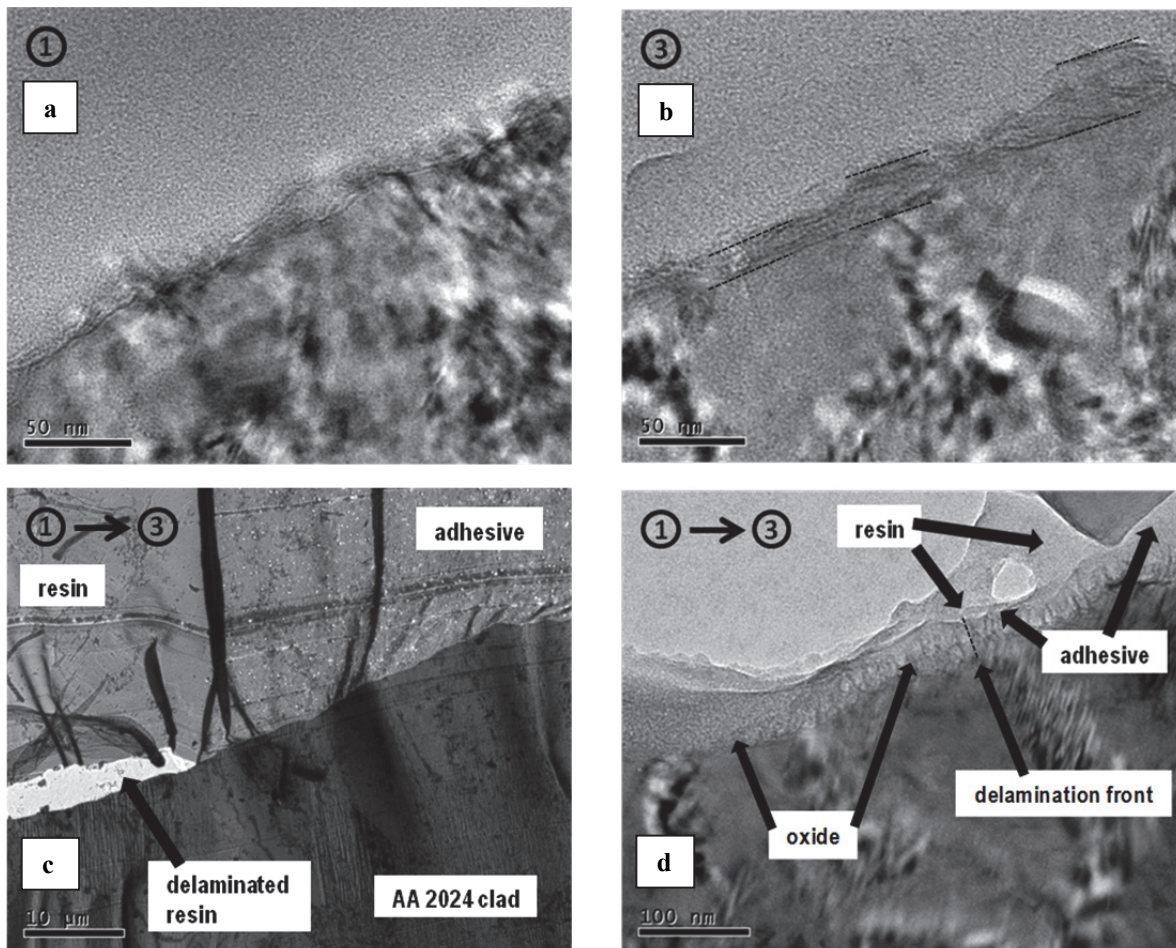


Fig. 4.35: TEM analysis of oxide transformation due to bondline corrosion of AC-130 coated AA 2024 bare etched in Smut-Go NC (a) & b)) and of GPS coated AA 2024 clad etched in HNO_3 (c) & d)); dashed lines in b) mark oxide borders

³¹ The oxide texture created by the Smut-Go NC etchant is less distinct than the one formed after HNO_3 pickling. Thus, the oxide would appear dark in the SEM image even if no oxide transition occurred, i.e. a visual differentiation of zone 2 and 3 at this magnification would be impossible.

The micrographs in Fig. 4.35 a) and b) confirm the increase in oxide thickness. The oxide located right in front of the delamination (zone 1) in picture a) looks like the natural oxide formed after Smut-Go NC conditioning, which is difficult to resolve due to its low thickness. Image b) suggests that the oxide has grown behind the delamination front, but the borders between base material, oxide and embedding resin remain difficult to determine. The dashed lines are added for approximately locating the interfaces.

As mentioned before, oxide transformation on bare substrates progresses rather slowly, and so the transition at the delamination front is additionally examined on clad material. Fig. 4.35 c) shows a TEM overview image of the transition section from zone 1 to zone 3 of a GPS coated, HNO₃ etched AA 2024 clad specimen. As the polymer-metal interface is stabilised by the silane, no hydrodynamic displacement occurs below the cohesively failed adhesive. Thus, the embedding resin covers only the degraded and delaminated part of the adherend. However, degradation proceeds so fast that the resin delaminates from the already corroded oxide directly behind the delamination front during sample preparation. Fig. 4.35 d) focuses on this transition zone. In the top left part of the image, the resin is delaminated. Only some residues remain close to the delamination front, where the resin is attached to the adhesive. GPS treatment produces very thin films with inhomogeneous thickness; here, the GPS solution has penetrated the pickling oxide, but does not form a closed film on top of it. Therefore, the GPS derived film is not clearly visible respectively distinguishable from the oxide. As distinction between embedding resin and adhesive is also not obvious, localisation of the actual delamination front is difficult. From the previous results it is deduced that delamination is accompanied by oxide growth (or vice versa), so, it is quite certain that the delamination front lies directly ahead of the point where a significant increase in oxide thickness is visible (marked with a dashed line). In front of this point, the oxide appears to be in its natural state. Directly behind it, the oxide not only starts to grow strongly, but also its structure begins to vanish. Within approximately 100 nm distance from the delamination front, the initial structure has completely disappeared and transformed into a thick, non-porous film. This gradual transition again confirms that the existing oxide grows out of its initial structure, respectively is covered by hydroxide and is not directly dissolved.

The SEM images displayed above already showed that the sol-gel layer is delaminated from the oxide directly with the adhesive, but this finding also needs to be ascertained for surfaces pickled in nitric acid, where open pores are penetrated by the silane films. EDX elemental analysis of an ultramicrotomed specimen is employed to further investigate the precise location of the silane/sol-gel films during oxide transition. The top left of Fig. 4.36 displays a TEM image of the beginning bondline corrosion on a HNO₃ pickled AA 2024 bare adherend coated with AC-130. The delamination front is located inside the red rectangle. Left of the rectangle, the sol-gel film and the adhesive are still covering the oxide, whereas significant oxide degradation is visible on its right side. A STEM image of the area in the rectangle is shown on the right hand side of Fig. 4.36. Visual inspection already confirms the SEM results, suggesting that the sol-gel film delaminates from the oxide. EDX spectra are taken to verify this assumption. A reference spectrum of the sol-gel layer (1) is compared to the spectrum taken at the degraded oxide (2). As the embedding resin contains silicon, zirconium needs to be used as tracer for the coupling film. A distinct Zr signal is observed with the reference, whereas no signs of Zr are detected behind the delamination front. This confirms the displacement of the silane based coupling film from the oxide. With the strong interfacial bonding of the silanes being proven, this finding also suggests that hydration starts from the substrate, respectively from the oxide, and not from the adhesive side. This explains why silane based treatments have a limited effect on bondline corrosion reduction.

XPS analysis of the corroded bondline of GPS and AC-130 coated clad joints (Table 4.17) reveals almost identical results for both the metal and the adhesive side with distinct Al and O signals. They indicate that the top surface of the oxide remains attached to the coupling film, i.e. that the locus of failure lies within the HNO₃ derived oxide. Contrarily, the failure mode with Smut-Go NC appears to be more interfacial due to the absence of the open texture. In any case, failure is always preceded by oxide hydration, which differs from the uncoated substrates, where hydration follows displacement.

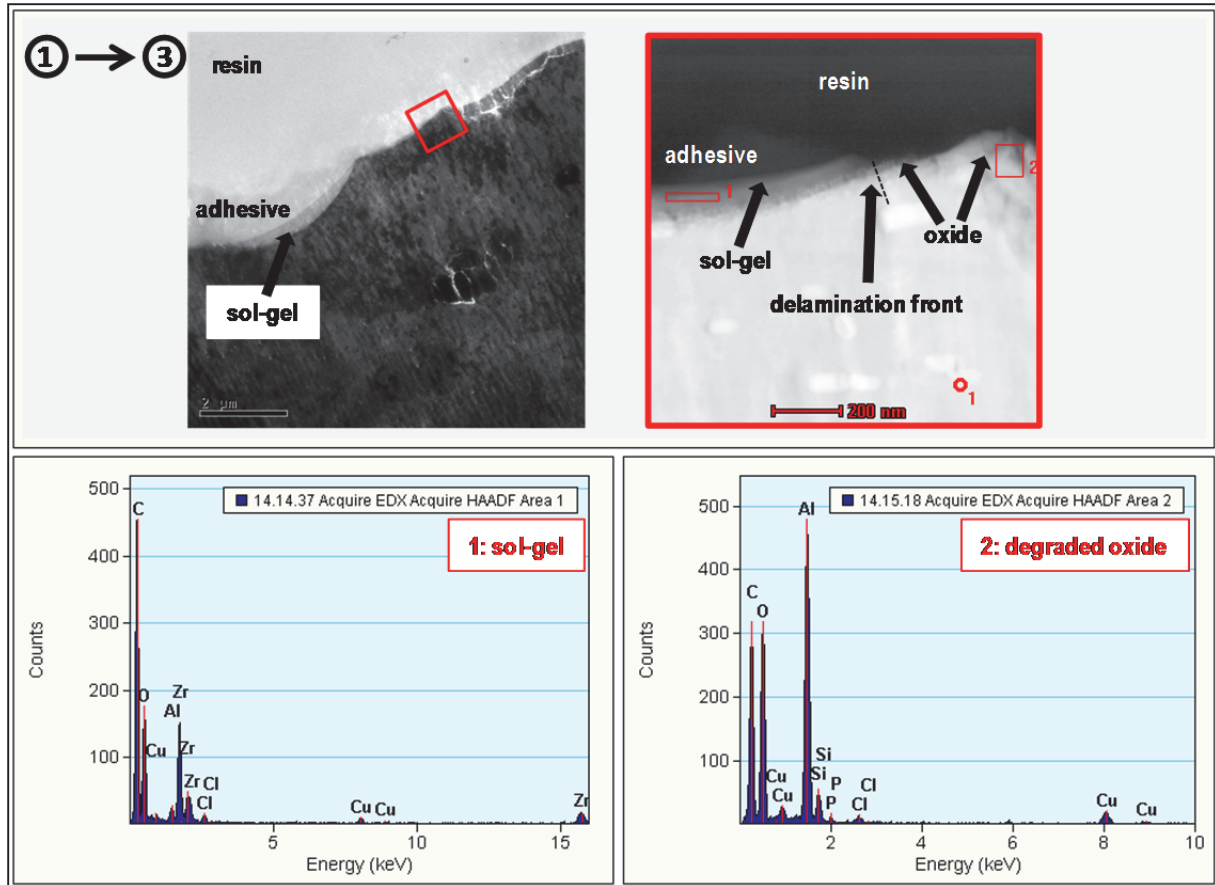


Fig. 4.36: TEM/STEM + EDX analysis of bondline corrosion front on AC-130 coated AA 2024 bare (HNO₃); (produced by IFAM)

Table 4.17: XPS elemental analysis results [at.%] of the delaminated surface of AA 2024 clad adherend surface and corresponding area on the adhesive side after bondline test

	side	C	N	O	Na	Al	Si	Zr	Cl	degradation path
GPS (aq)	m	26.8	0.2	50.6	2.6	16.9	-	-	2.8	fracture through oxide/hydroxide
	a	34.0	0.2	48.1	1.8	15.6	-	-	0.5	
AC-130	m	18.5	-	54.7	7.9	16.4	-	-	2.4	fracture through oxide/hydroxide
	a	16.5	-	59.0	2.0	18.8	-	-	3.7	
GPS Plasma	m	53.5	0.7	31.6	2.2	7.6	4.1	-	0.3	mostly interfacial or even cohesion-near-interface contamination by Al-hydroxide precipitation
	a	45.9	0.6	41.9	-	11.0	-	-	0.5	
TEOS Plasma (5 SLM)	m	23.7	-	56.3	2.2	15.4	2.0	-	0.4	interfacial and mostly fracture through oxide/hydroxide
	a	23.1	0.4	58.2	0.7	16.8	-	-	0.5	

Despite its homogenous appearance in the overview SEM image, zone 3 of the AC-130 coated, Smut-Go NC conditioned bare substrate is not uniform. Beside the region close to the delamination front, where the oxide surface remains in its original shape, variations of oxide surface structure are found. Fig. 4.34 c) and e) show this continuing transformation of the oxide structure. After losing its initial surface morphology, a very smooth and compact film of around 60 nm thickness is formed (c). This is coherent with TEM results

on clad substrates where the transition to the non-porous, plain oxide occurs already close to the delamination front. In addition to a further increase of oxide thickness, first small craters are formed on the surface indicating the beginning dissolution of the hydroxide. As displayed before, similar craters are detected on AC-130 coated samples after exposure to 100 % rh but only after longer exposure time and only on clad samples, where hydration progresses faster. This confirms that hydration and dissolution are enhanced in salt fog compared to mere humidity. The oxide transformation observed is similar to the one on uncoated substrates, which is not surprising as the coupling film is already removed at this stage. SEM inspection of the adhesive side (right of Fig. 4.33) shows that the zones are mirrored onto this side. A closer inspection of the surface of zone 3 of the adhesive side displayed in Fig. 4.34 e) reveals that its topography is the precise negative of the initial oxide structure, which means that the image represents a bottom-up view on the sol-gel film. Distinct Si and Zr signals are observed in the EDX analysis of this area (Fig. 4.34 f)), whereas the Al signal is insignificant. This again shows that the coupling film is delaminated from the Smut-Go NC derived oxide, but it is neither dissolved nor visibly degraded.

Different than indicated by the overview SEM image, no distinct border between zone 3 and 4 is visible in high resolution. The transition between zones 3 and 4 is a continuation of the transition within zone 3, with the similar hydration mechanism. The corresponding SEM images (Fig. 4.34 g) and h)) display an increased roughness caused by dissolution and reprecipitation of the hydrated oxide. As soon as strong dissolution and precipitation occurs on the oxide surface (zone 4), hydroxide residues are also detected on the adhesive side. Hydration proceeds further, followed by continued film growth as well as increased dissolution and precipitation. This leads to the creation of an approximately 500 nm thick oxide/hydroxide film, which is non-porous at the substrate side and which has very open dendritic surface (Fig. 4.34 i)). This structure confirms that the previously hydrated oxide is dissolved from the adhesive side, which implies that a crevice filled with electrolyte has been formed.

Hydration continues until the area of visible corrosion is reached (zone 5), where Al-hydroxide flakes of the size of a few micrometres are observed. Once again, no differences between silane/sol-gel coated and untreated samples are observed in this region.

Bondline failure analysis AA 2024 substrates coated with plasma films

No detailed investigations on bondline corrosion of bonded joints of APPJ-CVD coated aluminium adherends have been published. Nevertheless, comparable plasma films have already proven to significantly reduce the corrosive undermining of a silicone sealant on casted aluminium and of some epoxy-aluminium joints [37], [39], [146]; however, alloys and adhesives diverge from those used here. In particular, studies on the corrosion mechanism and the functionality of the plasma films are missing.

The bondline corrosion test results displayed earlier point to a significant reduction of degradation by deposition of both GPS and TEOS derived plasma polymers. In some cases, the degree of degradation on bare substrates is so low that not all aspects of the corrosion mechanism can be observed. For this reason, the degradation process is primarily studied on clad substrates. The analysis is performed in a similar manner as before, where investigations are separated in different zones. Fig. 4.37 a) displays a SEM overview of the corroded area of the bondline of a HNO₃ etched and TEOS (5 SLM) plasma coated AA 2024 clad joint. Visible differentiation of zones 2 and 3 is impossible at this magnification, but all degradation states found for the solely conditioned substrates are detected with higher resolution as well.

The transition from cohesion to interfacial failure is shown in Fig. 4.37 b). No signs of further delamination below the cohesively failed adhesive are observed. The adhesive is delaminated from the interspersed oxide-plasma polymer layer, which remains attached to the substrate. No significant degradation of this 80 to 100 nm thick film is visible, which indicates that hydrodynamic displacement of the adhesive is the predominant failure mechanism. As no visible changes due to hydration or corrosion occur, it is assumed that this region has not yet (or only for a short time) been openly exposed to the aggressive electrolyte. This limited degradation may also be caused by the stable barrier of the TEOS derived plasma film.

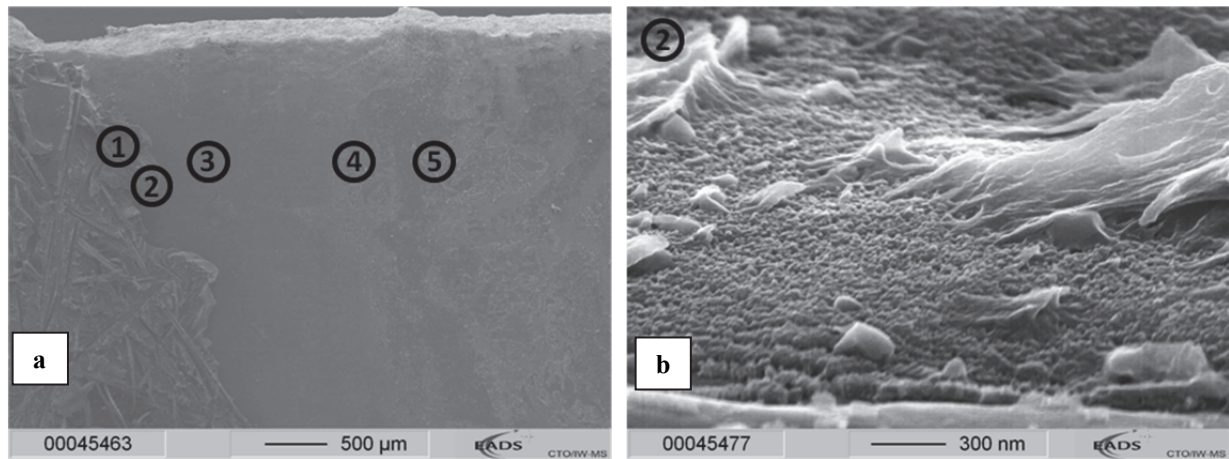


Fig. 4.37: SEM analysis of bondline corrosion of a TEOS (5 SLM) plasma coated AA 2024 clad (HNO_3) sample
 a) SEM overview on corroded area; b) high resolution of delamination front

TEM is employed to investigate the behaviour of the thinner GPS derived plasma coatings at the delamination front. The interspersed film of a HNO_3 pickled and GPS plasma coated substrate before and after delamination are presented Fig. 4.38 a) and b), showing a certain increase of oxide thickness. Unfortunately, in this analysis the exact delamination front could not be located due to folding of the ultramicrotomed sample. Therefore, it cannot be fully ascertained whether the observed oxide film growth starts in front of or directly at the delamination front or even occurs post-failure. In any case, the structure of the oxide remains intact and no compact oxide/hydroxide film, as observed for silane treatments, is formed yet. Hence, the detected oxide modification is less advanced, which means that the transformation process appears to be significantly slower.

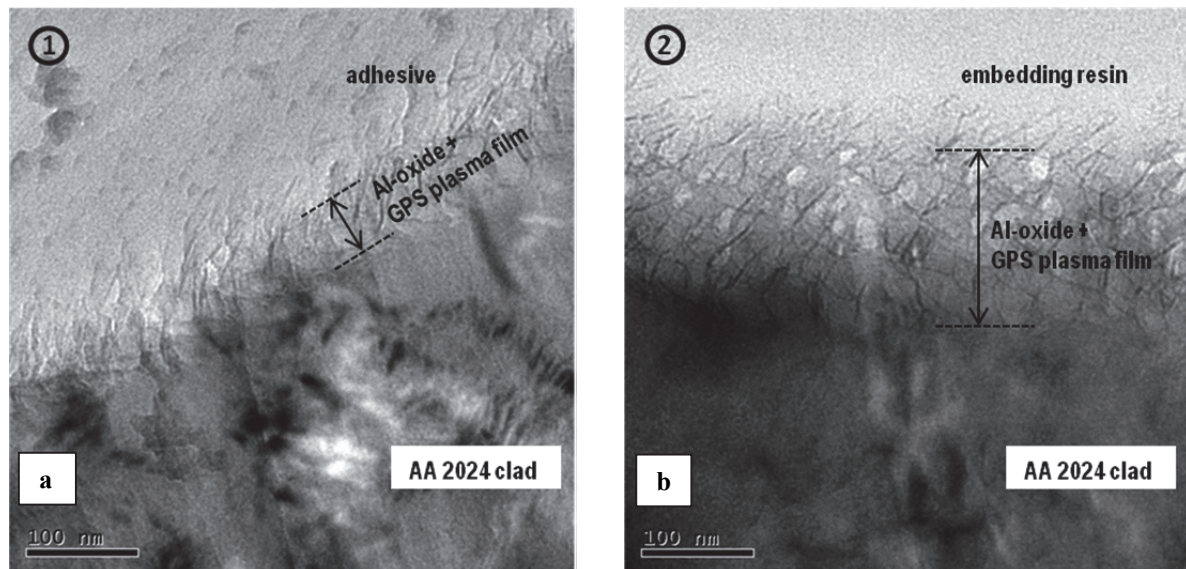


Fig. 4.38: TEM analysis of interspersed oxide-plasma polymer film derived from GPS APPJ-CVD on HNO_3 etched AA 2024 clad after bondline corrosion testing;
 a) ahead of delamination front (unharmred) b) behind delamination front

Examination of the delamination front on bare substrates suggests that displacement precedes hydration. As for the solely etched substrates, a certain delamination below the cohesively failed adhesive is observed for a GPS plasma coated bare specimen (Fig. 4.39), albeit to a lower extent. Analogous to the uncoated samples, this delamination in zone 1 is likely to occur during sample preparation but can be seen as indicator for an already weakened interface. No changes of the oxide-plasma polymer layer are apparent

when comparing the left and right sides of the delamination front, which proves that hydration, at least for bare substrates, is not the main failure cause. These findings are also consistent with the results obtained in



Fig. 4.39: TEM image of the delamination front of a GPS plasma coated AA 2024 bare (HNO_3) adherend after bondline corrosion test

the humidity test. Although plasma coatings improve the adhesion at the interface, they cannot completely prevent displacement of the adhesive due to moisture. The increased bondline corrosion of clad substrates, where oxide growth is more distinct, indicates that hydration may also have a certain influence on the failure process on plasma coated clad material. Still, hydration is strongly decreased compared to wet-chemical silane based treatments.

Additional TEM investigations of a TEOS plasma coated grit-blasted AA 2024 clad sample confirm this influence of hydration on clad. Fig. 4.40 a) shows the interface below the cohesively failed adhesive after exposure to salt fog. In spite of the cohesion failure, areas of distinct oxide degradation are already visible between sectors with an intact interface. The local delamination observed here is certainly not caused by sample preparation, but is formed during the SST. Due to the high roughness of the grit-blasted surfaces with peak and valleys the

bondline degradation does not advance as evenly as on etched coupons and the intact areas are sufficient to obtain cohesion failure.

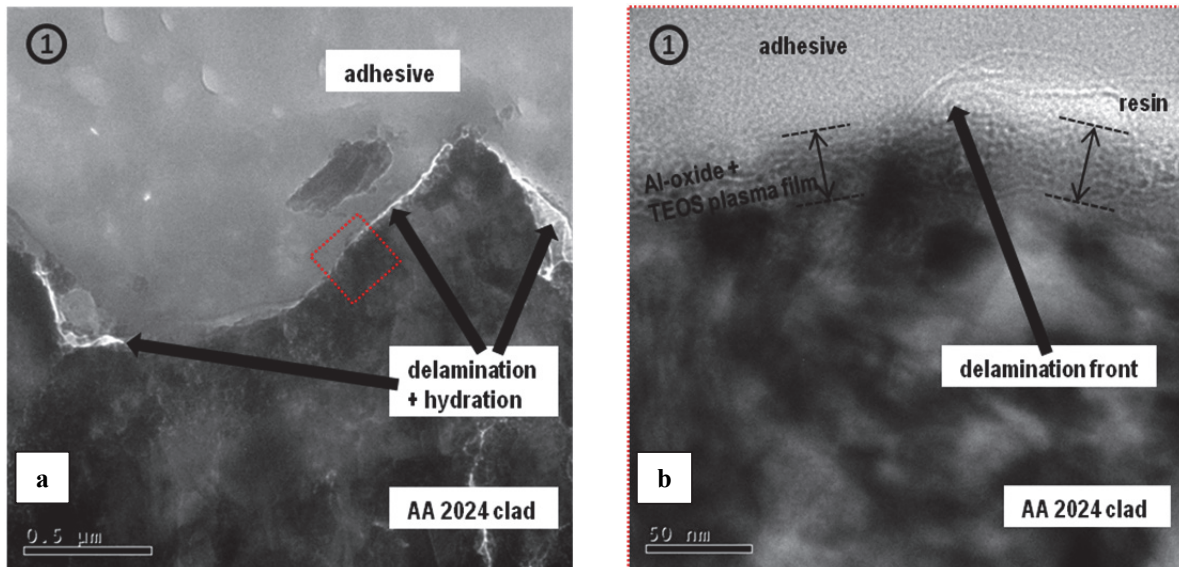


Fig. 4.40: TEM analysis of a TEOS (5 SLM) derived plasma polymer film on grit-blasted AA 2024 clad after bondline corrosion testing

Analysing the transition from intact to damaged interface (Fig. 4.40 b)), the delamination front can be precisely located in this instance. No significant discrepancies between the plasma film before and after the delamination are apparent, which shows that the interface between oxide and coupling film is stable; the plasma film remains on the adherend without distinct oxide film growth directly after delamination. Still, film growth after the displacement cannot be completely suppressed even by the thicker TEOS film leading to an obvious deterioration after several hundreds of nanometres. In contrast, this effect of hydration on the extent of total delamination appears marginal on plasma coated bare substrates.

Summarising the degradation process that occurs at the crack tip, it is assumed that the prevailing damage mechanism consists of a weakening of the interface between plasma polymer and adhesive due to moisture ingress. This leads to displacement of the polymer, which is then followed by advancing hydration that is more distinct on clad material. Oxide dissolution is not observed at the crack tip, while displacement and hydration are significantly reduced by the silica-like plasma films. It appears that the thicker TEOS derived film provides a better barrier against hydration than GPS plasma films, where the higher degree of hydration is likely to have a more distinct influence on the delamination. Overall, GPS deposition is still superior due to more stable bonding to the epoxy.

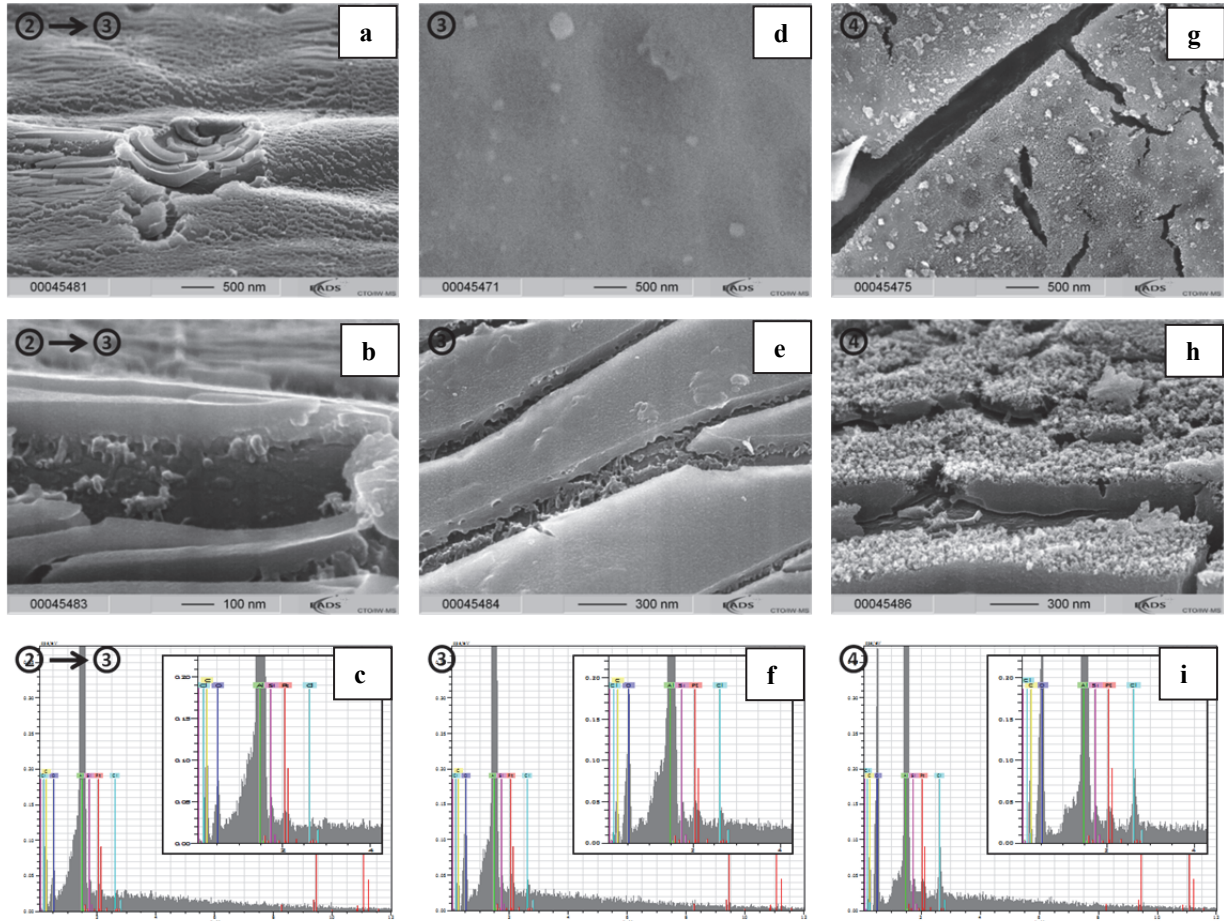


Fig. 4.41: SEM/EDX analysis of bondline corrosion of TEOS (5 SLM) plasma coated AA 2024 clad (HNO_3)

As just discussed, a narrow delaminated zone without distinct oxide modification is formed (zone 2) even on clad substrates. The width of this sector is strongly dependent on the employed surface pre-treatment, meaning the thicker HNO_3 derived oxides are more resistant to hydration than the thin oxide films formed after grit-blasting. This explains the pronounced difference in the degree of the bondline corrosion test when combined with plasma deposition. Adjacent to the relatively narrow zone 2, a several hundred micrometres wide sector with a very smooth surface (zone 3) is found on the HNO_3 conditioned TEOS plasma coated clad sample shown in the overview before. The whole surface within this area is covered with a compact and very even oxide/hydroxide layer, with thickness ranging from approximately 100 nm to 200 nm (Fig. 4.41 d) and e)). No sign of the initial interspersed oxide-plasma polymer layer is visible when examining from the top (d)). The side view on the cracked oxide layer (e)) indicates that the plasma film might be covered by the hydrated oxide. Further analysis of the transition between zone 2 and 3 (Fig. 4.41 a) and b)) supports this assumption and reveals that hydration actually does occur through the plasma film. This means that aluminium base material is dissolved and diffuses through the interspersed layer forming hydroxide concealing the film structure. Image a) shows that hydration does not advance

homogeneously along the delaminated bondline, but progresses locally after apparent ingress of the electrolyte. Areas of severe hydration, like the pit in the centre of the image, adjoin unharmed areas. Higher magnification (b) illustrates that the hydroxide growth proceeds right through the interspersed oxide-plasma polymer film. The coupling film remains on the substrate, which suggests that hydration occurs after the delamination.

As outlined before, hydroxide growth continues forming a smooth layer, before the surface of the layer becomes rough (zone 4). Dissolution and precipitation of hydrated oxide forms a porous surface structure on the meanwhile approximately 300 nm thick film. This is similar to the observations on uncoated and silane treated specimens. Consistent with previous results, the hydroxide layer is compact on the substrate side and porous only at the surface. As in zone 3 the plasma polymer is completely concealed by the hydrated oxide at that stage. Though not being visible, the plasma film can still be detected by EDX. Fig. 4.41 c), f) and i) display results of the EDX elemental analysis of three areas with different extents of hydration, reaching from first local oxide growth up to a fully hydrated oxide with a porous surface. In all measurements a stable Si signal is observed, whereas the O signal increases significantly. This finding is coherent with the results of the XPS analysis (Table 4.17), as Si is also only detected on the substrate side.

Even if hydration cannot be fully suppressed on clad base material, it does not cause delamination of the plasma derived coupling film from the oxide allowing at least a deceleration of the degradation. This aspect of the failure mechanism diverges entirely from the process found with silane based treatments and explains the positive effect on resistance to bondline corrosion by the employed plasma deposition.

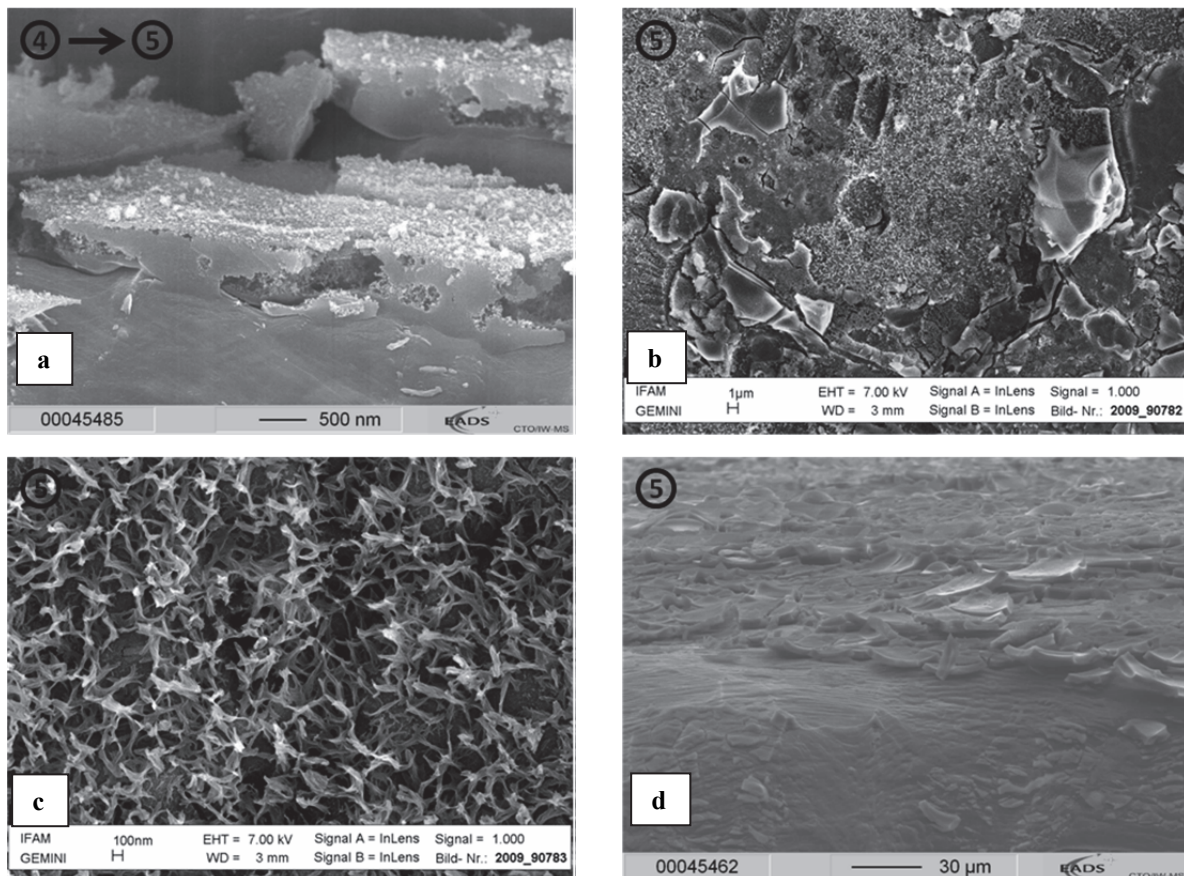


Fig. 4.42: SEM images of bondline corrosion on 5 SLM TEOS plasma coated AA 2024 clad (HNO₃)

The degree of hydration increases further towards the edge of the sample despite the mitigation of the degradation process. The corresponding detailed SEM analysis is displayed in Fig. 4.42. Hydroxide growth continues until a layer thickness of 500 nm to 1 μm is reached (a). At this point, not only the film surface is

porous, but almost the complete film is openly structured. The top view on the beginning of zone 5 (b), reveals that both severe hydration and precipitated hydroxide flakes (corrosion) are present simultaneously. The high resolution image of the hydrated area (c) reveals an interesting structure: the oxide exactly matches the one found on aluminium after immersion in boiling water. Venables detected an identical morphology after 25 min immersion of AA 2024 in DI water at 80 °C and could assign its modification to pseudoboehmite [77]. Similar pseudoboehmite structures were also found by Underhill and Rider on AA 2024 bare and 7075 clad alloys after 60 min immersion in DI water at merely 50 °C. These researchers also demonstrated that pseudoboehmite with a less distinct surface structure is formed already at 40 °C [159], which is not far from the bondline test temperature of 35 °C. The pH drop in the crevice apparently enhances the hydration intensity. Thus, oxide hydration is a key aspect of the degradation that occurs during exposure to salt fog, as well as in service.

Image d) displays the corroded clad surface in zone 5 further towards the edge of the coupon. There, exclusively the large and compact hydroxide flakes, which have already been observed for uncoated and silane/sol-gel coated samples, are formed. Oxide and aluminium are again dissolved directly by the electrolyte in that zone.

4.3.2.3 Bondline corrosion mechanism for Si-based treatments

Any previously described degradation was referred to as bondline corrosion independent of the underlying mechanism. The detected degradation processes are, in principle, similar for all inspected samples, but with variations depending on cladding, surface pre-treatment and applied coupling film. The aim of this chapter is now to summarise and group the previous findings on individual degradation steps and to correlate them to the postulated bondline corrosion mechanism. Moreover, electrochemical analyses are performed to enlarge the comprehension of the diverging joint behaviour. By doing so, the understanding of the mechanism itself is largely increased and the limitations and capabilities of the investigated coupling films are explained.

As a first step, the role of the adhesive in bondline corrosion is considered. Existing publications suggest an effect of adhesives on the degree of bondline corrosion and, for some adhesives, even on the mechanism. In spite of their impermeability to corrosive Na^+ or Cl^- ions, cured epoxy adhesives are permeable to water, and, thus, to potential pH changes. These changes can cause displacement or degradation at the interface. Furthermore, water can leach low-molecular substances, like hardener compounds, out of the polymer

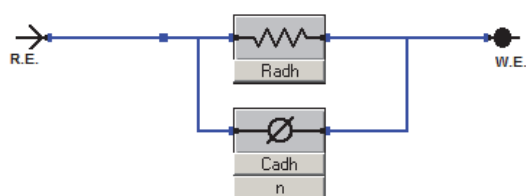


Fig. 4.43: Simple equivalent circuit model for fitting experimental data obtained for AA 2024 bare covered with FM 73 M.03
R.E.: reference electrode;
W.E.: working electrode

network; these can degrade aluminium oxide due to their alkalinity. The mobilisation of these components and the associated basic environment at the interface are referred to as alkaline failure mechanism.

However, Brockmann and co-workers already found that the FM 73 adhesive employed in this thesis is stable in water; hardly any leaching was detected. Even immersion in water at 70 °C for many weeks did not significantly increase the conductivity of the water and no increase of pH was observed – the water either remained neutral or the pH slightly decreased [2]. Similar stability of this adhesive was also observed after exposure to 95 % rh at 70 °C [229]. The electron microscopic studies presented earlier do not display any visual deterioration either. Moreover, extensive investigations on water diffusion in FM 73 aluminium joints at 50 °C revealed relatively slow water ingress through the bulk [221], which is by far not advancing quickly enough to explain the test results of exposure to humidity or especially to salt fog. Thus, neither an alkaline environment is created nor diffusion through the bulk adhesive does influence the corrosion mechanism.

To confirm this assumption, the change of the adhesive properties during exposure to an aqueous solution is investigated by electrochemical impedance spectroscopy (EIS) of so-called open bonds.³² It has been demonstrated that EIS is a powerful technique for assessment of stability and protection capabilities of high resistance polymer coatings on aluminium substrates [232], [233]. Due to the high insulating properties of the polymer, an FM 73 film with a lower nominal thickness of 0.13 mm is used (FM 73 M.03) in order to reduce the barrier. To investigate a potential effect of the surface treatment, two largely differing techniques are employed prior to bonding: PSA that showed the highest stability and etching in Smut-Go NC that displayed the lowest stability against bondline corrosion. Similar to the EIS investigations on coated aluminium alloys described by Raps [57], a tank filled with 0.05 m NaCl (aq) solution is placed on top of the adhesive, allowing water penetration perpendicular to the surface (Fig. 3.4). Impedance is measured over a frequency range from 10^5 to 10^{-2} Hz after various immersion periods.

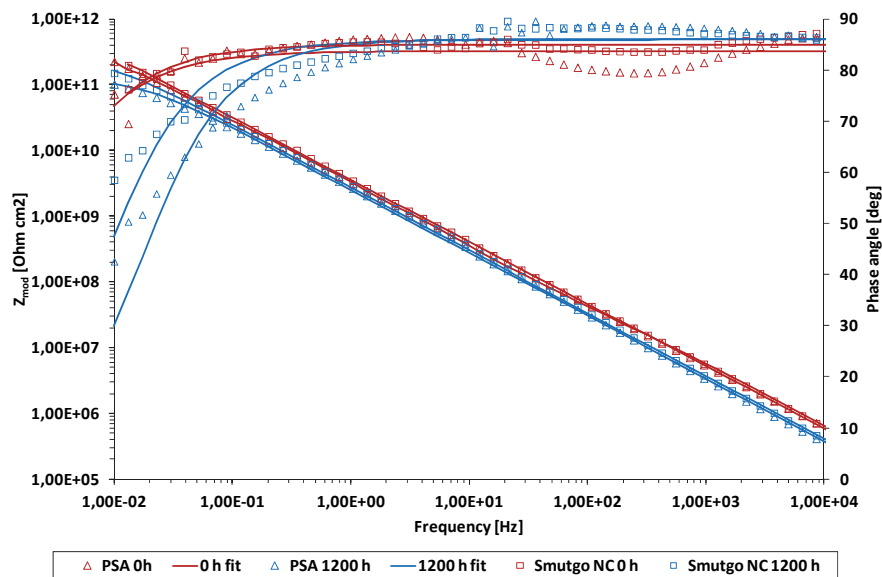


Fig. 4.44: EIS Bode plot of PSA and Smut-Go NC treated AA 2024 bare covered with FM73 M.03 after exposure to 0.05 m NaCl (aq) at RT

As examples, Bode plots of the impedance measured directly after immersion (red curves) in electrolyte and after 1200 h (blue curves) including the corresponding fit lines are shown in Fig. 4.44.³³ Interpretation of the impedance spectra is done by curve fitting based on equivalent circuits. A very simple circuit model (Fig. 4.43) containing a constant phase element (CPE) and a resistance in a parallel circuit is used for all exposure times, because the dielectric polymer remains stable. The high polymer resistance fully conceals the oxide and the electrolyte resistance over the complete frequency range, which makes additional circuit elements obsolete. Due to deviations from an ideal capacitor-like behaviour of the polymer film, capacitance needs to be substituted by the CPE, whose impedance is defined as

$$Z_{\text{CPE}} = (1/Y)(j\omega)^{-n}$$

where Y is the pseudo-capacitance, ω the frequency and n the variable describing the ideality, i.e. homogeneity, of the tested system. For all measurements n is between 0.93 and 0.96, which is very close to the ideal behaviour of $n = 1$, where true capacitance equals the pseudo-capacitance. In all cases the goodness of fit is below $0.9 \text{ E-}03$.

The impedance curves at the beginning of the exposure clearly display the capacitive behaviour of increasing impedance with decreasing frequency. Only one time constant is observed, which levels off at

³² Open bond: one AA 2024 bare adherend is “coated” with the adhesive without being bonded to another adherend; the adhesive is heat- and pressure-cured in an autoclave at similar conditions as regular bonded joints.

³³ All curves measured within this time interval are located in-between the 0 h and the 1200 h curves (not shown).

very high impedance values at low frequencies. Different from typical corrosion protection coatings, no general change of the capacitor-like behaviour is visible even after 1200 h. The impedance values reach the range of several hundred G Ω for low frequencies, where the oxide ($|z| \approx 10^6 \Omega$) usually becomes visible on polymer coated aluminium. Due to this immense barrier, the interface to the oxide and the oxide itself is completely hidden and only the time constant of the polymer is observed over all frequencies. A certain change of adhesive properties – visible as reduced impedance – is seen after the higher exposure time. Moreover, the slope of the double-logarithmic curve decreases slightly towards low frequencies for 1200 h immersion and the corresponding phase angle is further reduced. This is a clear indicator for water uptake in the adhesive. Still, these changes are relatively small in perspective to the long immersion time of 1200 h.

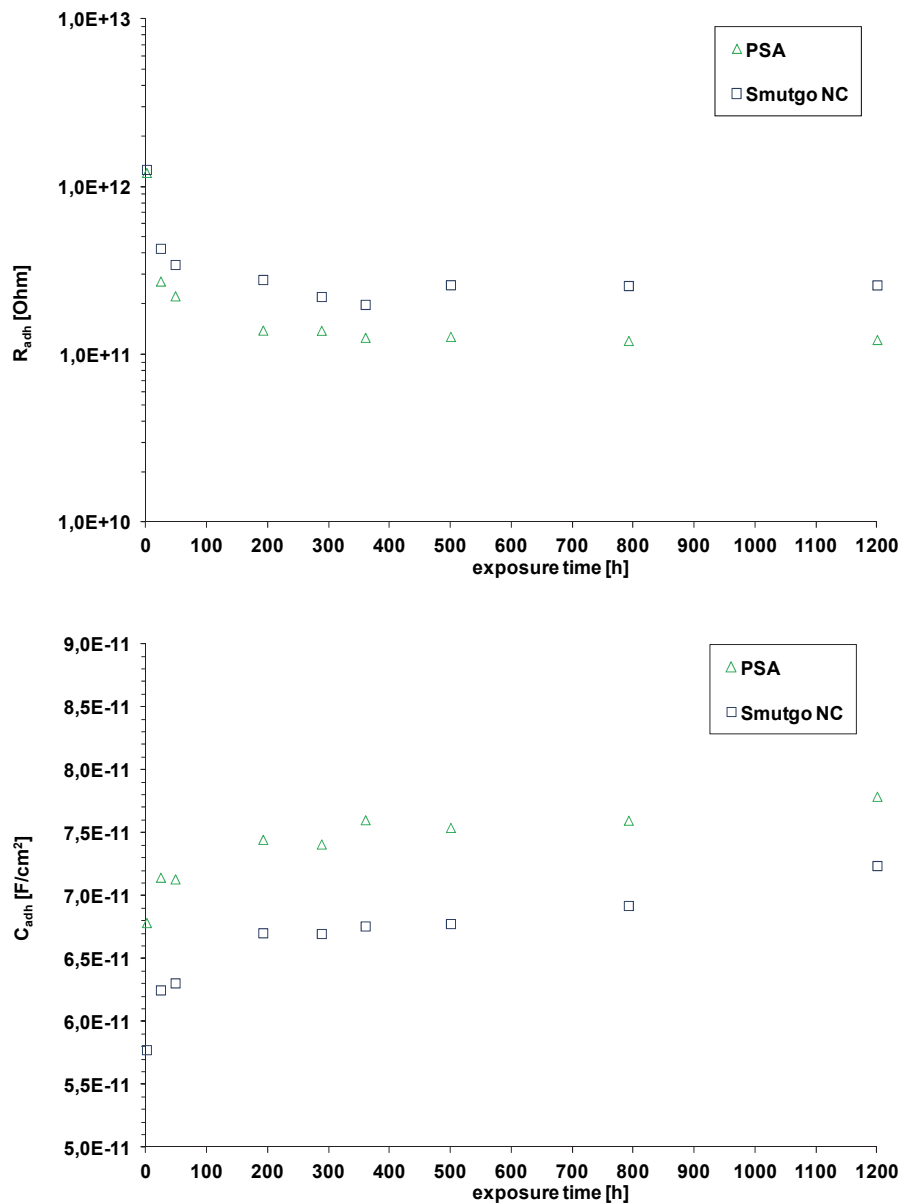


Fig. 4.45: Calculated resistance (top) and capacitance (bottom) of FM 73 film (0.13 mm nominal thickness) on AA 2024 bare adherends exposed to 0.05 m NaCl (aq) solution

Fig. 4.45 displays the corresponding calculated resistance and capacitance values for various immersion times up to 1200 h. On the one hand, polymer resistance decreases after immersion, reaching a stable

minimum already after ca 200 h, whereas, on the other hand, capacitance increases with time up to 1200 h. No further increase of capacitance is observed after 1200 h (not shown), which means that saturation level is achieved – even at the aluminium interface. As expected, due to the significantly higher dielectric constant of water ($\epsilon_w = 80$, RT) compared to epoxy polymers ($\epsilon = 3-4$) the film capacitance is increased while resistance is reduced. The relatively fast water uptake at the beginning, which decelerates more and more approaching saturation level, roughly indicates Fickian type diffusion. This is consistent with published investigations of FM 73 bulk diffusion [2], [221]. As previously stated, bulk diffusion of epoxy polymers was found to be too slow to explain the obtained bondline corrosion results. However, interface diffusion within some structural adhesive was found to be six to 14 times faster [154], [155], which means that water saturation of the polymer is achieved more rapidly at the interface. Water permeation can be easily quantified from the ratio of capacitance using the empirical equation proposed by Bierwagen et al. for high-barrier epoxy films [232]:

$$\phi = \frac{C(t)/C_0}{\epsilon_w} - 1/\epsilon_w$$

where ϕ is the volume fraction of water in the adhesive, $C(t)$ is the capacitance after immersion time t and C_0 is the initial capacitance directly after immersion. For the samples employed, the calculated saturation concentration of water is 0.18 % (Smut-Go NC) and 0.32 % (PSA). This water ingress can be considered as very low and insufficient to harm the metal surface below. SEM analysis of the aluminium surfaces after 4800 h of immersion did not reveal any visible changes of the oxide films, neither for PSA nor for Smut-Go NC surfaces. Despite its water uptake, the adhesive film is still intact and protects the surface from degradation, which explains that no difference due to the surface conditioning techniques is apparent. Even if diffusion through FM 73 might progress significantly faster at the interface (when compared to the bulk), water uptake and diffusion through the adhesive cannot explain the degradation found after bondline corrosion testing. Therefore, the diffusion through the employed adhesive does not play a decisive role in the degradation mechanism in this investigation.³⁴

Due to the absence of any significant degradation and leaching, alkaline cathodic corrosion (chapter 2.3.2) does not occur when using FM 73. Thus, only the anodic corrosion mechanism is relevant.

In summary, there are 3 major forms of damage observed in all previously presented samples. They all are part of the bondline corrosion and must be distinguished from each other:

- hydrodynamic displacement of the adhesive,
- hydration (including hydroxide dissolution and reprecipitation) and
- corrosion, i.e. direct anodic aluminium dissolution.

The extent of these processes varies depending on the choice of coupling films, surface pre-treatment and cladding. In the following paragraphs, these damage types are discussed individually with a specific focus on the effect of coupling films.

Hydrodynamic displacement

All tested samples, as well as the published test results of anodised specimens, display an area of delamination close to the crack tip, without visible signs of corrosion after bondline testing. However, electron microscopy reveals apparent changes in the oxide of this region. These oxide changes can either be the origin of the failure or the outcome of interfacial disbonding upon contact with moisture. Such delamination without detectable oxide damage in humid environments is referred to as hydrodynamic displacement. The SEM investigations on uncoated adherends clearly show that hydrodynamic displacement at the bondline precedes the oxide transformation in humidity, as well as in salt fog. When comparing mere humidity with the corrosive environment, the overall extent of delamination is significantly increased (factor 2) by the occurrence of initial corrosion. It is likely that the associated reduction of pH in the crack tip is the reason for the enhanced displacement. This is not surprising, as the

³⁴ The use of a polymer primer with higher water saturation concentration may lead to a different behaviour.

prevailing pH values of approximately pH 3-4 are below the stability range of the amphoteric aluminium oxide.

An increase in stress, induced by the formation of the corrosion products in the bondline would also be a feasible cause for this augmentation. However, reference samples containing a wedge in the bondline to investigate the influence of additional loads did not show any increase in delamination at the crack tip; bondline corrosion still advances from the sample edges similarly to unstressed joints. Hence, enhanced displacement due to higher stresses caused by formation of corrosion products in the bondline can be excluded. The detected lack of influence of mechanical stresses is consistent with the absence of a dependency of the bondline corrosion on the thickness of the adherends reported before [2].

Sole delamination without oxide degradation has not been observed for anodised samples. It is assumed that the microcomposite formed between the porous anodising oxides and the penetrating polymer with its associated tremendous increase of interface fully prevents any impact of hydrodynamic displacement.

The obtained results show that the presence of silanes at the interface suppresses the hydrodynamic displacement completely. Besides enhanced adhesion due to strong bond formation to the oxide and the epoxy, it is likely that the hydrocarbon part repels water molecules and reduces moisture ingress at the interface. Despite this distinct interface stability, silane/sol-gel coated substrates are not very resistant to bondline corrosion, because failure is caused by a pronounced oxide transformation. This delamination entailed by degradation must be distinguished clearly from hydrodynamic displacement and will be discussed at a later stage.

Analogous to the damage behaviour detected during cyclic fatigue and wedge tests, plasma coupling films decrease the hydrodynamic displacement, but cannot fully suppress it. Displacement is still considered as the main rate-determining mechanism for plasma coated substrates, in particular on bare substrates. Among the two APPJ-CVD precursors, GPS reduces hydrodynamic displacement to a larger degree than TEOS, which confirms the effect of functional groups at the film surface.

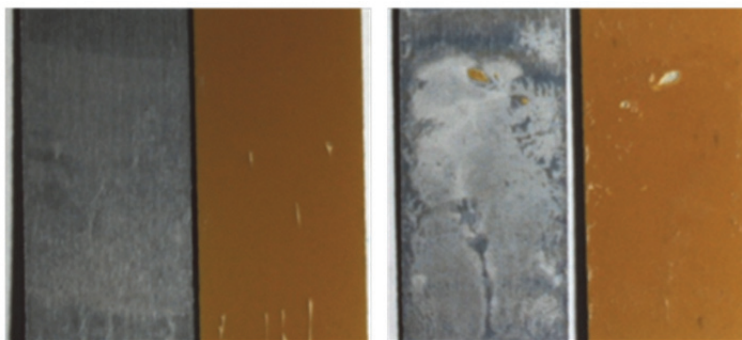


Fig. 4.46: Bondline corrosion of 1 SLM HMDSO plasma coated AA 2024 bare (left) and clad (right) after 30 d SST

Even though hydrodynamic displacement precedes hydration and aluminium dissolution, it cannot be considered autonomously, because corrosion amplifies the extent of delamination: the delaminated area of plasma coated samples is significantly larger after exposure to salt fog than after exposure to a mere humid environment. Moreover, the difference in affected area between clad and bare adherends is by far more pronounced in corrosive atmosphere. This effect can, on the one hand, partly be ascribed to the higher rate of hydration on clad substrates; the role of hydration becomes more important with the strong displacement decrease for GPS-plasma coated substrates. On the other hand, it is assumed that the pH reduction significantly affects the displacement of the polymer-film interface. This is supported by bondline corrosion test results of HNO_3 conditioned AA 2024 bare and clad adherends coated with a 1 SLM HMDSO plasma barrier film. After 30 d of SST the compact 200 nm thick plasma film still completely suppresses hydration and aluminium dissolution on both bare and clad samples. However, the plasma film cannot prevent corrosion at the open edges. As discussed before, the dissolution of the sacrificial clad layer creates a more aggressive environment than the local elements of the bare material. Therefore, the clad

joints are fully delaminated, whereas the bare joints are completely intact (Fig. 4.46). Chapter 4.1.3 already excluded HMDSO plasma deposition from being a suitable surface preparation. Due to its poor adhesion to the epoxy, bonds fail interfacially even if the bondline is not degraded. Nevertheless, the difference in delamination during or after the salt spray test can be clearly distinguished on the metal surface.

In summary, acidity-enhanced hydrodynamic displacement is considered the primary degradation cause for uncoated and plasma coated bare joints. The same is assumed for plasma coated clad adherends. With uncoated clad substrates, oxide degradation advances so rapidly that displacement and degradation cannot be clearly separated. In any case, the displacement is strongly decreased by the plasma derived coupling films. Silane and sol-gel coupling films even prevent this aspect. As the extent of bondline corrosion is significantly higher for silane/sol-gel treatments than for plasma films, it seems clear that displacement is only one part of the overall degradation mechanism and may not be considered in isolation from hydration and corrosion. However, dissolution of the initial oxide at the crack tip, as described in the initial study on the bondline corrosion mechanism, is not observed.

Hydration

Chapter 2.3.1 points out that aluminium oxide is prone to hydration in hot-wet atmosphere causing an initial increase in film thickness and a loss of porosity [77], [234]. This oxide growth is observed on all joints exposed to salt fog and on most of the joints immersed in a hot-wet environment (if exposure time is sufficiently long). Hydration is found to be either delamination-cause, like for the silane/sol-gel coated substrates, or an effect following displacement at the interface. In some cases, the question of cause and effect of hydration and displacement cannot be answered unambiguously, because both processes contribute to delamination in parallel. Nevertheless, bondline corrosion test results reveal that the influence of hydration on the delamination mechanism increases with stability of the interface. The hydration process detected during SST is quite similar to the one found by Venables on AA 2024 bare immersed in DI water at 80 °C, who observed a reduction of porosity due to pore-filling followed by a roughening until the characteristic pseudoboehmite structure (Fig. 4.42 c)) is formed [77]. The pseudoboehmite structure is not found on all samples as the region of pronounced hydration overlaps with the sector where corrosion occurs. In any case, hydration precedes direct anodic aluminium dissolution, which is consistent with the bondline corrosion studies by Brockmann et al., who detected oxide hydration within the bright crescent and who indicated that oxide change is the primary cause of failure [2]. However, Brockmann et al. identified the acidic dissolution of the initial oxide as primary failure cause. Here, hydration is found to occur before the formed hydroxide is then dissolved. It is also assumed that hydration is enhanced by the acidic environment in the crack tip.

In any case, the distinct influence of hydration on bondline corrosion and the associated importance of oxide quantity is another aspect that explains the superiority of anodising compared to sole pickling. Furthermore, the prevailing hydration is very likely to be the reason why PAA treated adherends perform at least as good as chromic acid anodised ones, even though PAA oxides are thinner and more porous. While CAA oxides consist of Al-oxide with a very low chromate concentration, PAA films contain a significant amount of phosphates that prevent hydration.³⁵ Both surface pre-treatments employed here, however, do not contain any phosphates or other hydration retardants. Hence, solely the oxide quantity is decisive, which explains that HNO₃ conditioned samples are by trend more resistant to bondline corrosion than grit-blasted specimens.

Distinct differences in the degree of bondline corrosion are apparent, when considering the degradation of coated joints. Even though silanes stabilise the interfacial bonds against aqueous attack even under external loads, plasma treated joints are even more stable in mere humidity if no loads are applied. Different than the silane/sol-gel coatings, the plasma film fully suppresses hydration in this hot-wet environment. Regarding the degree of hydration, it is evident that it is significantly impacted by the climate formed at the delamination front. Thus, hydroxide growth is more pronounced on silane/sol-gel treated clad joints

³⁵ Phosphates are known as sealing poison, i.e. PAA cannot be sealed in water even at elevated temperatures.

exposed to humidity compared with bare ones. This effect becomes more distinct in the SST, where hydration is more severe than in humidity, in particular on clad substrates, where the pH reduction is more distinct. This special bondline behaviour is antithetic to the hydration observed on not bonded, uncoated AA 2024 in water, where bare tends to hydrate stronger than clad [77], [159]. Consequently, the observed trends suggest that hydration is enhanced by the pH decrease; it is assumed that the pH shift is sufficient to reduce passivation and that it increases the hydration without dissolution of the existing oxide film. Therefore, signs of intensive hydration are found in spite of the relatively moderate temperature of 35 °C (Fig. 4.42 c)). Hence, the stability of oxide, respectively coupling film, in acidic environments appears to be crucial for the bondline corrosion resistance.

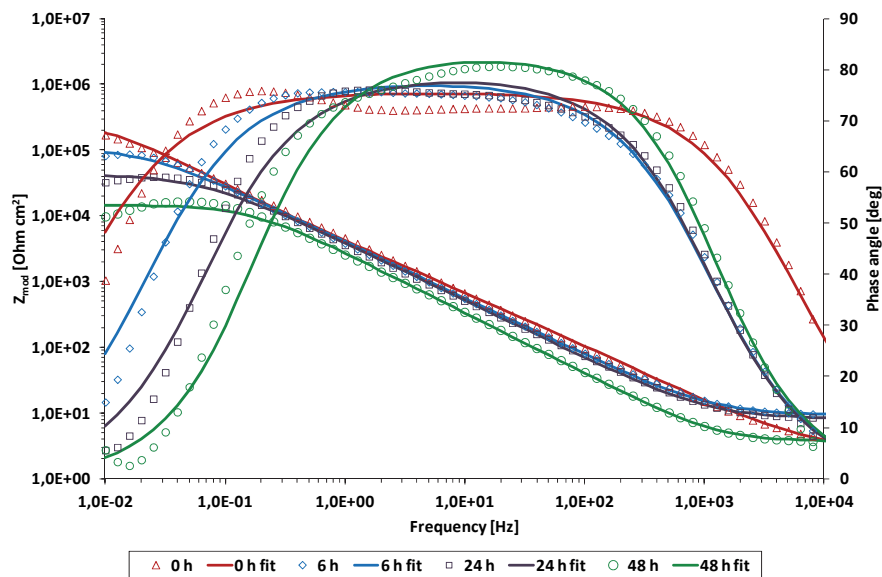


Fig. 4.47: EIS Bode plot for HNO_3 etched AA 2024 clad aged at pH 4 (23 ± 2 °C)

To explain the diverging behaviour of adherends coated with wet-chemical silane based and with plasma deposited coupling films, EIS measurements after exposure of the substrates to pH 4 buffer solution are conducted. In these measurements an electrolyte cell is placed directly on the oxide or coupling film without additional application of a polymer. The EIS measurement on the open bonds above have shown that the adhesive fully covers the metal surface, which is the reason why the oxide and coupling film need to be directly exposed to the electrolyte. pH 4 is chosen as it is still in the detected bondline pH range and as its acidity is close to the stability limit of the amphoteric aluminium oxide, which is preferred to keep transformation speed low. As impedance measurements in the buffer solution do not lead to meaningful results, the substrates are only exposed to this solution. After exposure, impedance is measured in a 0.05 m potassium sulphate solution (pH 7). After that, the sulphate solution is exchanged again by buffer solution to continue the ageing. The low concentrated sulphate solution is chosen as measuring solution, because only very limited reaction with the oxide is expected. EIS is an integral measurement, considering the wetted surface as a whole. Therefore, HNO_3 conditioned clad samples are used, because this combination of surface pre-treatment and base material provides the most homogeneous surfaces and, thus, the most reproducible results.

Fig. 4.47 displays the bode plots with corresponding fit curves of EIS measurements of HNO_3 etched AA 2024 clad after different immersion intervals in pH 4 solution. Like for the impedance measurements of the open bonds, interpretation of the results is done by numerical fitting. Due to low reactivity of the measuring solution, the oxide does not significantly change or react during the measurement. A simple CPE equivalent circuit model provides the best fit with measured data for all ageing periods. The corresponding electrical circuit model for this stable oxide/hydroxide contains the capacitance in parallel to the oxide resistance and the solution resistance in series (Fig. 4.50 a)). As the oxide does not behave like an ideal

capacitor, it is replaced by a CPE. This circuit is also referred to as simplified Randles cell (circuit). Measurements are performed from 10^5 to 10^{-2} Hz, but the oxide becomes visible only at around 10^3 Hz and below. At higher frequencies, the electrolyte characteristics (its resistance) can be seen.

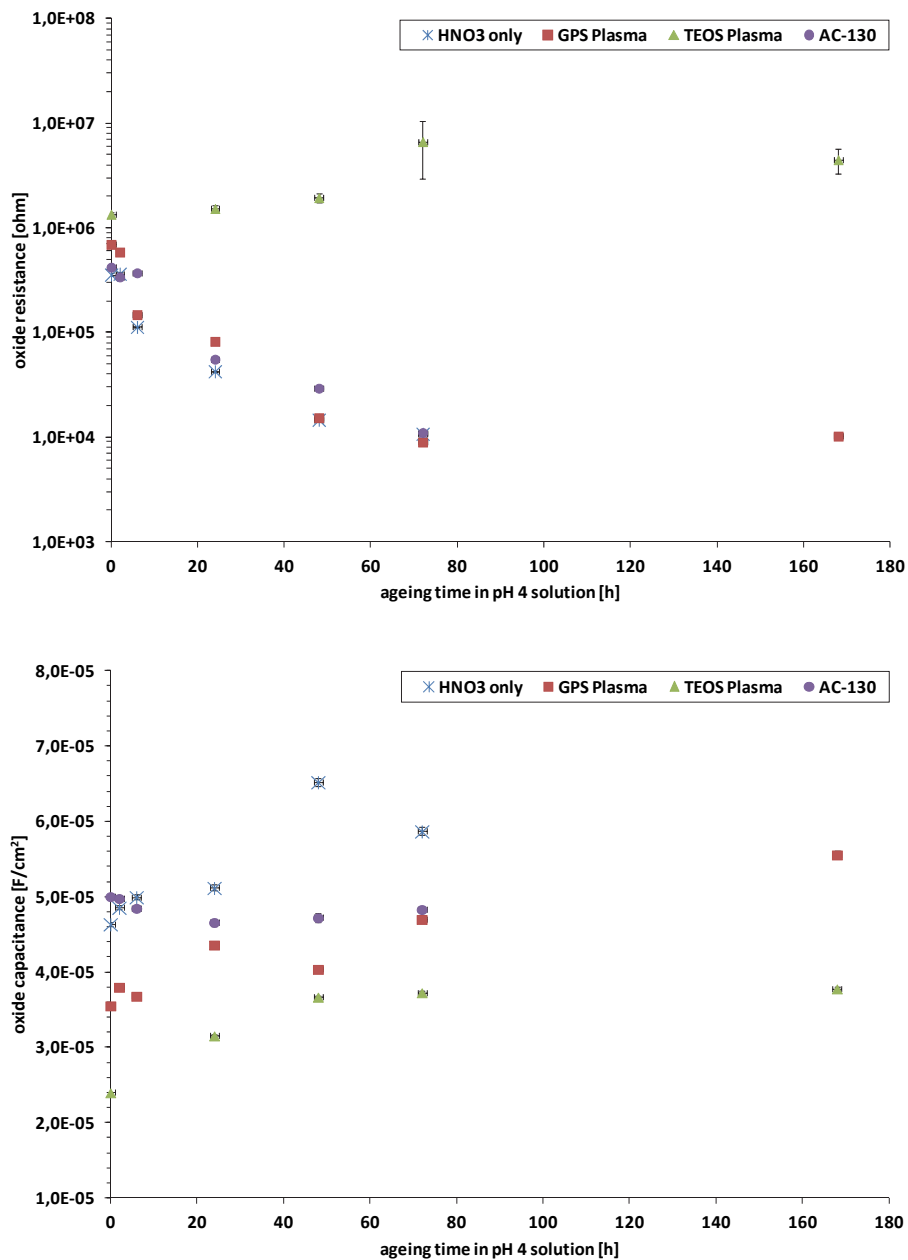


Fig. 4.48: Calculated resistance (top) and capacitance (bottom) of oxide or interspersed oxide-plasma films on HNO_3 etched AA 2024 clad

Before ageing in acidic puffer solution, the HNO_3 derived oxide shows capacitive behaviour with only one time constant across almost the whole frequency range. Only at frequencies below 0.1 Hz, the resistive element becomes visible by a drop of the phase angle. Hence, the oxide can be considered as intact insulator. Already after 6 h of immersion at pH 4, the resistive part becomes more pronounced resulting in an impedance decrease at low frequencies and a shift of the phase angle drop to the right (towards higher frequencies). This effect continues with ageing. After 48 h immersion, the impedance is already significantly lower across all frequencies. After 24 h, and even more so after 48 h in pH 4 solution, another time constant starts to become visible, which cannot be fully explained: It is assumed that some diffusion

effects through the hydrated but still porous oxide occur, as well as some repassivation effect in the less acidic solution. Yet, no other equivalent circuit model including Warburg impedance (diffusion limitation) or virtual inductor (repassivation) provides better matching of the measured impedance at low frequencies. The simple model of a stable oxide remains the best fit and is considered as sufficient to estimate oxide resistance and capacitance. Both the reduction of impedance and the calculated oxide resistance (Fig. 4.48) that appear with ageing time, reveal that the oxide is not stable in aqueous media at pH 4. The attack of the oxide is accompanied by an increase of oxide capacitance, which is very likely to be caused by hydration, as capacitance typically rises with concentration of hydroxide or incorporated water within the oxide film.

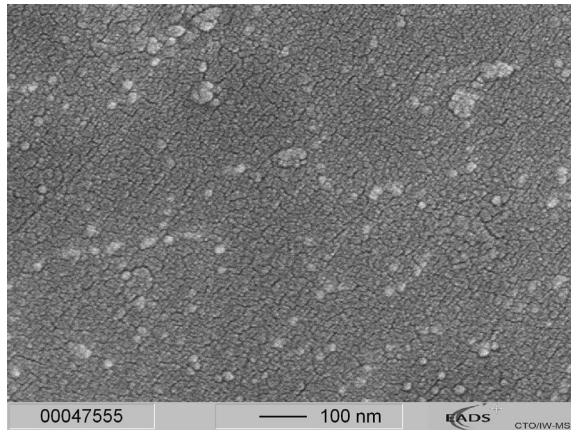


Fig. 4.49: Top-view SEM image of a HNO_3 etched AA 2024 clad surface after 72 h immersion in pH 4 buffer solution

Fig. 4.49 shows an SEM image of the oxide after 72 h exposure to pH 4 solution. Compared to the initial state (Fig. 4.12), the topography has clearly changed, displaying strongly reduced porosity due to hydroxide growth. Despite the increase in oxide thickness, the barrier properties (the resistance) has decreased due to the transformation of oxide into hydroxide. Moreover, the oxide film is riddled with various valleys or cracks, which provides another explanation for the distinct decrease of oxide resistance. Evidently, the degree of hydration in solution at RT is not as pronounced as during immersion in salt fog at 35 °C. Nevertheless, the test conditions and the observed degradation are very similar to bondline corrosion testing, and thus, EIS can serve to explain the bondline corrosion characteristics of an aluminium surface. In the

following paragraphs, the impedance measurement of the HNO_3 derived oxide are used as reference for the measurements of the coated substrates to determine the protective effect of the coupling films.

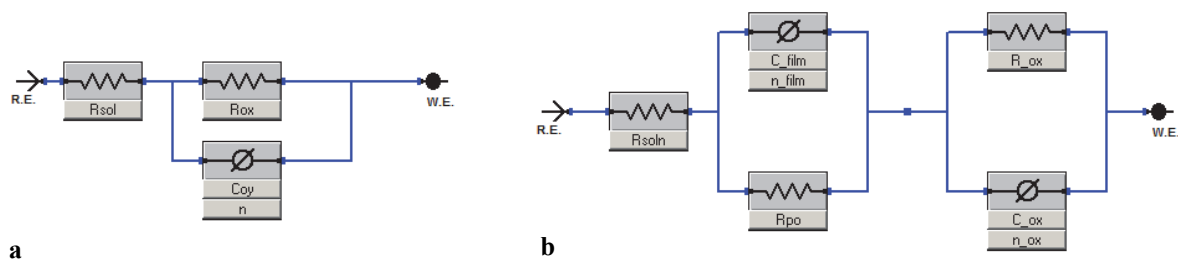


Fig. 4.50: Equivalent circuit models for HNO_3 pickled AA 2024 clad (R.E.: ref. electr.; W.E.: working electr.)
 a) solely etched or coated by APPJ-CVD
 b) coated with AC-130

Similar EIS measurements are performed on substrates after deposition of AC-130 to evaluate the resistance of silane based films to acidity. Measurements of GPS coated substrates are found to be neither stable nor reproducible. Moreover, capacitance and resistance do not differ significantly from the results of sole HNO_3 etching. This is not surprising, because GPS treatment forms very thin films of uneven thickness that penetrate the oxide but do not form a closed film on top. As electrolyte diffusion occurs normal to the surface with this analytical technique, the GPS film alone is not sufficient to create a stable and measurable barrier. For this reason, only AC-130 is considered. As the adhesive is thermally cured, the AC-130 film is cured for 60 min at 120 °C to simulate any increased cross-linking of the sol-gel film that might occur during this process.

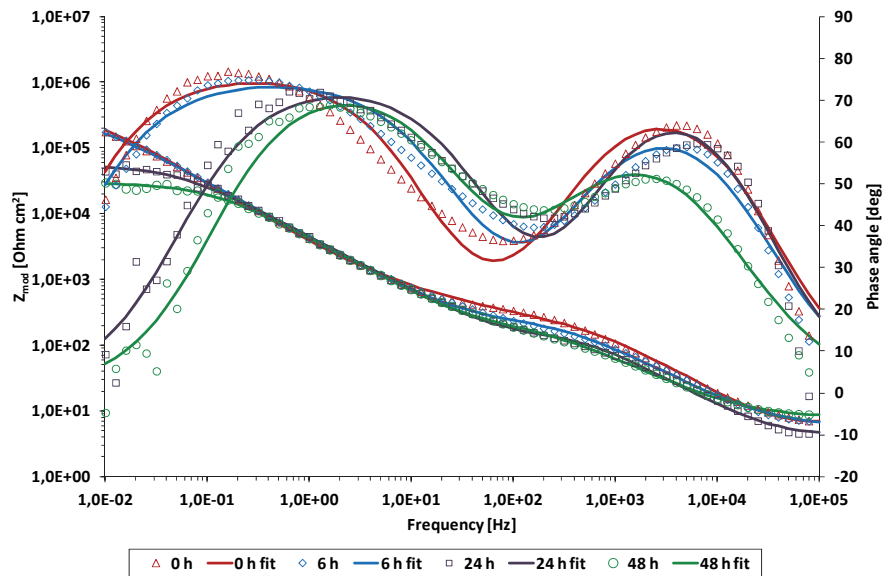


Fig. 4.51: EIS Bode plot for AC-130 coated HNO_3 etched AA 2024 clad aged at pH 4 (23 ± 2 °C)

Fig. 4.51 shows Bode plots of the measured impedance of the AC-130 coated AA 2024 clad sheet after different exposure intervals. Prior to ageing, the impedance curve differs significantly from the one of the solely etched base material. A distinct increase of impedance roughly between 2×10^4 and 10 Hz is observed, which can be associated to the sol-gel coating. This local impedance increase is accompanied by an additional time constant around 100 Hz. The corresponding drop of phase angle indicates resistive behaviour of the coating, which is consistent with published EIS results of sol-gel barrier coatings [57]. However, the impedance increase is relatively small and no distinct plateau is formed, which suggests that the barrier is not very strong and that the coating resistivity is very low. For low frequencies, the curve progression is very similar to the uncoated reference, which means that only the oxide film is visible in that region.

As for the uncoated oxide, no dissolution of the sol-gel coating by the neutral low concentrated sulphate solution is expected. Thus, the basic “stable oxide” model simply needs to be extended by an additional circuit, consisting of coating resistance and CPE (Fig. 4.50). It must be emphasized that a model of circuits in series needs to be applied with care, because various values will lead to a good fit. Therefore, values need to be assigned attentively; as starting point, oxide capacitance and resistance values of the sole HNO_3 measurements are employed in this case. Moreover, they are constraint to deviate less than an order of magnitude from this reference. Nevertheless, comparing the AC-130 spectra with the HNO_3 oxide spectra, the mathematical model is very likely to correspond to a physical model of an electrolyte that penetrates the coupling film due to its low barrier. The electrolyte is then in direct contact with the more stable oxide. Continued ageing confirms this assumption of weak barrier properties, as the impedance increase, i.e. the coating, becomes less and less distinct with time. After 24 h in pH 4 solution, the film is hardly visible when looking at the impedance, whereas the time constant is still apparent. The lack of stability of the silane based film in pH 4 solution is consistent with the pH dependent stability investigations of GPS films conducted by Johnsen and co-workers. These researchers observed a strong increase of GPS film desorption from AA 6060 alloys in pH 4 at 40 °C compared to pH 7, whereas the silane film was found to be stable in alkaline environments [228]. The left part of the Bode plot (low frequency) reveals similar behaviour as observed for the plain oxide. The only difference is a certain time delay. Despite an already deteriorated sol-gel film the oxide appears to be fully intact after 6 h, whereas the HNO_3 reference displays a reduction of impedance towards resistor-like behaviour at the same exposure time. This drop is observed with the coated sample only after 24 h.

When calculating the oxide resistivity, the above mentioned time delay becomes apparent as well: for the first 6 h, the oxide resistance remains at the level of an unharmed film, whereas degradation of the reference is observed already after 2 h. After 24 h, the difference between coated and solely conditioned substrate is only marginal, meaning that both oxides are degraded to the same degree. With regard to the oxide capacitance, no significant changes are observed over ageing time, which indicates that no further hydration occurs. However, the capacitance is already at a relatively high level, which lies above the initial level of the reference oxide at the very beginning of the ageing process. As the pH of the AC-130 sol lies also between 3 and 4, a certain acidity-enhanced hydration of the oxide might already have happened during deposition. In any case, the observed hindrance of further hydration is consistent with a retarding effect on hydration of AA 2024 clad caused by a GPS film, which was described by Arnott et al.. They showed that the silane film delays hydration of the open surface exposed to 50 °C, 98 % rh until it is leached off the surface [126]. Rattana et al. confirmed this finding and demonstrated that the silane needs to be hydrodynamically displaced before hydration occurs like on unprotected substrates [124].

No delay of oxide deterioration is detected using EIS of GPS coated samples, which is likely to be caused by the low film thickness and the acidic solution. In general, the water repelling behaviour of silanes is thought to have a greater effect on the stability of the interface limiting water ingress than on actual ageing resistance. As seen with AC-130 sample, an increase of coating thickness apparently entails an increase of barrier properties and a certain delay in oxide ageing. Regardless, the protection capabilities of the sol-gel film in acidic media have to be considered as comparatively low.

Bondline corrosion tests are also performed after deposition of an approximately 1 µm sol-gel film of quite similar chemistry as AC-130, but with higher crosslink-density derived from changes in chemical formulation and dedicated temperature curing. This serves to illustrate the positive effect of a barrier increase on the one hand, but also to show the limitation of the silane based films on the other hand. Independent of cladding or surface pre-treatment, the delaminated area is reduced to about 50 % when compared to AC-130 results. This significant improvement clearly demonstrates a positive effect of the enhanced barrier properties; diffusion of the acidic solution through the coating is decreased. Nevertheless, this system is still by far inferior to the few nanometre thick plasma coatings. A closer examination of the barrier sol-gel coated interfaces reveals that the oxide is already hydrating below the intact sol-gel film. Contrary to AC-130 and GPS, where oxide growth directly leads to delamination of the coupling film (and thus the adhesive), hydration occurs underneath the apparently intact film, where the joint still fails cohesively. Fig. 4.52 a) displays the zone of hydration beneath the apparently unharmed sol-gel coating. Oxide thickness has largely increased and the oxide/hydroxide layer has ruptured. The oxide around the crack tip (Fig. 4.52 b)) has also already lost its characteristic HNO₃ structure. Hence, hydration progressing along the oxide film is the primary degradation mechanism. As the detected degree of hydration is distinctively lower during exposure to mere humidity, it is evident that the pH reduction multiplies this degradation effect. This failure mechanism can be described as acidity-enhanced hydration mainly along the oxide film.

Therefore, the diffusion barrier through the film is less important than the increase of the oxide barrier by penetration of the oxide: Silane and sol-gel films penetrate the pores (Si is found throughout the oxide) but, as shown by EIS, they do not provide a stable barrier in acidic environments. In the vicinity of the degradation front, not all parts of the hydrated oxide are ruptured, whereas degradation intensity augments towards the edges, leading to macroscopic interfacial failure. Closer inspection of this area confirms that failure occurs again within the oxide/hydroxide film. SEM analysis of the adhesive side close to the beginning of the delamination area reveals that the adhesive is covered with the apparently intact sol-gel coating, which itself is covered by the hydrated aluminium oxide (Fig. 4.52 c)). Fig. 4.52 d) shows that about 100 nm hydroxide remain attached to the sol-gel film. This hydration derived failure is consistent with other hydration derived damages found in literature. Venables, who investigated oxide transformation during wedge testing of AA 2024 joints in 65 °C 100 % rh, observed that the crack propagates through the already hydrated oxide, which is found to be weaker than the initial oxide [77]. The fact that similar

hydration occurs during SST at significantly lower temperatures, again supports the assumption that the pH drop strongly enhances hydration.

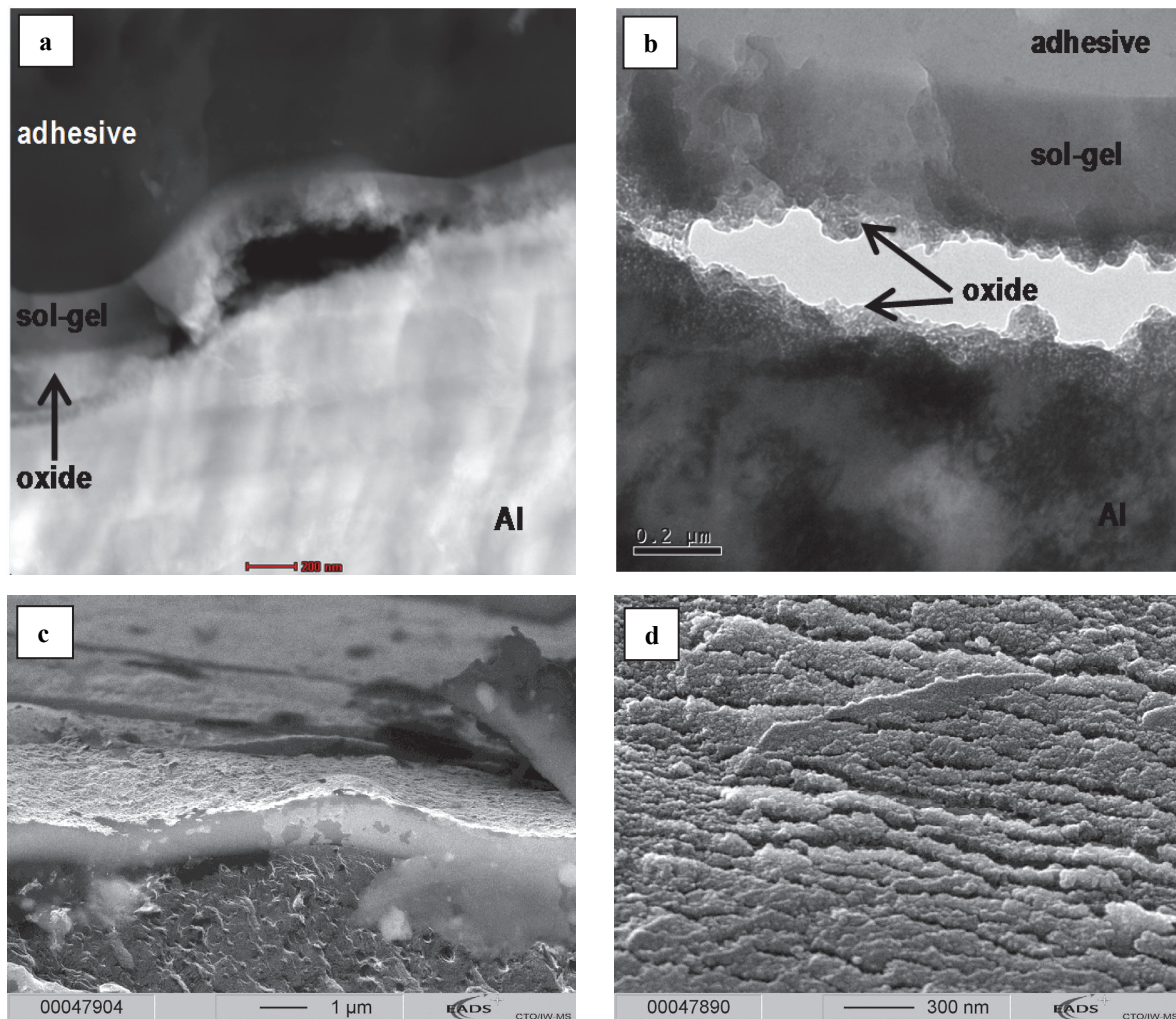


Fig. 4.52: Electron microscopy images of bondline corrosion failure of AA 2024 clad with barrier sol-gel film
 a) STEM below cohesively failed adhesive
 b) TEM at degradation front (below adhesive)
 c) SEM of delaminated adhesive
 d) SEM of hydrated oxide film covering the adhesive

Both, penetration into the oxide as well as the barrier properties of the penetrating medium against acidic aqueous solutions are crucial for bondline corrosion resistance. Despite the excellent barrier of the epoxy adhesive itself, the solely etched samples perform worst in the bondline corrosion test, because the adhesive does not enter the fine pores of the HNO_3 derived oxide. Normally, it can penetrate the larger pores of anodising layers to a certain extent. Full penetration is indeed decisive for the durability of anodising layers. PAA treated aerospace grade aluminium alloys were found to perform poorly in cyclic fatigue test in water if the epoxy adhesive is not penetrated. In that case, the PAA oxides displayed distinct signs of hydration in spite of the presence of phosphates [79]. However, similar tests with identical systems have shown stable joints without any pre-failure hydration if the oxide is filled with the polymer [163]. For this reason, the application of a low viscous primer onto the anodised surface is desired. Comparison of a bonding primer with and without chromate inhibitors showed that major reductions of bondline corrosion for anodised substrates is caused by the polymer – not the inhibitor [229]. Besides pure oxide quantity, the formation of a microcomposite with a high-barrier polymer is another factor explaining the excellent bondline corrosion resistance of anodising layers.

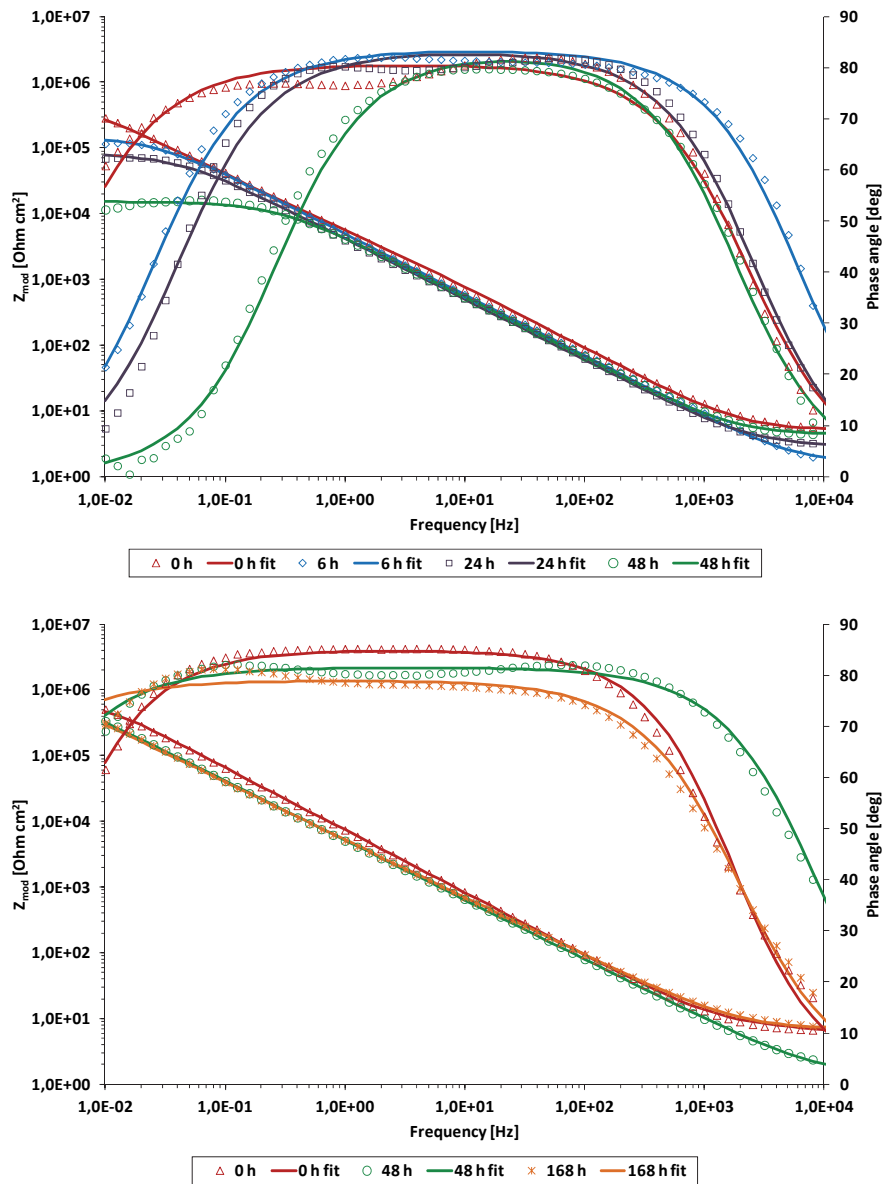


Fig. 4.53: EIS Bode plots for plasma coated HNO_3 etched AA 2024 clad aged at pH 4 ($23 \pm 2^\circ\text{C}$)
top: GPS Plasma (5 SLM) bottom: TEOS Plasma (5 SLM)

Reconsidering the bondline corrosion and the humidity exposure test results, the high stability of the thin plasma films is even more surprising: neither oxide quantity nor polymer penetration not even comes close to anodising. Yet, the absence of any hydration in the 35°C 100% rh test indicates that the silica-like plasma polymers are more resistant to aqueous attack than aluminium oxides. EIS measurements reveal a significant difference between oxide and silane behaviour. Bode plots of the GPS and TEOS plasma coated substrates are presented in Fig. 4.53. In contrast to the sol-gel film, the plasma film cannot be distinguished from the oxide. The interspersed layer appears as one homogeneous film with significantly higher impedance than the initial oxide. Therefore, the same equivalent circuit model of a stable oxide film is used for curve fitting purposes (Fig. 4.50). Before ageing in pH 4 solution, the impedance after GPS plasma deposition is roughly 50% higher across the whole frequency range than in cases without coupling film. With TEOS APPJ-CVD impedance is increased by a factor of approximately 2.5, i.e. impedance increases with coating thickness.

During immersion, the behaviour of the two plasma coated systems diverges: GPS derived plasma films do not provide enduring protection of the oxide under the test conditions, whereas the stabilising effect remains with TEOS plasma films.

With GPS deposition, only a slight delay of degradation is apparent in the calculated resistance diagram (Fig. 4.48). This is not unexpected, as the film thickness is below 10 nm and it is not assumed that the oxide is concealed. With EIS being an integral measurement over the whole exposed area, it is not suitable to estimate the stabilising effect of thin, not fully concealing films. Nevertheless, the bondline corrosion results strongly suggest that degradation occurs along the interface and there, the positive effect of the GPS plasma film is obvious. The resistance calculation (Fig. 4.48) shows that the resistance increase by the GPS plasma film only lasts for 2 h. After 6 h of exposure the film resistance is similar to that of uncoated oxide. Yet, the capacity of the interspersed film remains below the oxide/hydroxide capacitance over all ageing times, which indicates that the plasma polymer does not leach off the surface and that it does hardly hydrate. As expected, the capacitance of the silica-like film is lower than the one of the aluminium oxide/hydroxide, which is coherent with published results [235].

The stabilising effect of the plasma coating becomes apparent if a closed film, which seals the oxide, is deposited. The EIS Bode plots of a 5 SLM TEOS sample show stable capacitor-like behaviour over ageing time at pH 4. Contrary to the other systems, the drop of the time constant at low frequencies becomes less pronounced with time, which indicates that the barrier properties even increase during ageing. A calculation of the corresponding film resistance illustrates this effect, showing that the resistance actually increases with time. The observed reduction of impedance is caused by an increase of capacitance, which outweighs the slight augmentation of the resistance. Both effects can be explained by the continuous hydration of aluminium oxide. As seen in previous SEM investigations of the TEOS plasma coated substrates, the structure of the deposited layer is globular, i.e. the formed film consists of different spheres that accrete to each other. It is likely that some porosity remains at the sphere interfaces. Thus, it is assumed that hydration causes hydroxide growth through these pores similar to the findings in the bondline corrosion examination. Hydroxide growth clogs the pores, which is accompanied by a certain increase in resistance. Due to the high capacity of the hydroxide, this increase is rather low, whereas the increase of capacitance is more pronounced. In total, the capacitance of the interspersed film remains indeed significantly below the oxide reference, as the SiO_2 network is unlikely to hydrate. Relatively similar APPJ-CVD plasma layers with even higher organic content have been reported to be durable in acidic and alkaline environments between pH 2 to 11 [236].

SEM analysis of the EIS sample confirms the hydration assumptions based on the impedance measurements. Fig. 4.54 displays a HNO_3 pickled AA 2024 clad specimen coated with a 5 SLM TEOS derived plasma film used for 336 h EIS measurements. Images a) and c) show the surface area outside the measuring cell, images b) and d) show the surface inside the cell, i.e. after the exposure to pH 4 solution. The comparison of acidic ageing with mere exposure to ambient atmosphere reveals differences in film structure and thickness. Film thickness of the aged interspersed layer is around 130 nm, whereas the thickness of the non-aged film remains at the 80 to 90 nm of the initial state after deposition. Moreover, the film topography, which also remains unaltered in ambient air, has become smoother during exposure to the acidic solution; a more uniform and compact, i.e. less porous, film is formed. Hence, the degradation mechanism is comparable to that of bondline corrosion. The degree of the hydration is not as high as during exposure to salt fog due to the lower ageing temperature and exposure time. An associated EDX analysis, where a significant increase of oxygen concentration is detected, affirms the hydroxide growths. The ratio of the sum of elemental concentration of Al and Si divided by the oxygen concentration $(\text{Al}+\text{Si})/\text{O}$ decreases from 3.74 to 2.71 after the 336 h immersion.

Even though the positive effect of plasma deposition could only be demonstrated by EIS with the thick TEOS derived film, it should be kept in mind that the hydration either follows hydrodynamic displacement or advances through the oxide. As GPS plasma deposition strongly reduces displacement and hydration that

progresses through the oxide, similar or even better bondline corrosion resistance is detected for this system.

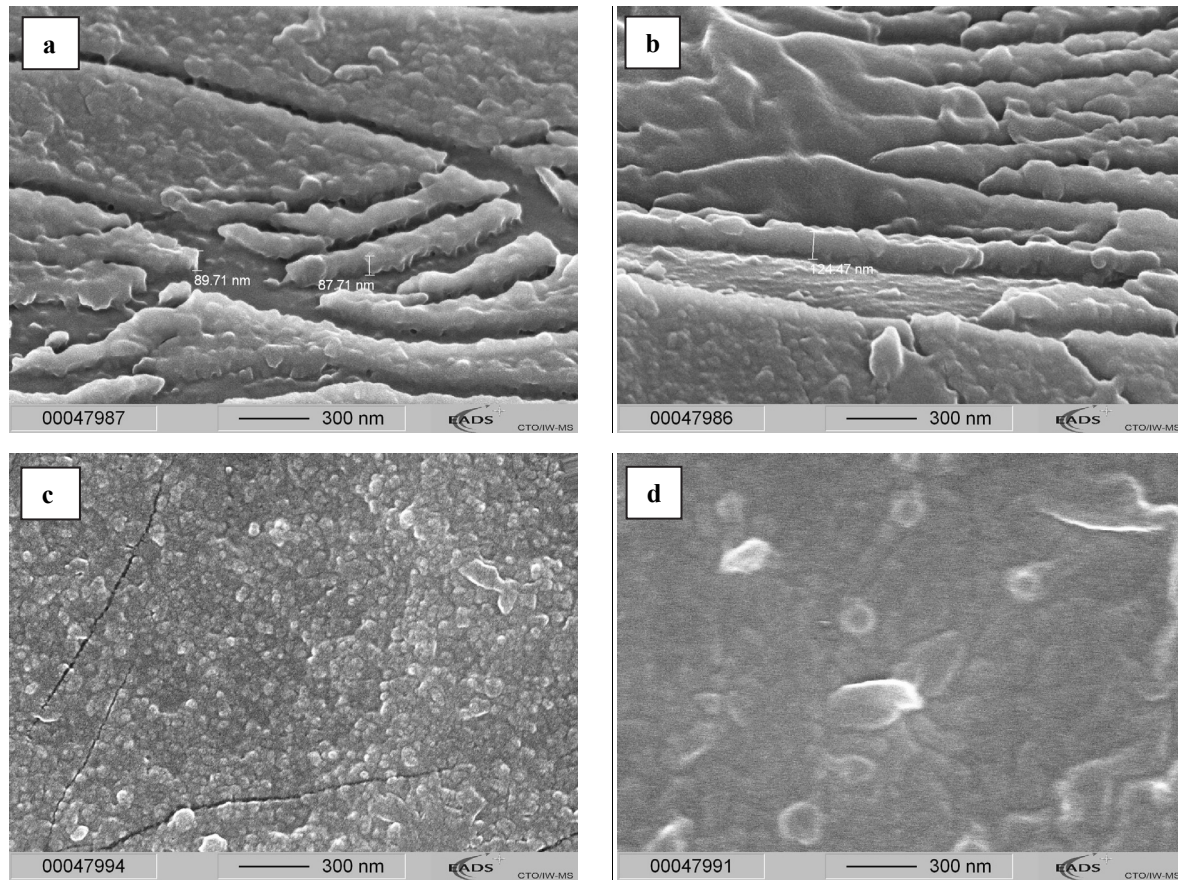


Fig. 4.54: SEM analysis of 5 SLM TEOS plasma coated AA2024 clad (HNO_3) after 336 h in ambient air (a, c) or pH 4 solution (b, d)

Summarising the effects observed for silane and plasma coated substrates, the postulated degradation mechanism of acidity-enhanced hydration can be confirmed. This part of the overall bondline corrosion process becomes more dominating with decreasing pH in the crack, e.g. on clad samples, as well as with increasing interface stability, i.e. when hydrodynamic displacement is suppressed. EIS of aluminium substrates exposed to pH 4 solution is shown to be a suitable and differentiating method to assess the protection potential of oxide and coupling films, as long as the films fully cover of the surface. Silane based films are very sensitive to acidic environments and, thus, can hardly reduce hydration. An increase of coupling film thickness does only have limited effect, because moisture diffusion advances mainly through the porous/textured oxide layer. This means that the penetrating part of the deposited films defines to a large extent the degree of hydration. Plasma films are immune against hydration or acidic attack and remain on the oxide, forming a stable protection barrier. On bare substrates, hydration of the bondline is almost completely prevented by plasma deposition due to the milder environment in the crack tip. On clad substrates, full suppression is not achieved, because of the more aggressive acidic environment; humidity progressing from the edges through pores in the coupling film and through the oxide itself. Under these conditions, hydrodynamic displacement is not the only rate-defining process and hydration contributes to the overall degradation speed of plasma coated adherends.

In any case, the formation of interspersed aluminium oxide plasma polymer layers strongly reduces degradation even with very low film thicknesses. Both, nature of the coupling film and initial oxide quantity influence the resistance against hydration. Consequently, HNO_3 etching is superior to grit-blasting. The distinct differences between pickling and air-formed oxides on AA 2024 clad, when combined with

plasma deposition, can also be explained by means of oxide texture. The open pores of the pickling oxide allow a better penetration by the stable plasma film. Thus, a better barrier against moisture diffusion through the oxide is created. Similar to hydrodynamic displacement, the hydration is enhanced by the pH drop and should not be regarded independently of anodic corrosion.

It should be noted that the process of acidity-enhanced hydration followed by hydroxide dissolution referred to in this thesis is quite likely the same mechanism that Brockmann et al. referred to as acidic oxide dissolution, when analysing anodised substrates. It is also likely that hydration is not as apparent with anodising layers as with the thin oxides investigated here. Moreover, with anodising films, hydroxide dissolution and reprecipitation occurs very close to the delamination front due to the relative slow progression. Kelm showed that an acidic environment is not sufficient to dissolve anodic oxide films and postulated a degradation mechanism via Al-chloro-complexes. Yet, it will be shown in the next paragraph that this degradation is unlikely to happen. Thus, it is assumed that even with anodised substrates the hydration occurs first and is then followed by hydroxide dissolution with both mechanisms enhanced by the acidic environment.

Corrosion – direct anodic aluminium dissolution

Both hydrodynamic displacement and hydration are enhanced by a reduction of pH in the bondline. As presented in chapter 2.3.2, this decrease is triggered by initial galvanic corrosion, i.e. anodic dissolution of the aluminium by hydrolysis, at the open edges. Hydrogen ions are created, which then diffuse into the interface and the oxide. This reaction is accelerated by chlorides. On clad samples, a distinct galvanic element between the pure Al layer and the base material is formed, leading to anodic dissolution of the sacrificial clad layer. On bare substrates, this reaction only happens at local galvanic elements around the intermetallics. Even though Al-Cu-Mg intermetallic phases are anodically dissolved in the beginning, the copper remnants lead to dissolution of the surrounding matrix later on; Al-Cu-Fe-Mn intermetallics are cathodic to the Al-matrix from the start [59]. Obviously, the degradation driving force around local elements is lower than that of the macro-element, which explains the different extent of bondline corrosion between bare and clad. Corrosion progresses into the bondline from the edges, creating an acidic climate at the delamination front. Moreover, pH is generally reduced in crevices as O₂ diffusion to the crack tip is limited. This causes the anodic reaction to be predominant. Both, low pH and migration of mobile chlorides towards the anodic region (for charge balancing reasons), then inhibits the repassivation [237].

Brockmann et al. initially postulated that the acid hydrogens dissolve the anodic oxide, causing the primary failure of the joint [2]. This mechanism was questioned by Kelm, who demonstrated that the anodic oxides

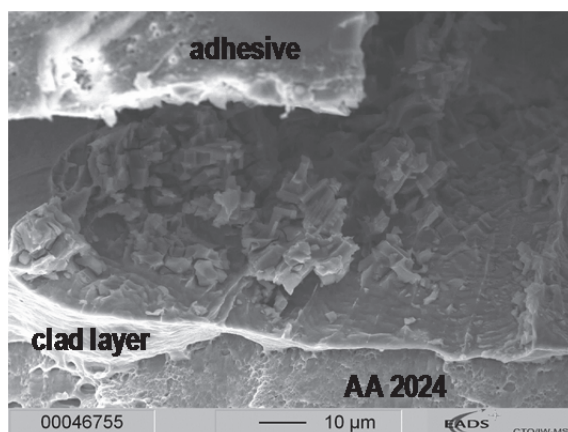


Fig. 4.55: AA 2024 clad (HNO₃) adherend after immersion in AlCl₃ (pH 3) solution

cannot be dissolved in acidic chloride solutions without the presence of Al³⁺ ions and who assumed that the observed oxide degradation is caused by aluminium-chloro- and aluminium-hydroxo-chloro-complexes [171]. A HNO₃ etched AA 2024 clad joint is immersed into acidic AlCl₃ (pH 3) solution for several days to simulate this failure mechanism and to check whether an analogous failure mode is found. The sample is cathodically polarized in galvanostatic mode ($\approx 20 \mu\text{A}/\text{cm}^2$) to reduce the aluminium dissolution, i.e. to decelerate the dissolution process. Fig. 4.55 displays the surface of the adherend after immersion very close to the degradation front. Despite the polarisation, heavy dissolution of the clad layer occurs. However, degradation advances slowly from the sample edge

through the aluminium layer; sometimes dissolution even occurs below the oxide and not along the interface. The oxide surface/interface in front of the degradation appears intact. Consequently, appearance

is dissimilar to the sector 5 of the bondline corrosion. Some large aluminium hydroxide flakes are formed, but most of the material is dissolved in the aggressive solution. No oxide transformation or growth due to hydration is observed. Hence, the creation of a highly concentrated Al-chloro-complex solution is unlikely. Even if that is the case, it will only dissolve the aluminium and the oxide close to the sample edges and not at the delamination front. This is coherent with the work of Kelm, who could not detect the chloro-complexes at the crack tip.

Nevertheless, even if this acidic aluminium dissolution is not predominant, the direct bimetallic based aluminium dissolution is considered as the cause of bondline corrosion. For this reason, the capability of the surface preparation to reduce the direct hydrolysis of aluminium is important for the durability of bonded joints. The high barrier properties of anodising layers are known to reduce this effect, but even these powerful treatments cannot completely suppress bondline corrosion if primary corrosion occurs at the edges. Chromate loaded primers highly inhibit the primary corrosion by chromate leaching onto exposed edges. Bondline corrosion tests of AA 2024 clad samples in combination with a chromate loaded primer reveal a drastic reduction of degradation. Exemplary images of plasma or silane coated joints primed with the Cr(VI) loaded BR 127 after exposure to salt fog are shown in appendix Fig. A.31 a) and b). For grit-blasted GPS treated specimens, the area affected by bondline corrosion is only about 20 – 30 % after 120 d of exposure to salt fog (compared to 100 % after 15 d without primer). Even on Smut-Go NC etched clad coupons no bondline corrosion is detected after 120 d if GPS plasma deposition is followed by BR 127 application. However, all plasma treated joints fail interfacially at the plasma polymer-primer interface, which illustrates that this primer is not compatible to the plasma coupling films applied here.³⁶

In any case, the use of carcinogenic chromates is not desired and will be banned in the near future. Investigations with an alternatively inhibited, chromate-free primer (Fig. A.31 c) and d)) also show a certain reduction of bondline corrosion. Full degradation of GPS coated, grit-blasted AA 2024 clad is reached not before 45 d if the primer is applied before bonding. Without primer, similar degradation is observed after only 15 d. However, the stabilising effect of the primer is still not sufficient to achieve satisfactory protection. A more encouraging improvement is observed for the GPS plasma coated substrates. Even on Smut-Go NC pre-treated specimens, no bondline corrosion is detected after 45 d, compared to ca 35 % delaminated area without primer. Thus, bondline corrosion can be further reduced by application of a chromate-free bonding primer. Yet, the interface between primer and plasma film is again not very stable causing predominantly adhesion failure.³⁷

With a future ban of chromates, it becomes evident that an even higher resistance against anodic Al-hydrolysis at the interface needs to be achieved by the surface preparation. As mentioned above, the high barrier of anodising oxide is beneficial, but the merely several nanometre thick plasma films can also provide distinct protection, especially after HNO₃ etching. Potentiodynamic polarisation measurements directly after immersion in 0.05 m NaCl (aq) are employed to assess the impact of the coupling film on the anodic corrosion reaction. The corresponding polarisation curves are presented in Fig. 4.56. Potentials are relative to SCE.

³⁶ Surprisingly, similar 100 % adhesion failure is observed on solely etched substrates, i.e. the adhesion of the bonding primer to aluminium oxide is significantly lower than the one of the adhesive. However, this low-viscous primer works well with porous anodising layers, which means that interface stability is derived mainly from the penetration of the oxide film and the associated mechanical interlocking.

³⁷ The investigations on joint stability after using bonding primers are carried out to gain more confidence in the postulated corrosion mechanism. The detailed study on optimisation of bonding primers for plasma coated aluminium adherends lies beyond the scope of this dissertation and is not investigated further.

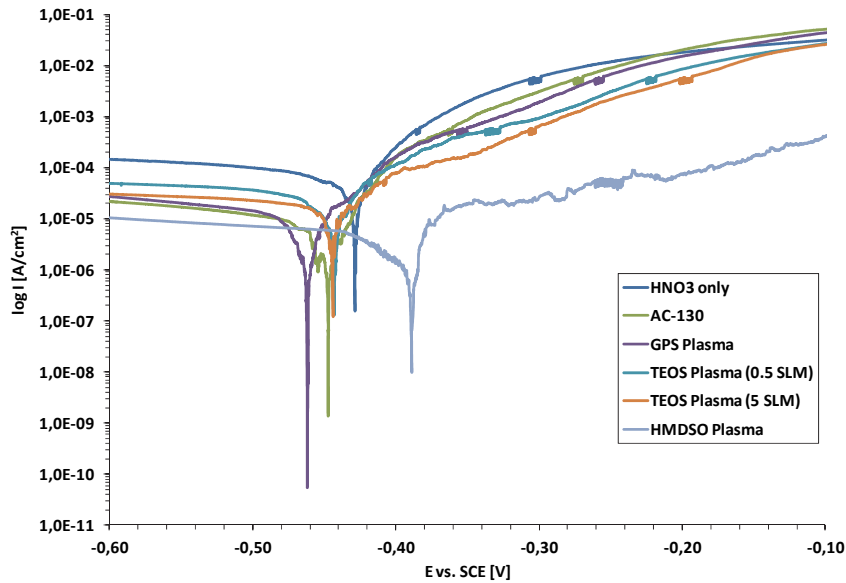


Fig. 4.56: Potentiodynamic polarisation curves of AA 2024 bare (HNO_3) in 0.05 m NaCl solution

On the left hand side (the more negative side) of the open circuit corrosion (breakdown) potential, the cathodic branch of the curve is visible, where the cathodic partial reaction is predominant. It shows the expected diffusion-limited plateau with constant corrosion current density. Compared to sole HNO_3 pickling, a certain reduction of current density is apparent for all coupling films due to the coverage of the copper-rich intermetallics. Wet-chemical GPS treatment is not shown, because obtained current-density values did practically not deviate from those obtained with solely etched specimens.

As the anodic partial reaction is decisive for the bondline corrosion, focus should lie on the right hand side of the breakdown potential. The AC-130 coating hardly affects the curve progression on this side, i.e. the current density is hardly reduced and the anodic reaction is not significantly inhibited. Contrarily, plasma films display a certain reduction of the corrosion current. As with EIS, samples are exposed to the electrolyte over a certain surface area which makes the measurement susceptible to local effects. Therefore, the reduction achieved with 5 SLM GPS and 0.5 SLM TEOS deposition is relatively low, but it increases with film thickness. With 5 SLM TEOS derived plasma films, a significant decrease of current density close to the breakdown potential is observed. The TEOS plasma film with its globular structure is, however, not free of pores. The protective effect of plasma films becomes most distinct if an approximately 200 nm thick homogeneous HMDSO plasma film is deposited on the surface. Despite a similar film thickness as AC-130, the anodic current density is lower by approximately two orders of magnitude. Hence, silica-like plasma polymer films strongly reduce the anodic aluminium dissolution reaction; the insulating character of silica-like plasma films has already been observed for low pressure plasma coated galvanised steel [42]. Grundmeier and Stratmann also showed that thin non-conducting plasma intermediate films inhibit electron transfer reactions on epoxy-coated Fe, suppressing electrochemical de-adhesion [238]. In any case, the polarisation curves clearly reveal the stabilising effect of the silica-like coatings against the anodic corrosion reaction, which is not observed with silane/sol-gel film. It is assumed that this is another factor explaining the obtained bondline corrosion test results.

Summary of the bondline corrosion mechanism

The overall bondline corrosion process consists of three partial failure mechanisms that can be clearly distinguished, but also have an effect on each other: acidity-enhanced hydrodynamic displacement and hydration, as well as anodic aluminium dissolution.

Upon exposure to a corrosive atmosphere, initial corrosion occurs at the open edges of the test coupons, respectively at damages of the sealing of bonded aircraft structures. Due to direct anodic Al-dissolution,

H^+ ions are created that diffuse into the bondline, creating an acidic environment. Limited oxygen diffusion into the crack tip is also assumed to contribute to this pH drop. Hence, the acidic failure mechanism discovered by Brockmann et al. is principally confirmed. As a galvanic macro-element is formed between the sacrificial clad layer and the base alloy, aluminium dissolution is especially pronounced on clad material. Al-dissolution creates an aggressive environment that attacks the protective oxide film and the interface. However, this damage mechanism must be extended by acidity-enhanced hydrodynamic displacement, and the primary oxide degradation needs to be specified as acidity-enhanced hydration that precedes hydroxide dissolution. Especially on not anodised substrates, these degradation aspects play an important role, because of the low oxide quantity and the absence of a polymer-oxide microcomposite at the interphase. In general, the weaker the interfacial adhesion the more dominant is the acidity-enhanced hydrodynamic displacement, whereas hydration becomes prominent with increasing interface stability. Direct anodic aluminium dissolution at the edges accelerates oxide transformation and increases the degree of hydration at the crack tip. If interfacial displacement is prevented, acidic moisture advances through the oxide layer below the interface, hydrating the oxide and base material. Any degradation of the adhesive due to H^+ diffusion is not detected.

The outstanding bondline corrosion resistance of the state of the art anodising processes are derived from the large oxide quantity, which helps to withstand hydration and dissolution for long times, and from the formation of a microcomposite with the high barrier epoxy polymer. The hydration inhibiting properties of phosphates that remain in the oxide film (PAA, PSA) are also very likely to be beneficial for bondline corrosion resistance.

Silane/sol-gel based treatments display excellent adhesion promotion properties that fully suppress displacement at the interface, but are very sensitive to low pH environments and hardly reduce the anodic aluminium dissolution. In contrast, the employed plasma derived coupling films are stable in acidic conditions. Moreover, they remain attached to the oxide layer even during hydration and corrosion due to a very stable interface to the aluminium oxide, whereas silane/sol-gel based films tend to detach. The inert silica-like composition of the plasma polymer coatings allows a significant reduction of hydration and an inhibition of the anodic hydrolysis of the aluminium. Their inorganic nature is however detrimental to the adhesion to the epoxy polymer. Therefore, the stability against hydrodynamic displacement of the adhesive is decisive for the performance of plasma treated joints. For this reason, the GPS derived plasma polymer film with its higher concentration of functional groups is superior in the bondline corrosion test compared to the TEOS derived films, in spite of its lower film thickness.

4.4 Summary of findings and plasma-silane-combination

This chapter summarises all major findings, providing an integral view on the connection between film or surface properties and joint stability. As an “applied conclusion” of the results, different surface pre-treatments and coupling films are combined into a single surface preparation process; this verifies that the capabilities that have been associated to the individual pre-treatments or coupling films are correct. The resulting optimised treatment should combine the best properties and should perform better than all individual treatments discussed previously.

Investigations of the plasma film properties reveal that the employed precursors lead to relatively uniform layer deposition with film thickness mostly depending on vapour pressure ($HMDSO > TEOS \cong OMCTS > GPS$) and feed flow rate. GPS derived films are found to be principally uniform but obtain also some “drop-like” structures of higher thickness. With the used plasma jet device maximal film thickness of > 200 nm can be reached with HMDSO in one deposition cycle, but, here, the maximal thickness is limited to approximately 110 nm for better comparability of the films derived from different precursors. Due to the use of air as plasma gas in combination with the relatively high gas temperatures, inorganic silica-like films with slightly over-stoichiometric oxygen concentrations and hardly any carbon in the bulk film are

deposited independent of the employed precursor. The inorganic nature of the plasma layers allows strong bonding to the aluminium oxide. Interspersed films are formed between the aluminium oxide and the plasma coating which cannot be easily separated, especially if the aluminium oxide is porous. The GPS and TEOS derived plasma films cannot be distinguished from the underlying HNO₃ derived oxides in electrochemical impedance spectroscopy.

ToF-SIMS analysis reveals several fragments that suggest covalent bonding between aluminium oxide and the silicon oxide of the coating. The plasma films remain attached to the oxide surface even during oxide transformation due to hydration or corrosion. Besides the excellent adhesion, the insulating character of the silica represents also a strong barrier against transformation reactions over a wide pH range, which protects the surface against hydration and dissolution in acidic environments formed in the bondline during ageing. However, the brittleness of the films becomes disadvantageous with increasing film thickness. First signs of delamination due to the intensive deformation of the base material during peel testing are detected with film thickness of about 50 nm.

More importantly, the inorganic composition is rather detrimental for the bonding to the epoxy adhesive. Despite the similar chemistry of the bulk film, the analysis of the surface carbon functionality reveals distinct differences depending on the used precursor, which is assumed to be caused by the presence of some not fully fragmented precursor. The bonding state of this surface carbon is found to be crucial for polymer adhesion and, thus, joint stability. Contrary to the siloxane based HMDSO and OMCTS derived films, the silane based GPS and TEOS derived films showed a significant broadening of the XPS C 1s peak towards higher oxidised species. It is demonstrated that the peel strength of the plasma treated joints correlates well with the presence of these oxidised carbon groups. Furthermore, the existence of not or only partly fragmented hydrolysable silanes, which are widely used adhesion promoters, at the surface is beneficial compared to the presence of non-polar siloxanes that act more as release agents. Hence, only TEOS and GPS can come into consideration as precursors for plasma derived coupling films with the employed deposition process. Both silane based plasma films strongly enhance adhesion to the epoxy polymer. In combination with grit-blasting, full cohesion failure is achieved. Nevertheless, even with silane plasma deposition, the interface to the adhesive is the weaker one and needs to be considered as critical. Plasma deposition of GPS, which is yet uncommon as precursor for atmospheric plasma deposition due to a very low obtained deposition rate, leads to the highest concentration of oxidised carbon species and, thus, to most stable plasma coated joints in all adhesion and durability tests.

Due to their pronounced organic character consisting of approximately 50 % carbon and with their high amount of not cross-linked glycidyl groups, wet-chemical silane based films display excellent adhesion to the adhesive. Furthermore, silane/sol-gel treatments completely suppress hydrodynamic displacement of the adhesive during ageing in moist environments. Compared to plasma films, their interface to the aluminium oxide is more critical. Oxide transformation tends to delaminate the silane based films. Additionally, their low barrier against moisture diffusion along the oxide, in particular in acidic climate, does not allow sufficient protection of the oxide during ageing.

Besides the coupling film properties, the influence of the surface pre-treatment is considered. Blasting with 50 µm alumina grit obviously leads to significant increase in roughness creating a ragged surface covered with sharp edges and undercuts. The corresponding naturally formed oxide is only a few nanometres thin without any distinct texture. Contrarily, chemical etching creates macroscopically rather smooth surfaces with a certain oxide structure. HNO₃ derived oxide films are 30 to 40 nm thick and obtain a distinct texture with fine pores of a few nanometres in diameter. Due to a laterally more homogeneous material removal caused by fluorides, conditioning in Smut-Go NC does not create a similarly pronounced structure. The formed oxide is below 10 nm and without significant nano-texture. However, a specific microstructure is created on bare substrates. Generally, etching of bare substrates leads to rougher surfaces due to removal of the intermetallics forming pits. Surface structure and oxide thickness are found to be the main influencing factors of the surface pre-treatments on joint strength and durability as the chemical state of the oxide films turned out to be very similar. Detailed XPS analyses including calculation of elemental concentration and

constraint curve fitting reveal that both etching and grit-blasting form hydrated oxyhydroxides with Al-OH concentrations in the range of 30 to 60 %. The exposure to ambient air of the grit-blasted surfaces is sufficient to hydrate the oxide surface comparably to etching and rinsing leading to relatively similar surface hydroxyl concentrations.

These groups are potential bonding partners for secondary or even covalent bond formation with the coupling film. ToF-SIMS measurements reveal a significant presence of aluminosilicates at the interface, namely SiOAl^+ ions in positive mode, as well as of $\text{SiO}_2\text{AlO}_2^-$, SiO_2AlO^- and $(\text{SiO}_2)_2\text{AlO}_2^-$ in negative mode. These aluminosilicates are very likely to be an indicator for covalent bond formation at the interface. The intensities of all of these interfacial ions follow the trend of Si or silicate, which confirms that the considered ions are not just Al-oxide fragments. However, even if ion bombardment is rather gentle, a potential formation of fragments due to sputtering cannot be completely excluded and, thus, the question whether covalent bonding occurs cannot be indisputably affirmed. Yet, the strong adhesion of the plasma polymer to the oxide even during oxide transformation in durability tests is certainly an indicator that very stable chemical bonds are formed between plasma polymer and the oxyhydroxide layer.

Altogether, the adhesion results of the floating roller peel test in dry conditions and after injection of water into the bondline correlate with the surface structure and roughness with macro-roughness being more important than microstructure and nano-texture. The enhanced mechanical interlocking with rough surfaces is the most pronounced effect as stresses at the interface are reduced and more energy is dissipated in the interphase region compared to plain samples. Only grit-blasting leads to full cohesion failure in combination with all plasma and solution derived coupling films achieving peel strengths around 13 kN/m. Therefore, grit-blasting or an equivalent abrasion technique should be employed as surface pre-treatment before coupling film application to gain satisfactory joint strength. HNO_3 and Smut-Go NC etching leads to inferior peel resistance and are not desired as stand-alone surface pre-treatments.

Contrary to peel testing, good differentiation of coupling films performance on grit-blasted substrates is possible when exposing the joints to dynamic loads during immersion in 50 °C DI water. This test aims to verify if the joints withstand a normal fatigue life of 10 million load cycles even under severe aqueous attack and can be considered as very demanding. Still, APPJ-CVD highly enlarges the fatigue life and samples coated with GPS derived plasma films, as well as most of the ones coated 0.5 SLM TEOS plasma, reach the required load cycles. However, analysis of the delamination at the interface reveals that the fatigue performance of the employed plasma coupling films is inferior to the solution derived silane/sol-gel treatments due to weaker bonding to the epoxy adhesive. Besides their strong adhesion promotion properties, the silanes are thought to have a certain water repellent effect inhibiting water ingress at the interface, which suppresses hydrodynamic displacement. Plasma films strongly reduce the displacement but do not match the interface stabilisation of the solution derived films. Static load wedge tests at 50 °C, 95 % rh confirm the results obtained with cyclic loading.

Though the highest mechanical joint strengths are achieved with grit-blasting, it is not the most desirable surface conditioning technique with regard to long-term stability of the bondline. During ageing of bonded joints in hostile environments, the quantity of the oxide is of significant importance as both hydration and dissolution of the oxide occur. Even without the application of external loads, the bondline can fail due to mere degradation of the adherend-surface or displacement at the interface. The thin Smut-Go NC derived oxide that provides neither strong barrier properties nor a large interface already delaminates drastically in mere hot-wet atmosphere. In contrast, the thicker and more textured HNO_3 derived oxide is more resistant to delamination and oxide hydration and, thus, corresponding joints are more stable during accelerated ageing in humidity or corrosive environments. In particular, if HNO_3 pickling is combined with plasma film deposition, the extent of bondline degradation is lower. If interfacial displacement is inhibited by a coupling film, oxide transformation and decomposition proceed within the oxide film. With HNO_3 pickling the open pores are filled by the resistant plasma film reducing the oxide degradation.

Special attention is paid to a detailed investigation of the bondline corrosion process to gain further understanding on all degradation aspects that occur during exposure to corrosive atmosphere. Three

interdependent failure mechanisms are identified: acidity-enhanced hydrodynamic displacement and hydration, as well as direct anodic dissolution of aluminium. During exposure to a corrosive environment, initial galvanic corrosion occurs at the open edges. The associated anodic Al-dissolution is followed by a drop of pH in the surrounding, i.e. the bondline. Once a crevice is formed, the continuous aluminium dissolution as well as the limited oxygen diffusion maintains the acidic climate in the crack tip. As a galvanic macro-element is formed between the sacrificial clad layer and the base alloy, aluminium dissolution is especially pronounced on clad material.

DEGRADATION TRIANGLE

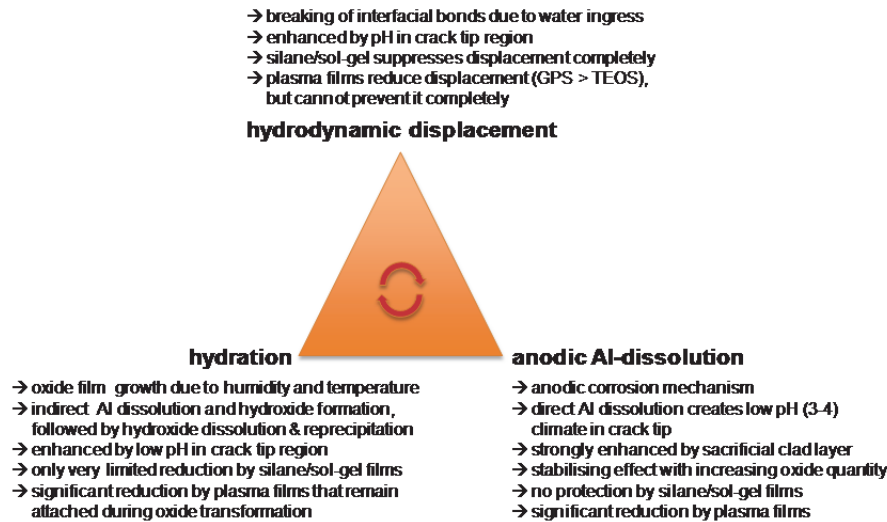


Fig. 4.57: Degradation Triangle: overview on detected degradation mechanisms and effects of coupling films

Hydrodynamic displacement is already thermodynamically favoured if moisture is present at the interface, but it is found to be even accelerated at low pH. Still, solution based silane/sol-gel treatments are capable to suppress this mechanism completely due to their outstanding adhesion promotion properties and their water-repelling nature, which is consistent with the results of the dynamic and static loading in moisture. The employed plasma derived coupling films significantly improve the resistance against hydrodynamic displacement, but cannot completely prevent it. Besides enhanced displacement, the acidic climate also significantly accelerates oxide transformation by hydration and hydroxide dissolution. If interfacial displacement is prevented, hydration advances through the oxide layer below the interface. Silane based coupling films are more sensitive to low pH environments than the oxide film and, hence, do not provide sufficient protection against oxide hydration. Furthermore, they do not reduce the anodic aluminium dissolution. Contrarily, the employed plasma derived coupling films are stable in acidic conditions and remain on the oxide layer even during oxide transformation, whereas silane/sol-gel based films rather tend to detach. Due to the inert silica-like composition plasma polymer coatings significantly reduce hydration and can also inhibit anodic hydrolysis of the aluminium. Even with a thickness below 10 nm the GPS derived plasma film strongly reduces the oxide degradation at the bondline during the SST. As a result of its superior bonding to the epoxy adhesive, GPS plasma treated joints display the highest resistance to bondline corrosion of all tested samples, but anodised ones. Overall, long-term joint stability after plasma deposition is by far superior to the one achieved with silanes.

When reviewing the degradation results, which are summarised in Fig. 4.57, a certain complementarity of solution and plasma derived Si-based films becomes apparent. Silane/sol-gel films clearly enhance interface stability, which is, despite a distinct stabilisation, still the weakest point of the plasma films, whereas silica-like coatings reduce oxide and aluminium degradation in acidic environments, which solution derived films cannot achieve. Moreover, HNO₃ etching and grit-blasting are complementary as well. Grit-blasting leads to the highest mechanical joint strength, but is less favourable than HNO₃ etching

with regard to bondline corrosion resistance due to the low oxide thickness and the missing porous texture. Therefore, all of these four steps are now combined creating one surface preparation process consisting of grit-blasting, followed by HNO_3 pickling before GPS plasma deposition and application of AC-130. If all assumptions are correct, this combined treatment should lead to more durable joints than any of the individual treatments investigated before.

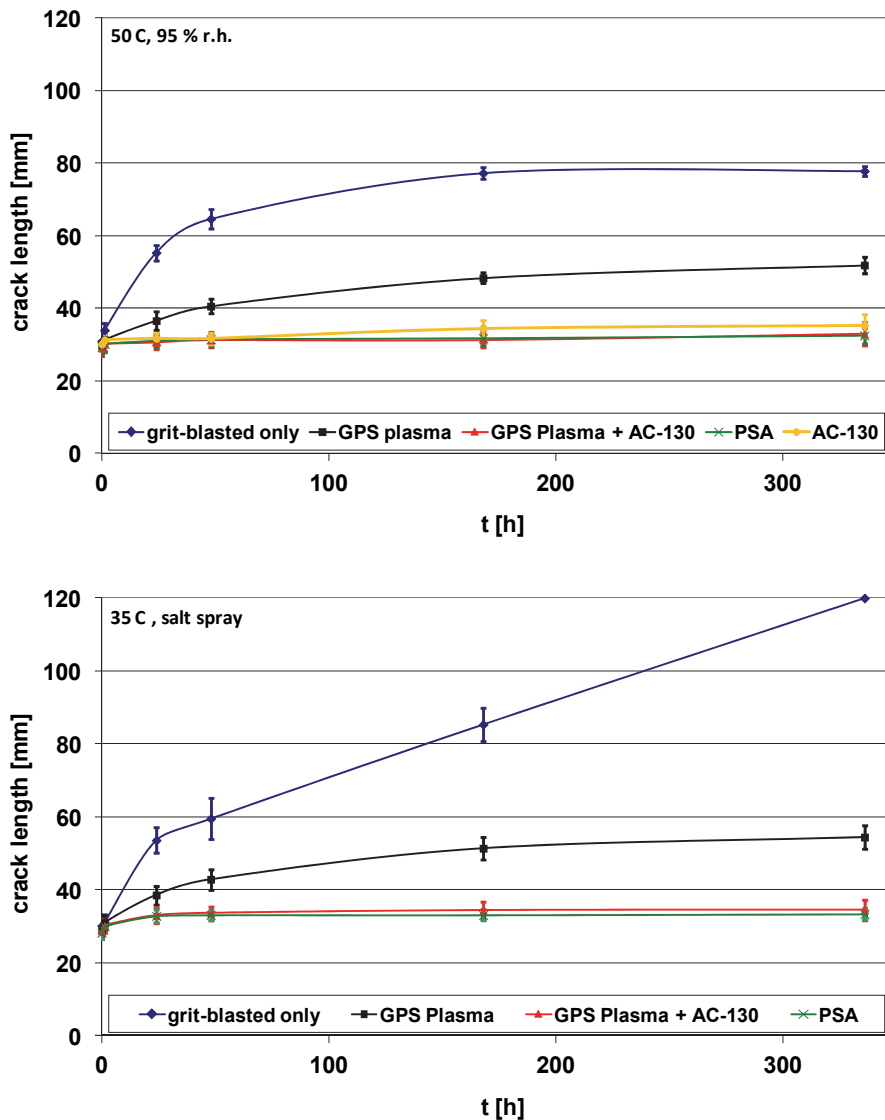


Fig. 4.58: Wedge test results of AA 2024 clad joints with different surface preparation methods in 50 °C, 95 % rh (top) and in 35 °C salt fog (bottom)

Peel strength of around 14 kN and full cohesion failure floating roller peel results in dry and wet conditions already indicate the high stability of the bonded joints after the combined treatment (not shown). This is further confirmed by more demanding wedge tests. Fig. 4.58 (top) presents the results of wedge test performed with AA 2024 clad joints after different surface treatments in hot-wet conditions. The combination of GPS plasma deposition and AC-130 coating clearly creates more durable joints than the GPS plasma treatment by itself. Interface stability appears to be even superior compared to the solely AC-130 coated substrates. With exposure times above 500 h this tendency becomes more pronounced as the sol-gel coated joints show adhesion failure (Fig. A.21), whereas combined treatment still entails cohesion failure (Fig. 4.59). This positive effect is assumed to be caused by the suppression of oxide reactions by the plasma coating. Even wedge testing in aggressive salt fog does not deteriorate the results, whereas this test

does not lead to meaningful results with silane/sol-gel treated joints due to bondline corrosion from the edges. Both in humid and corrosive atmosphere delamination is completely inhibited by the combined process, i.e. cohesion failure is achieved and results are equivalent to the reference anodising treatment.

Moreover, bondline corrosion resistance of the combined treatment even exceeds the PSA level. While no bondline corrosion is observed with both techniques on bare substrates, significant differences are apparent on the more critical clad alloys as displayed in Fig. 4.60. PSA joints show roughly 5 to 15 % of degraded bondline after 30 d in salt fog; the degree of bondline corrosion is approximately 1 % with the combined treatment. This result is absolutely remarkable as, to the author's knowledge, no other coating process is capable of such a bondline corrosion reduction, while maintaining cohesion failure. Such bondline stability might even allow omitting the application of an additional polymer bonding primer.

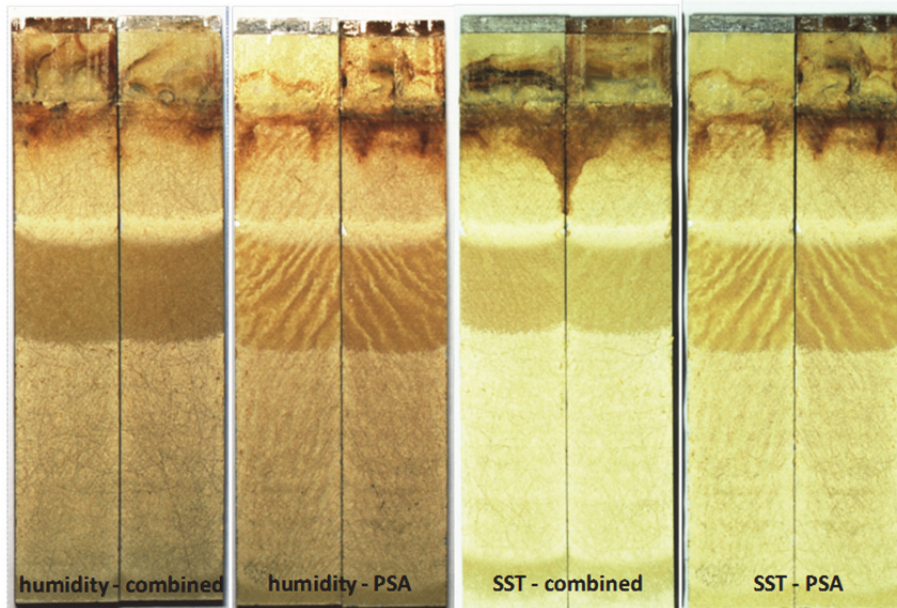


Fig. 4.59: Opened AA 2024 clad wedge test coupons of PSA and combined (grit-blasting, HNO₃, GPS plasma, AC-130) treatment



Fig. 4.60: Exemplary AA 2024 clad bondline corrosion test coupons (FM 73) after 30 d SST

Nevertheless, it needs to be stated that this combined treatment is a rather complex and time-consuming process which is not likely to be applied in service in civil aircraft industry. Yet, atmospheric plasma activation of the abraded surface prior to silane application has been reported as potential aircraft repair treatment for the defence sector [33]. Replacing plasma activation by deposition would be an uncomplicated step, so a certain potential for application is given. Moreover, an automated one-step process, where solution deposition is attached to the plasma jet, could be also feasible – at least in manufacturing.

In any case, the combination of the individual surface pre-treatment and coupling film processes demonstrates the immense potential of local treatments involving atmospheric plasma deposition. Furthermore, it confirms that surface preparation for adhesive bonding of aluminium structures can be tailored to suppress all the identified failure mechanisms.

5 Conclusion and outlook

For the first time, APPJ-CVD of Si based precursors by a controlled arc jet source was thoroughly investigated concerning its potential as alternative local surface treatment for adhesive bonding of aircraft structures. The high potential of this technology for usage in the aircraft industry is proven by a variety of tests and analyses.

Plasma deposition of silane precursors largely improves bonding between aluminium adherends and epoxy adhesive; bonded joints achieve the required mechanical stability if substrates are grit-blasted first, displaying full cohesion failure of a standard aerospace adhesive in dry and wet peel tests. Moreover, silane plasma coated test coupons fulfil the fatigue life demands even when exposed to DI water at 50 °C, whereas solely grit-blasted samples already fail after approximately 10 % of the required load cycles. Despite the strong stability enhancement by APPJ-CVD, the performance of solution derived silane films under mechanical loads and aqueous attack cannot yet be fully matched. However, plasma polymer coupling films distinctly outperform wet-chemical ones in corrosive atmosphere. Different than silane and sol-gel films, plasma films decrease the degree of bondline corrosion tremendously. The performance level of a state-of-the-art anodising technique is almost achieved, despite film thickness only lies in the nanometre range (anodising oxide thickness $\approx 2 \mu\text{m}$).

Besides the performance assessment of the bonded joints after APPJ-CVD treatment, this largely extends the overall understanding of capabilities and limitations of plasma coupling films in combination with different surface pre-treatments. Physical and chemical properties of the coupling films, the aluminium oxide and their interfaces before and during ageing are correlated to the behaviour of the joints in adhesion and durability tests.

Atmospheric plasma deposition with the set-up employed creates inorganic silica-like films of approximately 5-200 nm thickness. By trend, thinner films perform better in adhesion tests. Due to the inorganic nature of the deposited plasma coatings, the interface to the epoxy adhesive is weaker and is a critical aspect. A direct correlation between the concentration of oxidised species at the film surface and the interface stability to the epoxy is detected. This surface functionality largely depends on the precursor type, because some less fragmented precursor remains at the topmost surface of the coupling film. Silane precursors lead to a high concentration of oxidised carbon species like carbonyl or carboxyl groups, whereas siloxane derived films only obtain not-oxidised hydrocarbons at the surface. Consequently, only silane deposition is a suitable treatment with the employed device. Plasma deposition of GPS, which is normally not used as precursor for atmospheric plasma deposition due to low deposition rates, entails the highest concentration of oxidised carbon species and, thus, creates the most stable joints in all adhesion and durability tests.³⁸ Even though excellent adhesion levels are achieved, the interface to the polymer remains the weakest part of plasma coated joints and should be the major concern for further improvement.

With their distinct organic character and especially with their high concentration of unreacted glycidoxy groups, wet-chemical derived silane and sol-gel films display excellent adhesion to epoxy polymers. However, their intrinsic stability is found to be lower than the one of the plasma polymers, which can cause film rupture, in particular with higher layer thickness under peel loads. Moreover, silane/sol-gel films tend to detach from the oxide layer during oxide transformation caused by alteration in humid or corrosive environments.

In contrast, the excellent bonding behaviour of the silica-like plasma films to aluminium oxide needs to be emphasised. Especially with open porous oxide layers, an interspersed layer is formed and the coupling

³⁸ Although GPS is a relatively expensive precursor, its use seems reasonable considering the low quantity needed.

films remain attached to the oxide film even during ageing induced oxide transformation; strong indications of covalent bond formation are detected. Due to their inorganic nature, plasma films are stable in humid and acidic environments, which are formed in the bondline during ageing. Hence, they significantly reduce alteration of the oxide film and thus strongly enhance long-term joint durability.

For all coupling films, peel tests reveal a significant influence of the aluminium surface pre-treatment on the mechanical joint strength. Interlocking is required to distribute the stress in the interphase region of the aluminium-epoxy joint. Peel results correlate to the surface morphology, with macro-roughness being most crucial. While mechanical and chemical deoxidation techniques produce distinct differences in oxide texture, the chemical nature is similar: an oxyhydroxide layer is formed with hydroxide concentration increasing towards the surface. All oxides obtain enough free hydroxyl groups to bond to the coupling films. Moreover, oxide quantity is found to be beneficial for long-term joint stability. Thus, samples with 30-40 nm thick HNO_3 derived oxides perform better in humidity and salt fog exposure than those with air-formed films.

By studying corrosion-induced degradation of plasma and silane treated joints in greater detail, this thesis also increases the knowledge of the bondline corrosion mechanism for aluminium joints in general. The overall mechanism is found to consist of three interdependent degradation mechanisms: hydrodynamic displacement of the adhesive, hydration (both are enhanced by acidity) and direct anodic dissolution of aluminium (corrosion). Initial anodic dissolution at the open edge reduces the pH in the bondline, which amplifies and accelerates hydration and displacement. The degree of hydrodynamic displacement occurs predominantly if the epoxy-oxide interface is weak. If sufficient interface stability is achieved, hydration becomes the rate-defining failure cause. Hydration progresses mostly through the oxide; aluminium is dissolved and hydrated in the oxide layer, forming a hydroxide film. This process is associated with a distinct film growth, which finally leads to a rupture of the hydroxide film. Direct dissolution of the initial oxide film by an acidic or aluminium-chloro-complex solution, which has been proposed previously, has not been detected.

A detailed understanding of the above mentioned corrosion mechanism helps to precisely understand the capabilities of the coupling films. Solution based silane derived films are able to suppress any hydrodynamic displacement at the interface, but are hardly capable to protect the surface from hydration or dissolution in the acidic environment in the crevice. Hydroxide growth below the coupling film causes film delamination from the oxide layer, which explains the insufficient bondline corrosion resistance. Electrochemical characterisation confirms the sensitivity of sol-gel films to low pH solutions and the lack of inhibition of the anodic corrosion reaction. Generally speaking, EIS and potentiodynamic polarisation are found to be meaningful methods to evaluate film stability and, in combination with relatively quick adhesion tests like wet peel or wedge, provide good indication of bondline corrosion resistance of an oxide or coupling film. Contrarily, plasma films are very resistant to acidic environments and adhere strongly to the oxide. Therefore, plasma deposition of coupling films drastically reduces hydration and anodic aluminium dissolution, and thus, bondline corrosion. Hydrodynamic displacement is strongly reduced by TEOS and especially by GPS derived plasma films, but cannot be fully suppressed and remains the major cause of failure.

In summary, this elevated understanding of film and surface properties, as well as of degradation mechanisms not only allows assessment of the surface preparation processes employed, but also allows tailoring of surface treatments. Analysis of the individual degradation steps shows that the capabilities of plasma derived and solution derived Si-based coupling films are complementary. It is demonstrated that a combination of both techniques actually combines the advantages of each one; mechanical and durability performance levels of state-of-the-art anodising techniques are surpassed even in corrosive atmosphere. To the author's knowledge, no other environmentally benign and locally applicable surface treatment that does not grow an oxide from the base material provides such interface stabilisation. Even if such a combined preparation technique is time-consuming and might not be preferred in service, it nevertheless demonstrates the immense potential of local surface treatment involving atmospheric plasma deposition, which by itself

is already a powerful technique. Furthermore, the combination confirms that surface preparation for adhesive bonding can be tailored to suppress all of the failure mechanisms identified.

In conclusion, the results provide a strong foundation for progressing structural bonding of aluminium alloys in aeronautics. The knowledge gained should help to increase trust in local treatment techniques for structural bonded repair, which allows weight savings by adapting future design and sizing. Moreover, it should enlarge the field of possible bonding applications. Potential applications should not only be limited to local repair; local treatment in production should be considered as well. Exclusively treatment of the to-be-bonded areas could allow, on the one hand, a removal of large tank processes involving high amounts of environmentally critical liquid waste, and on the other hand, the use of adhesive bonding as joining technique for integrated or even equipped structures.

Concerning future developments, the results obtained allow a tailoring of new preparation processes according to the detected demands. It should be further investigated whether plasma and solution derived deposition could be combined into one single process step, e.g. by attaching a deposition nozzle to the jet source. Yet, not only the combination of plasma deposition and silane solutions is promising, but also other combinations like APPJ-CVD of HMDSO and GPS should be further examined. It is likely that the barrier properties of HMDSO are beneficial in many applications if a stable interface to a polymer can be achieved by GPS plasma deposition. Silane/sol-gel application after HMDSO plasma deposition could also combine the barrier and stable interface. Furthermore, a change of discharge method and plasma gas could open new possibilities: if the oxygen content of the plasma gas can be controlled during deposition, it seems promising to create gradient films, which are inorganic at the oxide interface and organic at the polymer interface.

Although the knowledge on the effect of the APPJ derived coupling films is largely supplemented, it is still reasonable to perform some additional analytical investigations; for example, the examination of the species formed inside the plasma were not subject of this thesis. Additionally, the nature of the surface groups that are decisive for the film properties should also be analysed further, ideally on model surfaces and with alternative techniques like RAIRS or EELS.

Not only coupling film application, but also surface conditioning could be optimised further. It is likely that grit-blasting (which is the not preferred in service) can be replaced by alternative abrasion techniques. In production, a combination with other physical oxide removal methods seems worth exploring; pulsed laser treatment is known to provide a stable oxide with distinct surface morphology that allows mechanical interlocking of the polymer. A follow-on plasma deposition would protect the oxide in corrosive environments. Together both techniques would represent a dry preparation process without creating any solid or liquid waste.

By all means, the use of a polymer primer is required for any aerospace application. First results presented in this dissertation reveal a high potential of plasma deposition followed by primer application. However, distinct difficulties have already become apparent: the tested primers are not compatible with the plasma derived coupling films, leading to interfacial failure. The standard bonding primers are optimised for penetration of the porous anodising oxides. Thus, polymer primers need to be adopted to maximise adhesion to the plasma polymer layers. As primers optimised for sol-gel treatments already exist, the use of a combined plasma-sol-gel treatment with off-the-shelf products seems to be unproblematic. Besides further technical analysis of surface preparation processes involving APPJ-CVD, cost and life-cycle assessments are needed to decide on potential applications in aircraft industry.

While above mentioned applications and optimisations lie in the future and must be carefully scrutinised, this dissertation provides a first comprehensive insight into the field of APPJ-CVD as surface preparation for adhesive bonding of primary metallic aircraft structures. It identifies all the necessary aspects that need to be considered and tested further in order to advance the application of this technique in the aircraft industry.

A Appendix

A.1 Thin film characterisation and influence on adhesion

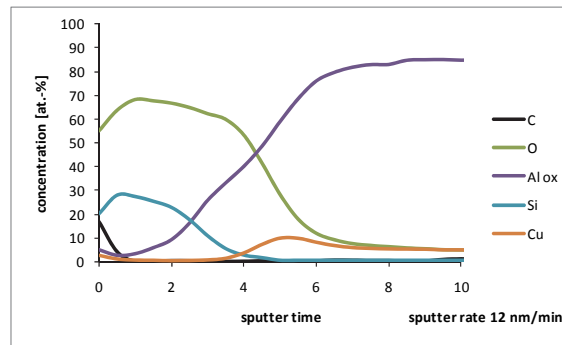


Fig. A.1: XPS depth profile of GPS derived plasma coating after several deposition cycles

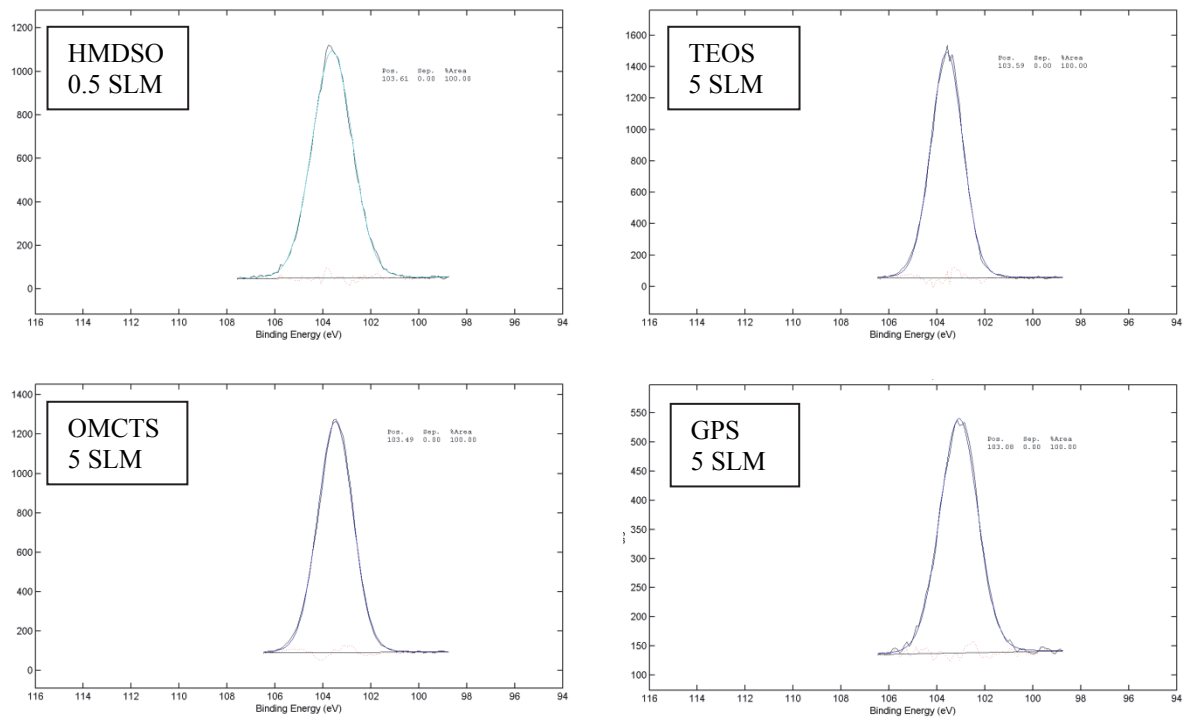


Fig. A.2: High resolution Si 2p XPS spectra of plasma films

Table A.1: Floating roller peel test results of AA 2024 bare (Smut-Go NC) – DP 490 joints

floating-roller peel test DP490		dry		wet	
		treatment	avg peel strength [kN/m]	deviation [kN/m]	avg peel strength [kN/m]
references	CAA	9.94	0.60	9.35	0.64
	Smut-Go NC	8.01	0.60	3.60	0.53
	plasma activated	8.17	0.64	4.64	0.60
Smut-Go NC + plasma film	HMDSO 0.5 SLM (90 nm)	3.45	0.69	2.25	0.75
	OMCTS 5 SLM (55 nm)	4.90	0.61	3.34	0.51
	TEOS 5 SLM (55 nm)	9.15	0.53	8.35	0.89
	TEOS 0.5 SLM (14 nm)	9.23	0.68	9.04	0.53
	GPS 5 SLM (6 nm)	10.33	0.49	9.96	0.56
Smut-Go NC + silane/sol-gel	GPS (aq)	9.75	0.69	8.72	0.84
	AC-130	9.40	0.68	4.49	0.62

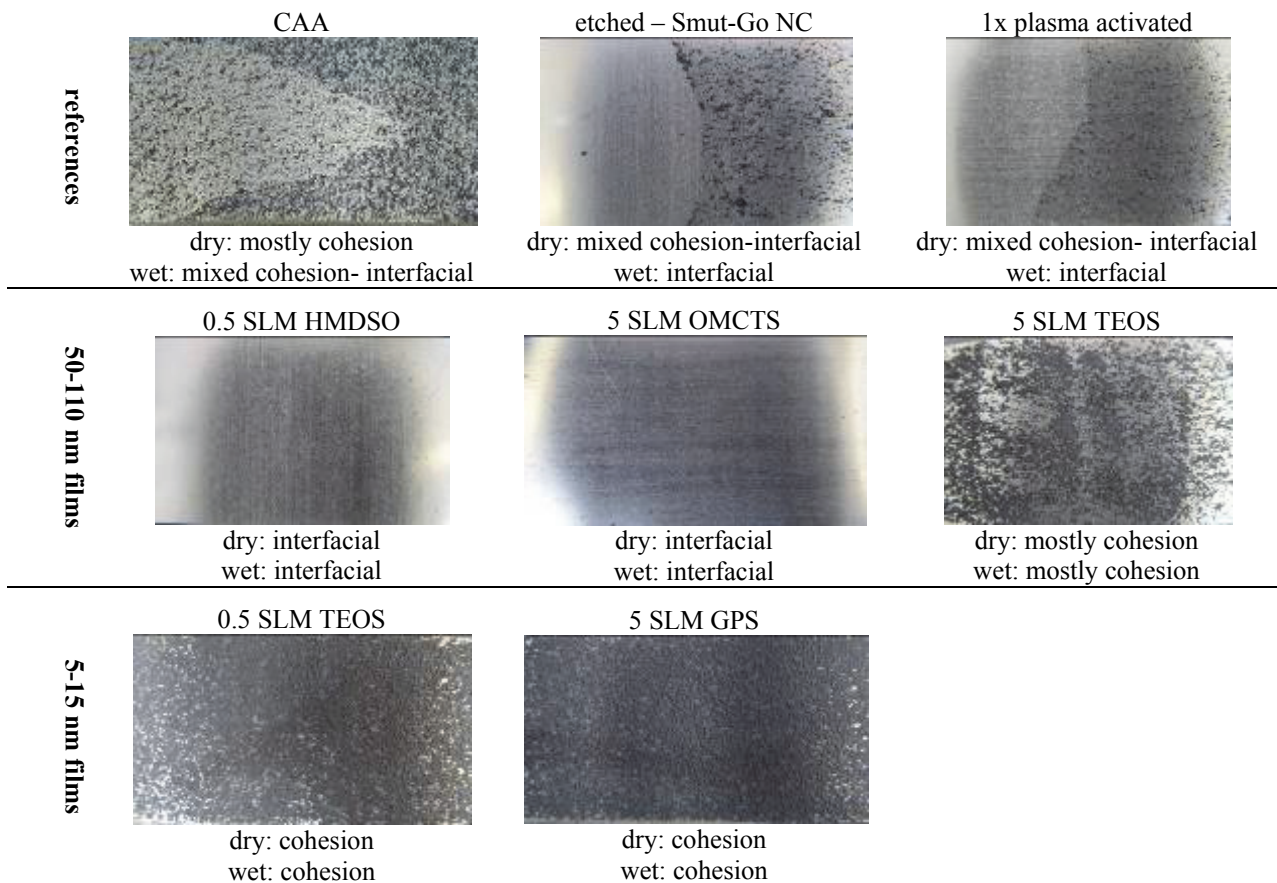


Fig. A.3: Fracture images of peel sheets of DP 490 joints: transition zone dry → wet

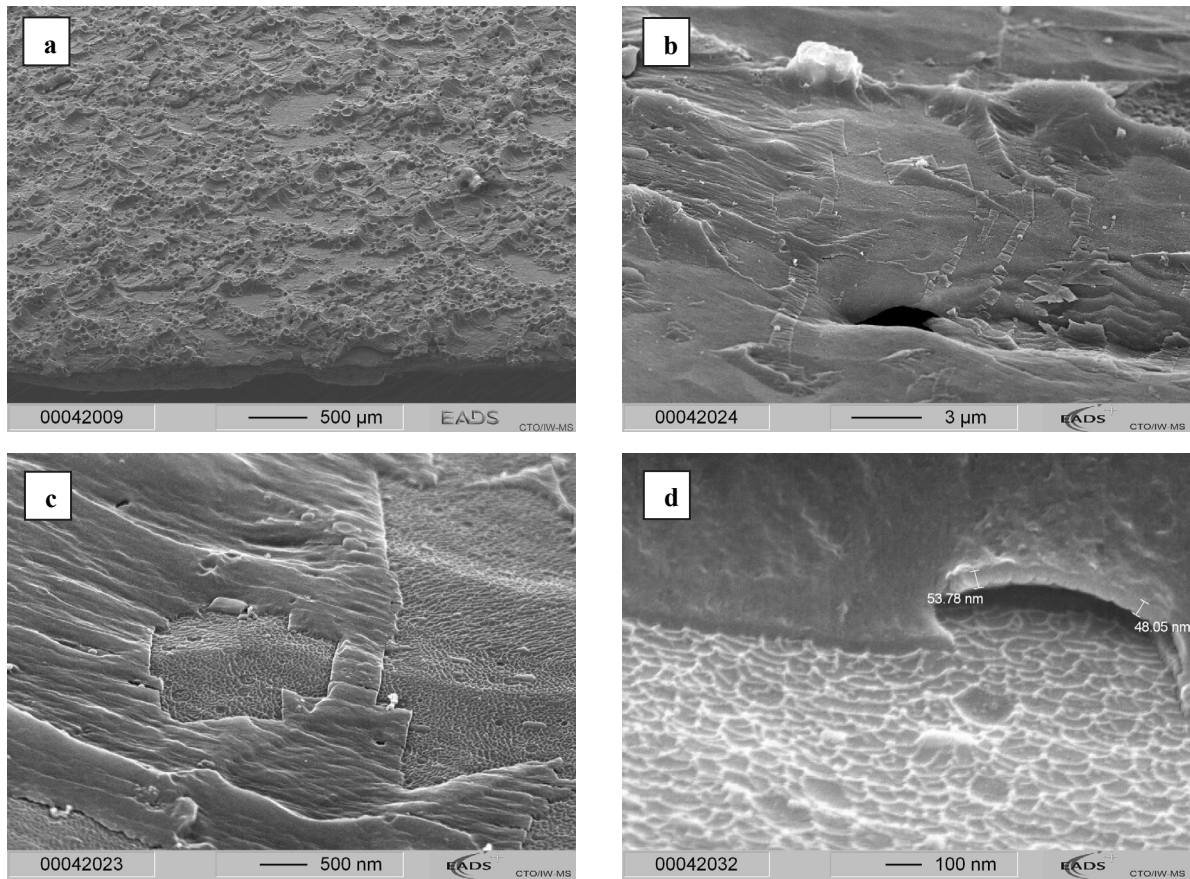


Fig. A.4: Fracture images of AA 2024 bare (Smut-Go NC) peel sheet of DP490 joint with 5 SLM TEOS film:
a) overview on fracture area (mostly cohesive): adhesion failure areas: flat "valleys"
b) transition cohesion → adhesion failure
c) adhesion failure: partly interfacial polymer/plasma film, partly plasma film/Al-oxide
d) cohesion failure: plasma film below polymer (front: adhesive failure due to cryo-fracture)

A.2 Oxide characterisation and influence on adhesion

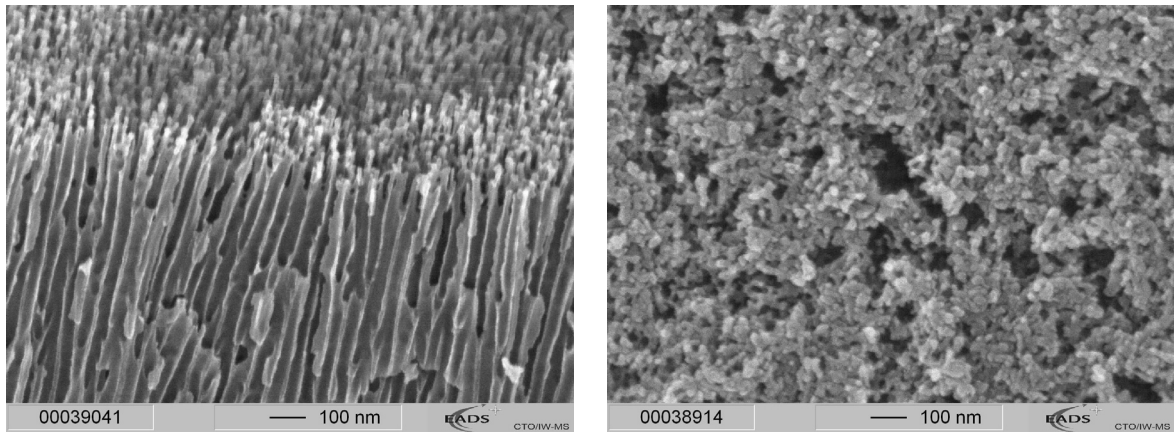


Fig. A.5: SEM images of porous PSA derived oxide surfaces on AA 2024 clad (left, side-view) and bare (right, top-view)

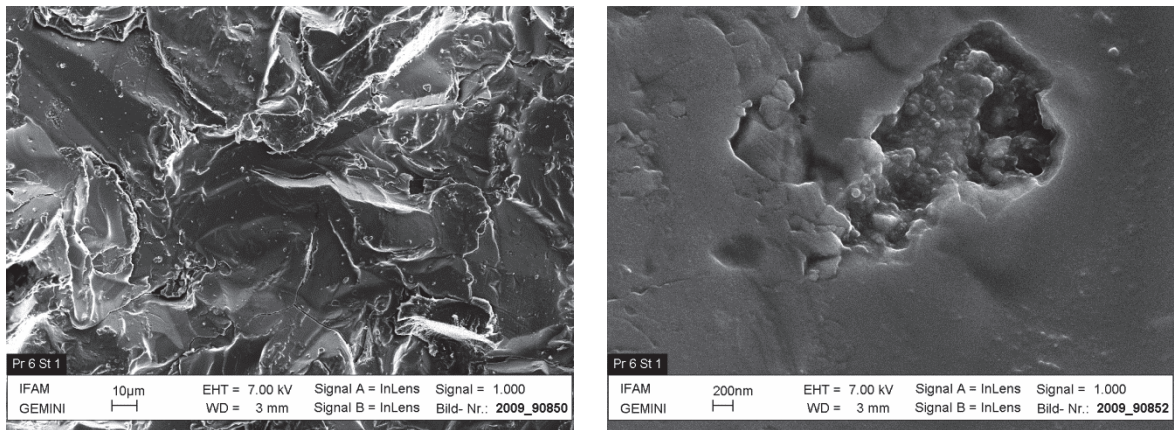


Fig. A.6: SEM images of oxides on AA 2024 clad after grit-blasting (alumina, 50 μm)

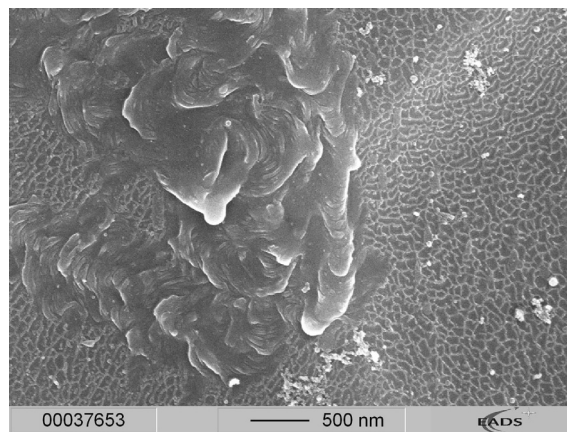


Fig. A.7: Top-view SEM image of AA 2024 bare (Smut-Go NC) after sparkover between plasma nozzle and substrate (6 mm distance) displays local melting the substrate surface; the area outside the sparkover is not affected

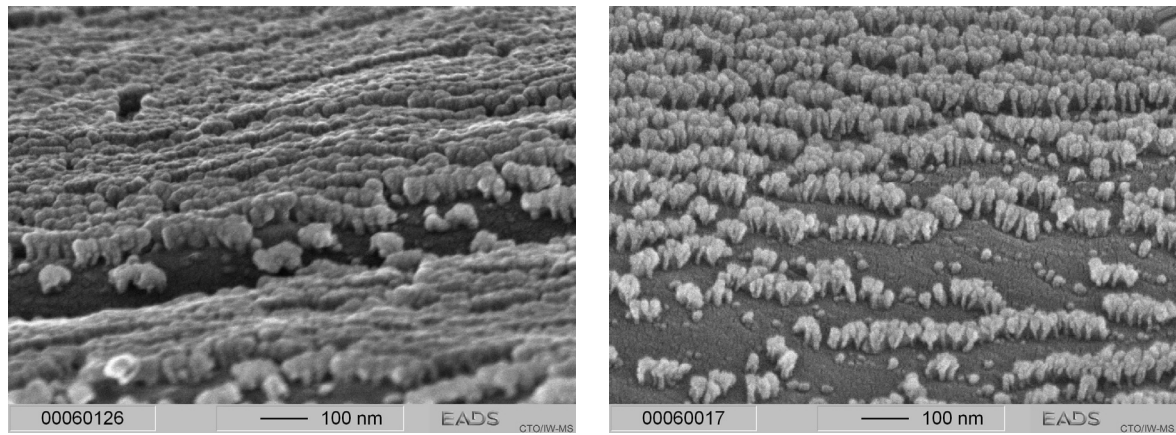


Fig. A.8: SEM images of HNO_3 pickled AA 2024 bare (left) and clad (right) surfaces after cryofracture

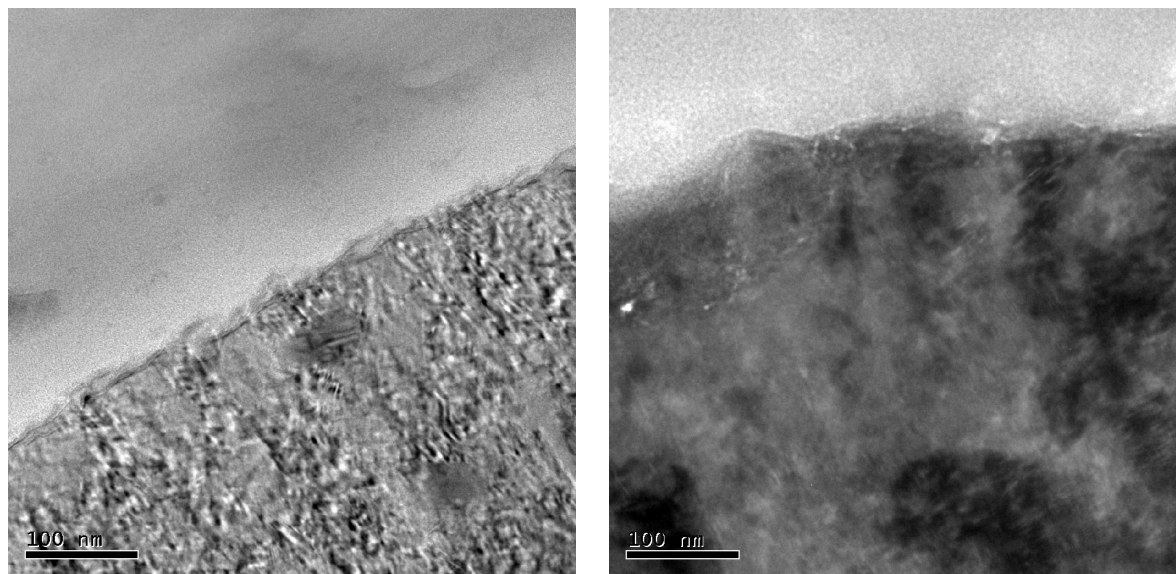
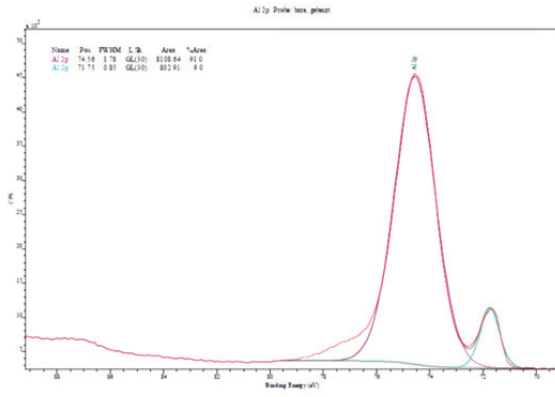
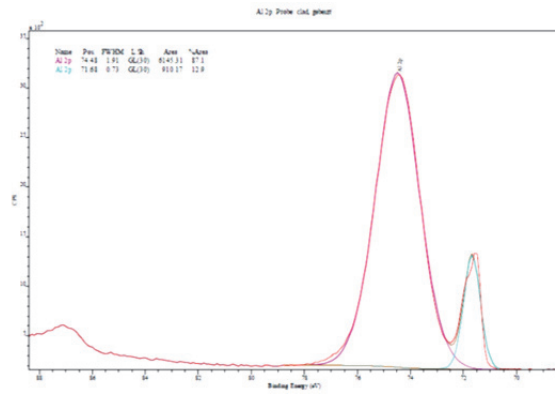


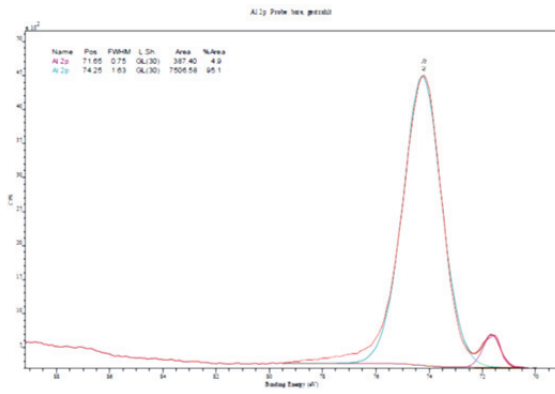
Fig. A.9: TEM images of crosscut through oxide films formed after pickling with Smut-Go NC (left) and grit-blasting (right) on AA 2024 bare



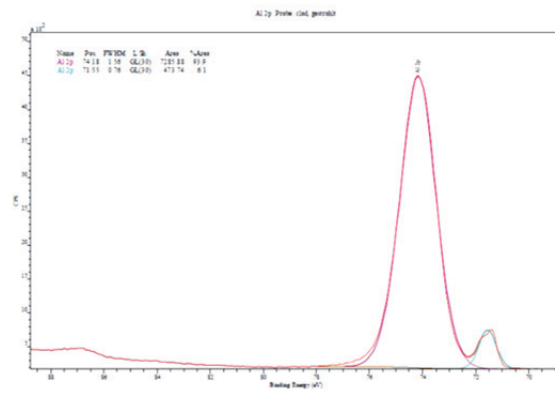
AA 2024 bare Smut-Go NC



AA 2024 clad Smut-Go NC

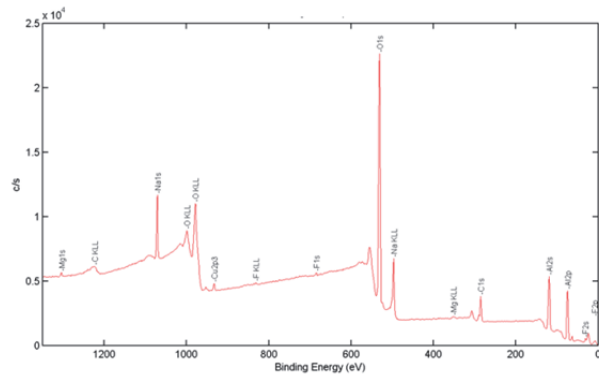


AA 2024 bare grit-blasted

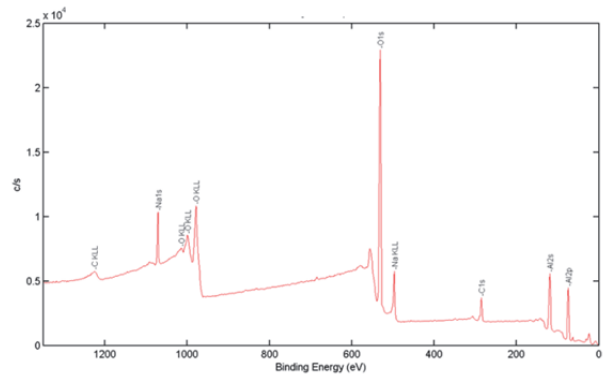


AA 2024 clad grit-blasted

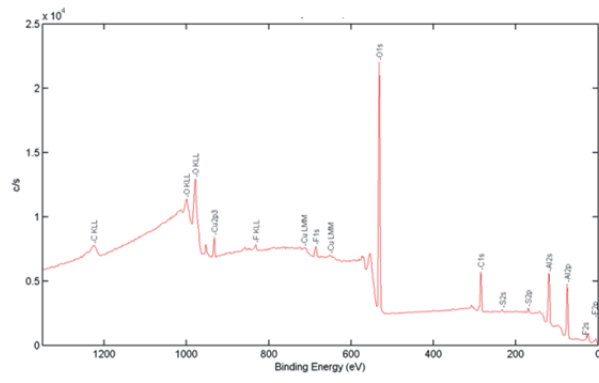
Fig. A.10: XPS Al 2p spectra of AA 2024 bare/clad samples after grit-blasting or pickling with Smut-Go NC (produced by BAM)



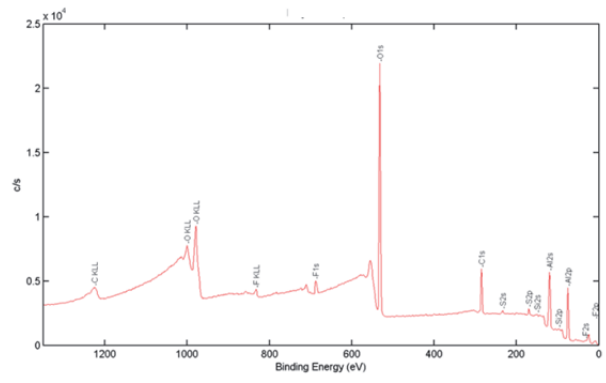
AA 2024 bare grit-blasted



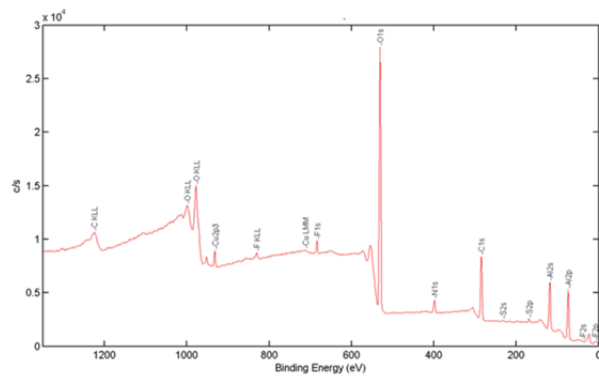
AA 2024 clad grit-blasted



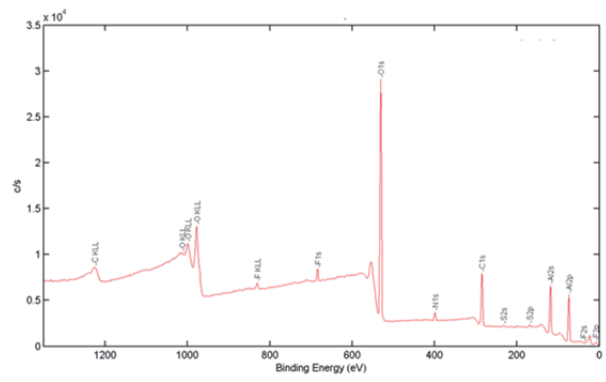
AA 2024 bare Smut-Go NC



AA 2024 clad Smut-Go NC



AA 2024 bare HNO₃



AA 2024 clad HNO₃

Fig. A.11: XPS survey spectra of AA 2024 bare and clad specimen after different surface pre-treatments

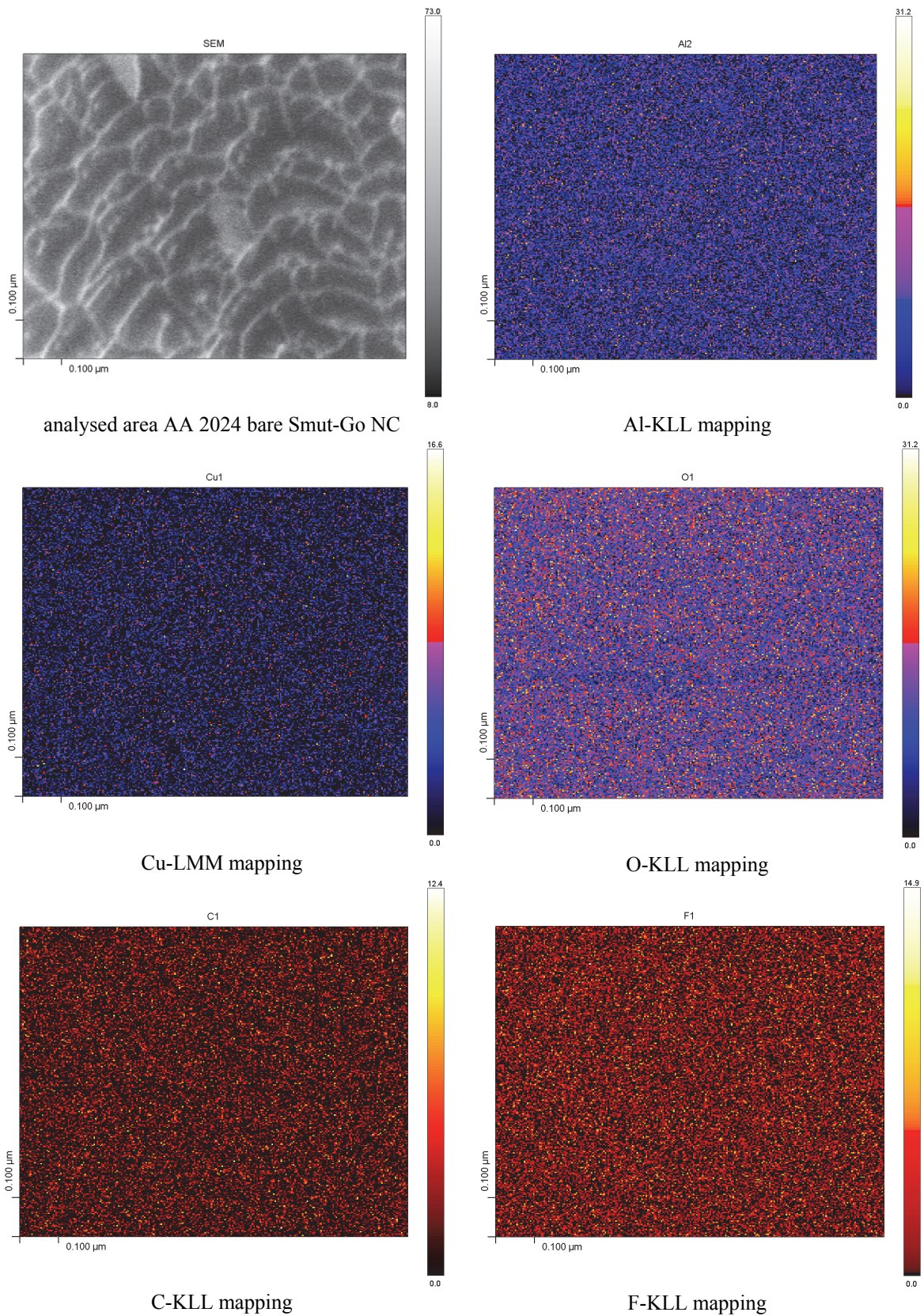
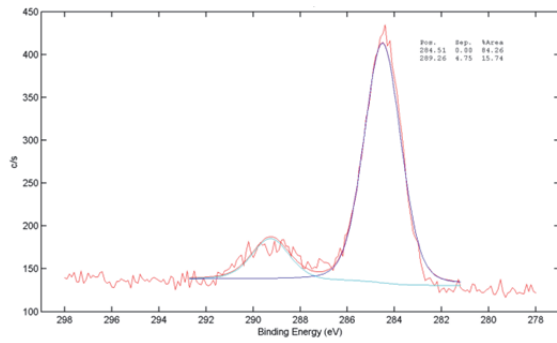
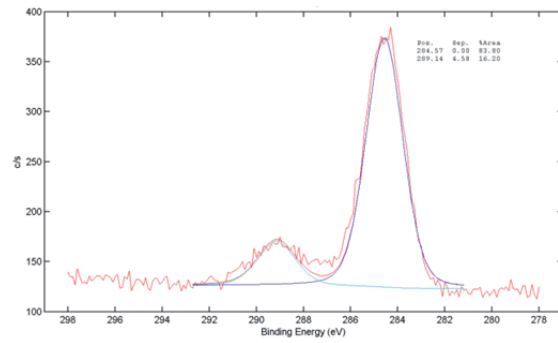


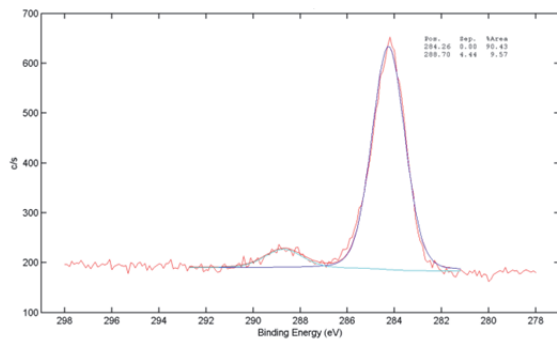
Fig. A.12: Scanning Auger mapping (produced by BAM) of AA 2024 bare surface after Smut-Go NC pickling



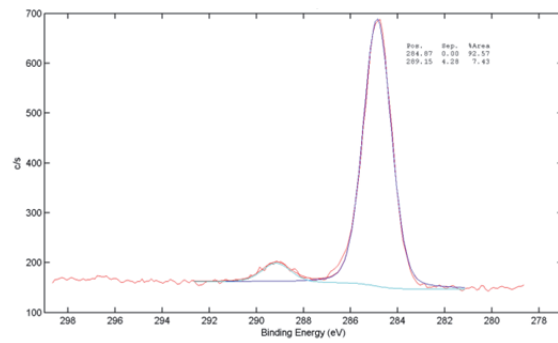
AA 2024 bare grit-blasted



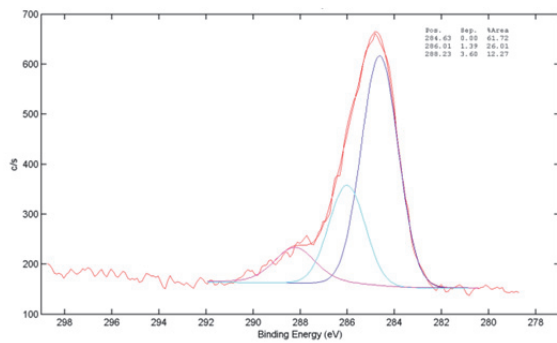
AA 2024 clad grit-blasted



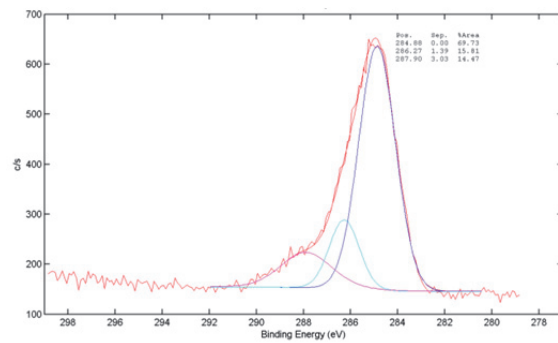
AA 2024 bare Smut-Go NC



AA 2024 clad Smut-Go NC

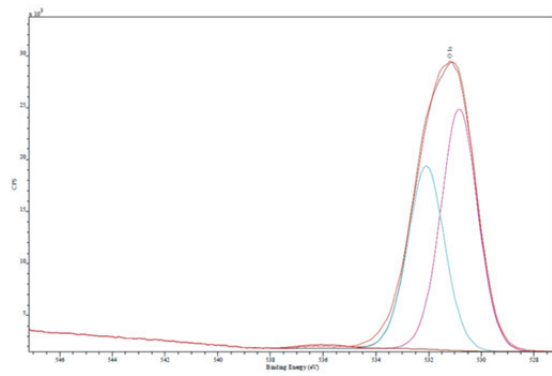


AA 2024 bare HNO₃

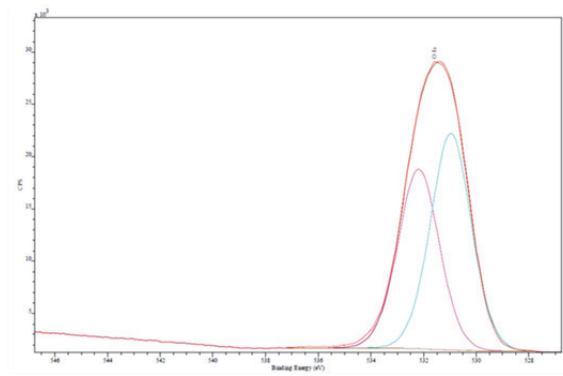


AA 2024 clad HNO₃

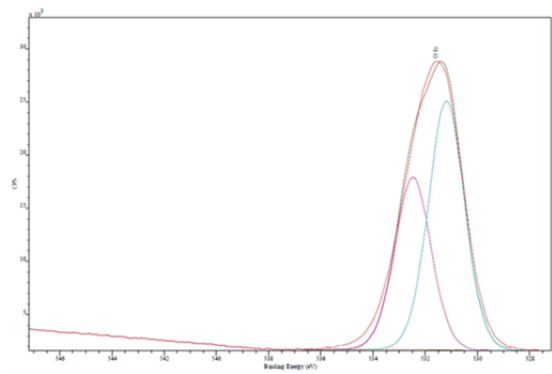
Fig. A.13: High resolution XPS C 1s spectra of AA 2024; percentages of oxide species used for Al-OH calculation



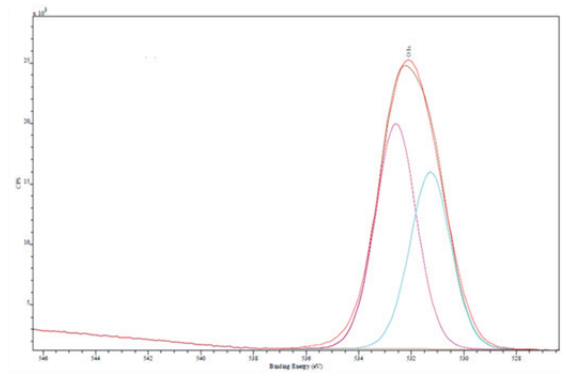
AA 2024 bare grit-blasted



AA 2024 clad grit-blasted



AA 2024 bare Smut-Go NC



AA 2024 clad Smut-Go NC

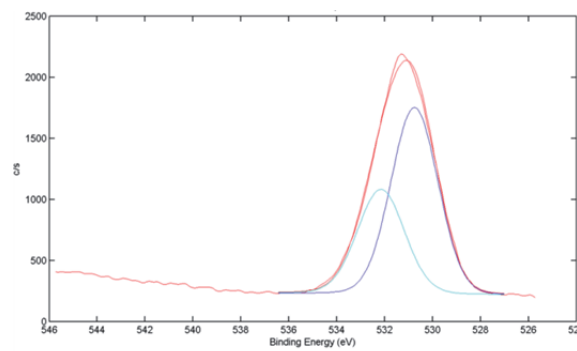
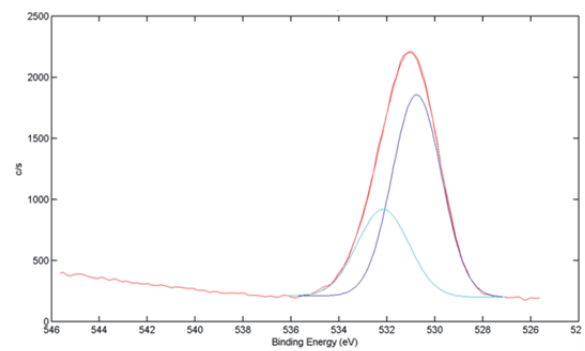
AA 2024 bare HNO₃AA 2024 clad HNO₃

Fig. A.14: High resolution XPS O 1s spectra of AA 2024; fitting of Al-O-Al and Al-OH components

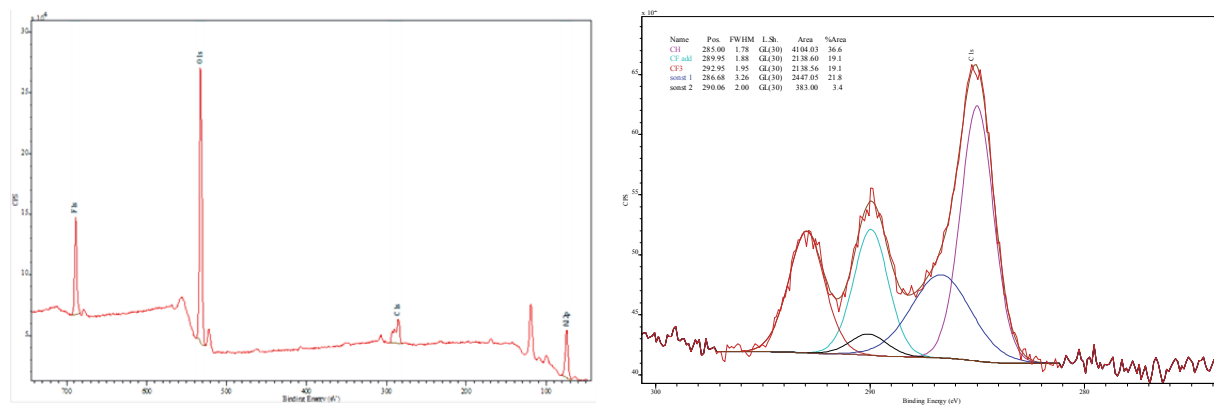


Fig. A.15: CD XPS survey spectrum and high-resolution C 1s spectrum of AA 2024 bare (Smut-Go NC); (produced by BAM)

Table A.2: Exact ion masses for ToF-SIMS analysis

Exact fragment masses [239][amu]			
positive spectrum		negative spectrum	
Al ⁺	26.9815386	AlO ₂ ⁻	58.9713678
28Si ⁺	27.9769265	63Cu ⁻	62.9295975
30Si ⁺	29.9737702	SiO ₃ H ⁻	76.9694954
63Cu ⁺	62.9295975	SiO ₂ AlO ⁻	102.943209
AlO ⁺	42.9809686	SiO ₂ AlO ₂ ⁻	118.938124
SiOAl ⁺	70.9533798	(SiO ₂) ₂ AlO ₂ ⁻	178.904879
SiOH ⁺	44.9796662	SiO ₂ ⁻	59.9667558
Al ₂ OH ⁺	70.9658169	AlO ⁻	42.9809686
		SiO ₃ H-(Al ₂ O ₃)	178.917316
		SiO ₂ H ⁻	60.9745808
		Si ₂ O ₅ H ⁻	136.936251
		Si ₃ O ₇ H ⁻	196.903007
		(Al ₂ O ₃)HO ⁻	118.950561
		(Al ₂ O ₃)AlO ₂ (H ₂ O) ⁻	178.929754
		AlO ₃ H ₂ ⁻	76.9819325

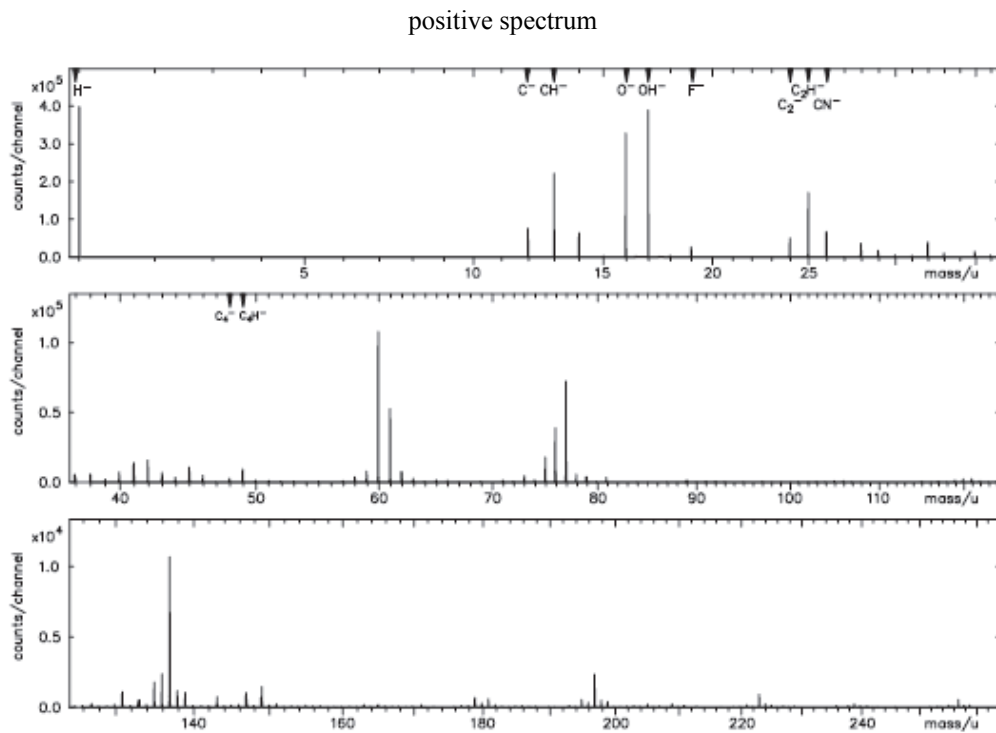
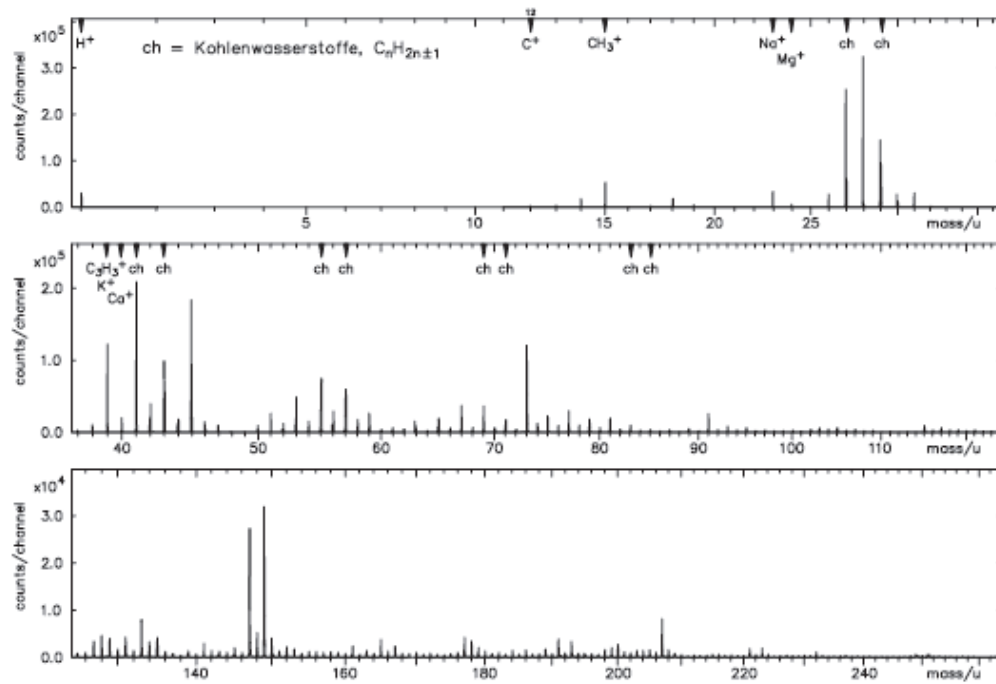
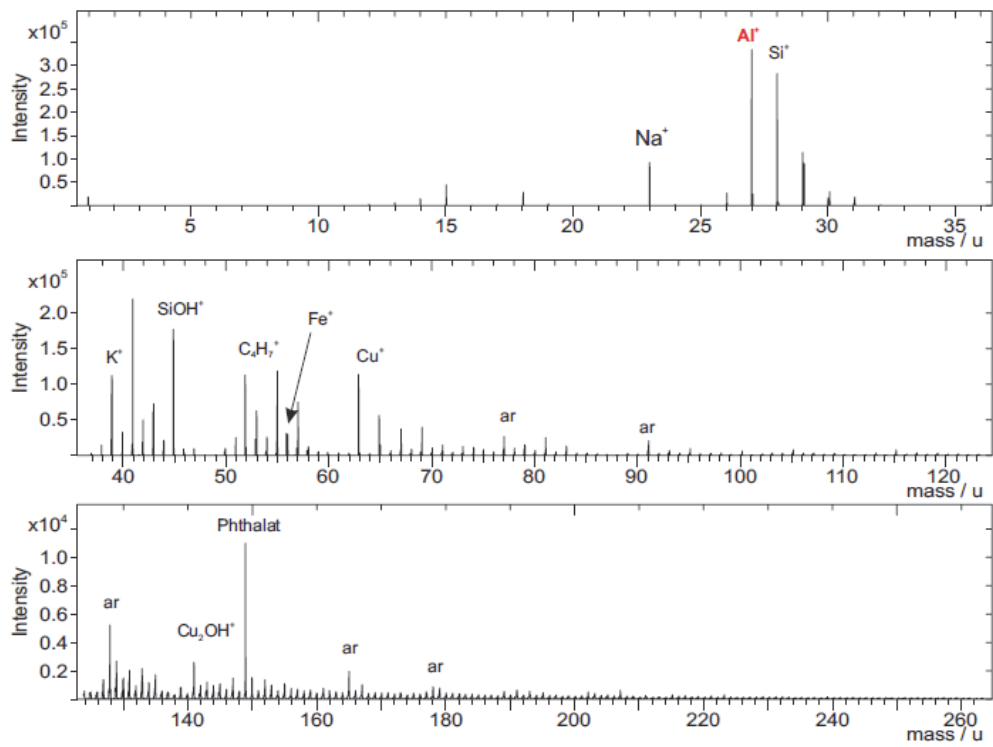
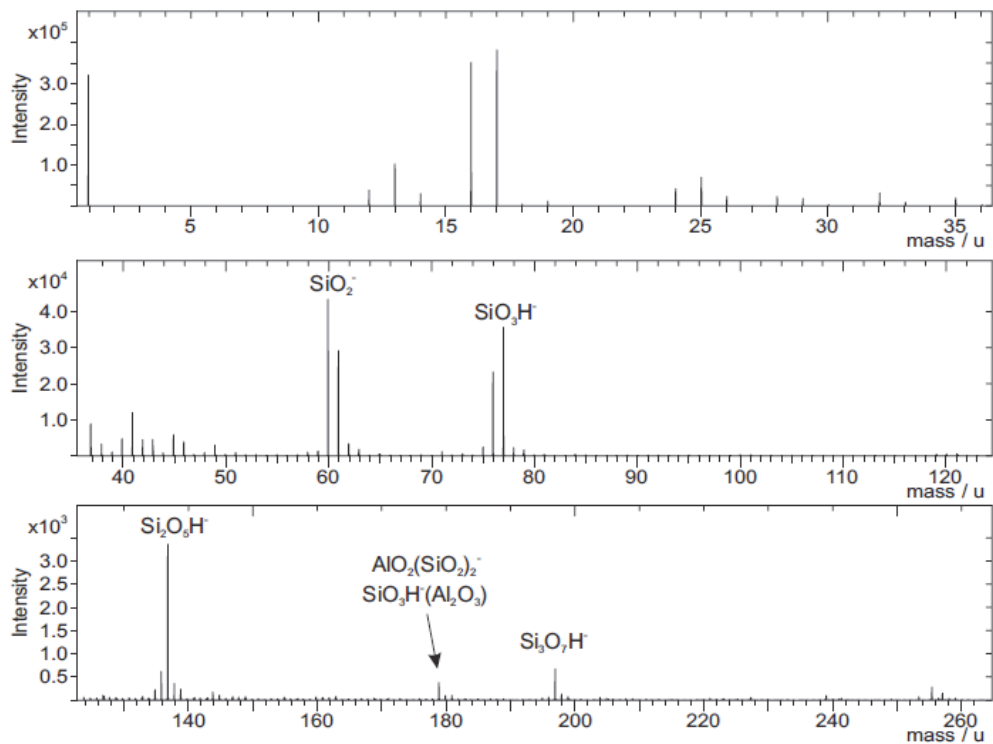


Fig. A.16: Positive/negative overview spectra of GPS derived plasma film on grit-blasted AA 2024 bare (produced by OFG Analytik, GmbH)



positive spectrum



negative spectrum

Fig. A.17: Positive/negative overview spectra of GPS derived plasma film on polished AA 2024 bare (HNO_3); (produced by OFG Analytik GmbH)

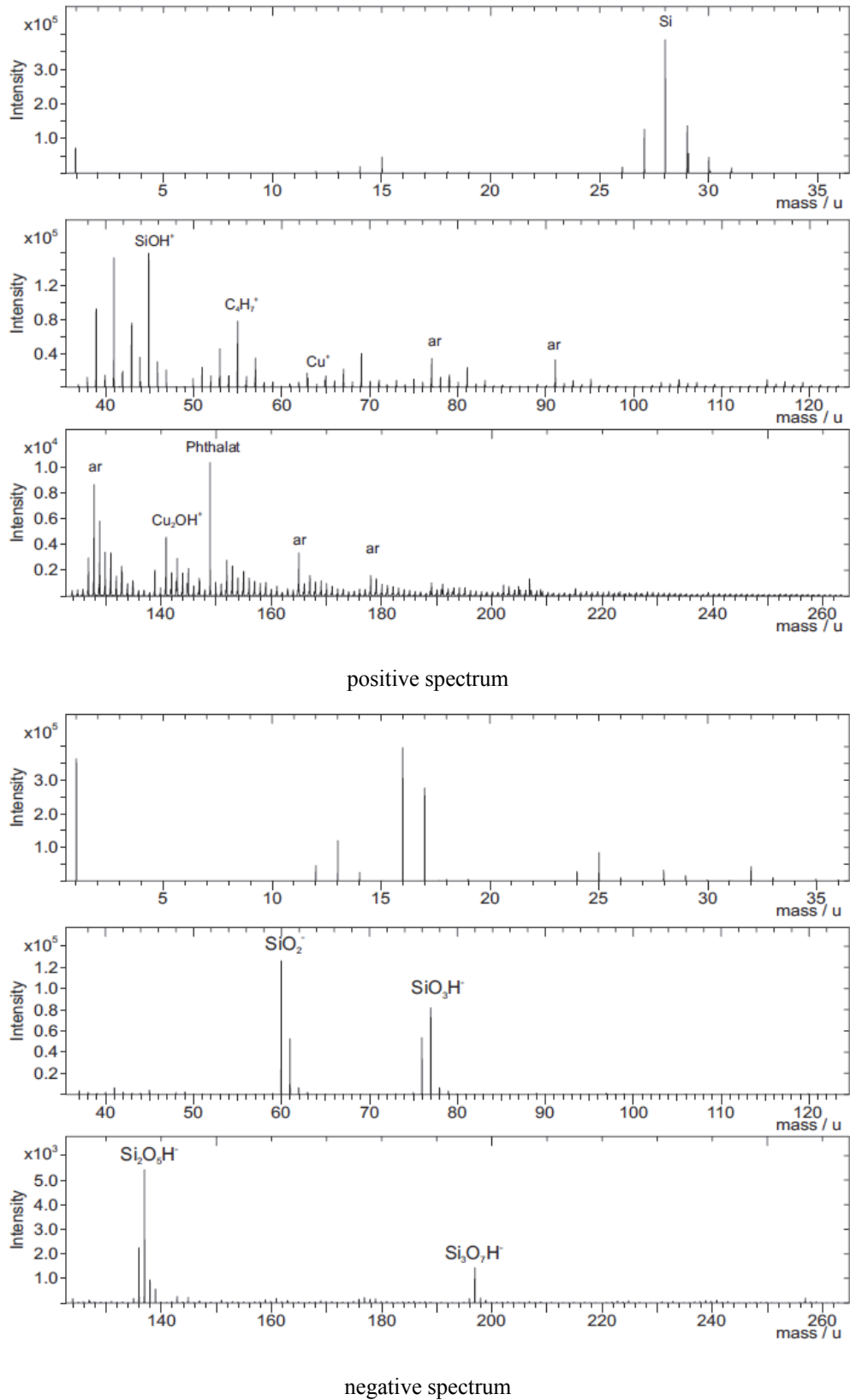


Fig. A.18: Positive/negative overview spectra of TEOS derived plasma film on polished AA 2024 bare (HNO₃); (produced by OFG Analytik GmbH)

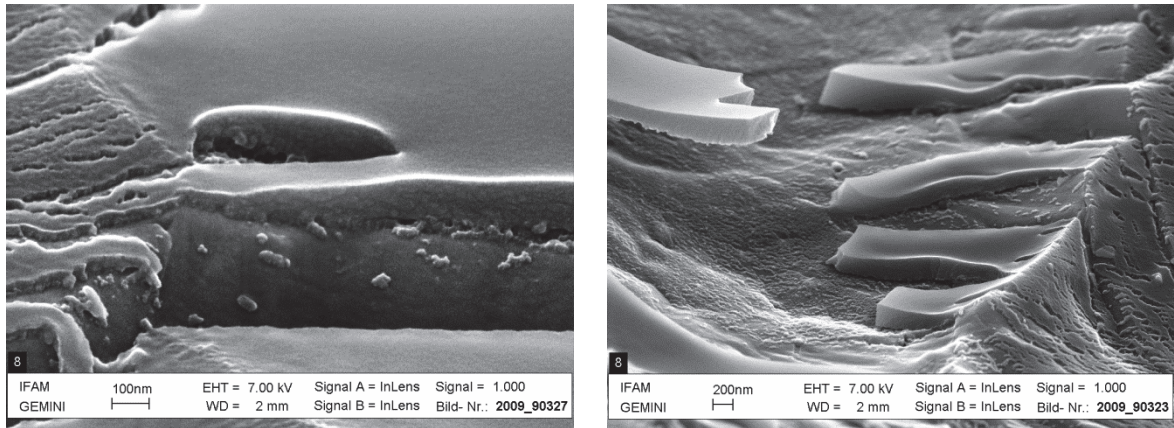
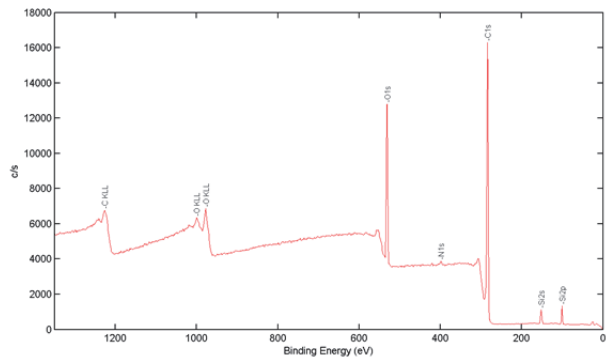
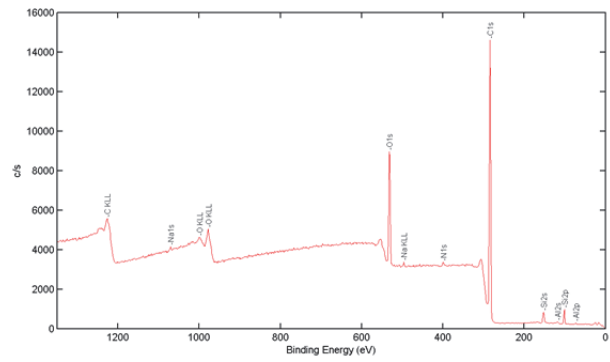


Fig. A.19: SEM images of AC-130 on AA 2024 bare (HNO_3) showing strong variation of film thickness

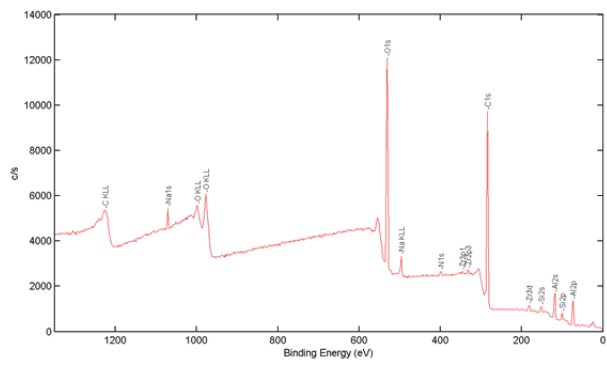
A.3 Joint durability



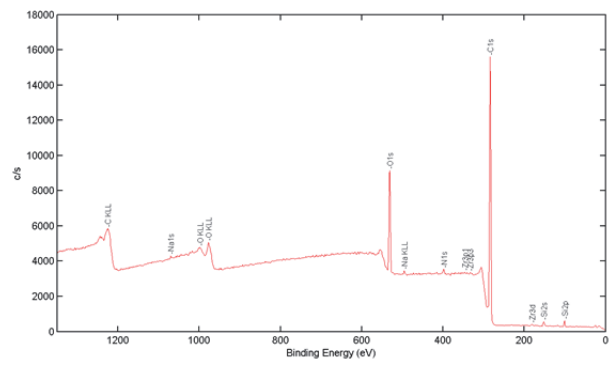
GPS (aq) – metal side



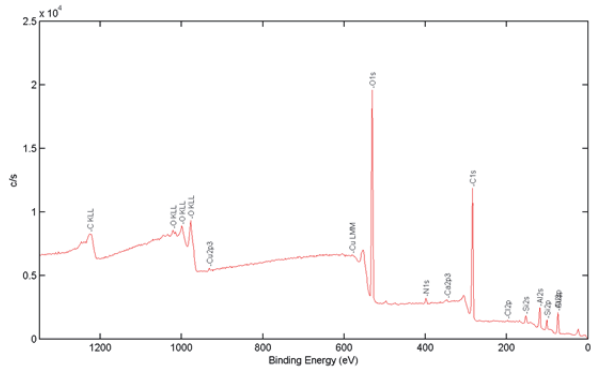
GPS (aq) – adhesive side



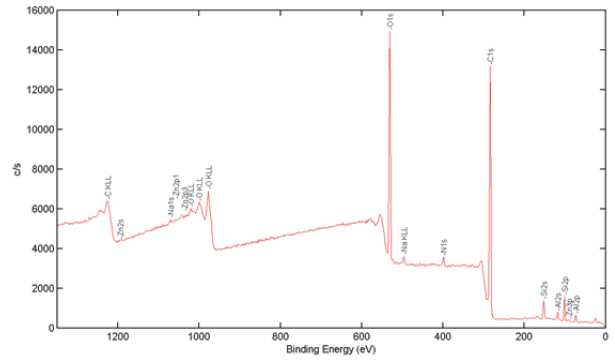
AC-130 – metal side



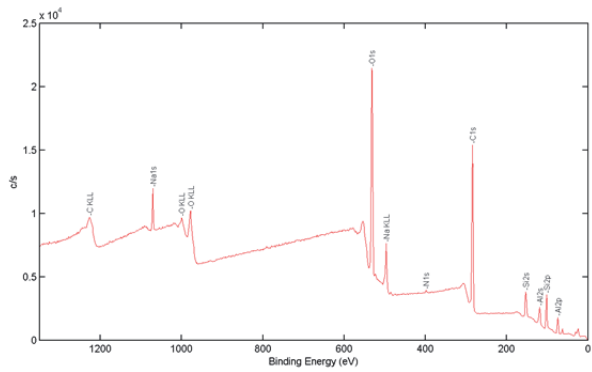
AC-130 – adhesive side



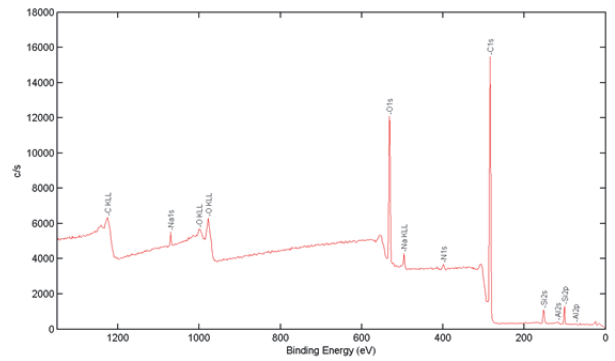
GPS plasma 5 SLM – metal side



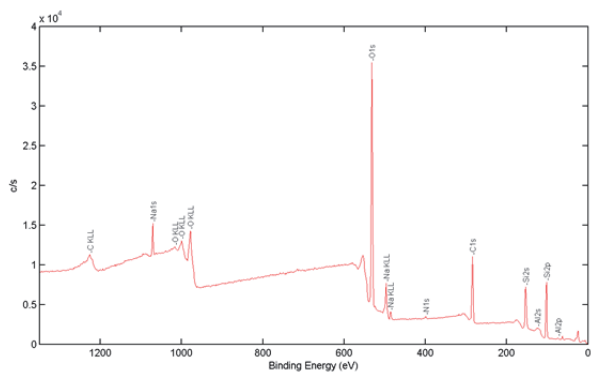
GPS plasma 5 SLM – adhesive side



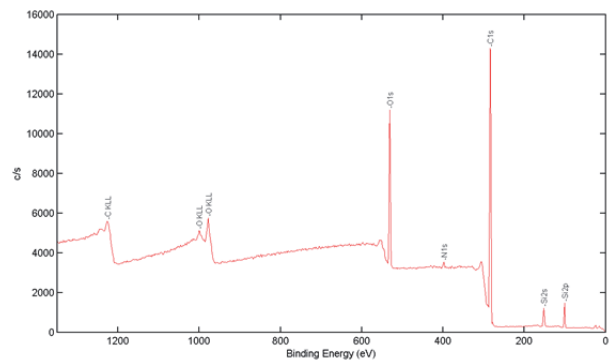
TEOS plasma 0.5 SLM – metal side



TEOS plasma 0.5 SLM – adhesive side



TEOS plasma 5 SLM – metal side



TEOS plasma 5 SLM – adhesive side

Fig. A.20: XPS overview spectra of apparent interfacial failure area after cyclic lap shear testing

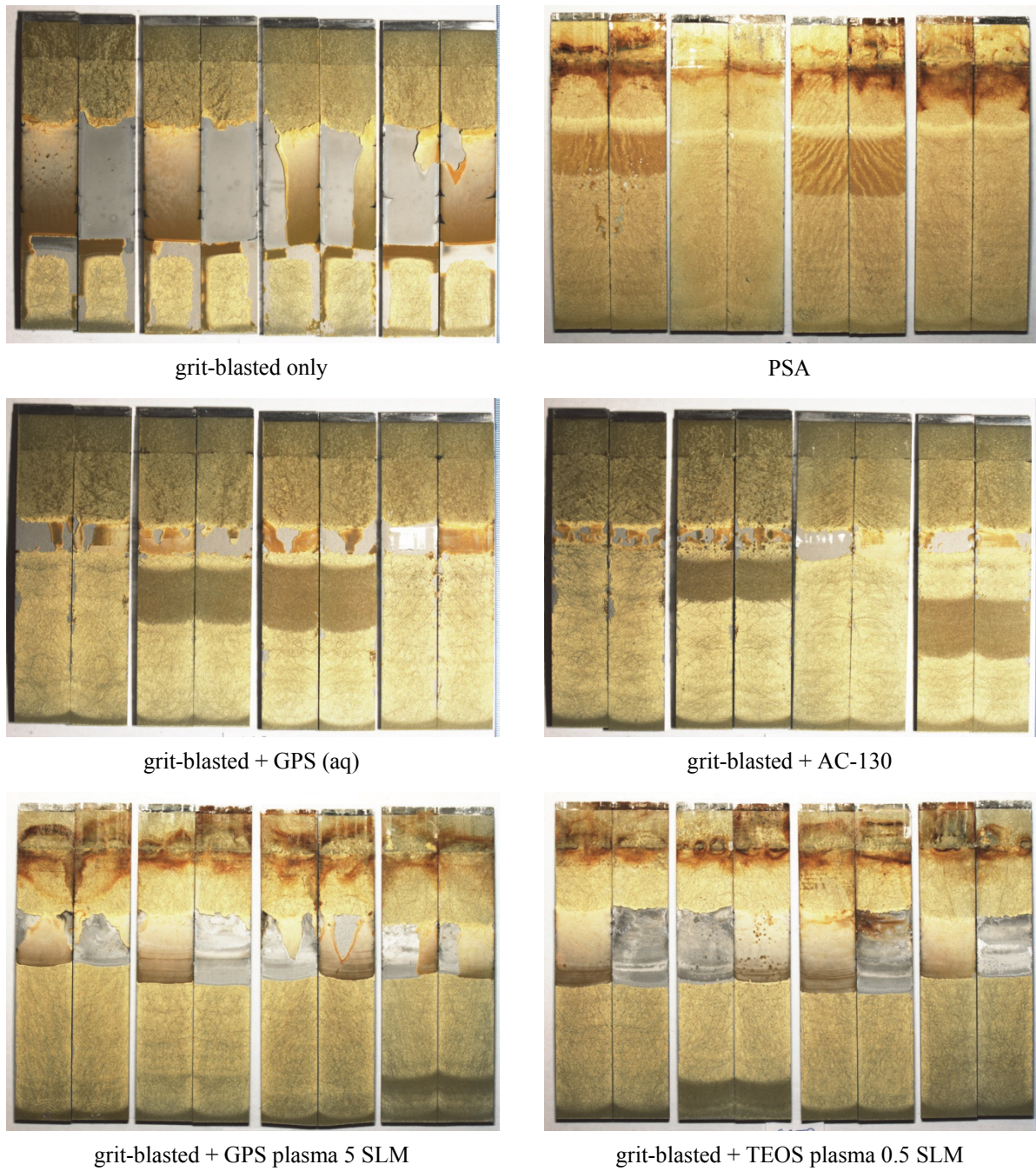


Fig. A.21: AA 2024 clad wedge test specimens after > 1000 h exposure to 50 °C, 95 % rh

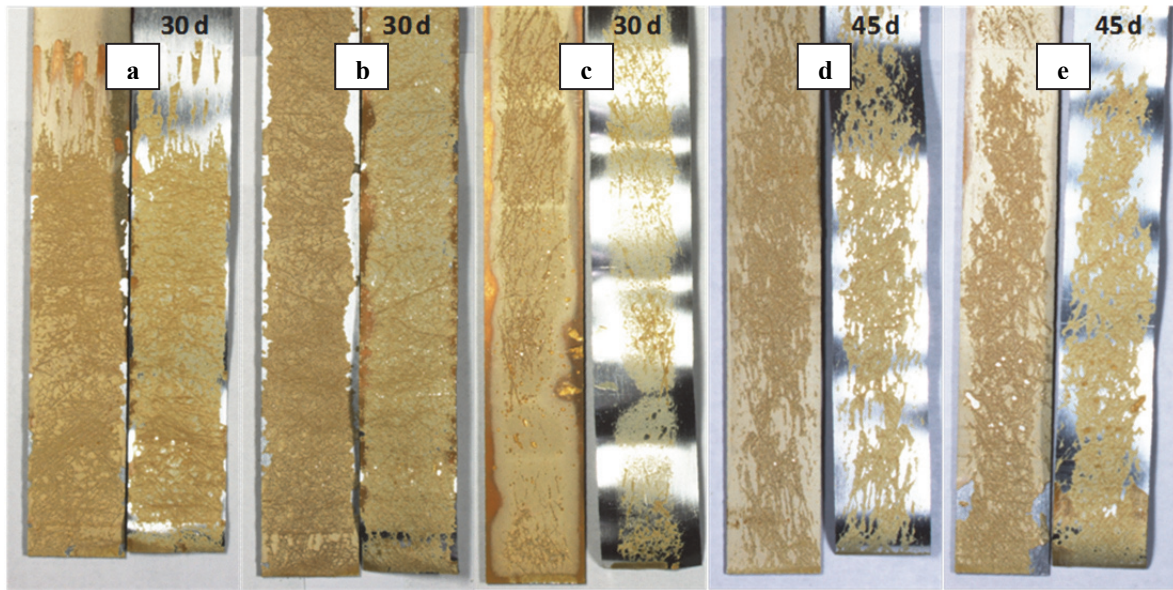


Fig. A.22: HNO₃ etched AA 2024 clad joints after exposure to 35 °C, 100 % rh
a) AC-130 b) GPS (aq) c) uncoated d) GPS plasma e) TEOS plasma (5 SLM)

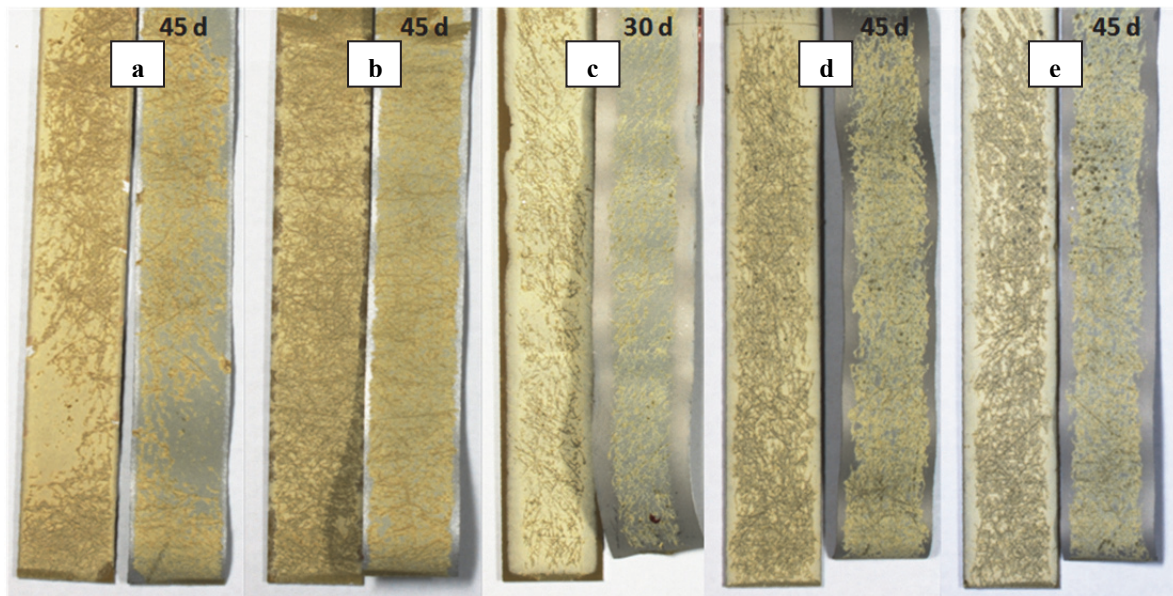


Fig. A.23: Grit-blasted AA 2024 clad joints after exposure to 35 °C, 100 % rh
a) AC-130 b) GPS (aq) c) uncoated d) GPS plasma e) TEOS plasma (5 SLM)

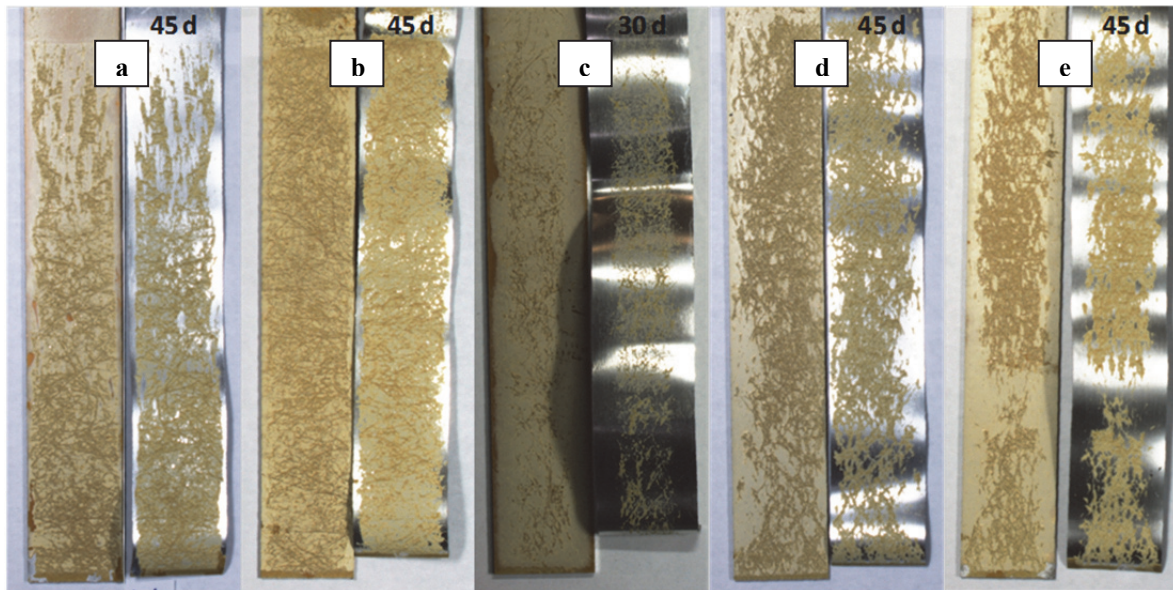


Fig. A.24: HNO₃ etched AA 2024 bare joints after exposure to 35 °C, 100 % rh
a) AC-130 b) GPS (aq) c) uncoated d) GPS plasma e) TEOS plasma (5 SLM)

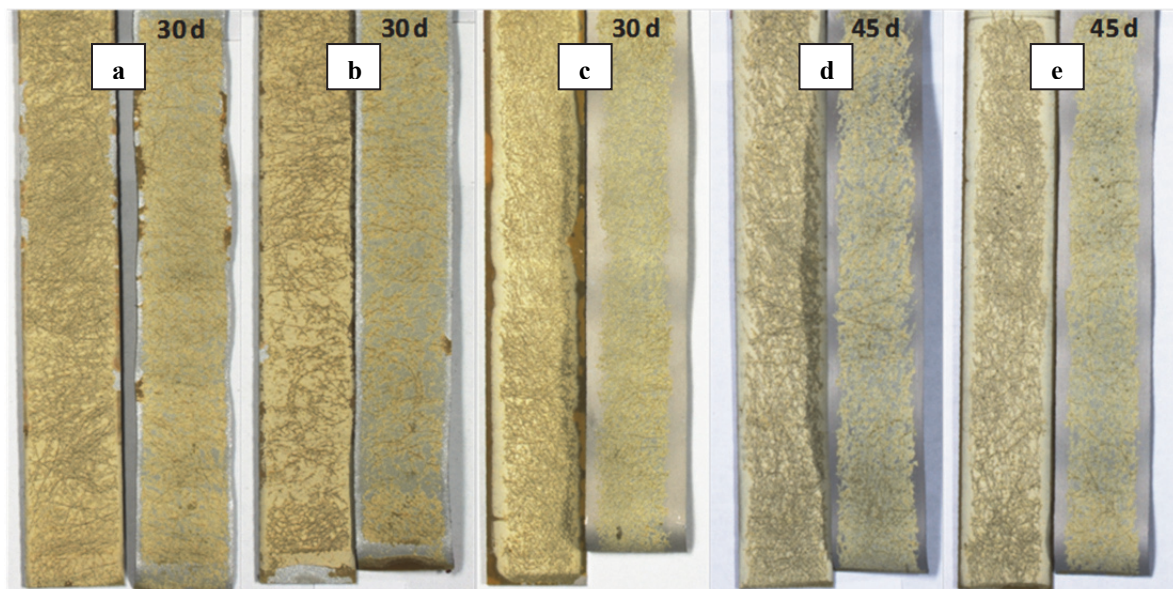


Fig. A.25: Grit-blasted AA 2024 bare joints after exposure to 35 °C, 100 % rh
a) AC-130 b) GPS (aq) c) uncoated d) GPS plasma e) TEOS plasma (5 SLM)

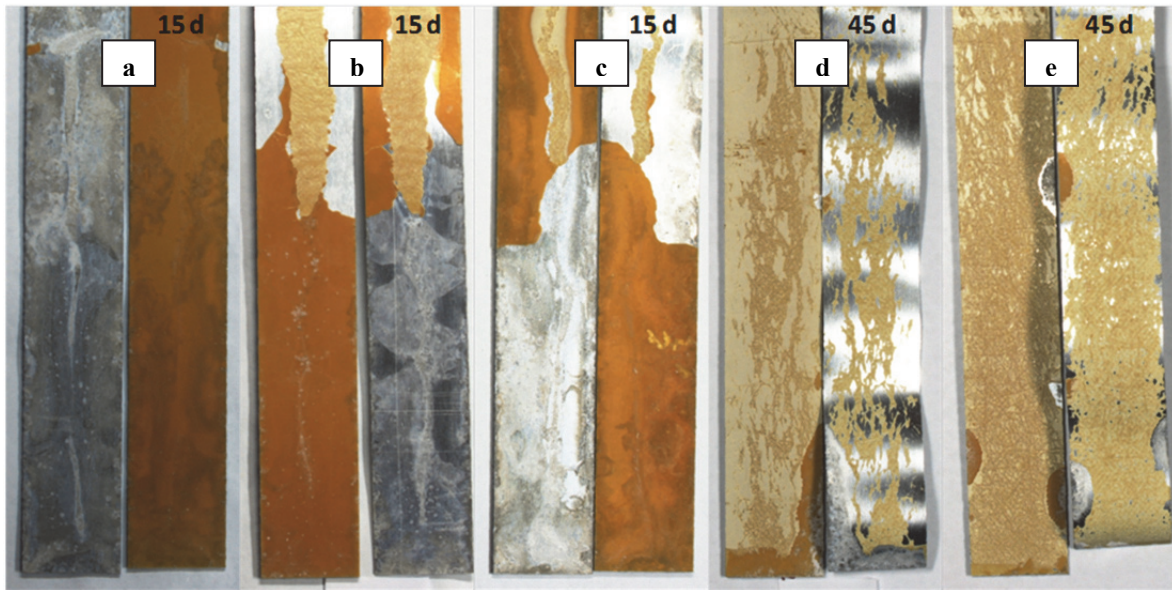


Fig. A.26: HNO_3 etched AA 2024 clad joints after exposure to SST
 a) AC-130 b) GPS (aq) c) uncoated d) GPS plasma e) TEOS plasma (5 SLM)

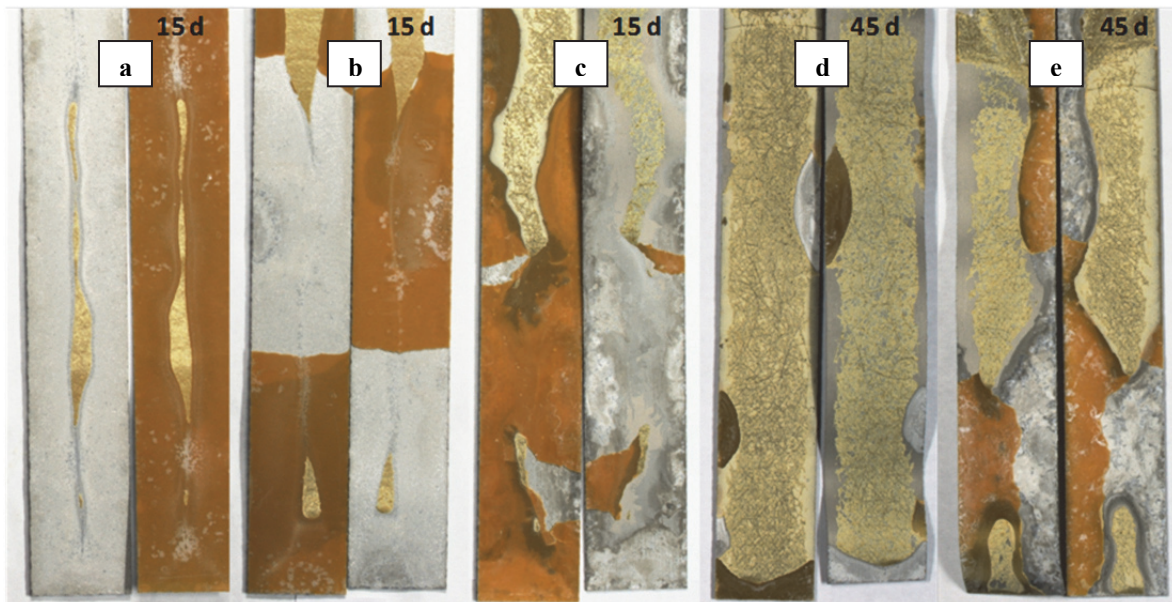


Fig. A.27: Grit-blasted AA 2024 clad joints after exposure to SST
 a) AC-130 b) GPS (aq) c) uncoated d) GPS plasma e) TEOS plasma (5 SLM)

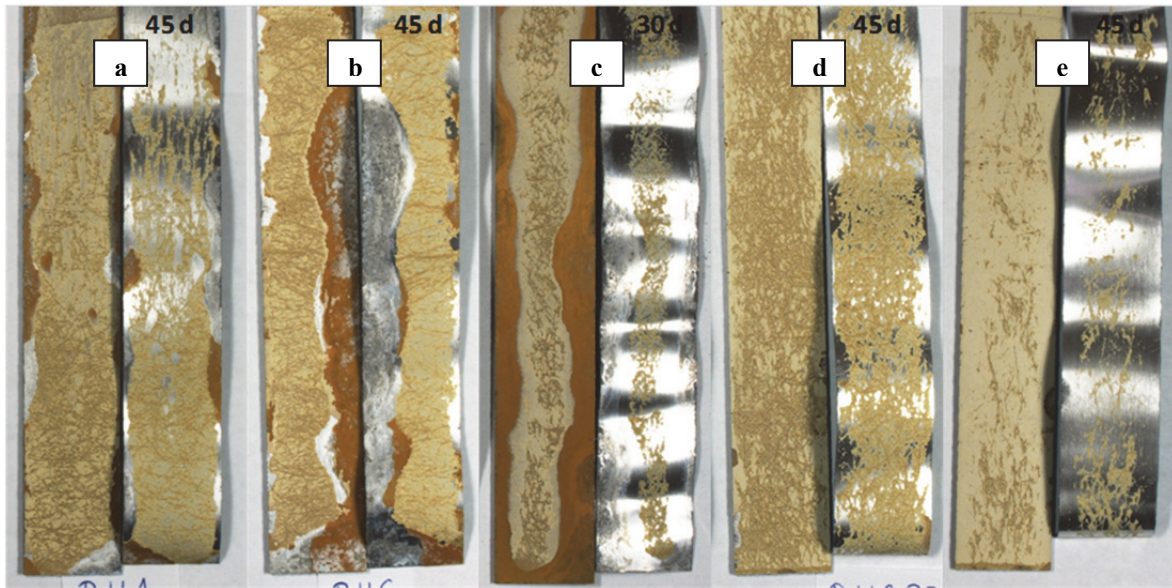


Fig. A.28: HNO₃ etched AA 2024 bare joints after exposure to SST
a) AC-130 b) GPS (aq) c) uncoated d) GPS plasma e) TEOS plasma (5 SLM)

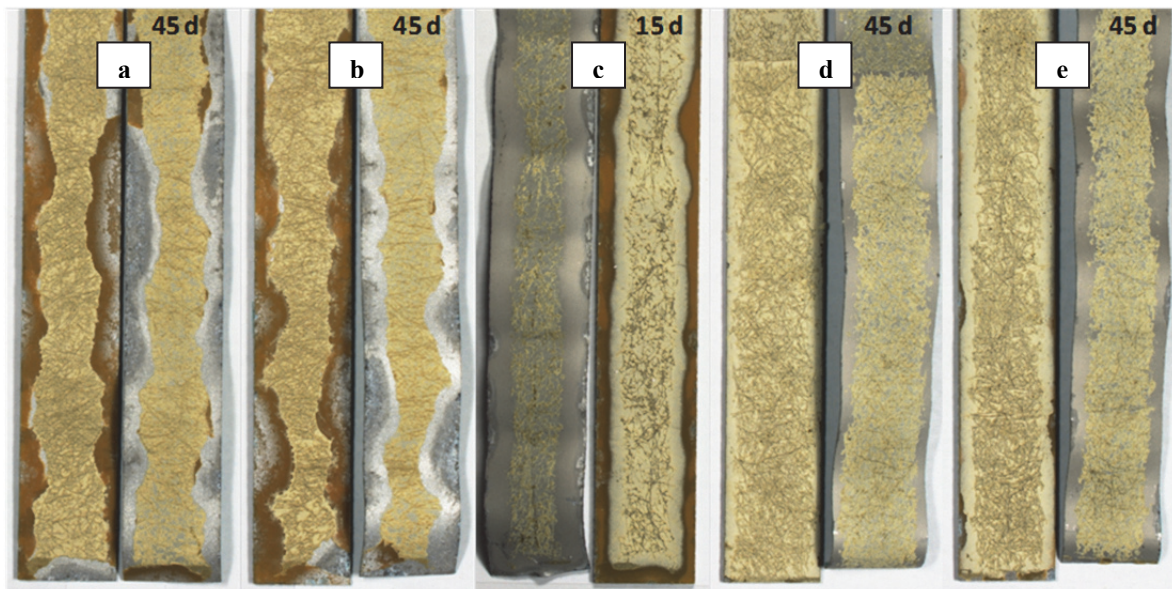


Fig. A.29: Grit-blasted AA 2024 bare joints after exposure to SST
a) AC-130 b) GPS (aq) c) uncoated d) GPS plasma e) TEOS plasma (5 SLM)

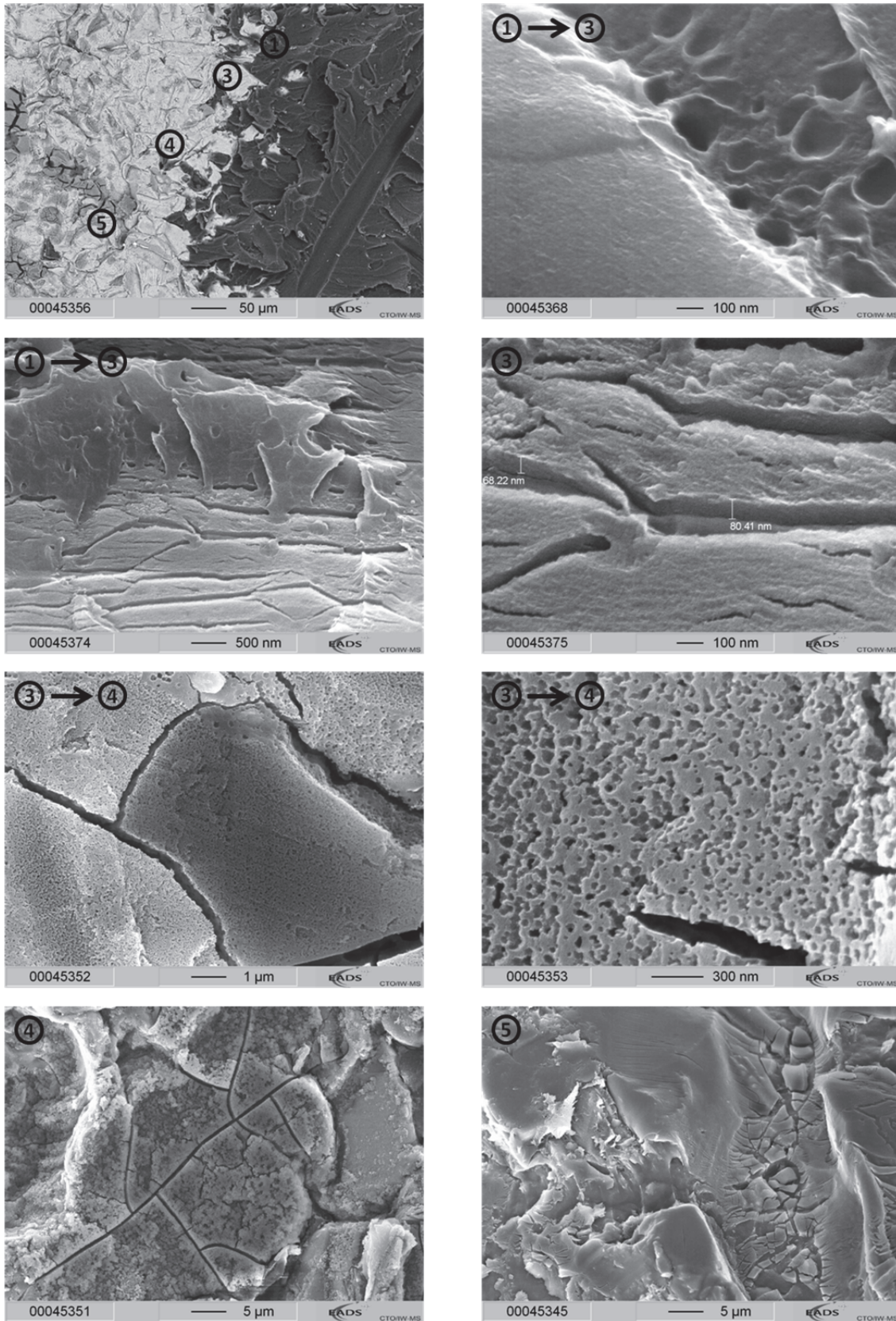


Fig. A.30: SEM images of bondline corrosion on GPS (aq) coated AA 2024 clad (grit-blasted)

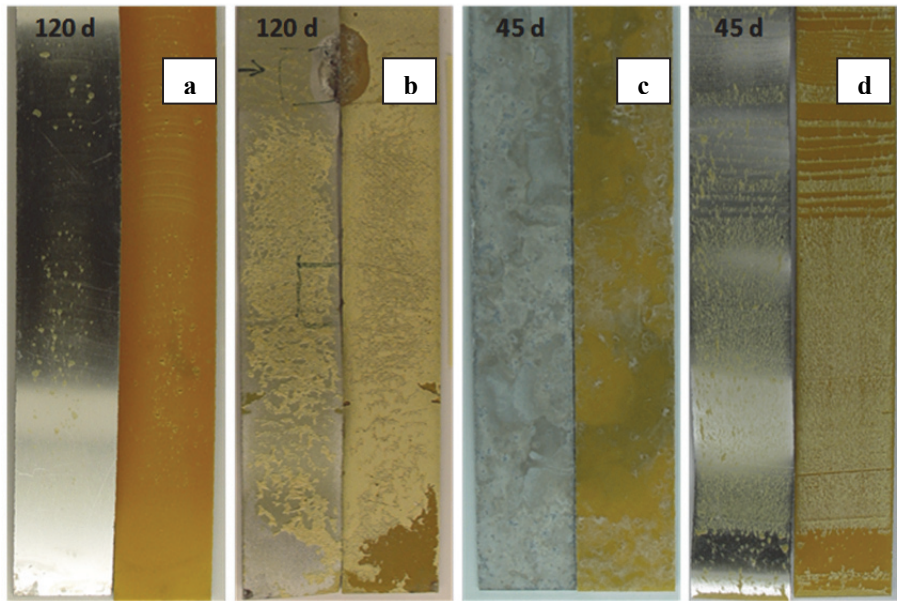


Fig. A.31: Exemplary AA 2024 clad bondline corrosion specimens with bonding primer:
a) Smut-Go NC + GPS plasma + BR127
b) grit-blasted + GPS (aq) + BR 127
c) grit-blasted + GPS (aq) + Cr-free primer
d) Smut-Go NC + GPS plasma + Cr-free primer

B Bibliography

- [1] A. Kinloch, "Adhesives in Engineering," in *Proceedings of the Institution of Mechanical Engineers - Eighty-fourth Thomas Hawksley Memorial Lecture*, 1996.
- [2] W. Brockmann, O.-D. Hennemann, H. Kollek and C. Matz, "Adhesion in bonded aluminium joints for aircraft construction," *International Journal of Adhesion & Adhesives*, vol. 6, no. 3, pp. 115-143, 1986.
- [3] N. de Bruyne, "Fundamentals of adhesion," in *Proceedings of Conference on Bonded Aircraft Structures*, 1957.
- [4] B. Räckers, "Bonding processes at Airbus," in *FAA workshop on adhesive bonding*, Sussex, 2004.
- [5] B. Pelouze, "Pre-treatment for bonding composites/metal," in *FAA workshop on adhesive bonding*, Sussex, 2004.
- [6] K. Armstrong, "Cautionary tales from experiences when working with adhesively bonded composite and metal structures used in aircraft," *Journal of Adhesion Science and Technology*, vol. 23, pp. 567-578, 2009.
- [7] G. Bengough and J. Stuart, "Process of protecting surfaces of aluminum or aluminum alloys". Unites States Patent US 1771910, July 28th 1924.
- [8] Boeing, "BAC 555 - phosphoric acid anodizing of aluminum for structural bonding".
- [9] A. Baker, "Introduction and overview," in *Advances in the Bonded Composite Repair of Metallic Aircraft Structure*, Elsevier Science Ltd., 2002, pp. 1-18.
- [10] The Technical Cooperation Program (Action Group 13), "Certification of bonded structures," 2001.
- [11] A. Higgins, "Adhesive bonding of aircraft structures," *International Journal of Adhesion & Adhesives*, vol. 20, no. 5, p. 367-376, 2000.
- [12] M. Davis, "Deficiencies in regulations for certification and continuing airworthiness of bonded structure," in *Proceedings of the International Aerospace Congress in Australia*, Sydney, 1997.
- [13] Federal Aviation Administration, "AC 20-107B - composite aircraft structure," 2009.
- [14] M. Davis and A. McGregor, "Assessing adhesive bond failures: mixed-mode bond failures explained," in *ISASI Australian Safety Seminar*, Canberra, 2010.
- [15] "AMC 20-29 composite aircraft structure," European Aviation Safety Agency, 2010.
- [16] G. Critchlow, K. Yendall, D. Bahrani, A. Quinn and F. Andrews, "Strategies for the replacement of chromic acid anodising for the structural bonding of aluminium alloys," *International Journal of Adhesion & Adhesives*, vol. 26, pp. 419-453, 2006.
- [17] K. Yendall and G. Critchlow, "Novel methods, incorporating pre- and post-anodising steps, for the replacement of the Bengough-Stuart chromic acid anodising process in structural bonding applications," *International Journal of Adhesion & Adhesives*, vol. 29, pp. 503-508, 2009.
- [18] L. Velterop, "Phosphoric sulphuric acid anodising: an alternative for chromic acid anodising in aerospace applications?," in *3rd International Symposium Aluminium Surface Science and Technology (ASST 2003) Proceedings*, Bonn, 2003.
- [19] R. Jones, L. Molent and S. Pitt, "Study of multi-site damage of fuselage lap joints," *Theoretical and Applied Fracture Mechanics*, vol. 32, no. 2, pp. 81-100, 1999.
- [20] M. Davis, M. Janardhana and A. Wherrett, "Adhesive bonded repair technology: supporting ageing aircraft," in *Ageing Aircraft Users Forum*, Brisbane, 2006.
- [21] A. Baker, "Crack patching: experimental studies, practical applications," in *Bonded Repair of Aircraft Structures (edited by A.A. Baker and R. Jones)*, Martinus Nijhoff Publishers, 1988, pp. 107-173.

- [22] M. Kuperman and R. Horton, in *Engineering Materials Handbook Vol. 3: Adhesives and Sealants*, Materials Park, ASM International, 1990, pp. 801-820.
- [23] W. Choi, "Bonded GLARE repairs - current status," unpublished report of joint research between Airbus-Korean Air-USC-KAU-Inha, 2009.
- [24] A. Baker and R. Chester, "Minimum surface treatments for adhesively bonded repairs," *International Journal of Adhesion & Adhesives*, vol. 12, no. 2, pp. 73-78, 1992.
- [25] E. Plueddemann, *Silane Coupling Agents*, New York: Plenum Press, 1982.
- [26] R. Kuhbänder and J. Mazza, "Understanding the Australian silane surface treatment," in *38th International SAMPE Symposium*, Anaheim, 1993.
- [27] M. Abel, R. Allington, R. Digby, N. Poritt, S. Shaw and J. Watts, "Understanding the relationship between silane application conditions, bond durability and locus of failure," *International Journal of Adhesion & Adhesives*, vol. 26, pp. 2-15, 2006.
- [28] K. Blohowiak, J. Osborne and K. Krienke, "Sol for coating metals". United States Patent US 5814137, November 4th 1996.
- [29] K. Blohowiak, J. Grob and W. Grace, "Improvements in sol-gel surface preparation methods for metal bonding applications," in *39th ISTC Conference*, Cincinnati, 2007.
- [30] D. McCray and J. Mazza, "Optimization of sol-gel surface preparation for repair bonding of aluminum alloys," in *45th International SAMPE Symposium*, Daytona, 2000.
- [31] S. Babayan, J. Jeong, V. Tu, J. Park, G. Selwyn and R. Hicks, "Deposition of silicon dioxide films with an atmospheric-pressure plasma jet," *Plasma Sources Science and Technology*, vol. 7, no. 3, pp. 286-288, 1998.
- [32] F. Massines, C. Sarra-Bournet, F. Fanelli, N. Naudé and N. Gherardi, "Atmospheric pressure low temperature direct plasma technology: status and challenges for thin film deposition," *Plasma Processes and Polymers*, vol. 9, no. 11-12, p. 1041-1073, 2012.
- [33] A. Rider, "DSTO-TR: surface treatments for field level bonded repairs to aluminium and titanium structure," Defence Science and Technology Organisation, Fishermans Bend, 2008.
- [34] K. Blohowiak, J. Grob and J. Seebergh, "AVTIP delivery order 0033: advanced sol-gel adhesion processes - transition support," Air Force Research Laboratory, Air Vehicle Technology Integration Program, Wright-Patterson Air Force Base, 2005.
- [35] B. Braune, "PlasmaPlus-Anwendung auf O-LED Bauteilen," in *Plasmatreat Anwendertagung: PlasmaPlus-Inline-Beschichtung unter Atmosphärendruck*, Birkenfeld, 2009.
- [36] B. Schwanitz, "Nachträgliche Integration von Openair-Plasma in eine bestehende Prozesskette der Automobil Zulieferindustrie," in *Plasmatreat Anwendertagung: PlasmaPlus-Inline-Beschichtung unter Atmosphärendruck*, Birkenfeld, 2009.
- [37] T. Beer, "Selektiver Korrosionsschutz für Alu-Gehäuse," *Journal für Oberflächentechnik*, vol. 47, no. 9, pp. 60-62, 2007.
- [38] U. Lommatzsch, "Plasmasbeschichtung bei Atmosphärendruck," *Adhäsion Kleben & Dichten*, vol. 52, no. 10, pp. 38-41, 2009.
- [39] U. Lommatzsch and J. Ihde, "Thin film deposition with a cold atmospheric pressure plasma jet for corrosion protection of aluminum and for tailoring adhesion properties," in *29th ICPIG*, Cancun, 2009.
- [40] G. Grundmeier and M. Stratmann, "Interfacial processes during plasma polymer deposition on oxide covered iron," *Thin Solid Films*, vol. 352, no. 1-2, p. 119-127, 1999.
- [41] V. Barranco, P. Thiemann, H. Yasuda, M. Stratmann and G. Grundmeier, "Spectroscopic and electrochemical characterisation of thin cathodic plasma polymer films on iron," *Applied Surface Science*, vol. 229, pp. 87-96, 2004.
- [42] T. Titz, F. Hörzenberger, K. Van den Bergh and G. Grundmeier, "Correlation of interfacial electrode potential and corrosion resistance of plasma polymer coated galvanized steel," *Corrosion Science*, vol. 52, no. 2, pp. 369-386, 2010.

- [43] C. Tendero, C. Tixier, P. Tristant, J. Desmanson and P. Leprince, "Atmospheric pressure plasmas: a review," *Spectrochimica Acta Part B*, vol. 61, pp. 2-30, 2006.
- [44] P. Bringmann, O. Rohr, F. Gammel and I. Jansen, "Atmospheric pressure plasma deposition of adhesion promotion layers on aluminium," *Plasma Processes and Polymers*, vol. 6, pp. 496-502, 2009.
- [45] K. Wefers and C. Misra, "Surface oxides on aluminum metal," in *Oxides and Hydroxides of Aluminum (19th Ed.)*, Alcoa Research Laboratories, 1987, pp. 64-73.
- [46] K. Wefers and C. Misra, "Properties of aluminum hydroxides and oxides," in *Oxides and Hydroxides of Aluminum (19th Ed.)*, Alcoa Research Laboratories, 1987, pp. 2-36.
- [47] H. Dunlop and M. Benmalek, "Role and characterization of surfaces in the aluminium industry," *Journal de Physique IV*, vol. Colloque C6, pp. C6-163-C6-174, 1997.
- [48] A. Nylund and I. Oleffjord, "Surface analysis of oxidized aluminium. 1. Hydration of Al_2O_3 and decomposition of $\text{Al}(\text{OH})_3$ in a vacuum studied by ESCA," *Surface and Interface Analysis*, vol. 21, pp. 283-289, 1994.
- [49] C. Bockenheimer, *Epoxid und Aluminium im Klebverbund nach mechanischer Vorbehandlung und nach Alterung*, Aachen: Shaker Verlag, 2005.
- [50] L. Jeurgens, W. Sloof, F. Tichelaar and E. Mittemeijer, "Thermodynamic stability of amorphous oxide films on metals: application to aluminum oxide films on aluminum substrates," *Physical Review B of the American Physical Society*, vol. 62, no. 7, pp. 4707-4719, 2000.
- [51] R. Alwitt, "The aluminum water system," in *Oxide and Oxide Films*, New York, Marcel Dekker Inc, 1976, pp. 169-254.
- [52] M. Alexander, G. Thompson and G. Beamson, "Characterization of the oxide/hydroxide surface of aluminium using X-ray photoelectron spectroscopy: a procedure for curve fitting the O 1s core level," *Surface and Interface Analysis*, vol. 29, pp. 468-477, 2000.
- [53] K. Wefers, "Properties and characterization of surface oxides on aluminium alloys," *Aluminium*, vol. 57, pp. 722-726, 1981.
- [54] T. Barr, "An ESCA study of the termination of the passivation of elemental metals," *The Journal of Physical Chemistry*, vol. 82, no. 16, pp. 1801-1810, 1978.
- [55] B. Strohmeier, "An ESCA method for determining the oxide thickness on aluminium alloys," *Surface and Interface Analysis*, vol. 15, pp. 51-56, 1990.
- [56] R. Winston Revie and H. Uhlig, *Uhlig's Corrosion Handbook*, New York: John Wiley & Sons, 2000.
- [57] D. Raps, *Development of a self-healing Corrosion Protection Coating for High Strength Aluminium Alloys*, Düsseldorf: VDI Verlag, 2008.
- [58] W. Mullins and B. Averbach, "The electronic structure of anodized and etched aluminum alloy surfaces," *Surface Science*, vol. 206, pp. 52-60, 1988.
- [59] F. Queiroz, H. de Melo and I. Costa, "Effect of intermetallics on the corrosion of Al 2024-T3 alloy in solution with different chloride concentration," *Materials Science Forum*, Vols. 587-588, pp. 415-419, 2008.
- [60] C. Blanc, S. Gastaud and G. Mankowski, "Mechanistic studies of the corrosion of 2024 aluminum alloy in nitrate solutions," *Journal of the Electrochemical Society*, vol. 150, no. 8, pp. 396-404, 2003.
- [61] A. Hughes, C. MacRae, N. Wilson, A. Torpy, T. Muster and A. Glenn, "Sheet AA2024-T3: a new investigation of microstructure and composition," *Surface and Interface Analysis*, vol. 42, no. 4, pp. 334-338, 2010.
- [62] ASTM International, *ASTM B209-10 - standard specification for aluminum and aluminum-alloy sheet and plate*, West Conshohocken, 2010.
- [63] G. Habenicht, *Kleben: Grundlagen, Technologien, Anwendungen (5.Auflage)*, Berlin : Springer, 2006.
- [64] D. Packham, "Adhesion," in *Handbook of Adhesion*, West Sussex, John Wiley & Sons, 2005, pp. 14-16.

- [65] A. Griffith, "The phenomena of rupture and flow in solids," *Philosophical Transactions of the Royal Society of London*, vol. A221, pp. 163-198, 1920.
- [66] E. Orowan, "Fundamentals of brittle behaviour in metals," in *Fatigue and Fracture of Metals*, New York, John Wiley & Sons, 1952, pp. 137-167.
- [67] K. Kendall, *Molecular Adhesion and Its Applications*, New York: Kluwer Academic/Plenum Publishers, 2001.
- [68] M. Davis and J. Tomblin, "Best practice in adhesive-bonded structures and repairs," Federal Aviation Administration, Washington DC, 2007.
- [69] A. Kinloch, *Adhesion and Adhesives*, New York: Chapman and Hall, 1987.
- [70] J. McBain and D. Hopkins, "On adhesives and adhesive action," *The Journal of Physical Chemistry*, vol. 29, pp. 188-204, 1925.
- [71] B. Deryagin and N. Krotova, *Doklady Akademii Nauk SSR*, vol. 61, p. 849, 1948.
- [72] S. Voyutskii, *Autohesion and Adhesion of High Polymers*, New York: Wiley Interscience, 1963.
- [73] D. Packham, "Some contributions of surface analysis to the development of adhesion theories," *The Journal of Adhesion*, vol. 84, pp. 240-255, 2008.
- [74] K. Allen, "Theories of adhesion," in *Handbook of Adhesion*, West Sussex, John Wiley & Sons, 2005, pp. 535-538.
- [75] D. Packham, "Surface energy, surface topography and adhesion," *International Journal of Adhesion & Adhesives*, vol. 23, pp. 437-448, 2003.
- [76] J. Venables, D. McNamara, J. Chen, T. Sun and R. Hopping, "Oxide morphologies on aluminum prepared for adhesive bonding," *Applications of Surface Science*, vol. 3, no. 1, pp. 88-98, 1979.
- [77] J. D. Venables, "Review - adhesion and durability of metal-polymer bonds," *Journal of Materials Science*, pp. 2431-2453, 1984.
- [78] D. Packham, "The mechanical theory of adhesion - changing perceptions 1925-1991," *The Journal of Adhesion*, vol. 39, pp. 137-144, 1992.
- [79] A. Kinloch, M. Little and J. Watts, "The role of the interphase in the environmental failure of adhesive joints," *Acta Materialia*, vol. 48, pp. 4543-4553, 2000.
- [80] D. Packham, "Roughness and adhesion," in *Handbook of Adhesion*, West Sussex, John Wiley & Sons, 2005, pp. 407-408.
- [81] F. Boerio and D. Ondrus, "Effect of substrates on the structure of polymer interphases - II. epoxy/anhydride adhesives cured against aluminum and copper," *Journal of Colloid and Interface Science*, vol. 139, no. 2, pp. 446-456, 1990.
- [82] M. Aufray and A. Roche, "Properties of the interphase epoxy-amine/metal: influences from the nature of the amine and the metal," in *Adhesion - Current Research and Application*, Weinheim, Wiley-VCH, 2005, pp. 89-102.
- [83] M. Aufray and A. Roche, "Epoxy-amine/metal interphases: influences from sharp needle-like," *International Journal of Adhesion & Adhesives*, vol. 27, pp. 387-393, 2007.
- [84] A. Kinloch, "The science of adhesion," *Journal of Material Science*, vol. 15, no. 9, pp. 2141-2166, 1980.
- [85] J. Huntsberger, in *Treatise on Adhesion and Adhesives - Vol. 1*, London, Edward Arnold, 1967, pp. 119-149.
- [86] J. Bikermann, *The Science of Adhesive Joints - 2nd edition*, New York: Academic Press, 1968.
- [87] W. Zisman, *Industrial and Engineering Chemistry*, vol. 55, no. 10, pp. 11-51, 1963.
- [88] K. Allen, "Adsorption theory of adhesion," in *Handbook of Adhesion*, West Sussex, John Wiley & Sons, 2005, pp. 38-40.
- [89] F. Fowkes, "Attractive forces as solid-liquid interface," in *Wetting*, London, Society of Chemical Industry Monograph No. 25, 1967, p. 3.

- [90] F. Fowkes, "Quantitative characterization of the acid-base properties of solvents, polymers, and inorganic surfaces," in *Acid-Base Interactions: Relevance to Adhesion Science and Technology*, Utrecht, VSP, 1991, pp. 93-116.
- [91] K. Mittal and H. Anderson, *Acid-Base Interactions: Relevance to Adhesion Science and Technology*, Utrecht: VSP, 1991.
- [92] D. Packham, "Acid-base interactions: introduction," in *Handbook of Adhesion*, West Sussex, John Wiley & Sons, 2005, pp. 5-7.
- [93] J. Watts, A. Rattana and M.-L. Abel, "Interfacial chemistry of adhesives on hydrated aluminium and hydrated aluminium treated with an organosilane," *Surface and Interface Analysis*, vol. 36, pp. 1449-1468, 2004.
- [94] J. Watts, "The interfacial chemistry of adhesion: novel routes to the holy grail?," in *Adhesion - Current Research and Application*, Weinheim, Wiley-VCH, 2005, pp. 1-15.
- [95] J. Bickermann, *The Science of Adhesive Joints*, New York: Academic Press, 1961.
- [96] A. Bjorgum, F. Lapique, J. Walmsley and K. Redford, "Anodising as pre-treatment for structural bonding," *International Journal of Adhesion & Adhesives*, vol. 23, pp. 401-412, 2003.
- [97] G. Critchlow, I. Ashcroft, T. Cartwright and D. Bahrani, "Anodising aluminum alloy". EU Patent EP 1836331, January 10th 2006.
- [98] Airbus Operations, "AIP - phosphoric sulphuric anodising (PSA) of aluminium alloys prior to structural bonding," 2010.
- [99] C. Ong, W. Shu and S. Shen, "The evaluation of non-tank surface treatments for aluminium bonding repairs," *International Journal of Adhesion & Adhesives*, vol. 12, no. 2, pp. 79-84, 1992.
- [100] D. McCray, G. Huff, J. Smith and J. Mazza, "An ambient-temperature adhesive bonded repair process for aluminum alloys," in *46th International SAMPE Symposium*, Anaheim, 2001.
- [101] A. Hughes, K. Nelson and P. Miller, "Desmutting of aluminium alloy 2024-T3 using rare earth electrolyte," *Materials Science and Technology*, vol. 15, pp. 1124-1132, 1999.
- [102] G. Critchlow, D. Brewis, D. Emmony and C. Cottam, "Initial investigation into the effectiveness of CO₂-laser treatment of aluminium for adhesive bonding," *International Journal of Adhesion & Adhesives*, vol. 15, pp. 233-236, 1995.
- [103] G. Critchlow and D. Brewis, "Review of surface pretreatments of aluminium alloys," *International Journal of Adhesion & Adhesives*, vol. 16, pp. 255-275, 1996.
- [104] R. Digby and S. Shaw, "The international collaborative programme on organosilane coupling agents: an introduction," *International Journal of Adhesion & Adhesives*, vol. 18, pp. 261-264, 1998.
- [105] M.-L. Abel, J. Watts and R. Digby, "The influence of process parameters on the interfacial chemistry of GPS on aluminium: a review," *The Journal of Adhesion*, vol. 80, pp. 291-312, 2004.
- [106] K. Blohowiak, "Factors influencing durability of sol-gel surface treatments in metal bonded structures," in *47th International SAMPE Symposium*, Long Beach, 2002.
- [107] C. Taylor, F. Boerio, S. Ward, D. Ondrus, R. Dickie and M. Brutto, "Plasma polymer films as adhesion promoting primers for aluminium. Part II: strength and durability of lap joints," *The Journal of Adhesion*, vol. 69, pp. 237-261, 1999.
- [108] S. Shaw, "Editorial," *International Journal of Adhesion & Adhesives*, vol. 26, no. 1-2, 2006.
- [109] C. Brinker and G. Scherer, *Sol-Gel Science - The Physics and Chemistry of Sol-Gel Processing*, San Diego: Academic Press, 1989.
- [110] C. Bertelsen and F. Boerio, "Linking mechanical properties of silanes to their chemical structure: an analytical study of γ -GPS solutions and films," *Progress in Organic Coatings*, vol. 41, pp. 239-246, 2001.
- [111] F. de Buyl and A. Kretschmer, "Understanding hydrolysis and condensation kinetics of γ -glycidoxypropyl-trimethoxysilane," *The Journal of Adhesion*, vol. 84, pp. 125-142, 2008.

- [112] D. Schaefer, "Polymers, fractals and ceramic materials," *Science*, vol. 243, no. 4894, pp. 1023-1032, 1989.
- [113] M.-L. Abel, J. Watts and R. Digby, "The adsorption of alkoxy silanes on oxidised aluminium substrates," *International Journal of Adhesion & Adhesives*, vol. 18, pp. 179-192, 1998.
- [114] D. Oostendorp, G. Bertrand and G. Stoffer, "Kinetics and mechanism of the hydrolysis and alcoholysis of alkoxy silanes," in *Silanes and other Coupling Agents*, Utrecht, VSP, 1992, pp. 159-179.
- [115] M.-L. Abel, R. Digby, I. Fletcher and J. Watts, "Evidence of specific interaction between γ -glycidoxypropyltrimethoxysilane and oxidized aluminium using high-mass resolution ToF-SIMS," *Surface and Interface Analysis*, vol. 29, pp. 115-125, 2000.
- [116] M.-L. Abel, R. Joannic, M. Fayos, E. Lafontaine, S. Shaw and J. Watts, "Effect of solvent nature on the interaction of γ -glycidoxypropyltrimethoxysilane on oxidised aluminium surface: a study by solution chemistry and surface analysis," *International Journal of Adhesion & Adhesives*, vol. 26, pp. 16-27, 2006.
- [117] G. Spijksma, G. Seisenbaeva, A. Fischer, H. Bouwmeester, D. Blank and V. Kessler, "The molecular composition of non-modified and acac-modified propoxide and butoxide precursors of zirconium and hafnium dioxides," *Journal of Sol-Gel Science and Technology*, vol. 51, pp. 10-22, 2009.
- [118] J. Mackenzie and E. Bescher, "Some factors governing the coating of organic polymers by sol-gel derived hybrid materials," *Journal of Sol-Gel Science and Technology*, vol. 27, no. 1, pp. 7-14, 2003.
- [119] T. Metroke, R. Parkhill and E. Knobbe, "Passivation of metal alloys using sol-gel-derived materials - a review," *Progress in Organic Coatings*, vol. 41, no. 4, pp. 233-238, 2001.
- [120] M. Grundwürmer, *Development and Characterisation of Liquid Impact Resistant Sol-Gel Coatings*, Düsseldorf: VDI Verlag, 2008.
- [121] A. Rattana, J. Hermes and M.-L. W. J. Abel, "The interaction of a commercial dry film adhesive with aluminium and organosilane treated aluminium surfaces: a study by XPS and ToF-SIMS," *International Journal of Adhesion & Adhesives*, vol. 22, pp. 205-218, 2002.
- [122] A. Rattana, M.-L. Abel and J. Watts, "ToF-SIMS studies of the adsorption of epoxy resin molecules on organosilane-treated aluminium: adsorption kinetics and adsorption isotherms," *International Journal of Adhesion & Adhesives*, vol. 26, pp. 28-39, 2006.
- [123] C. Bertelsen, "Effects of processing variables on the structure and properties of γ -glycidoxypropyltrimethoxysilane (γ -GPS) primers on aluminium," M.S. thesis, University of Cincinnati, 1997.
- [124] A. Rattana, M.-L. Abel and J. Watts, "Degradation of interfacial chemistry of epoxy/silane/aluminium interfaces as a result of aqueous attack," *The Journal of Adhesion*, vol. 81, pp. 963-988, 2005.
- [125] H. Schmidt, S. Langenfeld and R. Naß, "A new corrosion protection coating system for pressure-cast aluminium automotive parts," *Materials & Design*, vol. 18, no. 4/6, pp. 309-313, 1997.
- [126] D. Arnott, A. Wilson, A. Rider, L. Lambrianidis and N. Farr, "Studies of the degradation of metal-adhesive interfaces with surface analysis techniques," *Applied Surface Science*, vol. 70/71, pp. 109-113, 1993.
- [127] G. Woods, S. Haq, N. Richardson, S. Shaw, R. Digby and R. Raval, "Modelling the interaction of hybrid inorganic-organic molecules on oxide surfaces: glycidyl isopropyl ether and epoxyhexane on a γ -Al₂O₃(111) mimic," *Surface Science*, Vols. 433-435, p. 199-204, 1999.
- [128] K. Shimizu, M. Abel and J. Watts, "Evaluation of the interaction and adsorption of γ -glycidoxypropyltrimethoxysilane with grit-blasted aluminium: a ToF-SIMS and XPS study," *The Journal of Adhesion*, vol. 84, pp. 725-741, 2008.
- [129] M.-L. Abel, A. Rattana and J. Watts, "The interaction of γ -glycidoxypropyltrimethoxysilane with oxidised aluminium substrates: the effect of drying temperature," *The Journal of Adhesion*, vol. 73, no. 2-3, pp. 313-340, 2000.
- [130] A. Rider and G. Mathys, "The influence of organosilane condition on films formed on aluminium characterised using RAIR and XPS," *Journal of Adhesion Science and Technology*, vol. 21, no. 8, pp. 677-703, 2007.
- [131] J. Liu, M. Chaudhury, D. Berry, J. Seebergh, J. Osborne and K. Blohowiak, "Fracture behavior of an epoxy/aluminum interface reinforced by sol-gel coatings," *Journal of Adhesion Science and Technology*, vol. 20, no. 4, pp. 277-305, 2006.

- [132] J. Liu, M. Chaudhury, D. Berry, J. Seebergh, J. Osborne and K. Blohowiak, "Effect of processing conditions on adhesion performance of a sol-gel reinforced epoxy/aluminum interface," *Journal of Adhesion Science and Technology*, vol. 22, pp. 1159-1180, 2008.
- [133] J. Liu, M. Chaudhury, D. Berry, J. Seebergh, J. Osborne and K. Blohowiak, "Effect of surface morphology on crack growth at a sol-gel reinforced epoxy/aluminum interface," *The Journal of Adhesion*, vol. 82, pp. 487-516, 2006.
- [134] A. Schütze, J. Jeong, S. Babayan, J. Park, G. Selwyn and R. Hicks, "The atmospheric-pressure plasma jet: a review and comparison to other plasma sources," *IEEE Transactions on Plasma Science*, vol. 26, no. 6, pp. 1685-1694, 1998.
- [135] P. Förnsel, C. Buske, U. Hartmann, A. Baalman, G. Ellinghorst and K.-D. Vissing, "Verfahren und Vorrichtung zur Plasmabeschichtung von Oberflächen". German Patent DE 29919142, October 30th 1999.
- [136] V. Hopfe and D. Sheel, "Atmospheric-pressure plasmas for wide-area thin-film deposition and etching," *Plasma Processes and Polymers*, vol. 4, pp. 253-265, 2007.
- [137] J. Hodgekinson, D. Sheel, H. Yates and M. Pemble, "Atmospheric pressure glow discharge CVD of Al₂O₃ thin films," *Plasma Processes and Polymers*, vol. 3, pp. 597-605, 2006.
- [138] A. Ladwig, S. Babayan, M. Smith, M. Hester, W. Highland, R. Koch and R. Hicks, "Atmospheric plasma deposition of glass coatings on aluminum," *Surface & Coatings Technology*, vol. 201, pp. 6460-6464, 2007.
- [139] W. Polini and L. Sorrentino, "Adhesion of a protective coating on a surface of aluminium alloy treated by air cold plasma," *International Journal of Adhesion & Adhesives*, vol. 27, pp. 1-8, 2007.
- [140] C. Sperandio, J. Bardon, A. Laachachi, H. Aubnet and D. Ruch, "Influence of plasma surface treatment on bond strength behaviour of an adhesively bonded aluminium-epoxy system," *International Journal of Adhesion & Adhesives*, vol. 30, no. 8, pp. 720-728, 2010.
- [141] R. Wilken, J. Ihde and J. Degenhardt, "Lokaler Korrosionsschutz von Aluminiumbauteilen durch Atmosphärendruck-Plasmabeschichtungen," *Vakuum in Forschung und Praxis*, vol. 21, pp. 34-38, 2009.
- [142] C. Regula, T. Lukasczyk, J. Ihde, T. Fladung and R. Wilken, "Corrosion protection of metal surfaces by atmospheric pressure plasma jet treatment," *Progress in Organic Coatings*, vol. 74, pp. 734-738, 2012.
- [143] L. O'Neill, N. Shephard, S. Leadley and L.-A. O'Hare, "Atmospheric pressure plasma polymerised primer to promote adhesion of silicones," *The Journal of Adhesion*, vol. 84, pp. 562-577, 2008.
- [144] C. Nwankire and D. Dowling, "Influence of nm-thick atmospheric plasma deposited coatings on the adhesion of silicone elastomer to stainless steel," *Journal of Adhesion Science and Technology*, vol. 24, no. 7, pp. 1291-1302, 2010.
- [145] T. Mertens, F. Gammel, M. Kolb, O. Rohr, L. T. S. Kotte, S. Kaskel and U. Krupp, "Investigation of surface pre-treatments for the structural bonding of titanium," *International Journal of Adhesion & Adhesives*, vol. 34, pp. 46-54, 2012.
- [146] U. Lommatzsch, "Plasmabeschichtung bei Atmosphärendruck - 100 Prozent höhere Alterungsbeständigkeit," *Adhäsion Kleben & Dichten*, vol. 52, no. 10, pp. 38-41, 2008.
- [147] C. Taylor and F. Boerio, "Plasma polymer films as adhesion promoting primers for aluminum substrates. Part I: characterization of films and film/substrate interfaces," *The Journal of Adhesion*, vol. 69, pp. 217-236, 1999.
- [148] G. Grundmeier, P. Thiemann, J. Carpentier, N. Shirtcliffe and M. Stratmann, "Tailoring of the morphology and chemical composition of thin organosilane microwave plasma polymer layers on metal substrates," *Thin Solid Films*, vol. 446, pp. 61-71, 2004.
- [149] R. Turner and F. Boerio, "Molecular structure of interfaces formed with plasma-polymerized silica-like primer films: Part I. Characterization of the primer/metal interface using infrared spectroscopy in situ," *The Journal of Adhesion*, vol. 78, pp. 447-464, 2002.
- [150] R. Turner and F. Boerio, "Molecular structure of interfaces formed with plasma-polymerized silica-like primer films: Part II. Characterization of the primer/metal interface using x-ray photoelectron spectroscopy in situ," *The Journal of Adhesion*, vol. 78, pp. 465-493, 2002.
- [151] R. Dillingham, "Effect of deposition conditions on structure and properties of plasma-polymerized silica primers," *The Journal of Adhesion*, vol. 84, pp. 702-724, 2008.

- [152] K. Wapner and G. Grundmeier, "Scanning Kelvin Probe measurements of the stability of adhesive/metal interfaces in corrosive environments," *Advanced Engineering Materials*, vol. 6, pp. 163-167, 2004.
- [153] G. Doyle and R. Pethrick, "Environmental effects on the ageing of adhesive joints," *International Journal of Adhesion & Adhesives*, vol. 29, pp. 77-90, 2009.
- [154] R. Wilken, T. Fladung, P. Schiffels, S. Dieckhoff and O.-D. Hennemann, "Interfacial diffusion of water in epoxy-based adhesive joints," in *Adhesion '05*, Oxford, 2005.
- [155] C. Liljedahl, A. Crocombe, F. Gauntlett, M. Rihawy and A. Clough, "Characterising moisture ingress in adhesively bonded joints using nuclear reaction analysis," *International Journal of Adhesion & Adhesives*, vol. 29, pp. 356-360, 2009.
- [156] F. Mittrop, "Untersuchungen über das Alterungsverhalten, die Temperaturbeständigkeit und Zeitstandsfestigkeit von Metallklebverbindungen mit und ohne Füllstoffzusätze zum Klebstoff," Ph.D. dissertation, TH Aachen, 1966.
- [157] J. Minford, *Handbook of Aluminum Bonding Technology and Data*, New York: Marcel Dekker, 1993.
- [158] M. Zanni-Deffarges and M. Shanahan, "Diffusion of water into an epoxy adhesive: comparison between bulk behaviour and adhesive joints," *International Journal of Adhesion & Adhesives*, vol. 15, pp. 137-142, 1995.
- [159] P. Underhill and A. Rider, "Hydrated oxide film growth on aluminium alloys immersed in warm water," *Surface & Coatings Technology*, vol. 192, pp. 199-207, 2005.
- [160] K. Wefers and C. Misra, "Binary and ternary alumina systems," in *Oxides and Hydroxides of Aluminum (19th Ed.)*, Alcoa Research Laboratories, 1987, pp. 36-43.
- [161] I. Olefjord and A. Nyland, "Surface analysis of oxidized aluminium. 2. Oxidation of aluminium in dry and humid atmosphere studied by ESCA, SEM, SAM and EDX," *Surface and Interface Analysis*, vol. 21, pp. 290-297, 1994.
- [162] A. Kinloch, C. Korenber, K. Tan and J. Watts, "Crack growth in structural adhesive joints in aqueous environments," *Journal of Material Science*, vol. 42, pp. 6353-6370, 2007.
- [163] D. Bland, A. Kinloch, V. Stolojan and J. Watts, "Failure mechanisms in adhesively bonded aluminium: an XPS and PEELS study," *Surface and Interface Analysis*, vol. 40, pp. 128-131, 2008.
- [164] M.-L. Abel, A. Adams, A. Kinloch, S. Shaw and J. Watts, "The effects of surface pretreatment on the cyclic-fatigue characteristics of bonded aluminium-alloy joints," *International Journal of Adhesion & Adhesives*, vol. 26, pp. 50-61, 2006.
- [165] F. Riel, "Corrosive delamination," *SAMPE Journal*, vol. 7, no. 5, pp. 16-20, 1971.
- [166] N. Rogers, "Corrosion of adhesive bonded clad aluminum," *SAE technical paper 720344*, 1972.
- [167] N. Rogers, "A comparative test for bondline corrosion: clad versus bare aluminium," in *Proceeding of the 5th National SAMPE Technical Conference*, 1973.
- [168] Y. Moji, "New technology bonding corrosion protection and durability," *SAE Technical Paper 850703*, 1985.
- [169] W. Brockmann and O.-D. Hennemann, "Failure mechanisms in the boundary layer zone of metal/polymer systems," in *Adhesive Joints*, New York, 1984, pp. 469-483.
- [170] Airbus Industrie, "AITM 5-0009 - determination of resistance to bond line corrosion," 1999.
- [171] W. Kelm, "BMBF Forschungsbericht 03 M 1030 - Teil 1: Verbesserung der Adhäsionsstabilität von strukturellen Aluminium-Klebungen," 1993.
- [172] Henkel, *MSDS Turco Liquid Smut-Go NC*, 2009.
- [173] M.-L. Abel, R. Allington, R. Digby, N. Poritt, S. Shaw and J. Watts, "Understanding the relationship between silane application conditions, bond durability and locus of failure," *International Journal of Adhesion & Adhesives*, vol. 26, pp. 2-15, 2006.
- [174] Advanced Chemistry & Technology, "Application guide AC-130 - metal alloy surface preparation for bonding," Garden Grove.

- [175] C. Regula, Schichtbildung von Plasmapolymere bei Atmosphärendruck am Beispiel von Hexamethylsiloxan (HMDSO) als Monomer, Aachen: Shaker Verlag, 2012.
- [176] S. Bhatt, J. Pulpytel, F. Krcma, V. Mazankova and F. Arefi-Khonsari, "Porous silicon & titanium dioxide coatings prepared by atmospheric pressure plasma jet chemical vapour deposition technique - a novel coating technology for photovoltaic modules," *Journal of Nano- and Electronic Physics*, vol. 3, no. 1, pp. 1021-1034, 2011.
- [177] Plasmatrete GmbH, [Online]. Available: http://www.plasmatrete.co.uk/plasma-treatment/plasma-pretreatment/plasma-coating/how_does_plasma-nano-coating_work.html. [Accessed June 2013].
- [178] A. Baker, Advances in the Bonded Composite Repair of Metallic Aircraft Structure (Volume 1), Oxford: Elsevier, 2002.
- [179] T. Gross, "BAM Forschungsbericht VI.43i-0097/09 (not published)," Bundesanstalt für Materialforschung und -prüfung, Berlin, 2009.
- [180] S. Ono, O. Böse, W. Unger, Y. Takeichi and S. Hirano, "Characterization of lithium niobate thin films derived from aqueous solution," *Journal of the American Ceramic Society*, vol. 81, no. 7, pp. 1749-1756, 1998.
- [181] S. Pinson, J. Collins, G. Thompson and M. Alexander, "Atmospheric pressure plasma cleaning of aluminium," in *3rd International Symposium Aluminium Surface Science and Technology (ASST 2003) Proceedings*, Bonn, 2003.
- [182] D. Wavhal, J. Zhang, M. Steen and E. Fisher, "Investigation of gas phase species and deposition of SiO₂ films from HMDSO/O₂ plasmas," *Plasma Processes and Polymers*, vol. 3, pp. 276-287, 2006.
- [183] Sciencelab.com Inc., MSDS hexamethyldisiloxane, 2010.
- [184] Evonik Industries, Technical information - GPS safety summary - tetraethylorthosilicate, 2010.
- [185] Shin-Etsu Chemical Co. Ltd., MSDS octamethylcyclotetrasiloxane.
- [186] Evonik Industries, Technical information - GPS safety summary - 3-glycidoxypropyltrimethoxysilane, 2010.
- [187] D. Briggs and G. Beamson, High Resolution XPS of Organic Polymers: The Scienta ESCA300 Database, Wiley, 1992.
- [188] A. Rider, "Factors influencing the durability of epoxy adhesion to silane pretreated aluminium," *International Journal of Adhesion & Adhesives*, vol. 26, pp. 67-78, 2006.
- [189] F. Grunthaler, P. Grunthaler, R. Vasquez, B. Lewis, J. Maserjian and A. Madhukar, "Local atomic and electronic structure of oxide/GaAs and SiO₂/Si interfaces using high-resolution XPS," *Journal of Vacuum Science & Technology*, vol. 16, no. 5, pp. 1443-1453, 1979.
- [190] M. Grundner and H. Jacob, "Investigations on hydrophilic and hydrophobic silicon (100) wafer surfaces by X-ray photoelectron and high-resolution electron energy loss-spectroscopy," *Applied Physics A: Materials Science & Processing*, vol. 39, no. 2, pp. 73-82, 1986.
- [191] A. Rider, "Surface properties influencing the fracture toughness of aluminium-epoxy joints," Ph.D. dissertation, University of New South Wales, 1998.
- [192] K. Blohowiak, R. Anderson, R. Stephenson and K. Preedy, "AVTIP delivery order 0004: advanced sol-gel adhesion processes," Air Force Research Laboratory, Air Vehicle Technology Integration Program, Wright-Patterson Air Force Base, 2003.
- [193] B. Johnsen, K. Olafsen, A. Stori and K. Vinje, "Silanization of adhesively bonded aluminium alloy AA6060 with γ -glycidoxypropyltrimethoxysilane. I. Durability investigation," *Journal of Adhesion Science and Technology*, vol. 16, no. 14, p. 1931-1948, 2002.
- [194] S. Emrich, "Untersuchungen zum Einfluss von Oberflächenchemie und -morphologie auf die Langzeitbeständigkeit geklebter Aluminiumverbunde," Ph.D. dissertation, Universität Kaiserslautern, 2003.
- [195] J. Bolger and A. Michaels, Interface Conversion Coatings for Polymeric Coatings, New York: Elsevier, 1967.
- [196] E. McCafferty and J. Wightman, "Determination of the concentration of surface hydroxyl groups on metal oxide films by a quantitative XPS method," *Surface and Interface Analysis*, vol. 26, pp. 549-564, 1998.

- [197] J. van den Brand, W. Sloof, H. Terryn and J. de Wit, "Correlation between hydroxyl fraction and O/Al atomic ratio as determined from XPS spectra of aluminium oxide layers," *Surface and Interface Analysis*, vol. 36, pp. 81-88, 2004.
- [198] D. Mitchell, K. Clark, J. Bardwell, W. Lennard, G. Massoumi and I. Mitchell, "Film thickness measurements of SiO₂ by XPS," *Surface and Interface Analysis*, vol. 21, pp. 44-50, 1994.
- [199] S. Tanuma, C. Powell and D. Penn, "Calculations of electron inelastic mean free paths for 31 materials," *Surface and Interface Analysis*, vol. 11, pp. 577-589, 1988.
- [200] M. Alexander, G. Thompson, X. Zhou, G. Beamson and N. Fairley, "Quantification of oxide film thickness at the surface of aluminium using XPS," *Surface and Interface Analysis*, vol. 34, pp. 485-489, 2002.
- [201] S. Tanuma, C. Powell and D. Penn, "Calculations of electron inelastic mean free paths - II. Data for 27 elements over the 50-2000 eV range," *Surface and Interface Analysis*, vol. 17, pp. 911-926, 1991.
- [202] S. Tanuma, C. Powell and D. Penn, "Calculations of electron inelastic mean free paths - III. Data for 15 inorganic compounds over the 50-2000 eV range," *Surface and Interface Analysis*, vol. 17, pp. 927-939, 1991.
- [203] P. Jussila, H. Ali-Löytty, K. Lahtonen, M. Hirsimäki and M. Valden, "Effect of surface hydroxyl concentration on the bonding and morphology of aminopropylsilane thin films on austenitic stainless steel," *Surface and Interface Analysis*, vol. 42, pp. 157-164, 2010.
- [204] D. Papée, R. Tertian and R. Biais, *Bulletin de la Société chimique de France*, p. 1301, 1953.
- [205] F. Cordier and E. Ollivier, "X-ray photoelectron spectroscopy study of aluminium surfaces prepared by anodizing processes," *Surface and Interface Analysis*, vol. 23, pp. 601-608, 1995.
- [206] A. Chilkoti and B. Ratner, "Chemical derivatization methods for enhancing the analytical capabilities of X-ray photoelectron spectroscopy and secondary ion mass spectroscopy," in *Surface Characterization of Advanced Polymers*, Weinheim, VCH, 1993, pp. 221-256.
- [207] M. Abel and J. Watts, "Examination of the interface of a model adhesive joint by surface analysis: a study by XPS and ToF-SIMS," *Surface and Interface Analysis*, vol. 41, pp. 508-516, 2009.
- [208] N. Cave and A. Kinloch, "Self-assembling monolayer silane films as adhesion promoters," *Polymer*, vol. 33, pp. 1162-1170, 1992.
- [209] R. Cayless and D. Perry, "Adhesion promotion by silanes: a study of their interfacial chemistry in a model polystyrene coating by XPS and SIMS," *The Journal of Adhesion*, vol. 26, pp. 113-130, 1988.
- [210] K. Wapner and G. Grundmeier, "Spectroscopic analysis of the interface chemistry of ultra-thin plasma polymer films on iron," *Surface & Coatings Technology*, vol. 200, pp. 100-103, 2005.
- [211] S. Dieckhoff, private communication, Bremen, 2008.
- [212] Cytec Engineered Materials Inc., FM® 73 toughened epoxy film (data sheet), Tempe.
- [213] M. Shahid and S. Hashim, "Effect of surface roughness on the strength of cleavage joints," *International Journal of Adhesion & Adhesives*, vol. 22, pp. 235-244, 2002.
- [214] M. Bowditch, "The durability of adhesive joints in the presence of water," *International Journal of Adhesion & Adhesives*, vol. 16, no. 2, pp. 73-79, 1996.
- [215] E. Plueddemann, *Silane Coupling Agents* (2nd edition), New York: Plenum Press, 1991.
- [216] J. Jethwa and A. Kinloch, "The fatigue and durability behaviour of automotive adhesives. Part I: fracture mechanics tests," *The Journal of Adhesion*, vol. 61, pp. 71-95, 1997.
- [217] P. Underhill and D. DuQuesnay, "The dependence of the fatigue life of adhesive joints on surface preparation," *International Journal of Adhesion & Adhesives*, vol. 26, pp. 62-66, 2006.
- [218] E. Thrall, "Bonded joints and preparation for bonding," *Proceedings of the AGARD-NATO Lecture Series*, vol. 102, pp. 5-1 - 5-89, 1979.

- [219] M. Rushforth, P. Bowena, E. McAlpine, X. Zhou and G. Thompson, "The effect of surface pretreatment and moisture on the fatigue performance of adhesively-bonded aluminium," *Journal of Materials Processing Technology*, Vols. 153-154, pp. 359-365, 2004.
- [220] P. Briskham and G. Smith, "Cyclic stress durability testing of lap shear joints exposed to hot-wet conditions," *International Journal of Adhesion & Adhesives*, vol. 20, pp. 33-38, 2000.
- [221] A. Mubashar, I. Ashcroft, G. Critchlow and A. Crocombe, "Moisture absorption-desorption effects in adhesive joints," *International Journal of Adhesion & Adhesives*, vol. 29, pp. 751-760, 2009.
- [222] V. Shenoy, I. Ashcroft, G. Critchlow, A. Crocombe and M. Abdel Wahab, "Strength wearout of adhesively bonded joints under constant amplitude fatigue," *International Journal of Fatigue*, vol. 31, pp. 820-830, 2009.
- [223] M. Abdel Wahab, I. Hilmy, I. Ashcroft and A. Crocombe, "Evaluation of fatigue damage in adhesive bonding: Part 2: single lap joint," *Journal of Adhesion Science and Technology*, vol. 24, pp. 325-345, 2010.
- [224] H. Khoramishad, A. Crocombe, K. Katnam and I. Ashcroft, "A generalised damage model for constant amplitude fatigue loading of adhesively bonded joints," *International Journal of Adhesion & Adhesives*, vol. 30, pp. 513-521, 2010.
- [225] P. Underhill, A. Rider and P. Livingstone, "Fatigue behaviour of aluminum bonded joints as a function of wedge test performance," *Journal of Adhesion Science and Technology*, vol. 23, pp. 555-566, 2009.
- [226] M. Stone and T. Peet, "Technical memorandum Mat 349: evaluation of the wedge Test for assessment of durability of adhesive bonded joints," Royal Aircraft Establishment, 1980.
- [227] A. Rider, "DSTO-TR-1333: the durability of epoxy adhesive Bonds formed with titanium alloy," Defence Science and Technology Organisation, Fishermans Bend, 2002.
- [228] B. Johnsen, K. Olafsen, A. Stori and K. Vinje, "Silanization of adhesively bonded aluminum alloy AA6060 with γ -glycidoxypropyltrimethoxysilane. II. Stability in degrading environments," *Journal of Adhesion Science and Technology*, vol. 17, no. 9, pp. 1283-1298, 2003.
- [229] F. Nitschké, "BMBF Teilbericht: Verbesserung der Adhäsionsstabilität von strukturellen Aluminium-Klebungen," 1993.
- [230] C. Paul, "How thermodynamics drives wet-out in adhesive bonding: correcting common misconceptions," *Journal of Adhesion Science and Technology*, vol. 22, no. 1, pp. 31-45, 2008.
- [231] J. Fiebig, J. Mazza and D. McCray, "An ALC consideration of simple sol-gel preparations for improved durability of field and depot-level bonded repairs," in *Proceedings of the Aging Aircraft Conference*, 2002.
- [232] G. Bierwagen, D. Tallmann, J. Li, L. He and C. Jeffcoate, "EIS studies of coated metals in accelerated exposure," *Progress in Organic Coatings*, pp. 148-157, 2003.
- [233] K. H. B. Allahar, G. Bierwagen and D. Tallman, "Water transport in air force organic coatings," in *Tri-Service Corrosion Conference*, Denver, 2007.
- [234] W. Vedder and D. Vermilyea, "Aluminum + water reaction," *Transactions of the Faraday Society*, vol. 65, pp. 561-584, 1969.
- [235] R. Alwitt, "Some physical and dielectric properties of hydrous alumina films," *Journal of the Electrochemical Society*, vol. 118, no. 11, pp. 1730-1733, 1971.
- [236] J. Jhde and A. Knospe, "Plasmapolymerisation bei Atmosphärendruck - von den Grundlagen zu aktuellen Forschungsprojekten," in *Plasmatreat Anwendertagung*, Birkenfeld, 2009.
- [237] F. Ostermann, *Anwendungstechnologie Aluminium*, Berlin: Springer, 2007.
- [238] G. Grundmeier and M. Stratmann, "Adhesion and de-adhesion mechanisms at polymer/metal interfaces: mechanistic understanding based on in situ studies of buried interfaces," *Annual Review of Materials Research*, vol. 35, pp. 571-615, 2005.
- [239] T. B. Coplen, W. A. Brand, J. Meija, M. Gröning, N. Holden, M. Berglund, P. De Bièvre, R. D. Loss, T. Prohaska and T. Walczyk, Atomic weights of the elements 2013 (xls), published online by CIAAW, 2013.

- [240] W. van Ooij and T. Child, "Protecting metals with silane coupling agents," *CHEMTECH*, vol. 28, no. 2, pp. 26-37, 1998.
- [241] W. van Ooij and Song, "Bonding and corrosion protection mechanisms of γ -APS and BTSE silane films on aluminum substrates," *Journal of Adhesion Science and Technology*, vol. 17, no. 16, pp. 2191-2221, 2003.
- [242] B. Tilset, F. Lapique, A. Bjorgum and C. Simensen, "Amino- and bis-silane pre-treatments for adhesive bonding of aluminium," in *Silanes and Other Coupling Agents Vol. 3*, Utrecht, VSP, 2004, pp. 51-68.
- [243] J. Sauer, "Method of treating an aluminum surface". United States Patent US 6827810, December 7th 2004.
- [244] M. Ongle, S. Maddox and P. Threadgill, *Joints in Aluminium: INALCO '98*, Cambridge: Abbingdon Publishing, 1998.
- [245] J. Bishopp, "Surface pretreatment for structural bonding," in *Handbook of Adhesives and Sealants*, Elsevier, 2005, pp. 163-214.
- [246] sura instruments, "Pyrosil flame coating device," 2013. [Online]. Available: www.sura-instruments.de.
- [247] DELO, "DELO-SACO simple blasting technique for the pretreatment of components for bonding," 2013. [Online]. Available: www.delo.de.